Dissertation

submitted to the

Combined Faculty of Mathematics, Engineering and

Natural Sciences

of Heidelberg University, Germany

for the degree of

Doctor of Natural Sciences

put forward by

Carolin Nadja Kimmig

born in Tübingen, Germany

oral examination: 07.07.2025

Warped Disks in 3D

from the formation and evolution to synthetic observations

Referees: Prof. Dr. Cornelis P. Dullemond

Prof. Dr. Henrik Beuther

There's something magical about
pushing back the frontiers of knowledge.

Sally Ride

Abstract

Planets are born in disks around young stars called protoplanetary disks. It is therefore essential to understand the physical and dynamical conditions dominating these disks. In the past decade, highly resolved observations of protoplanetary disks have transformed the research field. Many observations revealed striking non-axisymmetric structures. Some of these structures can be explained by a shadow cast from a possibly unresolved misaligned inner disk region. The abundance of such observed shadows suggests that misalignments might be common.

In this thesis, I investigate the formation, evolution and appearance of warped protoplanetary disks. To study their dynamics, I use three-dimensional grid-based simulations, a method which is not commonly used in previous models of warps. I therefore extensively test its applicability to disks misaligned with the intrinsic geometry of the grid. I find that warps can be modeled accurately under the condition of a sufficient vertical resolution. My simulations show the expected wave-like warp evolution and additionall reveal an internal twisting of the disk, which is not included in standard one-dimensional models. My various tests suggest that the twisting is a physical effect intrinsic to the three-dimensional warp evolution.

I apply the grid-based method to a formation scenario of warps: inclined stellar flybys. I first investigate different configurations of the fly-by trajectory with respect to the disk. The simulations show that inclined fly-bys can excite a warp of a few degrees which can last for over ten thousand years. I then model RW Aur A, an observed star-disk system that recently experienced a close encounter with another star with a well constrained trajectory. My models show that a warp of about 5° misalignment is excited, which is consistent with the observations.

Shadows, mainly observed in scattered light observations, can give insight into the warp shape. In order to find limits on the observability of warps, I investigate the shadows in radiative transfer simulations of disks viewed edge-on, where warps can cause asymmetries. I find that under optimal conditions, small warps with a misalignment of only 2° can create observable asymmetries. As the strength of the asymmetry depends on the orientation of the warp with respect to the observer, it remains challenging to infer constraints on warps from observations. However, rare orientations can lead to a brightness swap between the disk surfaces, a clear indication of a warp, which is observed in a handful of disks.

Kurzfassung

Planeten entstehen in protoplanetaren Scheiben. Die physikalischen und dynamischen Bedingungen in diesen Scheiben sind daher wichtig. Im letzten Jahrzehnt haben neue hochauflösende Beobachtungen das Forschungsfeld grundlegend verändert. Viele dieser Beobachtungen zeigten auffällige, nicht-achsensymmetrische Strukturen. Manche dieser Strukturen können durch Schatten von einer inneren, geneigten Region der Scheibe entstehen. Scheiben mit einer solchen geneigten Region heißen S-förmig verformte Scheiben (engl. warped disks).

In dieser Arbeit untersuche ich die Entstehung, Entwicklung und das Erscheinungsbild dieser gewarpten Scheiben. Dafür simuliere ich die Dynamik der Scheiben mithilfe von dreidimensionalen, gitterbasierten Modellen. Diese Methode wurde bisher kaum für gewarpte Scheiben eingesetzt, weil die Geometrie des Gitters das Ergebnis numerisch beeinflussen könnte. Deshalb untersuche ich ausführlich, unter welchen Bedingungen die Methode für gewarpte Scheiben anwendbar ist. Meine Tests zeigen, dass Warps bei ausreichender vertikaler Auflösung gut modelliert werden können. Die Simulationen von gewarpten Scheiben ergeben die erwartete wellenartige Entwicklung des Warps. Zusätzlich beobachte ich eine innere Verdrehung der Scheibe, die bisher in eindimensionalen Modellen nicht gefunden wurde. Meine verschiedenen Tests legen nahe, dass diese Verdrehung durch einen physikalischen Effekt der Warpdynamik entsteht.

Ein Warp kann durch den Vorbeiflug eines Sterns entstehen, wenn die Flugbahn im Vergleich zur Scheibenebene geneigt ist. Solche Vorbeiflüge werden Fly-bys genannt. In meinen Simulationen untersuche ich zunächst verschiedene Bahnen der Fly-bys. Dabei entstehen Warps von wenigen Grad, die über zehntausend Jahre bestehen bleiben können. Anschließend simuliere ich RW Aur A, eine reale Scheibe, die kürzlich an einer nahen Begegnung mit einem anderen Stern beteiligt war. Meine Simulationen ergeben einen Warp von etwa 5°, was mit den Beobachtungen übereinstimmt.

In Streulichtbeobachtungen von gewarpten Scheiben sind Schatten sichtbar, die Aufschluss über die Form des Warps geben können. Ich untersuche die Schatten in Strahlungstransfersimulationen, um Grenzen der Beobachtbarkeit zu bestimmen. Dabei konzentriere ich mich auf Scheiben, die von der Seite mit Blick auf den Rand beobachtet werden. Aus diesem Blickwinkel können Asymmetrien durch Warps beobachtet werden. Ein Ergebnis meiner Arbeit ist, dass unter optimalen Bedingungen beobachtbare Asymmetrien bereits für kleine Warps von nur 2° entstehen können. Da die Stärke der Asymmetrie von der Orientierung der gewarpten Scheibe relativ zur Beobachtungsrichtung abhängt, bleibt es jedoch schwierig, aus Beobachtungen genaue Rückschlüsse auf die Warps zu ziehen. Seltene Orientierungen können jedoch zu einem Helligkeitstausch zwischen den Scheibenoberflächen führen, was ein klares Indiz für einen Warp ist und bereits in einigen Scheiben beobachtet wurde.

Contents

1 Introduction

What is shaping the gas and dust around a star to form planets, moons, and asteroids as in our Solar System? Protoplanetary disks hold the answer to this fundamental question that has been asked for centuries. A brief look at historical literature and art makes it very apparent that people have always been fascinated by the night sky. And truly, how can anyone not be fascinated by the sheer endlessness of the Universe? The image in Figure 1.1 shows an impressive insight into the deep Universe. Except for the few dots with cross-shaped diffraction spikes, which are stars and other bright objects within our Milky Way, most dots in this image are whole galaxies containing hundreds of millions of stars. And the vast majority of the stars in these galaxies likely hosts at least one planet. This is an estimation by Cassan et al. (2012) with respect to our own galaxy, but it is not far-fetched to extend this estimation to other galaxies as well.

Figure 1.1: A part of the Universe imaged by the JWST telescope, released on Dec. 4th, 2024. *Credit: ESA/Webb, NASA & CSA, H. Dannerbauer. CC BY 4.0*

Discovering planets outside our Solar System, called extrasolar planets or exoplanets in short, is far from easy. So far, it is only possible to detect planets within our Milky Way, as other galaxies are too distant to be resolved well enough. Even in our Milky Way, planets can only be detected within a confined region. One of the farthest detected exoplanets (called OGLE-2014-BLG-0124Lb) lies nearly 4 kpc away from our Solar System. For comparison, the Milky Way has a radius of about 13 kpc. As of now, 7454 exoplanets have been detected[1], with this number rapidly growing. Only a few years ago, when I started my undergraduate research in this field, there were merely 4000 discoveries. This is a big leap considering the challenges of exoplanet detection, as planets often have radii ten to a hundred times smaller than the radius of their star. Trying to catch their light is like trying to see a firefly next to a light house hundreds of meters away.

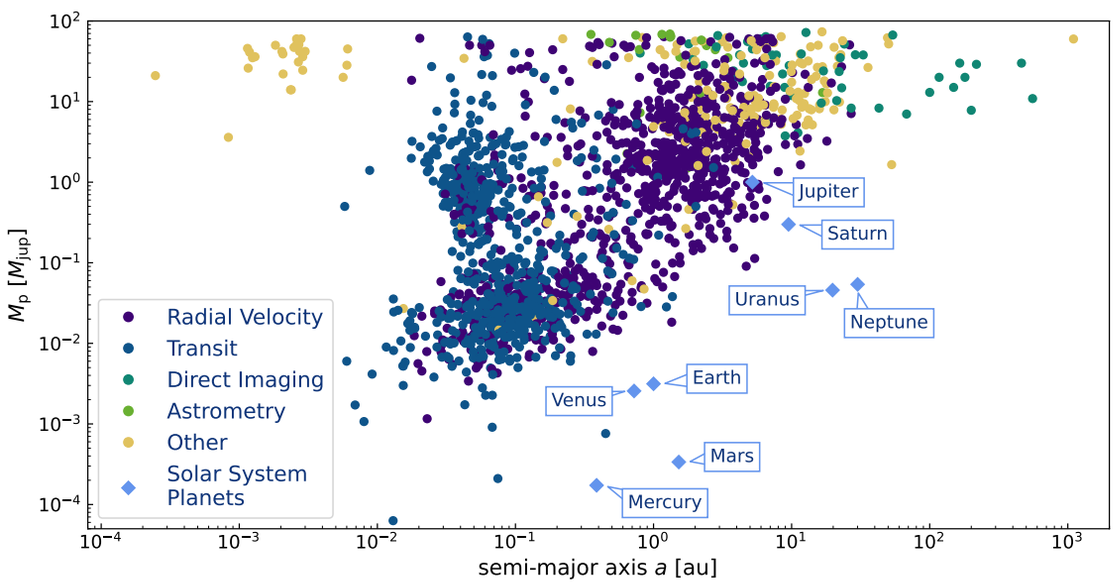

Figure 1.2: Discovered exoplanets with their mass and distance to the star. The colors indicate the detection method. For comparison, the Solar System planets are plotted with light blue diamonds. *Data for exoplanets obtained from the exoplanet.eu database, and for the Solar System planets from NASA.*

A trick to directly image a planet is to use a coronograph to block the light from the star. A famous system that contains four directly imaged planets is HD 8799. By monitoring the planets over time, astronomers have been able to trace their orbits. Another famous directly imaged planet is PDS 70b, a planet still embedded in a protoplanetary disk. Observations like these are technological marvels and offer invaluable insight into the formation of planetary systems. However, direct imaging is only possible for a few large (and therefore bright) planets with large orbital separation around stars close to the Sun.

[1] As of April 21th, 2025, https://exoplanet.eu/

There are multiple indirect methods to detect exoplanets. One of the two main methods is the *radial velocity method*, where the small motion of the star around the common center of mass with the planet can be measured (Mayor & Queloz, 1995). This method tracks the star's spectral lines, which are red- and blue-shifted as the star moves away from and toward us along the line of sight, respectively, and thereby indirectly reveals the presence of a planet. The first planet around a main sequence star was detected using this method. However, the radial velocity method is only feasible for massive planets, as they have a stronger effect on the star's movement.

The second main method is the *transit method*, where the flux of the star is continuously measured (Charbonneau et al., 2000). If the planet's orbit is oriented in such a way that it passes in front of the star in our line of sight, the planet covers a tiny portion of the star, which leads to a tiny but measurable decrease in the star's flux. With this method, the Kepler and TESS missions have found the vast majority of the currently detected exoplanets. It is especially reliable when multiple orbits can be captured, it therefore favors planets on close orbits with small semi-major axes.

Further methods involve astrometry, micro-lensing, kinematics, and transit-timing variations. Of course, each of the detection methods holds their own advantages as well as limitations. Together, they can reveal a larger picture of exoplanet diversity (see for example Lunine et al., 2009). The Gaia mission offers a promising future: Combining the use of three methods, namely astrometry, transit, and radial velocity methods, the mission might lead to the new detection of ten thousands of exoplanets. The next data release (DR4) is expected by the end of the year 2025.

Figure 1.2 shows the exoplanets discovered with the different methods. The planetary masses M_p (in terms of Jupiter masses M_jup) are shown on the y-axis, while the x-axis marks the distance to their host star, characterized by the semi-major axis a. This figure reveals a wide spread of planet properties. Especially the large population of massive planets very close by their host stars, often called *hot Jupiters*, was one of the surprising and puzzling finds in the history of exoplanet detection, as such planets do not exist in our Solar System. Knowing this variety of exoplanets, a very natural question is: How do those planets form? As the diversity of these planets suggests, the planet-forming environment is highly complex, governed by many dynamical processes. This is one of the reasons why it is important to research the planet-forming environment: protoplanetary disks.

1.1 Protoplanetary disks

Planets are born in protoplanetary disks. Those disks encircle a young star and contain gas, mainly hydrogen and helium, as well as dust. Let us take a closer look at the evolution and observation and characteristics of these birth environments of planets.

1.1.1 Origin of disks

A protoplanetary disk forms as a result of angular momentum conservation during the formation of a star, which in turn forms from a collapsing molecular cloud (Shu et al., 1987). A molecular cloud is governed by dynamical motions and flows, forming irregular structures in the large-scale star-forming region (Lada, 2005; Draine, 2011). This leads to local variations of density in the molecular cloud that form clumps, also called cloud cores. These cloud cores have a typical size of $\sim 0.1\,\mathrm{pc}$, and within this region pressure forces and gravity balance each other. Figure 1.3 shows observations of the Taurus star-forming region, which contains many cloud cores and already-formed stars hosting disks.

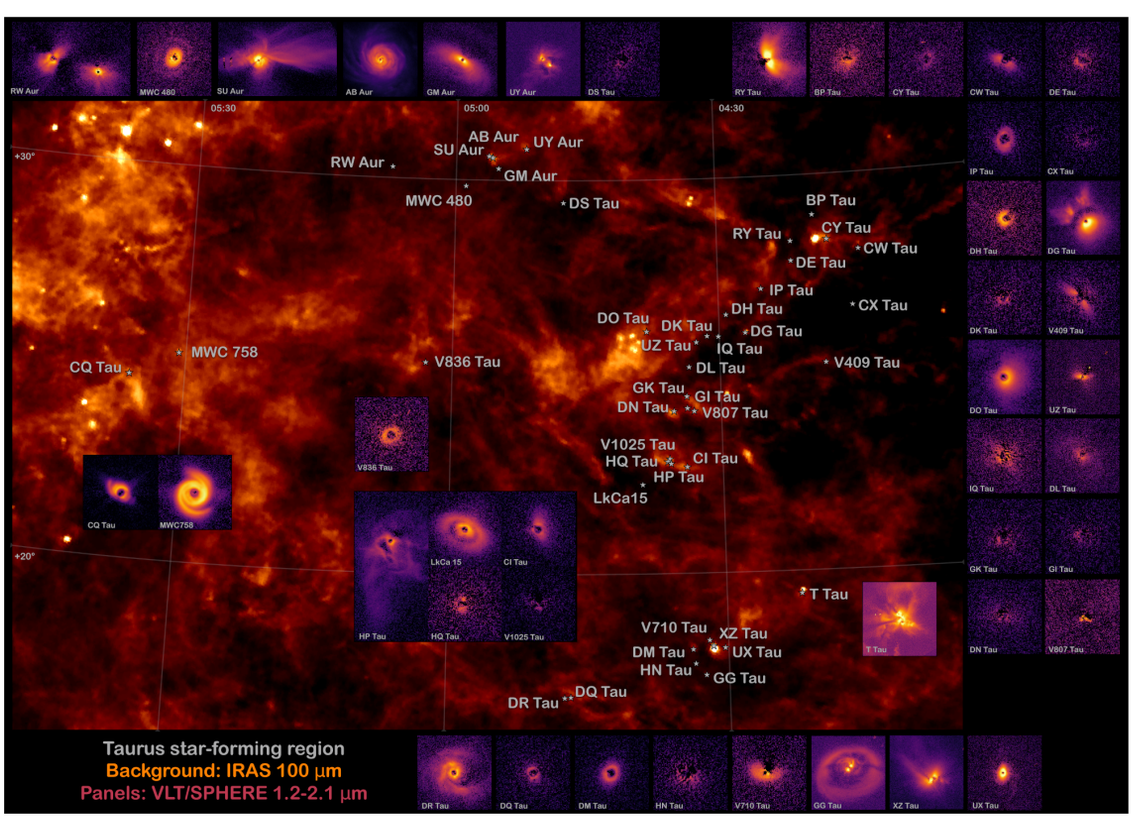

Figure 1.3: The Taurus star-forming region, showing substructures and many newly formed stars hosting a disk. *Credit: Garufi et al. (2024). CC BY 4.0*

Due to the dynamic flows, some cloud cores can become so dense that self-gravity wins over the thermal pressure forces, and the core begins to collapse. The collapse of a cloud core begins when the core's mass exceeds a critical mass, called Jeans-mass M_{J} (Jeans, 1902). This mass can be derived by energy considerations and reads

$$M_{\mathrm{J}} = 2.5\, M_{\odot} \left(\frac{T}{10\,\mathrm{K}}\right)^{3/2} \left(\frac{n}{10^4\,\mathrm{cm}^{-3}}\right)^{-1/2}, \tag{1.1}$$

where T is the temperature of the cloud core and n the number density of gas and dust particles in the core. Once the collapse has started, the material is free-falling toward the center of the cloud core, forming a pressure-supported protostar. The free-fall timescale depends on the cloud's density, but is typically on the order of $10^4 - 10^5$ years.

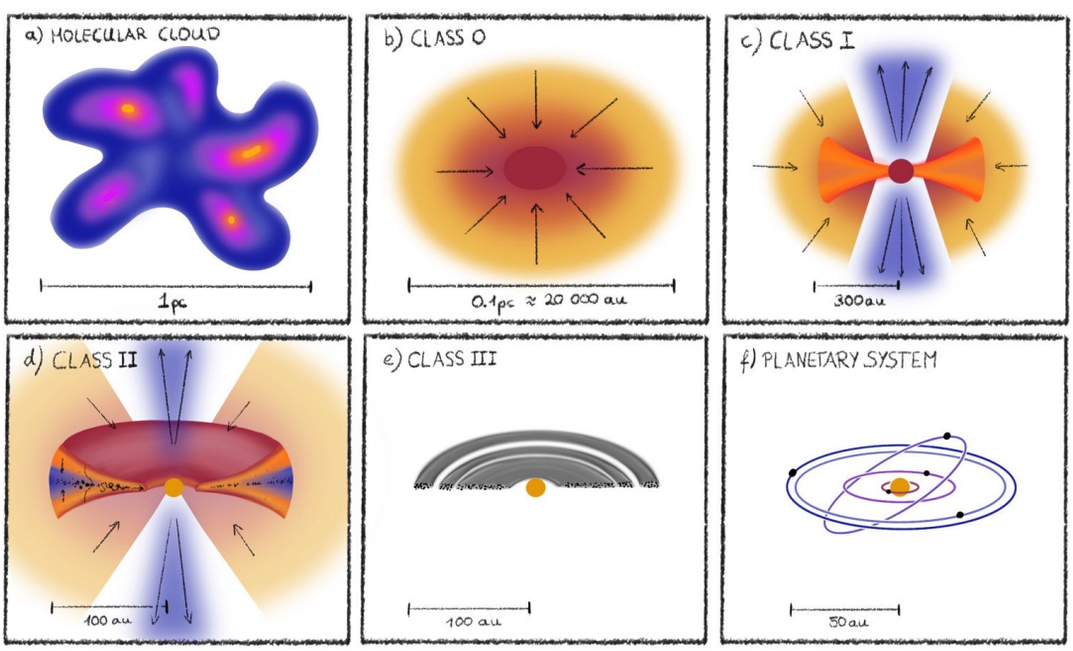

Figure 1.4: Sketch of star formation and different types of protoplanetary disks. **a)** Star forming region with dense (purple) cloud cores. **b)** Class 0: Collapsing cloud core. **c)** Class I: Circumstellar disk embedded in an envelope, where jet outflows are present. **d)** Class II: Planet-forming disk with accretion processes, residual inflow from the envelope, dust settling and trapping, and more. **e)** Class III: Debris disk containing dust and rocks, but no or little gas. **f)** Planetary system. *Inspired by Greene (2001).*

During this process, a disk can form around the young star. This occurs when the initial cloud contains angular momentum due to the natural dynamic movement and flows. In the collapse, the angular momentum is conserved, but because the cloud shrinks by several orders of magnitude, the orbital velocities increase, which allows some material to collect in a disk. Because a molecular

cloud is unlikely to have zero initial angular momentum, disks form around most young stars. However, disks are transient and only last up to several million years, which is $\sim 10^{-4} - 10^{-3}$ of the lifetime of a main-sequence star. This means that with respect to all stars, disks are rare (Armitage & Kley, 2019). Note that this is a simplified picture of star and disk formation and evolution. Additional processes, such as magnetic fields and turbulence, contribute to the complexity of the development.

Disk systems can be classified (see e.g. Williams & Cieza, 2011), as indicated in Figure 1.4. The classification scheme for this was created at a time when protoplanetary disks could not yet be spatially resolved in observations. The only indication for the presence of disks was found in the spectral energy distribution (SED, energy plotted against wavelength) of stars, which showed an excess of infrared radiation compared to a black body. This excess occurs because the disk is heated up by the star and thermally radiates, adding to the infrared emission. The classification scheme I describe in the following is based on this infrared excess in the SED (Lada, 1987).

Class 0 objects show no optical or near-infrared emission, because they are deeply embedded in surrounding material and therefore heavily obscured, leading to a peak emission in the sub-millimeter wavelength regime. This surrounding envelope typically has a size of around $\sim 0.1\,\mathrm{pc} = 20,000\,\mathrm{au}$. This class is usually interpreted as a very early stage where the molecular cloud is still collapsing and disks are only just starting to form.

On the other hand, Class I sources show emission in the optical and near-infrared with a strong excess and peak emission in the far-infrared regime. These objects are disks that are still embedded in an envelope, causing violent conditions as the material is falling onto the disk. Jets can form ejecting material and clearing a part of the envelope. Typical radii of Class I systems are around 300 au. On the other hand, Class II disks have a flatter excess in the infrared, which leads to an emission peak in the near-infrared. These disks are more compact with only little envelope surrounding the object. Here, angular momentum transport processes play a significant role and lead to an active accretion of material through the disk and onto the star. Class III disks consist mainly of rocks and dust with only little gas. Therefore, their emission peak lies in the visible regime of the spectrum, and they only show a weak infrared excess in the SED.

A special class of disks show a strong excess in the far-infrared radiation of the SED, but no excess at all in the mid-infrared wavelengths. This can be caused by a large cavity, as found for example by Calvet et al. (2002). Disks with a large cavity are called transition disks (see Espaillat et al., 2014), as they were originally thought to be a transitional phase between Class II and Class III disks. However,

developments in research have shown that the classification scheme is likely not an evolutionary sequence, as there is for example no evidence that Class III disks are generally older than Class II disks. Nevertheless, the term transition disks remains in use for these types of disks.

Disks of Class I and II and transition disks are thought to be the main sites for planet formation, therefore called protoplanetary disks. In the following sections, I will focus on these disks.

1.1.2 Observations of protoplanetary disks

For a long time, the only observational evidence of protoplanetary disks was the infrared excess in the SED of stars. In 2016, one of the very first spatially resolved observations of a protoplanetary disk amazed the research community: The disk around HL Tau (Figure 1.5) shows rings and gaps and other substructures that were previously thought to be rare. Together with further observations, the insight that substructures are common has advanced the research field, which led the focus of the research on the origin of the substructures.

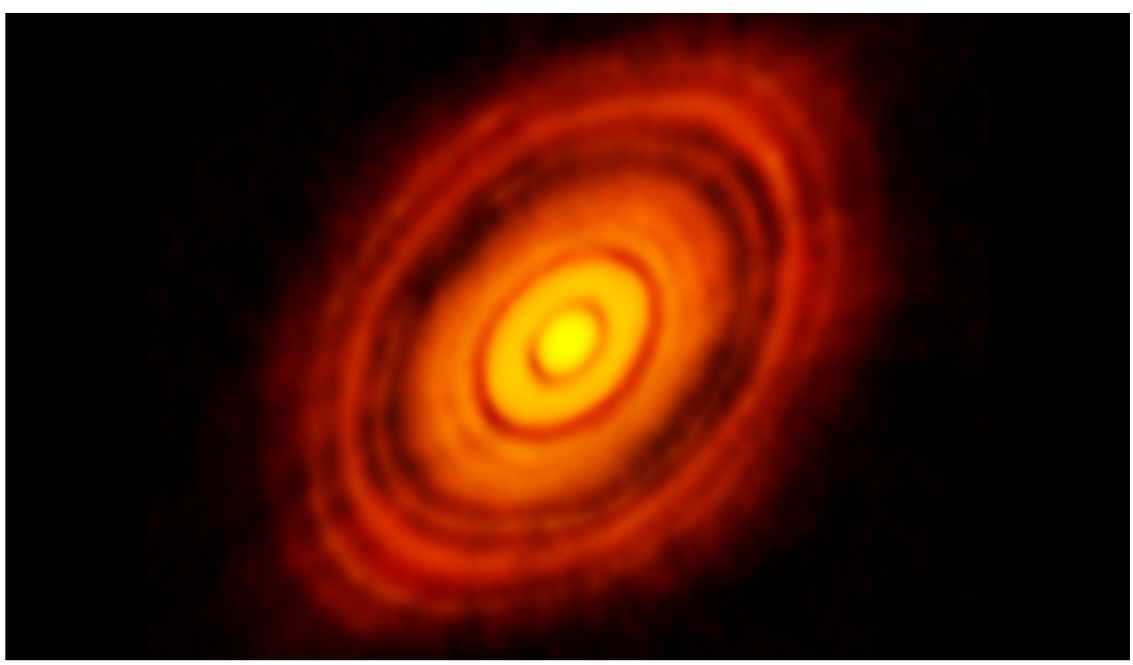

Figure 1.5: First spatially resolved image of the protoplanetary disk around HL Tau, revealing substructures such as rings and gaps. *Credit: ALMA (ESO/NAOJ/NRAO). CC BY 4.0*

Technology and imaging techniques have evolved even further since then, and nowadays, there is a plethora of beautiful and well resolved images (see Andrews, 2020, for a review), with a few examples presented in Figure 1.6.

In astrophysics, different astronomical objects emit light in different wavelengths, depending on their temperature and physical nature of the emission. Therefore, the optimal observational technique depends on the target. Because protoplanetary disks contain dust that is heated by the star, a good way to observe them is to look at the thermal emission by the dust. This occurs at long wavelengths, especially in the radio regime ($\sim \lambda = 1\,\text{mm} - 100\,\text{km}$). This is why the images in Figures 1.5 and 1.6 are taken by the Atacama Large Millimeter/submillimeter Array (ALMA) at $\lambda = 1.28\,\text{mm}$ (HL Tau) and $\lambda = 1.25\,\text{mm}$ (DSHARP, Andrews et al., 2018). As the dust is often settled to deeper layers, these observations trace the disk's midplane.

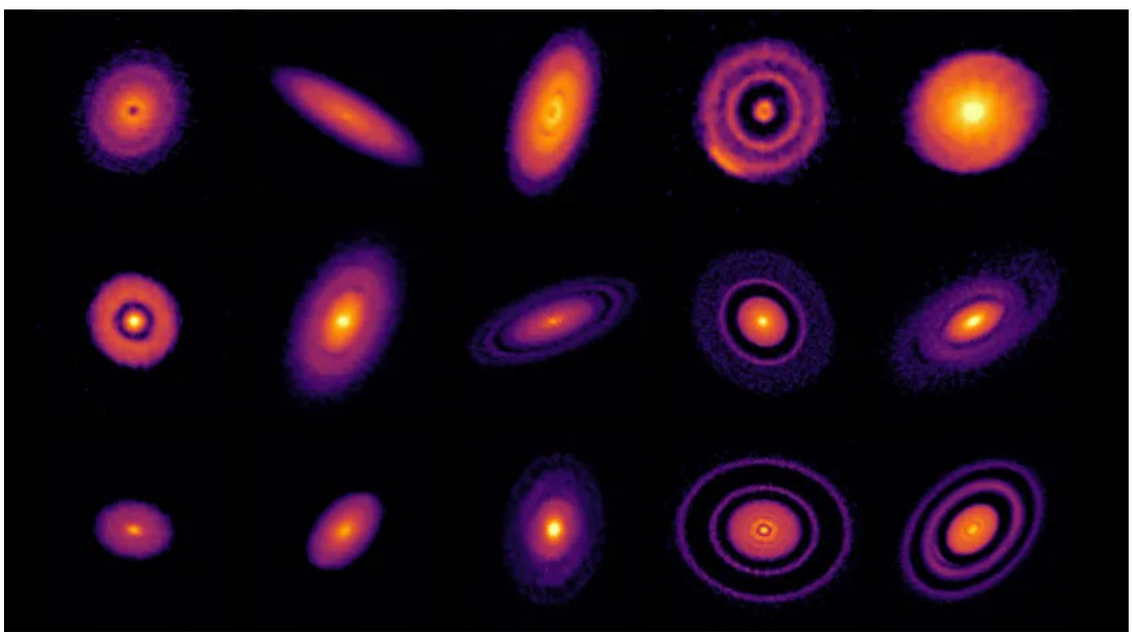

Figure 1.6: Observations of multiple protoplanetary disks, showing the diversity of substructures: rings, gaps, plateaus, spirals, cavities, non-axisymmetric arcs etc. *Credit: ALMA (ESO/NAOJ/NRAO), S. Andrews et al.; NRAO/AUI/NSF, S. Dagnello. CC BY 4.0*

The ALMA telescope is composed of 66 antennas[2] that can be interconnected using interferometry to achieve a high angular resolution. Interferometry takes advantage of the fact that light from the same source arrives at the different antennas slightly phase shifted, because it travels slightly different distances. This phase shift creates an interference pattern that can be evaluated to find the path difference from the light source, giving insight into the exact location where the light originated. This allows us to sample the two-dimensional structure of the light source by pairwise measurements of amplitude and phase between the different antennas (see e.g. Léna et al., 2012). These pairwise measurements can then be combined to obtain high resolutions.

[2] https://www.almaobservatory.org/en/about-alma/

The resolution of a (single instrument) telescope depends on the observed wavelength λ_{obs} and the diameter of the telescope D

$$\theta_{\text{res}} \approx 1.22 \, \frac{\lambda_{\text{obs}}}{D}, \tag{1.2}$$

where θ_{res} is the minimum angle that can be resolved with the telescope. The smaller θ_{res}, the larger the resolution. Interferometry can achieve a resolution as if the telescope had a diameter equal to the longest distance between antennas (= baseline b), with $D = b$. Therefore, longer baselines mean better resolutions and sharper images, though it comes with a trade-off of a lower measured brightness for longer baselines. The resolution depends not only on the distance of the telescope antennae, but also on their placement. ALMA's antennas are movable and can be rearranged in different configurations, with baselines ranging from 150 meters to 16 kilometers.

For ground-based observations, another factor that influences the resolution is Earth's atmosphere. The atmosphere can absorb and deflect light, and turbulence can induce phase changes, leading to aberration effects that are often summarized as *seeing* (see e.g. Chromey, 2010). For even better resolution, astrophysical observations can be corrected for these seeing effects, for example using the adaptive optics technology, which can change the shape of the telescope surface according to the current atmospheric effects. Luckily for radio astronomy, Earth's atmosphere is almost completely transparent to radio emission and usually does not cause strong aberrations. Additionally, radio telescopes are often built in dry and highly elevated locations (such as the Atacama desert) to achieve the least amount of water vapor that pollutes the ground-based observations.

Protoplanetary disks can not only be observed in the radio wavelength regime. In the visible light regime ($380 - 700\,\text{nm}$) to the near-infrared regime ($0.7 - 3\,\mu\text{m}$), disks can be observed in so-called scattered light observations. This is the light scattered by the disk from the star toward us observers, and can be separated from the direct, much brighter light emitted by the star. These observations typically trace the surfaces of the disks. Because the midplane of disks is optically thick in these wavelengths, which means that the light is absorbed or scattered before it reaches the midplane, disks in these wavelengths show a typical sandwich shape, as seen in Figure 1.7, left panel.

Additionally, molecular line emission can give insight into the dynamics of protoplanetary disks. Molecular lines are emitted because of transitions of excitation states or rotations or vibrations of molecules, and always occur at the same wavelength for the same transition. In protoplanetary disks, the most abundant molecule is hydrogen (H_2). However, most hydrogen in disks is cold and, there-

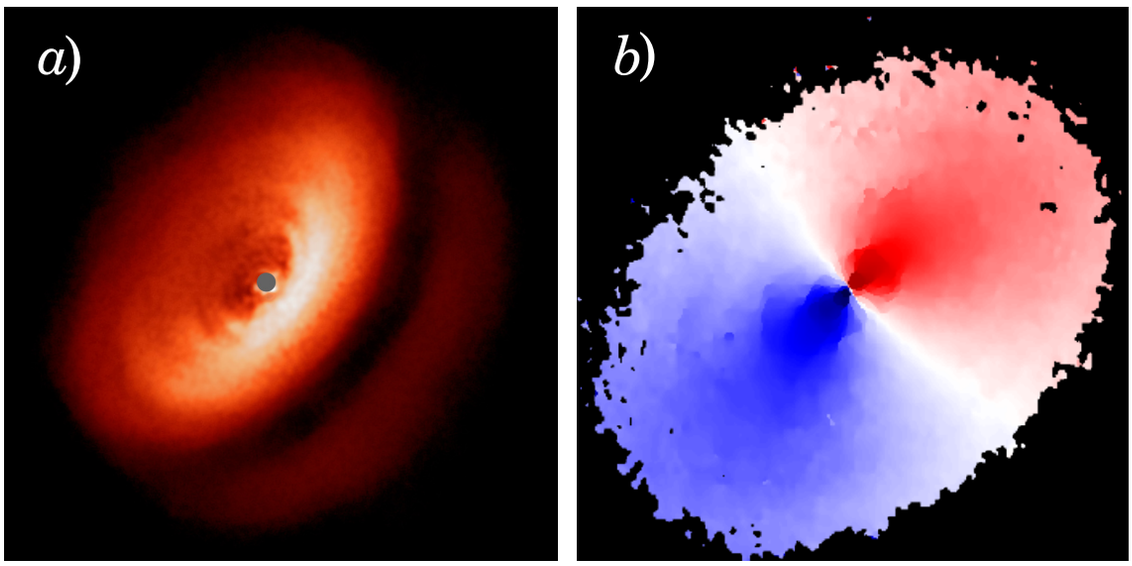

Figure 1.7: Observations of protoplanetary disks in different wavelengths. **a)** IM Lup observed in scattered light (near-infrared H-band, $\lambda = 1.62\,\mu$m) with the VLT/SPHERE telescope. *Credit: ESO/H. Avenhaus et al./DARTT-S collaboration. CC BY 4.0* **b)** HCN 3–2 line observation ($\lambda = 1.13$ mm) of HD 163296, showing the dynamics of the system. Presented is the velocity along the line of sight (called *Moment 1*), where blue means gas moving toward us and red means gas moving away. *Credit: Öberg et al. (2021), extracted from their Figure 3.*

fore, not in an excited state. Only in the hot surfaces of the disk, stellar radiation can excite hydrogen and cause low Lyman-alpha (Lyα) emission in the far ultra-violet wavelengths. Additionally, because the architecture of hydrogen is perfectly symmetric, it does not have rotational or vibrational transitions. This makes hydrogen very hard to observe. In order to trace molecular line emission in protoplanetary disks, it is therefore necessary to resort to the second most abundant molecule: CO, of which the main isotopologues are ^{12}CO, ^{13}CO, and C^{18}O. These molecules are asymmetric and therefore can be observed through their rotational and vibrational transitions in the near-infrared regime on the order of $\lambda = 100\,\mu$m. Other abundant molecules, such as CS, HCN, N_2H^+, or water (H_2O) can be observed as well (Dutrey et al., 2014). An example is shown in Figure 1.7, right panel.

The advantage of molecular lines is that the exact emission wavelength is known. This enables an investigation of the dynamics in a system by looking at slightly red- and blue-shifted components of the line due to the Doppler effect, tracing molecules moving away from or toward us, respectively. This method is called kinematics. For a moderately inclined (with respect to the line of sight) protoplanetary disk, we can thus observe the gas motion around the central star. Note that this method fails for disks viewed perfectly face-on, as there are no

velocity components along the line of sight. With kinematics, the dynamics of surrounding material, such as streamers onto the disk, can also be investigated (Pinte et al., 2023).

Observations play a vital role in the advancement of the research on planet formation. They are crucial to understand the conditions in disks and to test and refine the theoretical framework. On the other hand, theoretical insights are vital for interpreting observational data. This integral synergy requires close collaboration between the two departments. While this thesis looks more closely at the theoretical side, I aim to bridge the gap between theory and observations by creating synthetic images of the models that can easily be compared with observations (see Section 2.5 for an introduction on the methods to create synthetic observations).

1.1.3 Disk structure

Accretion disks have been investigated even before the discovery of planets and protoplanetary disks. The theoretical ground work laid out for these accretion disks applies well to protoplanetary disks and can give a good description of their structure.

Vertical disk structure

To describe the structure of disks, a fundamental property is the density ρ. The vertical density structure of a disk is a result of hydrostatic equilibrium, the balance between gas pressure and gravitation. The equilibrium can be expressed as

$$\frac{\mathrm{d}P}{\mathrm{d}z} = -\rho g_z, \tag{1.3}$$

where z is the height above the disk midplane, P is the pressure, and g_z the vertical component of the gravitational acceleration due to the host star $g = GM_*/r^2$, with M_* as the host star's mass. For low-mass disks, which seem to be common around young stars, we neglect the disk's self-gravity and obtain from a geometry consideration that

$$g_z = \frac{GM_*}{r^2+z^2}\sin\theta \;=\; \frac{GM_*}{\left(r^2+z^2\right)^3}z \;\approx\; \Omega_k^2 z, \tag{1.4}$$

with θ as vertical spherical coordinate, where we used the trigonometric relation $\sin\theta = z/(r^2+z^2)^{1/2}$. For the last term, we used the approximation of a thin disk, where $z \ll r$, and the Kepler frequency $\Omega_k = \sqrt{GM_*/r^3}$. Applying the

ideal gas equation

$$P = \rho c_s^2, \tag{1.5}$$

where c_s is the sound speed, leads to a differential equation of the hydrostatic equilibrium

$$c_s^2 \frac{d\rho}{dz} = -\Omega_k^2 \rho z, \tag{1.6}$$

which can be solved with a Gaussian

$$\rho(z) = \rho_0 \exp\left(-\frac{z^2}{2H_p^2}\right). \tag{1.7}$$

Here, we define the pressure scale height $H_p \equiv c_s/\Omega_k$ and the midplane density ρ_0. Figure 1.8, top right panel, shows the vertical density structure in an example.

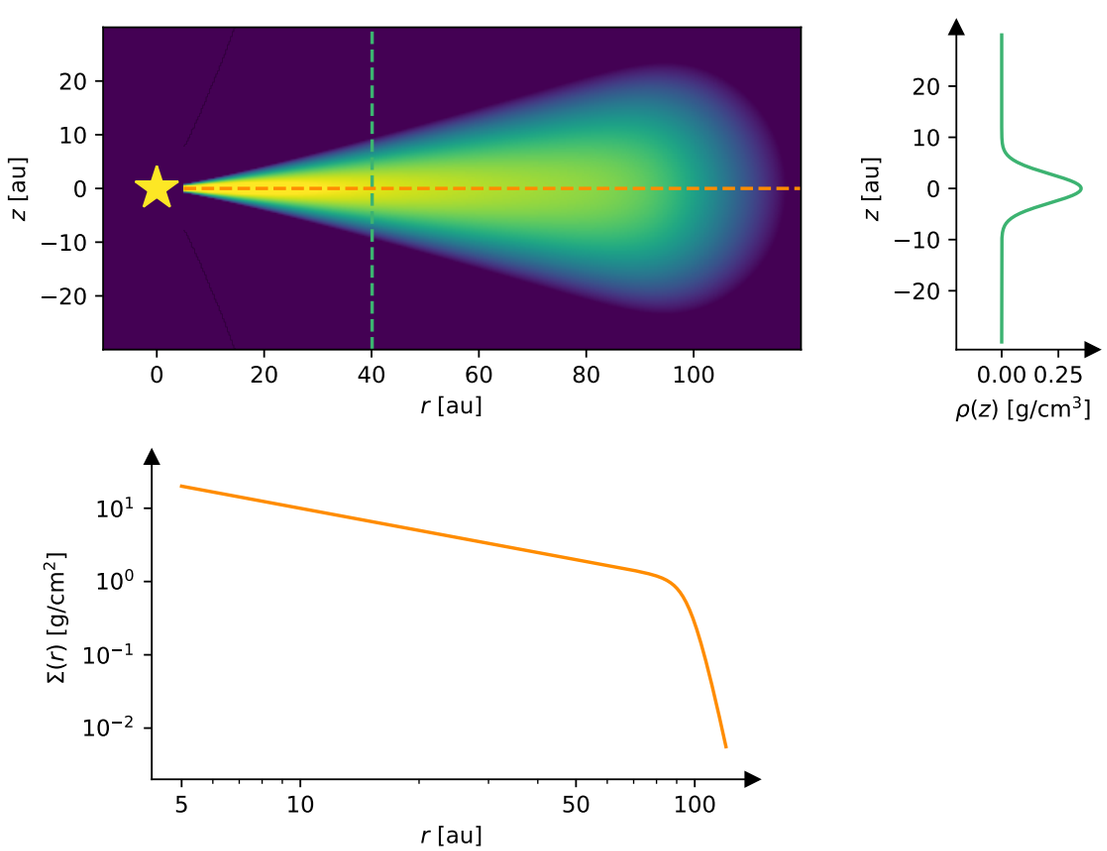

Figure 1.8: Cross-section of a standard protoplanetary disk model (top left panel). The orange dashed line in the cross-section indicates the disk midplane, and the green dashed line indicates the location of the vertical density structure (following Equation 1.7) shown in the right panel. The bottom panel shows the radial profile of the surface density (in log-log scale to highlight the power law, Equation 1.8). In this model, the surface density is exponentially cut off at the outer disk edge.

Radial structure

The radial density structure of a disk can not be easily derived in an analytical approach because disks can be stable for a variety of radial structures. It therefore needs to be measured in observations and/or investigated in numerical simulations. A convenient way to describe the radial density structure is to define the vertical column density $\Sigma = \int \rho dz$. This is commonly referred to as surface density as it is measured in units related to a surface g/cm^2. The surface density is often assumed to follow a power law depending on the distance from the star r

$$\Sigma \propto r^{-p}, \tag{1.8}$$

with the slope p typically ranging from $p = 0.4 - 1$, as often found in observations (Andrews et al., 2009). Additionally, a power law is convenient for numerical simulations as power laws are typically self-similar, meaning that the absolute value can be scaled without affecting the qualitative outcome of simulations. Integrating Equation 1.7, the surface density can be related to the density ρ with

$$\rho = \frac{1}{\sqrt{2\pi}} \frac{\Sigma}{H_\mathrm{p}}. \tag{1.9}$$

The azimuthal velocity of gas (velocity in the orbital direction) is typically assumed to be Keplerian, which can be derived from an equilibrium between centripetal and gravitational force

$$v_\phi = v_\mathrm{k} \equiv \sqrt{\frac{GM_*}{r}}, \tag{1.10}$$

where G is the gravitational constant.

Pressure gradients in the disk lead to an additional pressure support

$$\frac{v_\phi^2}{r} = \frac{GM_*}{r^2} + \frac{1}{\rho} \frac{\mathrm{d}P}{\mathrm{d}r}, \tag{1.11}$$

which means that the azimuthal velocity (at the disk midplane) needed for an equilibrium in the radial direction is less than the Keplerian velocity ($v < v_\mathrm{k}$). In most disk models, this is corrected using an additional velocity term, which is on the order of $(H_\mathrm{p}/r)^2$. Potential dust particles, on the other hand, are not influenced by the gas pressure gradients and therefore move at Keplerian speed. The difference between gas and dust velocities (usually) results in an inward drift of the dust. Note that this consideration relates to the velocity close to the disk midplane. The vertical velocity structure is usually more complex, as more pressure

gradients occur close to the disk surfaces.

Temperature structure

Another important quantity characterizing a disk is its temperature. The disk temperature is determined by heating and cooling processes within the disk. The heating in protoplanetary disks is mainly dominated by two factors: the irradiation from the host star, and the friction due to viscosity and perturbations in the disk. The effects causing viscosity will be discussed later in Section 1.2.2. For the cooling of the disk, the main mechanism is the disk's radiation, which occurs for example due to thermal emission from the dust or molecular line emission.

The temperature determines the vertical thickness of the disk, because the pressure scale height H_p is proportional to the sound speed, which depends on the temperature. The thermal physics in disks is very complex, and for a more detailed context, I refer to reviews such as Armitage (2007) and Armitage & Kley (2019). Even though it is not the most realistic treatment, the assumption of an isothermal disk is often adopted to greatly simplify the treatment of the disk temperature. As mentioned before, in an isothermal disk, we can use the ideal gas equation $P = \rho c_\mathrm{s}^2$, where the isothermal sound speed relates to the temperature as

$$c_\mathrm{s} = \sqrt{\frac{k_\mathrm{B} T}{\mu m_\mathrm{p}}}. \tag{1.12}$$

Here, k_B is the Boltzmann constant, μ is the mean molecular weight, which is $\mu = 2.3$ in typical disk conditions (see for example Armitage & Kley, 2019), and m_p the mass of a proton.

In reality, the assumption of a globally isothermal disk is not very close to the actual temperature, which is very likely to vary both vertically and radially. Vertically, the midplane is usually warmer than the layers above, with the exception of the surfaces, which are heated by the star. However, it is reasonable to assume the vertical temperature to be constant in an optically thick disk, meaning that light is not able to penetrate deep into the disk. Radially, a constant temperature is not a good assumption. Usually, a radial power law dependence is assumed for such so-called locally isothermal disks

$$T \propto r^{-q}. \tag{1.13}$$

The slope q can be approximated from the heating processes in a disk. The temperature is directly linked to the scale height in Equation 1.7. An optically thin, completely flat disk, which is only heated by the star's radiation, results in a slope $q = 3/4$ (see Armitage & Kley, 2019). However, this is not always a good assump-

tion for protoplanetary disks, as they have a significant vertical extent (Kenyon & Hartmann, 1987). A typical and often assumed value is $q = 1/2$, which results from an analysis of the disk's radiative equilibrium (Chiang & Goldreich, 1997).

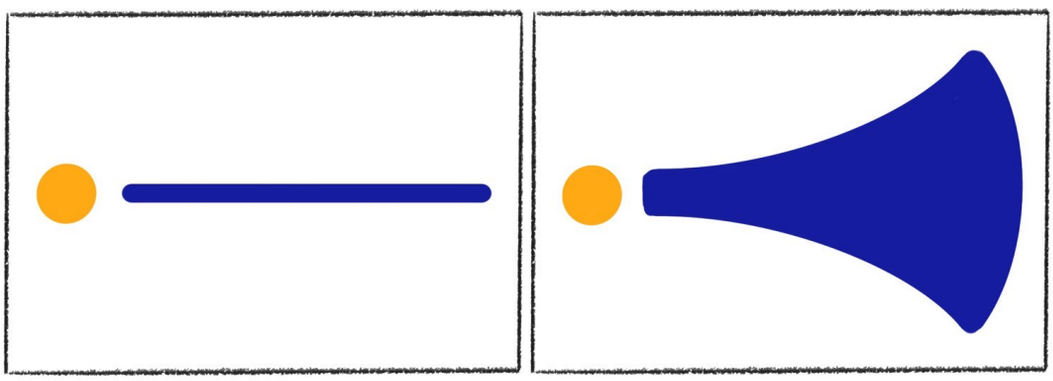

Figure 1.9: Schematic representation of the cross-sections of a thin, flat disk (left panel) and a flared disk (right panel).

Setting the slope of the temperature determines the vertical thickness of the disk: $T \propto r^{-q} \Rightarrow c_s \propto r^{-q/2}$. This means for the pressure scale height (as defined by Equation 1.7) that $H_p \propto r^{(3-q)/2}$. The vertical thickness of the disk is often expressed in the aspect ratio $h = H_p/r$, for which then $h \propto r^{(1-q)/2}$. For $q = 1/2$, the aspect ratio is $h \propto r^{1/4}$, which means that it increases for larger radii. This generally occurs for $q < 1$ and leads to a disk structure that is commonly called *flared*, an example shown in Figure 1.9.

1.2 Physical processes in protoplanetary disks

Like most things in the Universe, protoplanetary disks are not stable, but dynamic and evolve over time (Lesur et al., 2023). This evolution eventually leads to the formation of planets. The conditions for planet formation are regulated by the physical processes responsible for disk evolution, which I will summarize in this section.

1.2.1 Hydrodynamics

For a perfectly accurate description of the state of a system, we would need to take into account all molecules with all of their possible states and orientations, leading to an enormous parameter space. Obviously, this is not feasible. Hence, we need to use approximations in order to tackle the physics in protoplanetary disks. The gas in disks can be approximated as a fluid, and for now, let us neglect

the dust contained in disks. The gas motion can therefore be described with fluid dynamics, also called hydrodynamics (see e.g. Clarke & Carswell, 2007).

The fundamentals of hydrodynamics are three conservation laws. The first is the conservation of mass, described by the continuity equation

$$\frac{\partial \rho}{\partial t} + \vec{\nabla} \left(\rho \vec{v} \right) = 0, \tag{1.14}$$

with the time t and the velocity $\vec{v}$. This equation can be understood easily: The change of mass, or density more specifically (first term), at a specific location can only change if material is moving toward or away from this location, creating a flux (second term). The second conservation law follows the same idea, the conservation of momentum

$$\frac{\partial \left(\rho \vec{v} \right)}{\partial t} + \vec{\nabla} \left(\rho \vec{v} \cdot \vec{v} + P \right) = -\rho \vec{\nabla} \Phi, \tag{1.15}$$

where P is the pressure and Φ the gravitational potential. This equation is a form of the Navier-Stokes equation, which describes the motion of a fluid. Similar to the continuity equation, it states that the momentum can change (first term on the left-hand side) if momentum is added from the surroundings (second term on the left-hand side), but it additionally includes a force arising from pressure gradients (third term on the left-hand side). The right-hand side includes a source term, in this case an external gravitational potential. Finally, the third law is energy conservation

$$\frac{\partial \left(\rho \epsilon \right)}{\partial t} + \vec{\nabla} \left[\left(\rho \epsilon + P \right) \vec{v} \right] = S, \tag{1.16}$$

with the total energy ϵ, and radiative or gravitational sources S.

In this set of three equations, there are four unknown variables: density, pressure, velocity (vector), and energy. We can link the internal energy with pressure with the ideal gas equation, which reduces the dimensionality of the problem to three variables, closing the set of equations. We can further assume the (locally) isothermal case described above that links the pressure and density by a prescribed sound speed (Equation 1.12), which eliminates another dimension. In this case, we only need to solve the mass and momentum equations to describe the full system, and the energy equation does not need to be solved explicitly.

In hydrodynamics, there are two different approaches to treat these fundamental equations: the Eulerian and the Lagrangian approach. This means for simulations that there are two different ways to model the motion of fluids. The two approaches mainly differ in their frames of reference. Figure 1.10 provides a schematic view of these two ways. The above equations are expressed in the Eulerian way, focusing on specific locations in space through which the fluid flows.

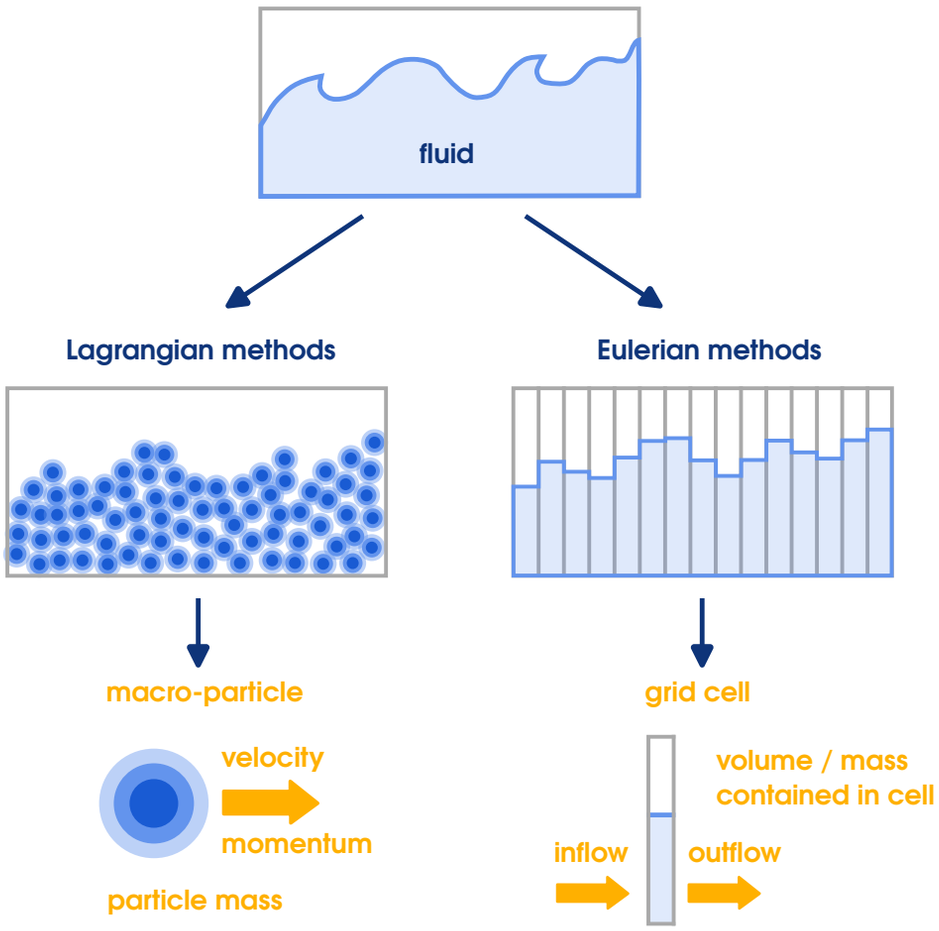

Figure 1.10: Schematics of the two main numerical ways to solve hydrodynamics. Lagrangian methods such as Smoothed Particle Hydrodynamics (left side) divide the fluid into macro-particles and follows the motion of these particles, while Eulerian methods (right side) create a fixed grid and keep track of the fluid motion through the grid, thus often called grid-based methods.

This concept is commonly used in grid-based simulations, where the computational domain is divided into grid cells tracking the fluid's motion through the cells. In contrast, the second way (Lagrangian approach) follows individual fluid (macro-)particles along their path. This is the basis for particle-based simulations, such as Smoothed Particle Hydrodynamics (SPH). Mixed methods exist, such as the Moving Mesh Method. Discussing the computational methods for hydrodynamics in detail would go beyond the scope of this thesis, which is why I refer to reviews such as Bodenheimer et al. (2006) and Springel (2010).

Both computational methods have their advantages, while also having their limitations. A closer comparison of grid-based to particle-based methods was conducted for example by Agertz et al. (2007). For example, Eulerian methods such as the finite difference methods solve the hydrodynamics equations in a

straight-forward fashion by appropriately approximating the differentials in difference quotients. Because of the fixed grid, these methods perform well in continuous flows, and boundaries can be well defined. However, the grid can influence the simulation in an unphysical way, and systems containing flows on different size scales can lead to computationally expensive simulations. Depending on the scheme, numerical diffusion can be an issue. Lagrangian methods, on the other hand, have very good conservation properties, for mass, energy, and both linear and angular momentum. They are not constrained by a specific grid geometry. But the disadvantages are that, depending on the number of particles, a simulation of a large system can quickly become unfeasible. Further, they resolution is low in regions of low density, which makes the application to low-density flows like streamers challenging. They are also intrinsically noisier, which is the reason for the high numerical diffusion in SPH methods. In physics, the appropriate method depends on the specific characteristics and goals of the hydrodynamic problem.

In this thesis, I chose to employ grid-based methods, which had not previously been applied to the particular scenario of warped disks. Traditionally, SPH methods were considered more suitable for these disks, because the grid was thought to create numerical interference. However, one of the key motivations behind my approach was the low viscosity typically observed in these disks, which is more accurately captured using grid-based models. I will address my choice of computational method in more detail in later sections.

1.2.2 Accretion processes in disks

Multiple processes can lead to accretion in protoplanetary disks. Although the term *accretion* technically refers to the flow of material from the disk onto the star, it is often used to describe the angular momentum transport processes leading to a flow through the disk. These flows are typically inward and hence lead to an accretion onto the star (Armitage, 2022). In current protoplanetary disk theory, there are two main mechanisms for angular momentum transport: *viscous accretion* and accretion due to *magnetically driven disk winds* (see Lesur et al., 2023). While these mechanisms were originally thought to be competitive theories, research in the field led to the understanding that both mechanisms are likely to operate at the same time. The interplay between both mechanisms is an ongoing topic in the field.

Viscous accretion

The viscous accretion is driven by turbulence in the disk. This turbulence is typically summarized with the term *viscosity*. However, it is important to understand that there are two different types of viscosity present in an accretion disk: the molecular viscosity (ν_{mol}) of the gas and the effects resulting from turbulence, which can be described analogously to a viscosity. A simple way to estimate the dominant viscosity type is the Reynolds number

$$\mathrm{Re} = \frac{UL}{\nu_{\mathrm{mol}}}. \tag{1.17}$$

Here, U is a typical velocity in the system and L is a typical length scale. One problem with this estimation is that these typical quantities are not well defined. A reasonable choice for protoplanetary disks is $U = c_{\mathrm{s}}$ and $L = H_{\mathrm{p}}$, as for example pointed out by Armitage & Kley (2019). However, even with a different choice, the Reynolds number turns out to be a large number in the case of protoplanetary disks, usually on the order of $\mathrm{Re} \sim 10^{11}$. Experiments have shown that for $\mathrm{Re} > 10^4$, turbulence always occurs (see review by Eckhardt et al., 2007). This demonstrates that protoplanetary disks are prone to turbulent effects and that turbulent viscosity is likely to dominate over effects due to molecular viscosity. Possible origins of turbulence are summarized in Section 1.2.3.

This turbulent viscosity is commonly parameterized using the Shakura-Sunyaev α-viscosity (Shakura & Sunyaev, 1973)

$$\nu = \alpha \frac{c_{\mathrm{s}}^2}{\Omega_{\mathrm{k}}} = \alpha c_{\mathrm{s}} H_{\mathrm{p}}. \tag{1.18}$$

The α-parameter is often assumed to be constant throughout the disk, both radially and in time. While this is a convenient assumption, it may not always reflect the nature of a realistic system. In the research field, there are efforts to obtain a more realistic treatment based on analytical and numerical analyses, as well as observations. Yet, a constant α is often used to parameterize the turbulence in protoplanetary disks.

In isolated protoplanetary disks, mass and angular momentum are conserved. We can therefore apply the continuity and Navier-Stokes equations. To investigate radial flows, we can take advantage of the circular geometry of disks and re-write the equations in cylindrical coordinates

$$\frac{\partial \Sigma}{\partial t} + \frac{1}{r}\frac{\partial}{\partial r}\left(r \Sigma v_r\right) = 0 \tag{1.19}$$

and

$$\frac{\partial L(r)}{\partial t} + \frac{1}{r}\frac{\partial}{\partial r}\left(L(r)\, v_r\right) = \frac{1}{r}\frac{\partial G(r)}{\partial r}, \tag{1.20}$$

where $L(r) = \Sigma r^2 \Omega_\mathrm{k}$ is the angular momentum, and $G(r)$ is the internal torque on an annulus in the disk. For the internal torque, we only consider viscosity at this point, and therefore can express the viscous stress

$$G = \nu \Sigma r^3 \frac{\mathrm{d}\Omega(r)}{\mathrm{d}r} = -\frac{3}{2}\nu \Sigma r^2 \Omega_\mathrm{k}, \tag{1.21}$$

where the last part applies to Keplerian disks with $\Omega(r) = \Omega_\mathrm{k}$. Note that in literature, the internal torque G is sometimes defined differently, for example with a factor of $-1/r$ in Martin et al. (2019) or a factor of $1/(2\pi r)$ in Ogilvie & Latter (2013a,b).

From these equations, radial velocity in a steady-state disk can be derived and results in

$$v_r = -\frac{3}{2}\frac{\nu}{r} \tag{1.22}$$

for a thin, Keplerian disk. The minus sign indicates an inward flow. The accretion flow through the disk can then be described by the accretion rate

$$\dot{M} = -2\pi r \Sigma v_r. \tag{1.23}$$

If we assume the power laws $\Sigma \propto r^{-p}$ and $T \propto r^{-q}$, we get from Equation 1.18 and 1.12 a relation of $\nu \propto T/\Omega_\mathrm{k} \propto r^{-q+3/2}$, and with Equation 1.22 we get $v_r \propto r^{-q+1/2}$. For a constant accretion rate $\dot{M} = \text{const.}$, we can derive that

$$p + q = \frac{3}{2} \tag{1.24}$$

for a steady-state accretion flow. With the typical assumption of $q = -1/2$ (see Section 1.1.3), we then need to set $p = -1$ for a steady-state disk.

We can additionally estimate the viscous timescale τ_ν, on which density gradients are smoothed out by diffusion due to the viscosity

$$\tau_\nu \approx \frac{r^2}{\nu}. \tag{1.25}$$

In recent years, measurements of viscosity in observed protoplanetary disks seem to indicate rather low viscosity on the order of $\alpha \approx 10^{-3} - 10^{-4}$ (Flaherty et al., 2017; Andrews, 2020). Only a decade ago, a typically assumed value was $\alpha = 10^{-1} - 10^{-2}$, which would be the strength of viscosity required to explain the observed accretion rate onto stars (Alexander et al., 2014; Hartmann et al., 2016). With the recent observational evidence that turbulence is low in protoplanetary

disks (Rosotti, 2023), different explanations for angular momentum transport are needed.

Magnetically driven disk winds

As an alternative process for angular momentum transport, magnetically driven disk winds gain in popularity (Pascucci et al., 2023). The theory for this was introduced by Blandford & Payne (1982) as *magneto-centrifugal wind* model. Note that the model I introduce here is greatly simplified, as full non-ideal magneto-hydrodynamics in protoplanetary disks is a highly complex field (Balbus, 2009; Béthune et al., 2017; Lesur, 2021). A full discussion would be outside the scope of this thesis.

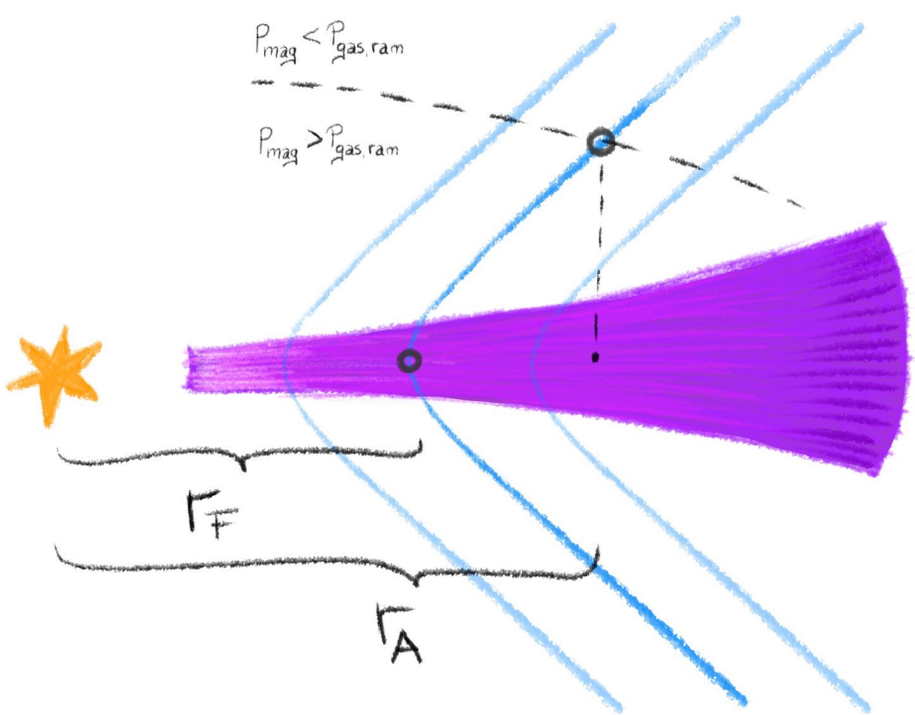

Figure 1.11: Magnetic field configuration in a protoplanetary disk for the magneto-centrifugal disk model. The blue lines indicate the magnetic field lines, the black dashed line represents the Alfvén surface, where the dominant pressure changes from magnetic to gas ram pressure.

As schematically indicated in Figure 1.11, the magnetic field lines in a disk are bent, which can develop during the formation process of the disk and star if an external, initially homogeneous magnetic field was present in the molecular cloud (Rodenkirch et al., 2020; Pattle et al., 2023). These bent magnetic field lines are anchored in the disk at the so-called foot-point r_F. Above the disk, the area is divided into two regimes, divided by the Alfvén surface, which is defined as a

balance between the magnetic pressure force

$$P_{\mathrm{mag}} = \frac{|\vec{B}|}{8\pi}, \tag{1.26}$$

where $|\vec{B}|$ is the absolute value of the magnetic field, and the gas ram pressure

$$P_{\mathrm{gas,ram}} = \rho v^2. \tag{1.27}$$

In the regime directly above the disk below the Alfvén surface, the magnetic pressure force dominates the gas ram pressure. Here, the magnetic field lines co-rotate like a solid rod with the angular frequency of their foot points. This is a key point of the model: If a charged particle is launched from the disk, it can only move along the field lines. Because the angular frequency is constant along the field line, the particle is accelerated because its distance from the star increases due to the bent shape of the field line. This outflow of particles resembles a wind, hence the name of the mechanism. Depending on the parameters of the magnetic field and the amount of outflowing particles, this wind can be highly effective. The particles in the wind gain angular momentum, which is in turn removed from the disk at the foot point of the magnetic field line. As the disk loses angular momentum, an inward accretion flow develops through the disk (Spruit, 1996).

The particle accelerates up to the point where it reaches the Alfvén surface at a distance r_{A}. In the second regime, the magnetic pressure is weaker than the ram pressure, and the magnetic field lines start to bend. Because of the disk's rotation, they wind up in this regime. At this point, the charged particle no longer accelerates. In order to estimate the angular momentum transfer, the magnetic lever arm λ is an important quantity, defined as

$$\lambda = \frac{r_{\mathrm{A}}}{r_{\mathrm{F}}}. \tag{1.28}$$

From a consideration of the magnetic torque arising from the disk wind, the accretion velocity can be estimated as

$$v_{r,\mathrm{w}} = -2r\frac{\dot{\Sigma}_{\mathrm{wind}}}{\Sigma(r)}\left(\lambda^2 - 1\right), \tag{1.29}$$

where $\dot{\Sigma}_{\mathrm{wind}}$ is the mass outflow due to the wind.

In a steady accretion flow, the accretion rate (Equation 1.23) is constant. Note that for this consideration, we assume the mass loss to be negligible, as in the general case, a steady accretion flow cannot be achieved (as for example discussed in Tabone et al., 2022). For the radial flow due to the magnetic wind $v_{r,\mathrm{w}}$ and a

mass outflow depending on the present surface density and the orbital frequency $\dot{\Sigma}_{\rm wind} \propto \Omega_{\rm k}\,\Sigma(r) \propto r^{-3/2-p}$ (as adopted in a model by Kimmig et al., 2020), the accretion rate $\dot{M} \propto r^{1/2-p}$, and a steady-state is reached for

$$p = \frac{1}{2}. \tag{1.30}$$

However, the actual outflow rate could differ, as disk winds are hard to measure in observations (Moscadelli et al., 2022), leading to a different surface density morphology in a steady-state disk.

1.2.3 Disk instabilities

Even with the observational evidence of low viscosity, the concept of viscosity and turbulence remains very relevant in accretion disks. The origin of turbulence often lies in hydrodynamic disk instabilities. In this section, I summarize some of the most important instabilities. I will keep each description brief as it is not the main focus of my thesis. Nevertheless, it remains important since I use the concept of viscosity in my disk models.

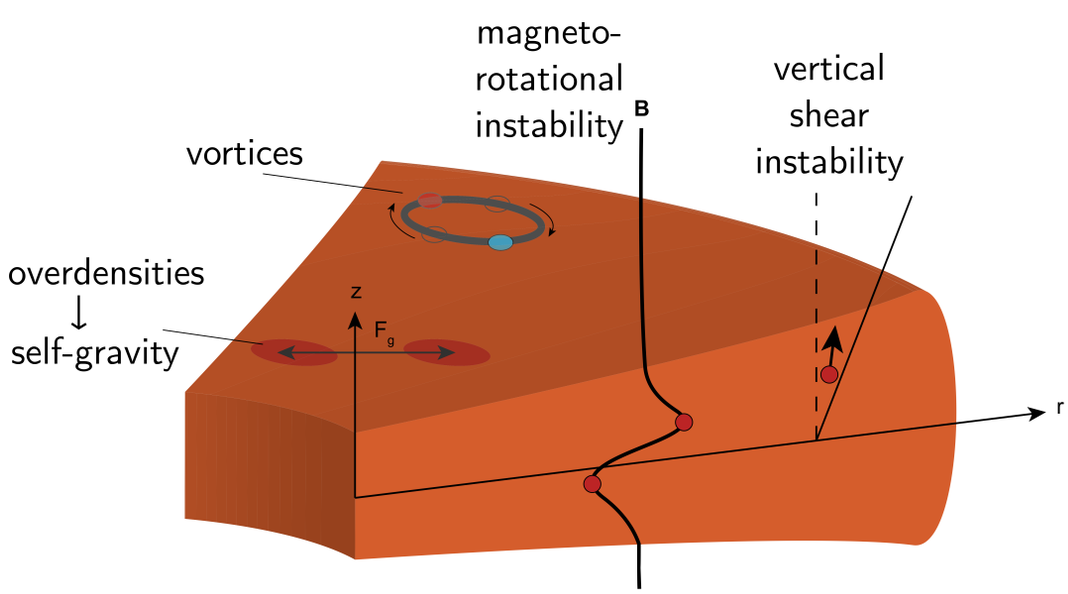

Figure 1.12: Overview on the main instabilities occurring in protoplanetary disks. *Figure adapted from Armitage & Kley (2019). Reproduced with permission from Springer Nature, License Number: 6004130189916.*

Gravitational instability

This instability occurs for massive disks. If the mass of the disk is so high that its own gravity (called *self-gravity*) becomes significant, the disk can become unstable to perturbations in the surface density if the gravitational contraction is stronger than the rotational support and the thermal pressure arising from the compression. In this case, overdense parts of the disk can collapse in a cascade effect, leading to fragmentation (Kratter & Lodato, 2016).

Comparing the different timescales, specifically the sound-crossing time (the time it takes for sound waves to cross a particular region) and the free-fall time (the time it would take for a region to collapse if no forces would act against the collapse) leads to a stability criterion called Toomre-Q (Toomre, 1964):

$$Q = \frac{c_s \Omega_k}{\pi G \Sigma}. \tag{1.31}$$

Here, G is the gravitational constant (not to be confused with the internal torque in protoplanetary disks). Disks with $Q < Q_{crit} (\approx 1)$ are unstable to self-gravity. A typical signature of a gravitationally unstable disk are large-scale spiral structures.

Magnetorotational instability

The magnetorotational instability (short: MRI; Balbus & Hawley, 1998) can occur when a magnetic field is present and coupled to the material in the disk. This coupling can occur when the disk material is electrically charged, for example by thermal ionization. This also implies that in cold, dense regions the magnetic field does not have an effect on the disk. These regions are called magnetic dead zones. Dead zones can gain importance when a lot of dust is present, as they can mediate recombination of ions, causing the material to be neutral.

In regions with sufficient coupling, the MRI can operate (in ideal magnetohydrodynamic conditions; Gammie, 1996), when

$$\frac{d\Omega}{dr} < 0. \tag{1.32}$$

This condition is always satisfied in Keplerian (and also close to Keplerian) disks, which is why the MRI is thought to play an important role. However, the range of dead zones is still unknown, especially in the inner disk regions, where the level of ionization is largely unknown due to a lack of resolved observations (Williams & Mohanty, 2025). The occurrence of dead zones may prevent the MRI in wide parts of protoplanetary disks.

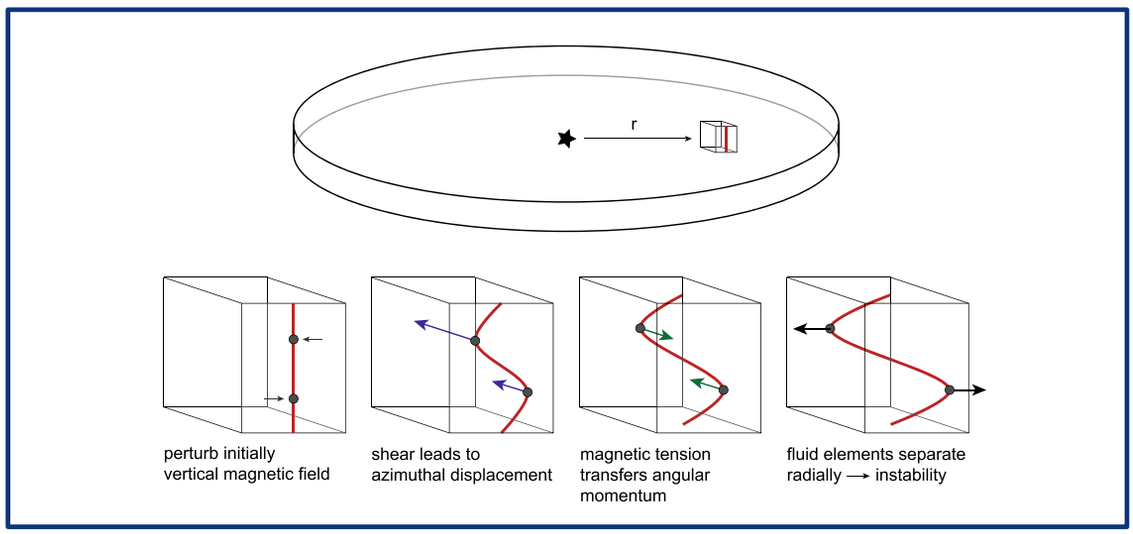

Figure 1.13: Schematic representation of the MRI, where a vertical magnetic field is radially disturbed, leading to an instability. *Credit: Armitage & Kley (2019). Reproduced with permission from Springer Nature, License Number: 6004130189916.*

The basic idea behind the MRI is a coupling of one magnetic field line to material at different radii due to a radial perturbation of a vertical magnetic field line. This idea is represented in Figure 1.13. A vertical magnetic field is radially disturbed so that a part of the line is coupled to material in the disk closer to the star. This material has a larger velocity due to its Keplerian velocity, therefore the field line is azimuthally distorted. Because of this distortion the magnetic field line is stretched, with the magnetic tension is acting against the stretching. Due to the magnetic tension angular momentum is transferred from the inner to the outer anchor of the field line. The material at the inner location therefore loses angular momentum and hence moves inward, while the outer material moves outward for the same reason. This leads to an even larger separation, creating an even stronger effect and eventually building up to the instability.

Vertical shear instability

The vertical shear instability (short: VSI; Urpin & Brandenburg, 1998) can arise when the angular frequency varies vertically, which naturally occurs when a disk has a radial temperature gradient. Typically, the gas is slower higher up in the disk because the gravity decreases with z. The vertical difference in angular frequency leads to a shear between material of different height. This shear generates free energy, triggering the VSI, which creates an upward and downward motion of the gas in the disk, shown in Figure 1.14.

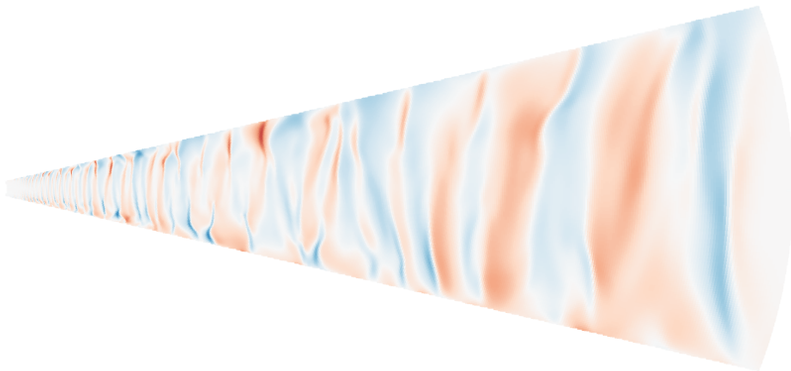

Figure 1.14: Cross-section of a protoplanetary disk, where the VSI is operating, creating upward (blue) and downward (red) motion. *Adapted from Dullemond et al. (2022b).*

Creating disk conditions for the VSI to be effective is easy in the assumption of vertically isothermal disks, but more complicated in more realistic disk models, where the temperature vertically varies. In the latter case, the VSI can only occur if the cooling is faster than the orbital timescale (Lin & Youdin, 2015; Malygin et al., 2017). If the conditions are right, the vertical shear instability can create turbulence leading to a viscosity on the order of $\alpha \sim 10^{-4}$ (Nelson et al., 2013; Stoll & Kley, 2014).

However, the importance of the VSI in realistic protoplanetary disks is disputed. For example, comparing models with observations, Dullemond et al. (2022b) found evidence against the VSI, at least in disks where larger dust grains are settled very strongly to form a thin dust disk at the disk's midplane.

Vortices

Vortices typically refer to a circular flow, often leading to local overdensities. They can form as a result of multiple different disk instabilities. There are two main mechanisms leading to the formation of vortices.

The first one is the *subcritical baroclinic instability* (SBI, Petersen et al., 2007), which is an instability linked to radial convection. It arises due to non-linear buoyancy forces in the disk and creates vortices leading to a significant turbulence in the disk (Lesur & Papaloizou, 2010).

The second mechanism is the *Rossby wave instability* (RWI, Lovelace et al., 1999), a global, non-axisymmetric instability that arises when extrema in the pressure (so-called pressure bumps) are present. Strictly speaking, the pressure is not the actual quantity setting the criterion for the RWI, but a combination of entropy and a quantity called vortensity (see for example Chang & Youdin, 2024). Vortensity is the vorticity, a measure for the rotation of a flow, divided by the den-

sity. However, vortencity bumps often correlate with pressure bumps and we can remain in the more illustrative picture of the latter for the purpose of this consideration. Pressure bumps can especially form at the gap edges, possibly created by planets (Li et al., 2005). In low-viscosity disks, these pressure bumps can become unstable, leading to vortex motion.

A recent study by Ziampras et al. (2025) investigated substructures caused by planets and found that both the SBI and the RWI can operate in low-viscosity disks. This means that both effects can coexist, creating vortices and turbulence in protoplanetary disks.

Hydrodynamical studies of vortices in low-viscosity disks found that the vortices should be long-lived (Rometsch et al., 2021; Rafikov & Cimerman, 2023). However, vortices are rarely observed in disks, which could be an indication that the viscosity of protoplanetary disks is larger than currently assumed, as vortices dissipate faster for larger viscosity (see for example Hammer et al., 2021). On the other hand, it could also mean that other effects leading to the destruction of vortices are present in disks. For the vortex destruction, cooling mechanisms can play a major role (Fung & Ono, 2021; Rometsch et al., 2021). Other destructive effects can be the elliptical instability (Lesur & Papaloizou, 2009) or dust in disks (Lovascio et al., 2022; Cui et al., 2025).

For now, the discrepancy between the predicted abundance of vortices in numerical simulations and their absence in observations remains unresolved. This highlights the dynamic nature of research in protoplanetary disks, where open questions like these emphasize that substantial refinement of current models, as well as further observational investigations, are urgently needed.

1.2.4 Planet formation

The desire to understand the origin of planets is one of the reasons for diving into the study of protoplanetary disks. In this section, I outline the basic principles of planet formation.

As planets form from dust, let us first have a look at the dust properties. Dust is often assumed to consist of silicates, which are compounds including silicon-oxygen bonds. These bonds can be negatively charged and are often compensated with positively charged aluminum, iron, or magnesium ions, building olivine $(\mathrm{Mg,Fe})_2\mathrm{SiO}_4$ or pyroxene $(\mathrm{Mg,Fe})\mathrm{SiO}_3$, for instance. These silicates are the building blocks for the rocky components of planets.

In the current state of research, there are two main ways to form a planet, however, other mechanisms can not be excluded (Drążkowska et al., 2023). The first one is a direct formation of planets via the gravitational instability discussed

in Section 1.2.3. In this scenario, parts of the disk collapse into solid bodies that can grow even further by collecting smaller dust particles and gas. While this theory remains plausible, current observational and theoretical research seems to suggest that protoplanetary disks rarely meet the conditions required for the GI. Therefore, a different model for planet formation is vital.

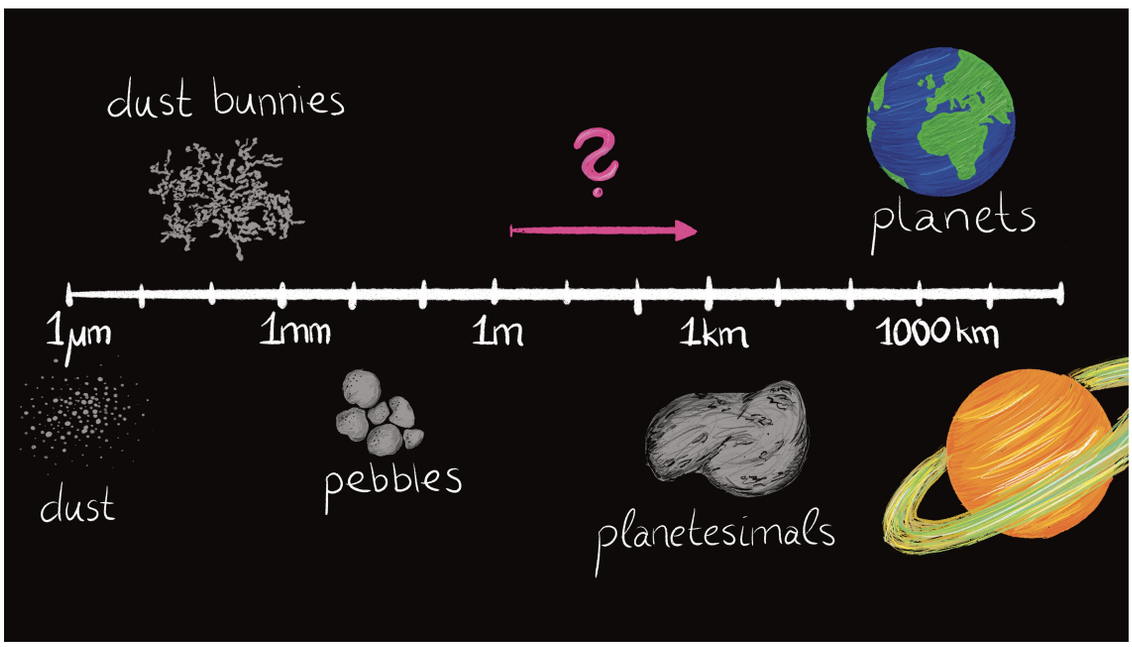

Figure 1.15: A schematic scale of the stages of planet formation in the core accretion model.

The second scenario for planet formation, the *core accretion model*, is based on the growth of small dust particles, summarized in Figure 1.15. These dust particles are on a size scale of 1 μm and hence need to grow many orders of magnitude in order to become a planet. The first step in this growth is rather intuitive, as dust can stick together to form larger dust bunnies[3]. These dust bunnies stick together mainly due to Van-der-Waals forces. The sticking properties can experimentally be studied (Blum & Wurm, 2008).

The fluffy dust bunnies can be compressed into small pebbles. This can for example occur in collisions with other dust aggregates. The outcome of the compression is often referred to as pebbles. However, the growth in this stage faces multiple challenges. One of these challenges is the inward drift of dust particles, which occurs because of the relative velocity difference between gas and dust. As described in Section 1.1.3, the gas orbits usually with a slightly slower velocity than the Kepler velocity because of pressure gradients in the disk. Dust particles do not feel this pressure gradient, therefore move at Kepler velocity. Thus the dust particles are faster than the gas and therefore experience a headwind

[3]Just like in the corner of a living room, when someone™ forgot to vacuum clean.

slowing down the dust particles. In slowing down, the particles lose angular momentum and therefore drift inward. In typical disk conditions, this inward drift can be very fast, which means for the growth of dust particles that they need to grow on a comparable speed to avoid being lost to accretion onto the star (Youdin, 2010). This challenge is called *drift barrier*.

Further growth challenges are related to the relative velocity of dust particles in collisions. If the velocity is too fast, colliding dust particles break and fragment into smaller particles instead of larger ones, which is referred to as *fragmentation barrier*. Zsom et al. (2010) have shown that depending on the disk conditions dust particles do not fragment, but bounce off each other (*bouncing barrier*) and therefore also do not grow.

All of these challenges together are often called *meter-sized barrier* (purple question mark in Figure 1.15). However, this is not an actual barrier, as the plethora of existing exoplanets proves that it is possible to overcome these challenges. A possible solution are dust traps, locations that allow the so-called Streaming Instability to occur, where the gas drag slows dust particles down, which allows the particles to collect and form overdensities. These overdensities can in turn slow down the surrounding gas, allowing even more particles to collect. This leads to the formation of filaments and structures that can gravitationally collapse to planetary cores. Once a core or boulder, often called planetesimal, has reached a size on the order of $\sim 10^5$ cm, it begins to have a significant gravitation so that the boulder can gravitationally collect smaller particles (called *pebble-accretion*) to form a planets.

Planets come in different sizes and characteristics, as our Solar System already shows. If a protoplanet formed under favorable conditions, so that it reached a mass on the order of $10\,M_{\mathrm{Earth}}$, it has the ability to absorb a significant amount of the gas in the disk. This leads to giant gas planets like Jupiter or Saturn. Protoplanets that do not reach such a large mass become rocky planets, which may collect a low to moderate amount of gas to form an atmosphere. Rocky planets are the only environment we know to host life as we know it.

1.2.5 Planet-disk interaction

Once planets have formed, they can have a large impact on the disk, shaping large-scale structures and regulate physical processes on the disk (Paardekooper et al., 2023). This is called *planet-disk interaction*. This interaction can also influence the evolution of the orbital parameters of planets, especially their distance to the star, known as *planetary migration*. The planetary migration might also be able to explain the diversity of exoplanets discussed at the beginning of this chapter.

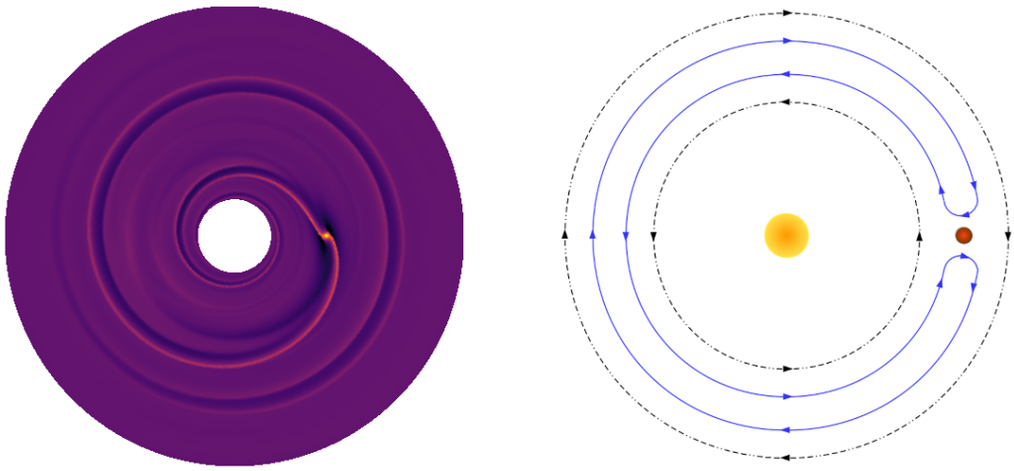

Figure 1.16: **Left:** Numerical simulation of a planet in a protoplanetary disk showing spiral arms excited by the planet. **Right:** Gas streamlines of the corotation region in the reference frame of the planet. Gas on the blue line follows a so-called horseshoe orbit. *Figure inspired by Kley & Nelson (2012).*

In disks, where the viscous accretion model is assumed, there are two main mechanisms causing planetary migration. Both mechanisms typically cause an inward migration. In the first mechanism, spiral wakes caused by the planet play an important role (Tanaka et al., 2002). These spiral wakes, pictured in Figure 1.16, left panel, occur because the planet excites radial overdensities which are smeared into a spiral shape by the Keplerian shear in the disk. The spiral arms act a torque on the planet, which is called *Lindblad torque* (Goldreich & Tremaine, 1979). The torque arises from both the inner and the outer spirals and usually leads to an inward migration of the planet.

The second mechanism is called *corotation torque* (Ward, 1991) and arises in the corotation region, a narrow radial range around the planet location (Figure 1.16, right panel). With respect to the planet, gas orbiting closer to the star is faster, whereas gas orbiting further out is slower. This leads to so-called *horseshoe streamlines* inside the corotation region, where the disk material turns inward in front of the planet and outward behind the planet. In each of the turns, angular momentum is transferred from the planet to the disk material or vise-versa. This leads to a net torque on the planet, especially if the horseshoe streamlines are not completely filled (or *unsaturated*). This can for example occur due to pressure gradients or radial flows in the disk.

The migration behavior of planets can be classified into different migration regimes, mainly depending on the mass of planet and disk. In the migration regime of type I, the planet has a low mass or the disk is very massive. In this case, planets only mildly influence the disk. The migration is directly governed

by the Lindblad and corotation torques and usually takes place on fast timescales (D'Angelo & Lubow, 2010). If the planet is massive, it migrates in a regime of type II (Kanagawa et al., 2018), where it opens a gap in the disk by pushing the material in the corotation region aside. Because in this scenario, the corotation region is mostly empty, the corotation torque is no longer important. However, an additional migration torque arises from the disk, as the material of the disk accretes inward due to viscosity, pushing the gap and hence the planet inward as well. This takes place on slower timescales than migration type I. A mixture of both migration scenarios is typically referred to as migration type III. This occurs for example when the planet only partially opens a gap, making the corotation torque significant again. Under some conditions, this can lead to a very fast migration, also called *runaway* migration.

Planets can also migrate in disks governed by other accretion mechanisms such as magnetic disk winds (Kimmig et al., 2020; Lega et al., 2022, Hammer & Lin, subm.). In this scenario, a radial inward flow of the gas (as discussed in Section 1.2.2) causes a highly asymmetric corotation region, which can lead to outward migration under favorable conditions.

1.3 Motivation and outline of this thesis

The exciting new observations of protoplanetary disks with high angular resolution in the past decade are a breakthrough in the research field for understanding the formation and evolution of planets. While the observations are able to shed light onto many research questions, they simultaneously raise a wide range of follow-up questions for further investigation. I dedicate my thesis to uncovering another piece of the Universe's puzzle.

The motivation for my work are non-axisymmetric features that are commonly seen in these new observations of protoplanetary disks. Such non-axisymmetric features are for example spirals, bright arcs or "blobs", broad dark regions, or dark lanes in the radial direction of the disk. Some of these features can be explained with an inner region tilted with respect to the outer part of the disk, which can cast a shadow onto the outer region. Disks containing such different orbital planes are called *warped disks*. It is crucial to understand the origin and evolution of the warp in order to interpret observations of non-axisymmetric features.

In recent years, the research around warps has been on the rise. More and more observations reveal these non-axisymmetric features, indicating that warps might be common in protoplanetary disks. Therefore, the research on warped disks gained new momentum. As warps can have a strong impact on the process of planet formation, a deep understanding of the physics in warped disks is essential to understand the morphology of fully formed planetary systems. My work is part of this effort and contributes to both the understanding of the dynamics and the link between simulations and observations of warped disks.

Chapter 2: What are warped disks? In this part of the thesis, I introduce the theory of warped protoplanetary disks. This includes observational indications, possible causes for warps, and the evolution of warps. At the end of this chapter, I outline radiative transfer methods, which are necessary for a good comparison between simulations and observations.

Chapter 3: Is it possible to model warps and misalignments using grid-based methods? The purpose of this chapter is to evaluate the applicability of grid-based (Eulerian) numerical methods to warped disks. In the research so far, most simulations of warps were performed using Lagrangian methods such as Smoothed Particle Hydrodynamics (SPH). However, SPH methods have a great disadvantage when it comes to modeling protoplanetary disks: most implementations of SPH contain a high numerical viscosity. Protoplanetary disks on the

other hand are likely to have much lower viscosity than possible with typical SPH integrations.

Grid-based methods are able to accurately model disks with such low viscosity. However, these methods have a disadvantage as well, as the grid might influence the disk's orbital plane if it is not perfectly aligned with the geometry of the grid. In Section 3.3, I thoroughly investigate this numerical effect on an unwarped disk, which is tilted with respect to the grid geometry.

In Section 3.4, I then apply the tested grid-based method to a set-up of an initially warped disk. The warp evolution of this disk is *undriven*, which means that no external torques act on the warp and the evolution is only driven by internal processes. In my simulations, I find an internal precession within the warped disk, which I then investigate to pinpoint whether this precession is of physical or numerical origin.

Chapter 4: Application of the grid-based method: Can a stellar fly-by scenario recreate the observations of the RW Aur system? The grid-based method established in Chapter 3 is a valuable tool to investigate various aspects of warps in protoplanetary disks. In this next chapter, I apply this tool to a physical formation scenario of a warped disk: a stellar fly-by. In this scenario, a star passes an initially unwarped disk around another star and creates a warp in the disk through its gravitational pull. This gives insight into physically motivated shapes of warps, as it is challenging to constrain the exact structure and geometry of warped disks from observations. Additionally, a fly-by scenario provides a great environment to further investigate the evolution of undriven warps, as the fly-by is a one-time event. After the fly-by, the newly warped disk is able to evolve independently from any external torques.

In order to use this knowledge to learn more about observed systems, I then apply the fly-by scenario to an observed star-disk system: RW Aur. This system consists of two stars with a disk around each star, with evidence of a recent close encounter. The orientation of the disk around the star RW Aur A is relatively well constrained from observations. The trajectory of star B around A can be either bound or unbound. In either case, the eccentricity of the trajectory is close to $e \approx 1$, which implies a highly eccentric binary for the bound case or a close to parabolic trajectory in the unbound case. For my simulations, I assume the latter case (which relates to a stellar fly-by scenario) in order to investigate the dynamics of this system. Using radiative transfer simulations, I create synthetic observations of the dust continuum, assuming small dust that is perfectly coupled to the gas and therefore follows the warp movement of the disk. I compare the synthetic observations to a real observation of the dust continuum.

Chapter 5: What do observations of warped disks look like when observed edge-on? In order to tighten the link between the theory of warps and observations, this chapter is dedicated to the appearance of shadows in warped disks. Specifically, I investigate disks observed edge-on in scattered light. An unwarped disk observed edge-on shows two bright spots separated by a dark lane which corresponds to the optically thick midplane of the disk. The two bright spots are the two disk surfaces and appear completely symmetric in a perfectly edge-on view. In a warped disk, however, these surfaces can be shadowed by the warp in the inner disk region. This can lead to an apparent shift of the bright spots with respect to the axis of the dark lane, called *lateral asymmetry*. The goal of this chapter is to explore the observability of this lateral asymmetry in edge-on disks.

Chapter 6: Conclusions and outlook. In this chapter, I summarize and conclude the results of this work. In addition, I present an outlook on planned and potential projects following up the work of this thesis.

2

The physics of warped disks

The introduction on protoplanetary disks in the preceding chapter gives a glimpse on the complexity of the physical processes occurring in disks. Additional processes and mechanisms affecting disk evolution complicate this picture even further. Warped disks, which are the focus of my work, include processes driving the evolution of warps in addition to the general processes in protoplanetary disks. My thesis is dedicated to understanding these additional processes, which I introduce in this chapter.

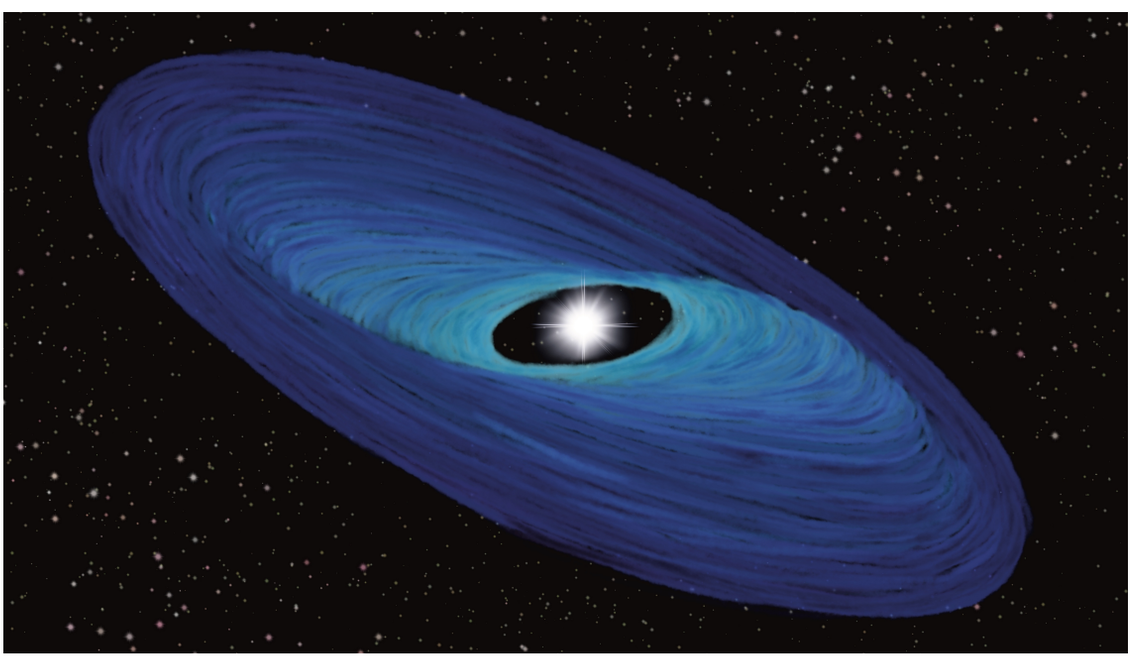

Figure 2.1: Artist's impression of a warped protoplanetary disk.

Warped disks are disks that contain different orbital planes. The shape of their warp varies greatly, depending for example on cause and evolutionary state of the warp. Figure 2.1 gives one example of what a warped disk could look like. Warped disks can additionally be *twisted*, meaning that the warp is additionally coiled up within the disk. The evolution of warps can also lead to broken disks

that have two or more disconnected parts of the disk misaligned with respect to each other. Examples are shown in Figure 2.2. Usually, both broken and warped disks are referred to with the umbrella term *misaligned disks*. As the possible configurations for misaligned disks are infinite, so are their appearances in observations. In addition, there are multiple different hypotheses of how misalignments and warps can form, and it is yet unclear which one is the most prevalent.

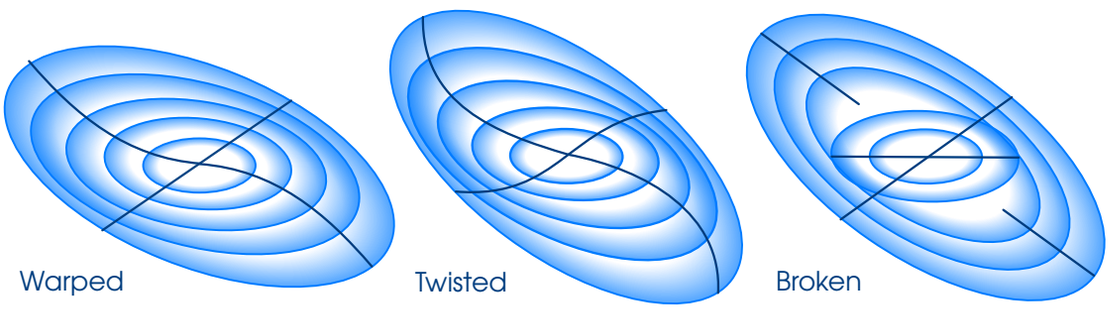

Figure 2.2: Different types of misaligned disks. *Credit: Anna Penzlin.*

I note that the theory behind warped disks can be more generally applied to other types of accretion disks, such as warped disks around black holes.

2.1 Observational evidence of warps

More and more observations of protoplanetary disks reveal non-axisymmetric features that could be linked to a shadow cast by a misaligned inner region of the disk. Non-axisymmetric shadows are a typical signature of warps in scattered light. Recall that scattered light is typically observed in the optical and near-infrared regimes, as discussed in Section 1.1.2.

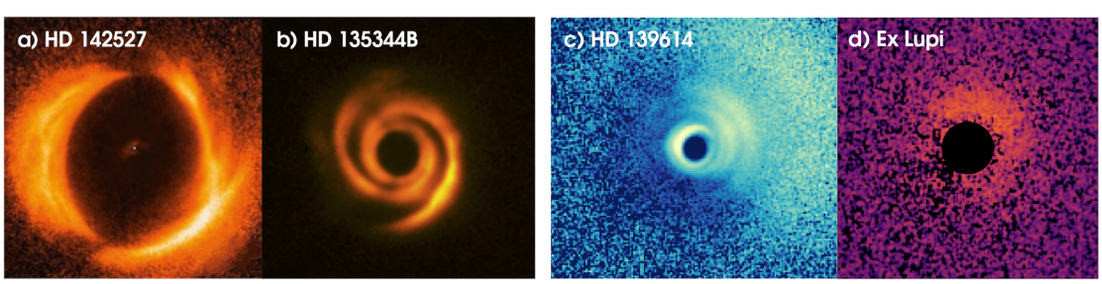

Figure 2.3: Observations of non-axisymmetric shadows in protoplanetary disks in scattered light. **a)** and **b)** exhibit narrow dark lanes, **c)** and **d)** have a broad region which is darker than the rest of the disk.
Credit: a) VLT/SPHERE, broad band filter ($\lambda \sim 600 - 900\,\mathrm{nm}$); Avenhaus et al., 2017. b) ESO, T. Stolker et al.; VLT/SPHERE J-band ($\lambda = 1.25\,\mu\mathrm{m}$). CC BY 4.0 c) VLT/SPHERE H-band ($\lambda = 1.6\,\mu\mathrm{m}$); Muro-Arena et al., 2020. d) VLT/SPHERE H-band ($\lambda = 1.6\,\mu\mathrm{m}$); Zurlo et al., 2024.

Depending on the architecture of the warp, the shadows can have different appearances. Figure 2.3 shows examples of observed shadows that are thought to be linked to a misaligned inner region of the disk. The first two panels show the disks around HD 142527 (panel a) and HD 135344B (panel b), which both display dark narrow lanes. These lanes occur for example in broken disks when the inner part is highly misaligned, as illustrated in Figure 2.4, left side. Warped disks with such high misalignments might also be able to produce narrow lanes if the connecting material between inner and outer disk is thin enough so that light can pass through. An interesting fact is that the dark lanes do not necessarily need to appear exactly opposite to each other, especially when the inner and outer disks are flared. Marino et al. (2015) were one of the first groups linking this shadow phenomenon to a misaligned inner region, with their work focusing on HD 142527 (Figure 2.3, panel a). Other disks exhibiting dark lanes are for example GG Tau (Keppler et al., 2020), RXJ1604.3-2130 (Pinilla et al., 2018), and HD 100453 (Benisty et al., 2017).

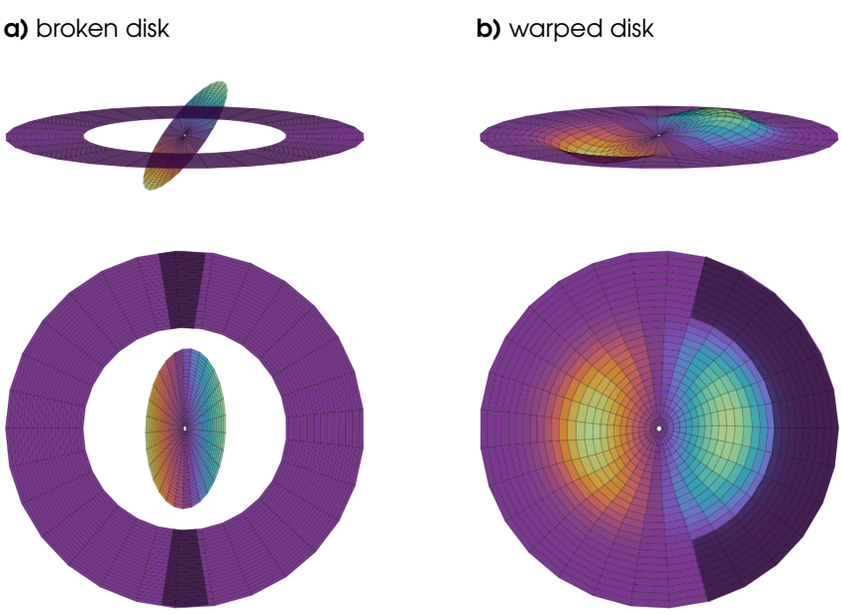

Figure 2.4: Shadows in with narrow lanes in broken disks (left) and broad regions in warped disks (right). Orange color indicates a region of the disk below the disk midplane, blue color above.

Warped disks with low or moderate inclinations show broad dark regions as for example in the disks around HD 139614 and Ex Lupi (Figure 2.3, panels c and d). This is illustrated in Figure 2.4, right side. Note that this scenario also can apply for broken disks with low mutual inclination. Broad shadows have also been observed for example in the disks around TW Hydra (Debes et al., 2017), HD 143006 (Benisty et al., 2018), and WRAY 15-788 (Bohn et al., 2019). In most

observations, the inclined inner region is either too close to the star to be resolved or obscured by a coronagraph, which blocks the star's light to prevent it from outshining the disk.

Because of the dark regions, shadowed disks are commonly less bright than unshadowed disks, making them more challenging to observe. Better technology and longer integration times now enable a sufficient resolution of these disks. This is why shadowed features are observed more frequently today than in the past. Garufi et al. (2022) for example specifically targeted faint disks in scattered light and revealed several disks with a tentative misaligned inner region. In order to constrain the prevalence of misalignments, Bohn et al. (2022) attempted to measure the orientation of inner and outer disk planes independently by combining different observations. Out of twenty targeted disks, they find significant misalignments in six of them. A summary of shadowed features in observations can be found in the review by Benisty et al. (2023).

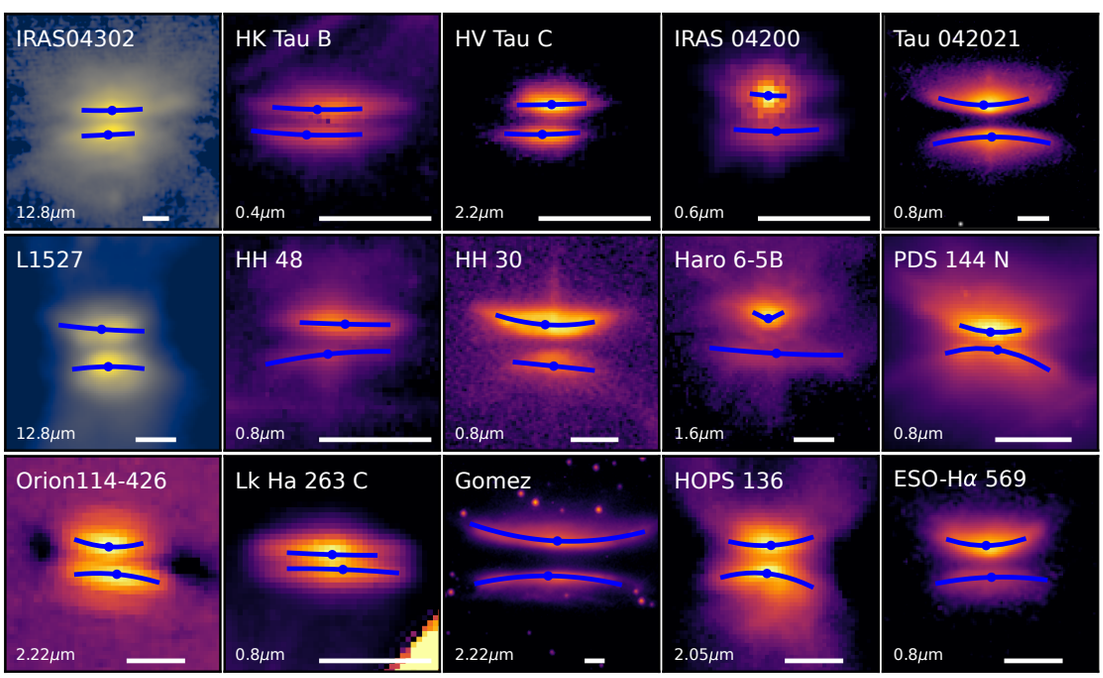

Figure 2.5: Protoplanetary disks observed edge-on that exhibit asymmetry between top and bottom disk surfaces. In this figure, the blue dots are the fitted midpoints of each surface. The disks are asymmetric, if the dark lane (corresponding to the disk midplane) is not orthogonal to the connection line between the blue dots, which is the case in all of these fifteen disks. *Credit: Adapted from Figure 8 by Villenave et al., 2024. CC BY 4.0*

The shadows in warped disks can also be observed when disks are oriented edge-on to our line of sight. As discussed in Section 1.1.2, edge-on disks in scattered light typically show a sandwich shape due to their top and bottom surfaces. If parts of the disk are shadowed, this sandwich shape can become asymmetric. A

survey by Villenave et al. (2024) shows a multitude of such asymmetric edge-on disks In their sample, fifteen out of twenty disks exhibit a significant asymmetry, shown in Figure 2.5.

Other observational signatures of a warp can also be found in the disks' kinematics. Recall that the kinematic signature of disks can be derived from the observation of a specific line feature (most commonly the CO 2-1 rotational line). As the emission from such lines is very narrow, the rotational motion of the disk is enough to create a measurable Doppler shift of the line position between the side of the disk moving toward and away from the observer. In a planar, Keplerian disk, the line separating the red- and blue-shifted velocities is straight (see Figure 1.7). If that line[1] is bending as in the two disks in Figure 2.6, it could indicate a warp (Pinte et al., 2023). Further disks with possible warp signatures in their kinematics are for example HD 100546 (Walsh et al., 2017), J16042165-J130284 (Mayama et al., 2018) and HD 143006 (Pérez et al., 2018).

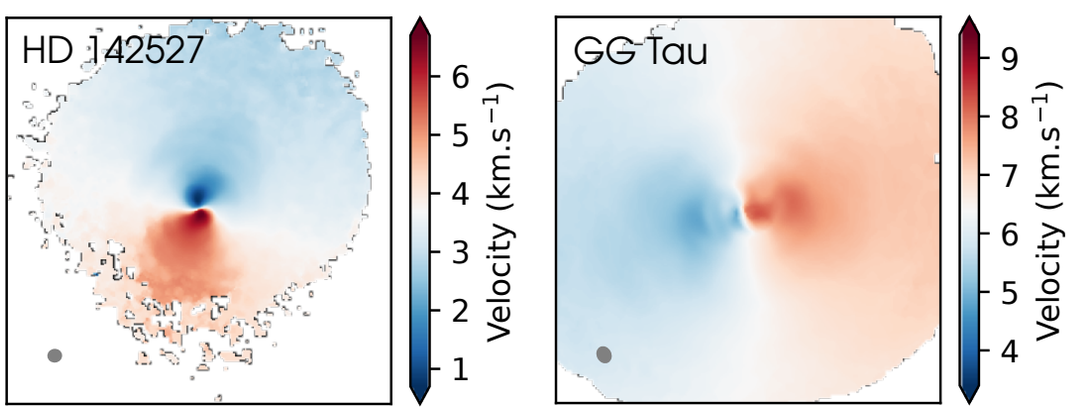

Figure 2.6: Kinematics possibly indicating a warp, as the white line between the red and blue regions of the disk is not straight. *Credit: HD 142527: Garg et al., 2021, GG Tau: Phuong et al., 2020.*

It is challenging to pinpoint warps in disk kinematics because other physical processes can lead to similar signatures in the velocity field, making it hard to distinguish observations. For example, radial flows or disk eccentricities can create similar structures in the observations. Synthetic observations are useful for distinguishing signatures for the different scenarios. The signatures of warps in kinematics were studied for example by Juhász & Facchini (2017). Recently, Zuleta et al. (2024) concentrated on signatures to distinguish warps from radial flows in kinematic models.

Even though there are multiple possibilities for observing warps, the specific

[1]The white line in the two observed disks in Figure 2.6 does not correspond to $v = 0\,\mathrm{km/s}$, because the systems have a systematic relative motion with respect to us.

parameters of existing warped disks, such as mutual inclination, warp shape, and twist, are not yet well constrained. This is one of the reasons why theoretical studies about the formation and evolution of warps are key to interpreting the observations. Improving the theoretical framework and tightening the link between models and observations will strengthen the knowledge in the field of planet formation.

2.2 Formation of warps

The wealth of warp observations suggests that warps might be common in protoplanetary disks. However, it is still unclear how most systems acquired the warp. There are many possible formation scenarios for warps, but it is yet to be probed which of the scenarios is the most common. It is even possible that more than one scenario play a significant role in nature. In this section, I introduce the different suggested formation theories.

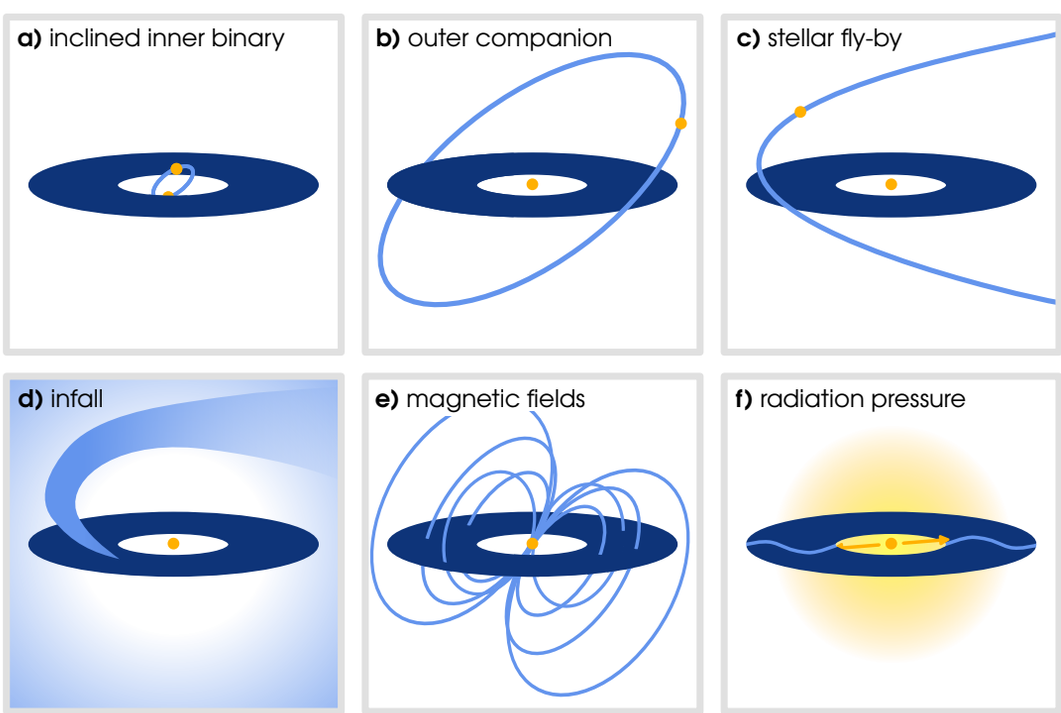

Figure 2.7: A summary of the different warp formation scenarios. The driving mechanism in the top row is the same: a misaligned bound or unbound companion gravitationally pulls the disk out of plane (panels **a-c**). The bottom row shows additional scenarios: **d)** Infalling material adds misaligned angular momentum. **e)** A misaligned magnetic field can deform the disk. **f)** Radiation pressure from the central star can trigger an instability leading to warps.

The most intuitive formation scenario is a companion inclined with respect to the disk plane. This companion acts a gravitational torque onto the disk, causing a change of the disk's orbital plane. Because the gravitational force strongly depends on the distance, specifically $F_G \propto r^{-2}$, the parts of the disk closer to the companion are affected more severely than the parts farther away, leading to a differential misalignment within the disk, or in other words: a warp.

The scenario of a gravitational companion can be split into three categories. The first category is a misaligned circumbinary disk (see Figure 2.7, panel a). The inner binary continuously drives a warp (Foucart & Lai, 2013; Lodato & Facchini, 2013; Deng & Ogilvie, 2022; Rabago et al., 2023), and depending on the system's properties, the disk can even break (Facchini et al., 2013; Nixon et al., 2013; Facchini et al., 2018; Rabago et al., 2024). The second category of gravitational companions is a wide outer binary companion (Papaloizou & Lin, 1995; Doğan et al., 2015; Zanazzi & Lai, 2018a; Doğan et al., 2023) or an inclined planet (Figure 2.7, panel b; Teyssandier et al., 2013; Nealon et al., 2018; Zhu, 2019). A planet could also be within the regime of the disk and then punch through the disk twice per orbit. Finally, the third category is an inclined fly-by (Figure 2.7, panel c), where a star or another massive object passes by the disk on an unbound parabolic or hyperbolic orbit (Clarke & Pringle, 1993; Cuello et al., 2019; Nealon et al., 2020a). In contrast to the first two categories, a fly-by is a one-time event and does not drive the warp continuously.

An alternative scenario creating a warp in a protoplanetary disk is the infall of material onto an initially planar disk. The infalling material is likely to be misaligned with respect to the rotational axis of the star and can therefore add a significant amount of misaligned angular momentum (Kuffmeier et al., 2024), which is shown to create a warp (Dullemond et al., 2019; Kuffmeier et al., 2021). Such infall can for example occur in the form of streamers or the capture of a cloudlet. This scenario is pictured in Figure 2.7, panel d.

Another possibility to generate a warp are magnetic fields. Especially young stars have a great deal of convection, which leads to strong magnetic fields. These fields are often misaligned with respect to the disk plane (Romanova et al., 2021), leading to a warp and precession especially of the inner region of the disk (Foucart & Lai, 2011).

A further suggested formation scenario is called self-induced warping. Warped disks can be influenced by the radiation pressure from the central object (Figure 2.7, panel f), enhancing and changing the warp of a disk (Petterson, 1977). This effect can even be triggered in initially planar disks (Pringle, 1996; Maloney et al., 1996). Although this scenario was originally derived for compact central objects such as black holes or neutron stars, it might also apply for disks around

main-sequence stars (Armitage & Pringle, 1997).

The diverse range of formation scenarios could explain the variety of observed warps. The most realistic warp shape likely depends on the specific formation mechanism and therefore remains unknown in the current state of research. Additionally, the warp evolution can be influenced by the formation scenario, in particular if the warp is continuously driven. However, not all warps remain driven, and to distinctly understand the intrinsic warp evolution, the next section focuses specifically on the evolution of undriven warps.

2.3 Evolution of warped disks

In typical conditions of protoplanetary disks, a warp is not stable. The cause of the warp evolution is a torque arising because neighboring orbits are misaligned with respect to each other. Because of the misalignment, orbiting gas parcels perform a vertical oscillation with respect to each other during their orbit. This can be seen in Figure 2.8, where a gas parcel on the blue orbit is above a parcel on the orange orbit on the right side ($\phi = 0$) and below the orange orbit on the left side ($\phi = \pi$). This causes pressure gradients, giving rise to a radial motion of the gas, as indicated by the green arrows. This radial motion is referred to as sloshing motion (sometimes also resonant motion; Dullemond, Kimmig, & Zanazzi, 2022a). The sloshing motion is the main driver of the warp evolution, as it causes the internal torque acting to change the orbital planes within the disk.

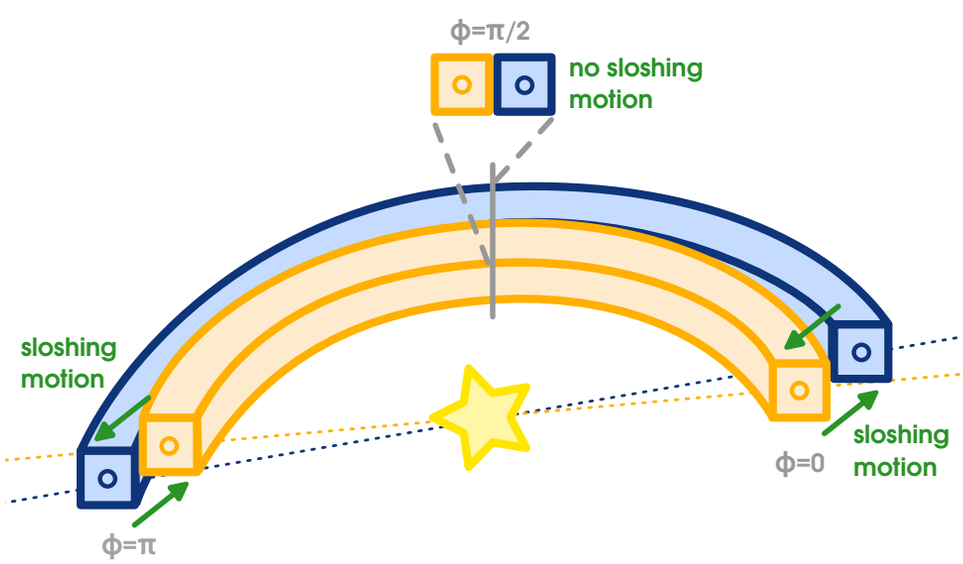

Figure 2.8: Misaligned neighboring annuli in a warped disk. The vertical displacement is greatest for $\phi = 0$ and π, where the radial sloshing motions (green arrows) are maximal. The annuli are at the same height for $\phi = \pi/2$ and $3\pi/4$ and no radial sloshing motion occurs.

The sloshing motions on the top side of the disk are directed toward the same side (i.e., both to the left in Figure 2.8), and correspondingly the motions on the bottom side toward the opposite direction. This means that the torques changing the orbital plane of orbits do not cancel out, enabling the evolution of the orbital plane. This is an intrinsic effect that occurs simply because neighboring orbits are misaligned. Therefore, a warp without any external warp driving effects is never stable. Of course, this consideration is only a simplified view on the evolution mechanism. The exact physics of the evolution depends on the detailed internal dynamics and pressure structure within the system.

In the end, the internal processes in a warped disk act to align the disk. This means that over time, the warped disk will lose its warp unless there is a mechanism that keeps the warp alive, such as an external torque from an inclined binary or a misaligned magnetic field. In an undriven case, the warp is dampened until it vanishes and the timescale of this damping depends on the properties of the disk. In typical conditions of protoplanetary disks (in especially vertically thick disks with low viscosity) this damping occurs on a timescale of $\tau_{\mathrm{damp}} = 1/\left[\alpha\Omega(r_{\mathrm{out}})\right]$, where α is the Shakura-Sunyaev viscosity in the disk and Ω the Keplerian frequency evaluated in the outer region of the disk r_{out} (Nixon et al., 2013).

2.3.1 Evolution equations

The effective evolution depends on the properties of the disk and takes place in two different regimes. The parameters determining the regime are the disk's viscosity α and its vertical thickness H_{p}/r. For low viscosities $\alpha < H_{\mathrm{p}}/r$, the evolution occurs in a *wave-like* manner, whereas a warp in high viscosity $\alpha > H_{\mathrm{p}}/r$ disks evolves *diffusively*.

The evolution equations can be derived when considering the internal torque and the sloshing motions in warped disks (see Ogilvie & Latter, 2013a,b). The equations describe the evolution of the angular momentum vectors of concentric annuli in the disk. For each annulus, the angular momentum vector is by definition orthogonal to the plane of the annulus, and thus the evolution of the vector describes the evolution of the orbital plane of that annulus. This way, the warp evolution can be described depending on the radial coordinate (i.e., the distance from the central star). This is the reason why these equations are usually called *one-dimensional* equations.

Historically, both the wave-like and the diffusive regimes have their own set of evolution equations. However, the underlying physics for the evolution of the warp is the same in both regimes. It is therefore possible to express the equations in a generalized way, which is valid in both regimes.

Even though protoplanetary disks typically fall in the wave-like regime, I will discuss in the following all three sets of equations as the equations in the limit of each regime helps to give a comprehensive view on the generalized set of equations and hence the understanding of the warp evolution in general.

Wave-like evolution

In the wave-like regime (recall $\alpha < H_\mathrm{p}/r$), the warp travels in a wave through the disk, as outlined in Figure 2.9. The warp wave is reflected at the disk edges as the density gets shallower, similar to ocean waves on the beach.

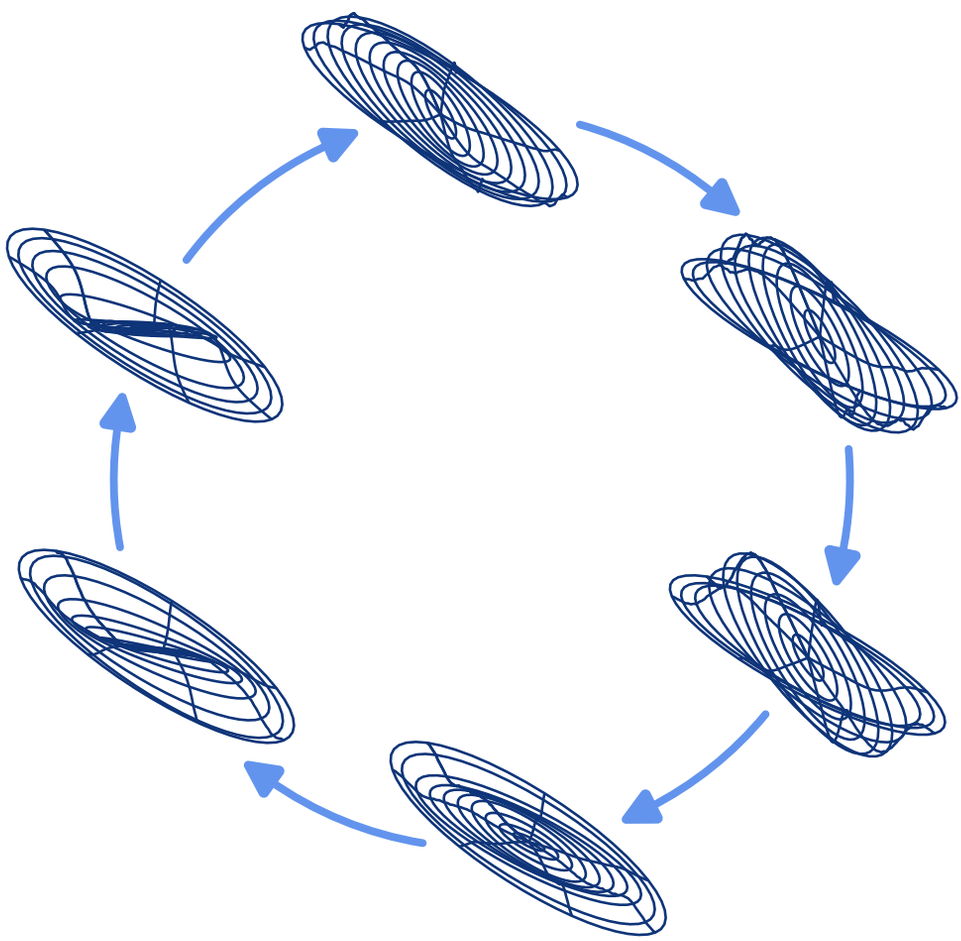

Figure 2.9: Wave-like evolution of a warped disk in a schematic representation. The warp travels as wave through the disk. In a viscous disk, the amplitude of the warp wave is dampened over time, leading to a planar, but tilted disk (not represented in this figure). *Adapted from Figure 1 in Peng et al., 2025. CC BY 4.0*

The set of equations in the wave-like regime can be written as (Papaloizou &

Lin, 1995; Demianski & Ivanov, 1997; Lubow & Ogilvie, 2000)

$$\frac{\partial \vec{G}}{\partial t} + \omega \left(\vec{l} \times \vec{G}\right) + \alpha\Omega\vec{G} = \frac{\Sigma H_\mathrm{p}^2 r^3 \Omega^3}{4} \frac{\partial \vec{l}}{\partial r} \tag{2.1}$$

$$\frac{\partial \Sigma}{\partial t} = 0 \tag{2.2}$$

$$\frac{\partial \vec{L}}{\partial t} = \frac{1}{r}\frac{\partial \vec{G}}{\partial r} + \mathbf{T}, \tag{2.3}$$

where $\vec{L} = \vec{L}(r)$ is the angular momentum vector with $\vec{l}$ as unit vector of the angular momentum, $\vec{G} = \vec{G}(r)$ is the internal torque, ω the apsidal precession frequency, and $\mathbf{T}$ a potential external torque. In the following, I go through the set of equations and the contained terms in detail.

(2.1) The first equation in this set describes the evolution of the internal torque $\vec{G}$.

The second term on the left-hand side of this equation can cause an internal precession in the disk, determined by the apsidal precession frequency $\omega = (\Omega^2 - \kappa^2)/(2\Omega)$, where Ω is the angular frequency in the disk and κ is the epicyclic precession frequency $\kappa = 4\Omega^2 + 2r\Omega\frac{\partial\Omega}{\partial r}$. For a perfectly Keplerian disk, the epicyclic frequency equals the angular frequency, which implies $\omega = 0$ and no internal precession. This is adopted in many one-dimensional models of protoplanetary disks. However in reality, pressure gradients occur in the disk, leading to a deviation of the azimuthal velocity from the Kepler velocity, and therefore a non-zero ω. This could have a great influence on the warp evolution.

The third term on the left-hand side describes the damping of the warp waves. This term determines the damping timescale $\tau_\mathrm{damp} \approx 1/(\alpha\Omega)$. Because the reason for damping in this model is the viscosity α, this is often referred to as α-damping.

The term on the right-hand side describes the wave behavior of the warp. This can be seen, following the consideration in Nixon & King (2016), in the case of an invicid disk ($\alpha = 0$), which is perfectly Keplerian ($\omega = 0$). This equation then reduces to $\partial\vec{G}/\partial t = \frac{1}{4}\Sigma H_\mathrm{p}^2 r^3\Omega^3\,\partial\vec{l}/\partial r$, which can be combined with Equation 2.3, using $\vec{L} = \Sigma r^2\Omega\vec{l}$

$$\frac{\partial^2 \vec{l}}{\partial t^2} = \frac{1}{\Sigma r^3\Omega}\frac{\partial}{\partial r}\left(\frac{\Sigma H_\mathrm{p}^2 r^3\Omega^3}{4}\frac{\partial \vec{l}}{\partial r}\right), \tag{2.4}$$

which compares to a classical wave equation if $\Sigma H_\mathrm{p} = \text{const}$. In this case, the speed of the warp wave is $v_\mathrm{warp} = c_\mathrm{s}/2$.

This means that the crossing time of the warp wave through the disk can be

estimated with $\tau_{\text{warp}} = \Delta r / v_{\text{warp}} = 2\Delta r / c_s$, where $\Delta r = r_{\text{out}} - r_{\text{in}}$ is the radial extent of the disk. For compact protoplanetary disks[2], the crossing time can therefore be $< 200\,\text{yr}$, which is extremely short for astronomical timescales.

(2.2) The second equation in this set states that the surface density does not evolve. However, this is not a result from the analytic derivation, but an assumption taken in order to simplify the consideration. This assumption is motivated by the fact that the evolution of the warp takes place on shorter timescales than the evolution of the surface density. This can be a valid assumption, especially when looking at the evolution of the orbital planes in the disk on short timescales. However, the surface density in protoplanetary disks evolves significantly on longer timescales due to viscosity. Therefore, this assumption can be problematic in long-term simulations. A possible solution for this are the generalized warp evolution equations, which I will discuss later in this section.

(2.3) Finally, the third equation states that the angular momentum vectors $\vec{L}(r)$ evolve because of the internal torque $\vec{G}$ and a possible external torque $\mathbf{T}$.

I note that throughout literature, different notations and different definitions can be found. For example, Ogilvie & Latter (2013a) define their internal torque as $\vec{G}_{\text{OgilvieLatter}} = -\vec{G}/(2\pi)$. An overview over some different notations and definitions can be found in the appendix of Dullemond, Kimmig, & Zanazzi (2022a).

Diffusive evolution

In the regime of high viscosity disks (specifically $\alpha > H_p/r$), the damping by viscosity is so strong that the warp does not travel as a wave, but is instead smoothed out over time, as shown in Figure 2.10.

In order to describe the evolution in the diffusive regime accurately, different assumptions need to be made. In especially, the evolution of the surface density can no longer be neglected, because the high viscosity leads to a stronger evolution. However in this regime, the internal torque is almost static, which makes the derivation of the warp evolution from conservation equations (Papaloizou & Pringle, 1983) more convenient. The full set of evolution equations in the diffusive regime then state (Pringle, 1992; Ogilvie, 1999):

[2] In the example of $h = H_p/r = 0.05$, $r_{\text{in}} = 1\,\text{au}$, $r_{\text{out}} = 10\,\text{au}$, around a sun-like star $M_* = M_\odot$.

$$\frac{\partial G}{\partial t} = 0 \tag{2.5}$$

$$\frac{\partial \Sigma}{\partial t} = \frac{3}{r}\frac{\partial}{\partial r}\left[r^{1/2}\frac{\partial}{\partial r}\left(\nu\Sigma r^{1/2}\right)\right] + \frac{1}{r}\frac{\partial}{\partial r}\left(\nu_2\Sigma r^2\left|\frac{\partial \vec{l}}{\partial r}\right|^2\right) \tag{2.6}$$

$$\begin{aligned}\frac{\partial \vec{L}}{\partial t} = {} & \frac{3}{r}\frac{\partial}{\partial r}\left[\frac{r^{1/2}}{\Sigma}\frac{\partial}{\partial r}\left(\nu\Sigma r^{1/2}\right)\vec{L}\right] \\ & + \frac{1}{r}\frac{\partial}{\partial r}\left[\left(\nu_2 r^2\left|\frac{\partial \vec{l}}{\partial r}\right|^2 - \frac{3}{2}\nu\right)\vec{L}\right] \\ & + \frac{1}{r}\frac{\partial}{\partial r}\left[\frac{1}{2}\nu_2 r\left|\vec{L}\right|\frac{\partial \vec{l}}{\partial r}\right] \\ & + \frac{1}{r}\frac{\partial}{\partial r}\left[\nu_3 r\left|\vec{L}\right|\left(\vec{l}\times\frac{\partial \vec{l}}{\partial r}\right)\right],\end{aligned} \tag{2.7}$$

where $\nu = \alpha\, c_s H_p$ is the kinematic viscosity, ν_2 the vertical shear viscosity due to the misalignments of neighboring orbits in a warp, and ν_3 a viscosity-like parameter causing an internal precession in the disk. These two parameters can be related to an α-parameter in the same way: $\nu_{2,3} = \alpha_{2,3}\, c_s H_p$. However, it is important to keep in mind that the parameter α_3 is only a viscosity-like parameter expressed in the same way. It does not describe a process of diffusion in the disk, but instead is responsible for a precessional motion. Under the assumption of small warp amplitudes, these "viscosity" parameters can be expressed in terms of the common Shakura-Sunyaev α-viscosity (Papaloizou & Pringle, 1983; Ogilvie, 1999)

$$\alpha_2 = \frac{2(1+7\alpha^2)}{4+\alpha^2};\ \alpha_3 = \frac{3(1-2\alpha^2)}{3(4+\alpha^2)}. \tag{2.8}$$

These equations simplify in linear theory to $\alpha_2 = 1/(2\alpha)$ and $\alpha_3 = 3/8$.

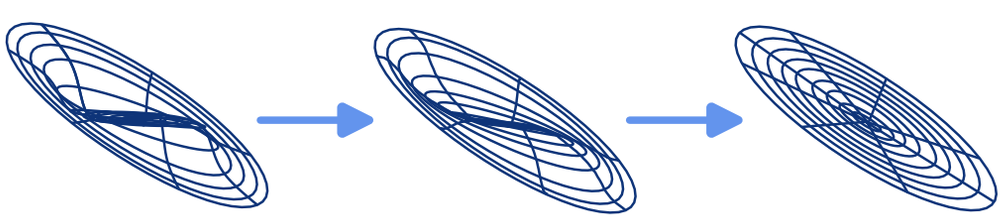

Figure 2.10: Schematics of the diffusive warp evolution. An initial warp is dampened over time by viscosity, leading to a planar disk (=unwarped, right panel). *Adapted from Peng et al. (2025). CC BY 4.0*

Protoplanetary disks usually do not fall in the diffusive regime, as their viscosity is typically low. I will therefore keep the discussion on this set of equations short. However, it is worth pointing out that the internal torque $\vec{G}$, which is hidden in these equations, is very similar to the wave-like regime. This fact is not surprising, as the cause for the internal torque in both regimes is the same: the sloshing motion because of the misalignment of neighboring orbits. To make the similarity of the internal torque apparent, it can be untangled from the set of equations. Because of the assumption of a static torque, it does not evolve in time, and can hence be expressed explicitly (Ogilvie & Latter, 2013a):

$$\vec{G}_{\text{diffusive}} = 2\pi r\,\Sigma r^2\Omega\left[\nu\left(\frac{\frac{\mathrm{d}\Omega}{\mathrm{d}r}}{\Omega}\right)\vec{l} + \frac{1}{2}\nu_2\frac{\partial\vec{l}}{\partial r} + \nu_3\vec{l}\times\frac{\partial\vec{l}}{\partial r}\right]. \tag{2.9}$$

If the relation from linear theory $\alpha_2 = 1/(2\alpha)$ is assumed, the second term on the right-hand side transforms to the right-hand side of Equation 2.1, the equation of internal torque evolution on the wave-like regime. This shows that it should be possible to describe both regimes in just one single set of equations.

Generalized equations

The idea to combine the two different sets of equations into a single set was originally proposed by Martin et al. (2019). Their approach is based on the empirical comparison between the two sets of equations, creating a generalized set of equations valid in both regimes. Dullemond, Kimmig, & Zanazzi (2022a) were able to physically derive the same set of equations from a consideration of the sloshing motions, proving the validity of this set:

$$\frac{\partial\vec{G}}{\partial t} + \omega\vec{l}\times\vec{G} + \alpha\Omega\vec{G} - \left(\vec{l}\times\frac{\partial\vec{l}}{\partial t}\right)\times\vec{G} = \frac{\Sigma H_{\mathrm{p}}^2 r^3\Omega^3}{4}\frac{\partial\vec{l}}{\partial r} - \frac{3}{2}\alpha\nu\Sigma r^2\Omega^2\vec{l} \tag{2.10}$$

$$\frac{\partial\Sigma}{\partial t} = -\frac{2}{r}\frac{\partial}{\partial r}\left[\frac{\frac{\partial\vec{G}}{\partial r}\cdot\vec{l}}{r\Omega}\right] \tag{2.11}$$

$$\frac{\partial\vec{L}}{\partial t} = -\frac{2}{r}\frac{\partial}{\partial r}\left[\frac{\frac{\partial\vec{G}}{\partial r}\cdot\vec{l}}{\Sigma r\Omega}\vec{L}\right] + \frac{1}{r}\frac{\partial\vec{G}}{\partial r} + \mathbf{T}. \tag{2.12}$$

This set of equations can be transformed into the respective set in the limit of each regime by taking the appropriate assumptions. For details of this transformation I refer to Martin et al. (2019). In comparison to the wave-like set of equations, the generalized set is the same, with some additional terms that I will discuss in detail.

(2.10) The evolution equation of the internal torque has two additional terms compared to the wave-like set.

The fourth term on the left-hand side is one of these additional terms, and actually differs between Martin et al. (2019) and Dullemond, Kimmig, & Zanazzi (2022a), with the version in this work being the version of the latter. In Martin et al. (2019), this term reads $+\beta\Omega\left(\vec{G}\cdot\vec{l}\right)\vec{l}$ and was introduced to suppress an unphysical behavior of the surface density evolution that occurs without this term. However, the parameter β was only introduced as an effective viscosity to avoid this unphysical behavior and does not have a profound physical meaning. Dullemond, Kimmig, & Zanazzi (2022a) found the reason behind the unphysical behavior: Without this term, the equations do not take into account the change in the orbital plane during the evolution, therefore the internal torque vector $\vec{G}$ becomes slightly misaligned over time, causing the surface density to behave unphysically in such a model. Therefore, they added this fourth term on the left-hand side in Equation 2.10, which accounts for the rotation of the orbital plane. In other words, it rotates the internal torque vector according to the change of the orbital plane.

The other additional term is the second term on the right-hand side. This term corresponds to the viscous stress in the disk and is especially important for the viscous evolution of the surface density. When dividing the whole equation by $\alpha\Omega$ (in order to scale the internal torque as suggested by the third term on the left-hand side), this second term on the right-hand side becomes identical to the viscous stress in typical models of planar (=unwarped) disks, see Equation 1.21.

(2.11) In comparison to the wave-like set, the surface density is now allowed to evolve. The term on the right-hand side describes the evolution of the surface density due to the internal torque. This additional term is derived from the mass and angular momentum equations, obtaining a radial velocity depending on the internal torque

$$v_r = \frac{\frac{\partial\vec{G}}{\partial r}\cdot\vec{l}}{r\Sigma\frac{\mathrm{d}(r^2\Omega)}{\mathrm{d}r}}. \tag{2.13}$$

Details of the derivation can be found in Martin et al. (2019). Physically, this evolution has both the contribution from the viscous evolution (because of the last term in Equation 2.10) and the contribution from the misalignment of neighboring orbits (all other terms in Equation 2.10).

(2.12) This equation has one additional term compared to the wave-like set, which is the first term on the right-hand side. As for the evolution of the surface density, this term results from the radial velocity given in Equation 2.13.

This generalized set of equations is useful for protoplanetary disks, especially when considering the long-term evolution, because it includes the evolution of the surface density. Additionally, because this set of equations is valid in both regimes, it also includes the parameter space of $\alpha \approx H_\mathrm{p}/r$, which can be important for some protoplanetary disks. Throughout the years, there have been many analytic studies aiming at extending the model more toward the non-linear effects that are currently not captured in these one-dimensional equations (Ogilvie, 2006; Paardekooper & Ogilvie, 2019; Fairbairn & Ogilvie, 2021a,b). This shows that there is more work to be done.

This one-dimensional view on the warp evolution is extremely useful to understand the physical mechanisms behind the evolution. Many works compared the results of this one-dimensional models to results from three-dimensional hydrodynamic models using SPH. Overall, the one-dimensional models compare well with the three-dimensional results (Lodato & Pringle, 2007; Lodato & Price, 2010; Nealon et al., 2015; Deng & Ogilvie, 2022; Fairbairn & Ogilvie, 2023). However, the one-dimensional treatment remains a simplified view and may not be able to accurately describe the warp evolution in all cases. Additional effects, such as cooling from shadows in the disk (Qian & Wu, 2024), can also influence the evolution of warped disks. In most models, this effect is not yet taken into account. All in all, it is useful to investigate the evolution of warps in three-dimensional models, which is a part of my work in this thesis.

2.4 Observational implications of the warp evolution

The relatively fast evolution of warped disks can have great implications on observations of warped disks. The wave-like evolution and possible precession can cause shadows to move, and if the timescales are short enough, the shadow movement may be possible to observe within the lifetime of a human (Pinte et al., 2023). The movement of shadows depend on the geometric properties of the warp (Facchini et al., 2018; Pinilla et al., 2018; Nealon et al., 2020b).

This is of particular interest to the research community of protoplanetary disks, since shadow movements have been observed in a few systems. For example, Debes et al. (2017) found a significant movement of the shadow in the disk around TW Hya in scattered light observations within just one year, as shown in Figure 2.11. Fast-moving shadows were also observed for example in HD 135344B

(Stolker et al., 2017) and MWC 758 (Ren et al., 2020). Whether the fast shadow evolution is indeed linked to warp evolution is a matter of ongoing research.

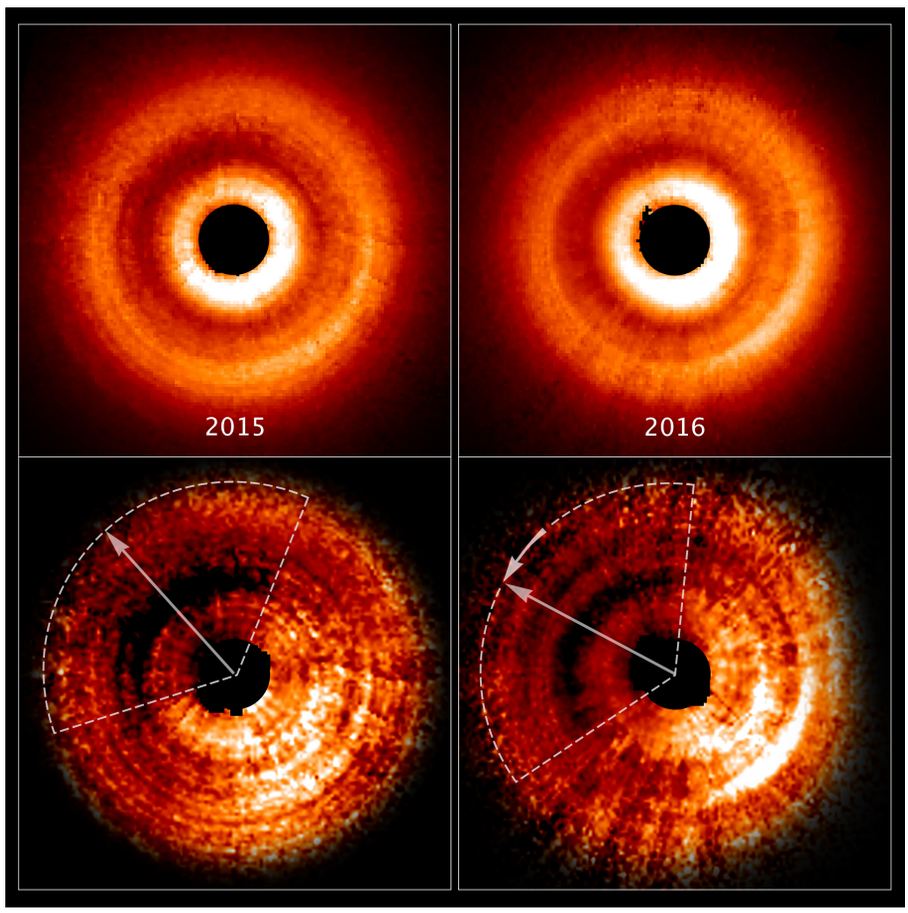

Figure 2.11: The movement of the shadow in the TW Hya system between scattered light observations ($\lambda = 0.5\,\mu$m) taken several months apart (left column in 2015, right column in 2016). The bottom row shows the observed flux after substracting the azimuthal mean value of the flux. *Credit: NASA, ESA, and J. Debes (STScI).*

Because of the internal processes in warped disks, especially the radial sloshing motions, the evolution of warps can also have a great influence on kinematic observations of disks. Distinguishing warps from other effects can be challenging (Zuleta et al., 2024).

It is therefore important to use the results from models of warp evolution to investigate the observational signatures of warps. This can be done in synthetic observations, which can be created using radiative transfer models. In the next section, I will introduce the idea behind these models.

2.5 Radiative transfer models

The purpose of radiative transfer models is often to create images of simulations as if they were observed by telescopes (so-called synthetic observations). These synthetic observations enable a thorough comparison between real observations and theoretical models. The basic idea behind synthetic observations is tracing light rays from their source to the hypothetical observer. In the case of protoplanetary disks, the light source are usually the central stars. However, depending on the temperature of the disk and the synthetically observed wavelength, the disk itself can become a light source due to its thermal radiation. The light of the central star irradiates the disk with emission peaking at visible and near-infrared wavelength. This light can either be scattered by the disk or absorbed and re-emitted at a lower wavelength of the dust equilibrium temperature. Radiative transfer models calculate for each these light rays from the star how it is scattered and/or absorbed.

Synthetic observations are not the only application of radiative transfer. In astrophysical systems, radiation is usually a key ingredient for the heating and cooling of the system, dictating its temperature. Additionally, radiation causes ionization of gas in astrophysical systems, which influences the chemical composition. This is why radiative transfer, also called radiation transport, is a major aspect of astrophysics.

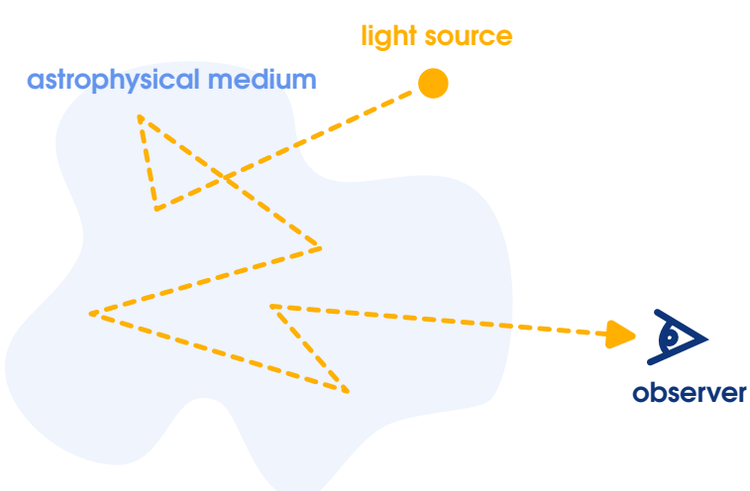

Figure 2.12: A possible path of a photon from a light source to an observer, scattered multiple times by material along the way.

The basic idea of radiative transfer might seem simple, but the true problem is highly complex. The radiative transfer problem contains seven dimensions: the

three spatial coordinates, the travel direction of the light which can be described with two angles, the frequency of the light, and the time. All of these parameters need to be taken into account to accurately describe the radiative transfer process. Additionally, the radiative transfer problem depends on the distribution and properties of the matter which the light is traveling through, because the light interacts with the matter through absorption, re-emission and scattering (indicated in Figure 2.12). In cases where the radiation also affects the state of the matter in the astrophysical system, the problem gains even more complexity. It is therefore challenging to solve straight-forwardly.

The formal radiative transfer equation

To solve the radiative transfer problem, it is important to understand the interaction of the radiation with the medium. Along the path of a light ray, this interaction can remove or add radiation to the ray, or change the ray's direction through scattering.

Radiation can be removed from a light ray by absorption of photons. This process is called extinction. The absorption of photons a random process that depends on the properties of the medium. We can describe the extinction properties of a medium with the absorption coefficient α_ν, which is defined as the inverse of the mean free path, the average path a photon can travel before being absorbed. It depends on the frequency of the light ν. This absorption coefficient depends on the density of the medium $\alpha_\nu = \rho\kappa_\nu$, where κ_ν is called mass-weighted opacity (or often simply called opacity). The opacity depends on the wavelength and material properties, for example the shape and temperature of the optical medium. For details about the opacity relevant to protoplanetary disks, see Dominik et al. (2021). We can quantify the absorption along a path s of a light ray with the integral over the absorption coefficient

$$\tau_\nu = \int \alpha_\nu(s)\mathrm{d}s. \tag{2.14}$$

This quantity τ_ν is called optical depth. A larger optical depth means a stronger absorption, thus less radiation is transmitted through the medium. In this case, specifically for $\tau \gg 1$, the medium is called *optically thick*. Vice versa, a medium with $\tau \ll 1$ is called *optically thin*.

Radiation can be added to a light ray if the medium is emitting photons. The emission can be quantified in the emission term $j_\nu(s)$. As both absorption and emission can change the intensity I_ν of a light ray along the way, we can establish

the *formal radiative transfer equation* (see e.g. Rybicki & Lightman, 1985)

$$\frac{\mathrm{d}I_\nu}{\mathrm{d}s} = \alpha_\nu \left[S_\nu - I_\nu\right], \tag{2.15}$$

with the source function S_ν defined as $S_\nu \equiv j_\nu/\alpha_\nu$. If the medium is in local thermodynamic equilibrium (LTE), which means that the medium locally emits the same amount of energy as it absorbs, the source function equals the Planck function $S_\nu = B_\nu(T)$. This is called *Kirchhoff's law* (Kirchhoff, 1860). At this point, let us recall the Planck function

$$B_\nu(T) = \frac{2h\nu^3/c^2}{e^{h\nu/k_\mathrm{B}T} - 1}, \tag{2.16}$$

where ν is the frequency of the light, T the emission temperature, h is the Planck constant, c the speed of light, and k_B the Boltzmann constant. Kirchhoff's law is not always applicable as the condition for local thermodynamic equilibrium is not always met in astrophysics. However, where it is valid, the radiative transfer equation simplifies, as it then states that the intensity will asymptotically approach the Planck function.

In addition to the absorption and emission, light rays can change their direction through scattering events, which complicate the radiative transfer problem as photons are no longer easily traced back to their origin. These scattering events usually occur because of dust particles. The simplest scattering is the case of isotropic scattering, where each new direction after the scattering event is equally likely. However, most dust particles lead to anisotropic scattering, usually where small scattering angles compared to the former direction are preferred. This phenomenon is called *forward scattering*. The likeliness of scattering angles can be expressed in scattering phase functions, which highly depend on the properties of the dust particle, such as particle size, chemical composition, and porosity properties. The scattering phase function of the dust in a medium has a great influence on the opacity. Obtaining the phase function for a specific dust composition is far from trivial. Discussing details of the phase function in detail would go beyond the scope of the thesis, I thus refer for example to Bohren & Huffman (1983).

In astrophysics, it is often not obvious which kind of dust can be present in a system. This makes the comparison of observations with synthetic images even more difficult. An often assumed dust composition is the DIANA standard model (Woitke et al., 2016), a mixed composition of carbon and a pyroxene silicate.

Computational methods for radiative transfer

The complexity of the radiative transfer problem requires a numerical approach to solve it. There are multiple methods to do this, and discussing them in depth would go beyond the scope of this thesis. Therefore, this section only gives a broad overview.

In general, two classes of methods can be distinguished: classical and stochastical methods. Classical methods approach the problem by numerically discretizing the radiative transfer equation, often using iterative computational schemes. This is the most straight-forward way of tackling the problem, but usually requires a very long computation time (so-called "expensive simulations"). Classical methods can be feasible if symmetries of the astrophysical system can be exploited, such as the spherical symmetry of a stars. For example, the Feautrier method (Feautrier, 1964) makes use of such symmetries and can re-write the radiative transfer equation in the form of a second order ordinary differential equation. This makes this method easy to implement and stable, but it needs to be limited to very few discrete points for the discretization, as the computation time scales with the cube of the number of these points. An approach to reduce the computation time is a method called *Accelerated Lambda Iteration* (ALI, Rybicki & Hummer, 1991), which is treating the dependence of the intensity on the source function as an operator (Cannon, 1973) that can be determined iteratively. However, the convergence of the iteration can be slow depending on the properties of the simulated system.

Stochastical methods provide a completely different approach to solving the radiative transfer problem. These methods do not solve the radiative transfer equation directly, but mimic the random path of photons through the medium. Because this *random walk* is modeled by drawing random numbers from distributions, these methods are commonly referred to as *Monte Carlo techniques* (Niccolini et al., 2003; Pinte et al., 2006). The basic concept of Monte Carlo methods is to follow a photon, which is emitted from a light source and travels some distance before it is scattered by interaction with the medium. Because it is not efficient to follow the path of single photons, they are usually bundled together in so-called photon packages that coincidentally experience the same interactions. For each interaction, the new travel direction is then randomly determined. Likewise, the length between interactions is determined randomly, but is related to the optical depth of the medium, which determines the mean free path of a photon package. Absorption and possible re-emission can also be taken into account by these methods.

Monte Carlo methods have some significant advantages over classical methods. For example, no convergence through iteration is necessary and it can be applied to highly complex geometries, taking into account the full dimensionality of the problem without increasing the computation time. Additionally, the energy of the photon packages is well defined and each package is traced from beginning to end. This means that the energy is conserved well, as it can not be accidentally lost in the process. There is one disadvantage compared to classical methods, as a photon package can be caught up in an optically very thick region, where it can only travel tiny distances before interacting with the medium again. This can lead to a zigzag path of millions of interactions before being able to leave the optically thick region. However, this can be avoided with advanced methods (Min et al., 2009; Robitaille, 2010). Due to the strong advantages, Monte Carlo techniques are usually the method of choice for solving radiative transfer problems in astrophysics.

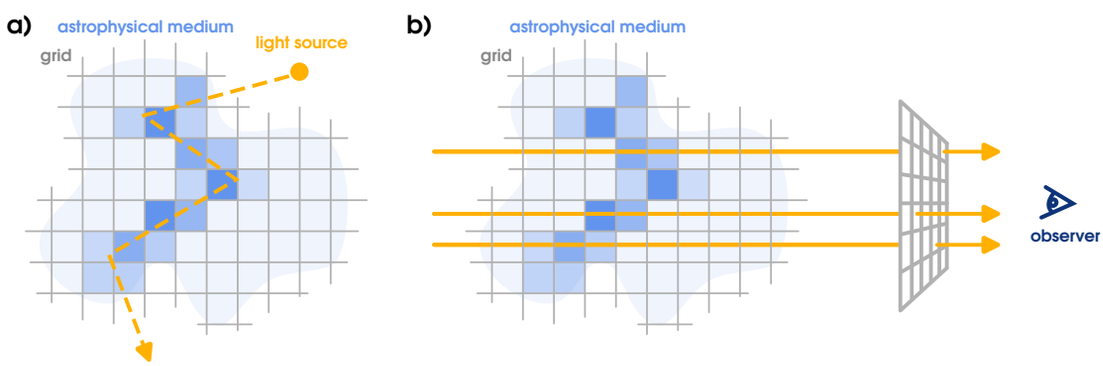

Figure 2.13: Two-step process to create a synthetic observation using the Bjorkman & Wood (2001) method. **a)** Path of an example photon package (orange dashed line) through an astrophysical medium contributing to the source function in the grid cells. **b)** Creating an image after determination of the source function using volume rendering. The radiative transfer equation is integrated along light rays originating from behind the astrophysical medium with respect to the observer (orange arrows). *Figure inspired by Dullemond, 2012.*

One of the most commonly used Monte Carlo methods is the Bjorkman & Wood (2001) method (Figure 2.13, panel a). The idea of this method is to determine the source function S_ν to calculate the temperature of the medium. For this, the medium is discretized with a grid and the photon packages can interact with the medium contained in these grid cells. The photon packages are sent out from a light source, and the initial frequency of each photon package is randomly drawn from a probability function. Each package then travels through the grid and performs random scattering interactions, as well as absorption and re-emission. An absorption and re-emission event can be treated very similar to a

true scattering event, only that the frequency of the photon package can change as well. This new frequency is again determined from a random distribution, in a way that was brought up by Bjorkman & Wood (2001). The difference in energy between the old and the new frequency remains in the grid cell where the photon package experienced this interaction. This can be used to determine the temperature of the medium consistently, which is a huge benefit.

However, with the Bjorkman & Wood method, only cells that have experienced such interactions with a photon package contain energy, which can lead to discontinuous temperatures, especially in optically very thin regions. To improve this, the so-called *cell-volume method* by Lucy (1999) is often used to obtain a smooth source function. The idea behind the cell-volume method is that a fraction of the photons contained in a photon package could interact with the material in cells along the straight path of a package. Here, the full package does not interact with the cell, meaning that it does not get scattered, but it distributes a part of the energy smoothly among the cells it traveled through. This enables a proper determination of the temperature even in optically thin regions. This combined method is for example used in the commonly used radiative transfer code RADMC-3D (Dullemond et al., 2012).

Once the source function is determined through this combined method, radiative transfer images can be computed through *volume rendering*. This is done by integrating the radiative transfer equation along rays originating from behind the medium we want to render. This process is indicated in Figure 2.13, panel b.

The resulting image usually gives a good impression on what the astrophysical system would look like if observed. However, synthetic observations obtained this way can not directly be compared to real observations, as the resolution on real observations is limited by the architecture of the instruments and, for ground-based instruments, also by atmospheric effects. In order to enable a quantitative comparison, the synthetic images are usually convolved with a point spread function to mimic these limiting effects and create images as if they were observed with a specific telescope. Evaluating synthetic observations without convolution can however be appropriate for qualitative results.

3

Warped disk evolution in grid-based simulations

This chapter is based on the paper Kimmig & Dullemond (2024) published in Astronomy & Astrophysics. I performed all simulations presented in this chapter and carried out the analysis of the data. The main part of the text as well as most figures were created by me. Only Section 3.5 and the corresponding sections in the chapter appendix, Sections 3.C and 3.D were written by my collaborator C. P. Dullemond, with contributions from me. Figures 3.24, 3.25, 3.26, and 3.C.1 were created by C. P. Dullemond using the data from my simulations. I included these parts in this thesis in order to provide a comprehensive view on the research presented in this chapter.

3.1 Background

As more and more observations of protoplanetary disks become available (Andrews et al., 2018; Andrews, 2020; Garufi et al., 2022, etc.), it is striking to note how many of them display non-axisymmetric features, such as the bright arcs as in HD 143006 (Pérez et al., 2018) or HD 135344B (Cazzoletti et al., 2018), spirals as in MWC 758 (Benisty et al., 2015), narrow shadow lanes as in HD 142527 (Marino et al., 2015) and in HD 135344B (Stolker et al., 2017), or the wide shaded regions as in TW Hydra (Debes et al., 2017) and in HD 139614 (Muro-Arena et al., 2020). Some of these asymmetrical features, in especially shadow lanes and wide shaded regions, can be traced back to a misaligned part of the disk casting a shadow.

Several misaligned disks have been detected, for instance: HD 142527 (Casassus et al., 2015), HD 100453 (Benisty et al., 2017), HD 143006 (Benisty et al., 2018), DoAr 44 (Casassus et al., 2018), GW Orionis (Kraus et al., 2020; Smallwood et al., 2021), KH 15D (Lodato & Facchini, 2013; Poon et al., 2021), and many more. Bohn et al. (2022) specifically targeted disks with shadow features and measured the misalignment angle between inner and outer regions of the disk by looking at each disk in near-infrared (NIR) observations to probe the inner disk and sub-

millimeter interferometric observations for the outer disk. Out of a sample of 20 disks, they found six disks with a significant misalignment and five disks showing no misalignment, while the remaining nine disks could not be analyzed with sufficient certainty based on the current data. A study by Min et al. (2017), involving analytical considerations of shadow locations, was used to deduce inner disk geometries. To investigate the shadow morphology, Nealon et al. (2019) studied shadows in synthetic scattered light observations. Nealon et al. (2020b) found that shadows cast by a misaligned inner disk can move in time and appear to rock back and forth depending on the misalignment angle and other disk geometry properties.

Misaligned disks can be classified into so-called "broken disks" that have two or more parts of the disk misaligned with respect to each other, and "warped disks," which contain a continuous misalignment, meaning that all parts of the disk are connected and the inclination angle changes with radius. The classification is, however, not perfectly sharp as there can be objects falling in between those categories or a mixture of both.

There are multiple mechanisms leading to the formation of misaligned disks. In all cases, a misaligned component, either external, internal, or a mix of both, is exerting a torque on the disk. In one scenario, a binary misaligned with respect to the disk plane, gravitationally torques the disk. The misalignment can form in a circumprimary or secondary disk with an outer companion (Papaloizou et al., 1995; Zanazzi & Lai, 2018a), as well as in a circumbinary disk (Facchini et al., 2013; Lodato & Facchini, 2013; Zanazzi & Lai, 2018b; Deng & Ogilvie, 2022). In the case of an inclined outer companion, the disk can (under certain conditions) precesses as a rigid body (Papaloizou & Terquem, 1995; Papaloizou et al., 1997) or break (Doğan et al., 2023; Rabago et al., 2024). An inner companion can drive a warp, leading to the alignment of the disk with the binary orbital plane (Foucart & Lai, 2013) or polar alignment (Zanazzi & Lai, 2018b; Rabago et al., 2023). The disk can also get warped if the companion is not bound to the system but, instead, passing by in a so-called "fly-by" event (Clarke & Pringle, 1993; Cuello et al., 2019; Nealon et al., 2020a). A misaligned planet can also cause a warp (Nealon et al., 2018). This scenario is similar to the misaligned binary case, however with much smaller masses of the perturber. Such a misaligned planet could have been captured by the star-disk system or kicked out of the disk plane by N-body interaction with other objects, such as other planets or fly-by objects (Nagasawa et al., 2008). Late infall of material onto a disk could be another cause for a warp (Kuffmeier et al., 2021). In this scenario, the infalling material adds angular momentum with a different direction to the disk. Warped disks in combination with infalling material have also been observed (Sai et al., 2020). Additionally,

the warping of disks has been found to affect planet formation (Aly et al., 2021).

In warped disks, pressure forces occur that act to change the disk's orbital plane which means that a warped disk without a component driving the warp is not static but evolves in time (Papaloizou & Lin, 1995; Papaloizou & Pringle, 1983). The type of evolution depends on the disk properties, namely, the viscosity described by the Shakura-Sunyaev turbulence parameter, α_t (Shakura & Sunyaev, 1973) and its thickness, or (more specifically) its aspect ratio $h = h_p/r$, where h_p is the pressure scale height of the disk and r the distance from the star. Disks with high viscosity compared to the aspect ratio $\alpha_t > h$ evolve in a diffusive manner. In this regime, the warp is directly dampened and dissipates (Pringle, 1992; Ogilvie, 1999; Lodato & Price, 2010). Disks with lower viscosity, namely, $\alpha_t < h$, fall in the so-called wave-like regime. In this regime, the warp travels as a wave through the disk with a wave speed of $c_s/2$ (Lubow & Ogilvie, 2000; Gammie et al., 2000; Ogilvie & Latter, 2013a,b). Over time, the warp is dampened as well in this regime, if $\alpha_t \neq 0$. Because protoplanetary disks are known to have low viscosities of $\alpha_t = 10^{-5}$–10^{-3} (Manara et al., 2023), they typically fall into the wave-like regime.

Historically, each evolution regime was described by a different set of equations for the warp evolution. Martin et al. (2019) were able to combine both equation sets to a generalized formalism. In their generalized set of equations, they included a damping term in order to suppress unphysical features. This damping term causes the equations to become stiff and challenging to solve numerically. Dullemond, Kimmig, & Zanazzi (2022a, hereinafter referred to as DKZ22) were able to derive the same set of equations from shearing box considerations and found the reason for these unphysical features, as the equations need to take the rotation of the orbital plane into account. They proposed an alternative, physically motivated term to correct for the orbital plane rotation. The generalized equation set includes mass and angular momentum conservation, both of which depend on the internal torque vector, $\vec{G}$. The equations are as follows:

$$\frac{\partial \Sigma}{\partial t} - \frac{2}{r}\frac{\partial}{\partial r}\left[\frac{\frac{\partial (r\vec{G})}{\partial r}\cdot\vec{l}}{r\Omega}\right] = 0, \tag{3.1}$$

$$\frac{\partial \vec{L}}{\partial t} - \frac{2}{r}\frac{\partial}{\partial r}\left[\frac{\frac{\partial (r\vec{G})}{\partial r}\cdot\vec{l}}{\Sigma r\Omega}\,\vec{L}\right] + \frac{1}{r}\frac{\partial (r\vec{G})}{\partial r} = T. \tag{3.2}$$

Here, Σ is the surface density, Ω the Kepler orbital frequency and $\vec{L} = \Sigma R^2 \Omega \vec{l}$ is the angular momentum density, with $\vec{l}$ as the angular momentum unit vector. The internal torque vector $\vec{G}$ arises due to the misalignment of neighbouring orbits

(DKZ22) and takes the form:

$$\frac{\partial \vec{G}}{\partial t} + \left(\frac{\kappa^2 - 1}{2}\right) \Omega \, \vec{l} \times \vec{G} + \alpha_t \Omega \vec{G} + \left(\vec{l} \times \frac{\partial \vec{l}}{\partial t}\right) \times \vec{G} = -\frac{\Omega^3 r \Sigma h_p^2}{4} \frac{\partial \vec{l}}{\partial \ln r} + \frac{3}{2} \alpha_t^2 \Omega^3 r \Sigma h_p^2 \vec{l}, \tag{3.3}$$

where $\kappa = \Omega_e / \Omega$ with Ω_e as epicyclic frequency. We note that we are using the definition of the internal torque vector $\vec{G}$ and the notation following DKZ22, which differs from the definition given in other works, for instance, Martin et al. (2019) or Nixon & King (2016), by a factor of $-1/r$ (see DKZ22, Appendix C).

As mentioned, the internal torque arises due to the misalignment of neighbouring orbits. More specifically, the annuli are deformed (see DKZ22, Figure 9) and, therefore, they put pressure on neighbouring annuli. This leads to a dynamic surface where material flows radially inward and outward within one orbit. This motion is called sloshing motion (DKZ22), often referred to as "resonant motion" in the literature (Nixon & King, 2016). The sloshing motion is the main drive for warp evolution.

Warped disks can be investigated in one-dimensional (1D) and three-dimensional (3D) models. In 1D models, the disk is to split into concentric annuli. Each annulus plane can be described by its normal vector, which is identical to the angular momentum unit vector. This angular momentum unit vector can then be updated following Equation 3.2. While 1D models offer a huge advantage in regard to computation time, they are obviously simplified. Additionally, the equations are derived from a linear approximation and contain additional assumptions, for instance, about their Keplerity. Therefore, it is useful to model warped disks in full 3D hydrodynamic simulations.

Three-dimensional simulations of warped disks are often performed using smoothed particle hydrodynamics (SPH) models (Gingold & Monaghan, 1977). However, the SPH method is usually implemented with an artificial viscosity that allows for shock treatment (Monaghan, 2005). Simulations of disks modeled in SPH need to have a disk viscosity higher than the artificial viscosity in order to capture the physical processes accurately. Protoplanetary disks, however, are known to have a rather low viscosity (Pinte et al., 2016; Villenave et al., 2020), which means that a method able to model lower viscosities would be more fitting. Additionally, in the most common SPH models, the resolution highly depends on density. For a protoplanetary disk, this means that the surface of the disk is always less resolved than its midplane. For warped disks, however, it is advantageous to resolve the surface structures and dynamics well due to the sloshing motion mechanism. More importantly, observations of protoplanetary

disks often trace the surface layers, which is why accurate model predictions for these regions are important.

In this work, we model warped disks in full 3D hydrodynamics using a grid-based code. This way, we are able to model protoplanetary disks with low viscosities, without the resolution dependency on density or any other physical quantity. However, we are aware that a grid can also cause numerical effects, as found by Hopkins (2015), for instance (see Figure 8 therein). Thus, to minimize them, we chose a spherical symmetry of the grid to take advantage of the disk's symmetry. As we still expect some numerical effects caused by the grid, we carefully tested the set-up in the test case of a planar and smooth disk inclined with respect to the grid geometry. Physically, this should give the same result as a planar disk aligned to the grid geometry and allow us to compare and extract the grid effects. A few studies used grid-based methods to model disks with out-of-plane features before (Sorathia et al., 2013; Fragner & Nelson, 2010; Rabago et al., 2023, 2024).

This chapter is organized as follows. We describe our numerical set-up in Section 3.2 and the investigation of the grid effects in the case of a disk tilted with respect to the midplane in Section 3.3. We present and discuss the results of a warped disk simulation in Section 3.4. In Section 3.5, we investigate the internal torque and sloshing motion in the 3D simulation. We present our conclusions in Section 3.6. Supplementary material is presented in the chapter appendix, Sections 3.A-3.C.

3.2 Numerical method

We performed 3D hydrodynamic simulations using the versatile code FARGO-3D by Benítez-Llambay & Masset (2016). In our simulations, we used the implemented hydrodynamics modeling a system, consisting of a central star and a surrounding disk. For our purposes, we did not consider any magnetic fields and, therefore, we did not use the magnetohydrodynamic features of FARGO3D. Furthermore, we did not include any planets or other companions.

To take advantage of the system's symmetry, we set up a model in spherical coordinates. To save on computation time, we restricted the vertical computation domain to a certain range, meaning that the poles of the grid sphere are cut off (see Figure 3.1). Because we are planning to look at features tilted with respect to the midplane of the grid, we need to consider a large enough regime in the vertical direction.

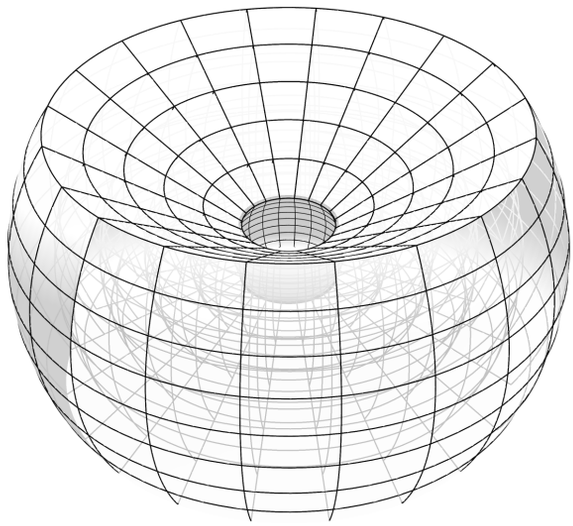

Figure 3.1: Schematics of the spherical grid set-up in our simulations. The poles are cut off in order to save computation time.

We set up a protoplanetary disk, where the surface density follows the following power law:

$$\Sigma(r) = \Sigma_0 \left(\frac{r}{R_0} \right)^{-p}, \tag{3.4}$$

with a slope, p, and reference scale, R_0. In FARGO3D, this reference scale is usually set to $R_0 = 5.2\,\mathrm{au}$, which we adopt in our models. In general, we assume a locally isothermal disk, which means that the temperature structure does not change in time. However, the temperature may very well vary within the disk and is not constant as a function of distance to the star. We set the temperature structure so that the disk is flared, such that the aspect ratio can be described as:

$$h(r) = h_0 \left(\frac{r}{R_0} \right)^{i_{\mathrm{fl}}}, \tag{3.5}$$

where h_0 is the unflared aspect ratio and i_{fl} the flaring index. For most of our simulations, we adopt a globally isothermal model by choosing $i_{\mathrm{fl}} = 0.5$. The initial velocity in azimuthal direction is set to the Keplerian velocity, with a correction term for pressure gradients.

In our simulations, we used reflective boundary conditions in the radial and vertical direction, namely, we did not allow for any inflow or outflow. While this gives the most control over the physics at the boundary, it is not very natural; therefore this condition should be relaxed in future works. We used the implemented wave-killing boundary conditions (de Val-Borro et al., 2006) to damp the wave reflections, where the damping zones have a width of 10% of the grid edge radius. We intentionally did not fix the ghost cells to an analytical extrapolation at the boundaries (as this is not possible for the warped disk case).

Aiming to investigate the capability of the code to simulate features out of the grid plane, we set up a planar disk tilted with respect to the midplane of the grid. For the rotation of the disk, we used the analytical initial disk model of the FARGO3D code and inclined it using appropriate coordinate transformations. In this way, we achieved a disk that is tilted with respect to the grid midplane (see Section 3.3.2).

For the warped disk model, we used the same coordinate transformation, only this time using a tilt angle depending on distance from the star instead of a constant tilt angle. The function we use is inspired by Martin et al. (2019) (Equation 19 therein) and is expressed as:

$$i(r) = i_{\max}\left[\frac{1}{2}\tanh\left(\frac{r - r_{\text{warp}}}{r_{\text{width}}}\right) + \frac{1}{2}\right], \tag{3.6}$$

where $i_{\max}$ is the maximum warp tilt, r_{warp} is the location of the steepest warp, and r_{width} is the width of the warp transition. Depending on the disk tilt or warp maximum inclination, we need to adjust the grid space in the vertical direction.

3.3 Investigating the grid effects

In this part, we aim to investigate the feasibility of simulating a warped disk using a grid-based method, in our case FARGO3D (Benítez-Llambay & Masset, 2016). A warped disk includes features that do not align with the grid geometry; more specifically, they are tilted with respect to the grid midplane. Such features can increase the numerical friction compared to features perfectly aligning with the grid geometry. To investigate the numerical influences of the grid on the out-of-plane features, we first investigated the case of a planar disk tilted with respect to the grid midplane. Physically, this is the same scenario as a planar disk aligned to the grid midplane. Comparing a tilted disk to an untilted disk allows us to extract the differences between both cases, which can only be caused by the misalignment between disk and grid midplanes. In this way, we can achieve a gauge for the grid effects.

In the untilted scenario, we would expect a standard viscous evolution. For low viscosities, the timescale for viscous evolution is long enough so that we do not expect the surface density to change much when looking at the short-term evolution. In an ideal set-up, a disk tilted with respect to the grid midplane should evolve in the same way. Intuitively, we might think the spherical coordinate system is spherically symmetric and, therefore, it would not numerically influence the set-up. However, a spherical grid always includes directions, namely, an equator and two poles. This means that because the orbital motion in a tilted

disk is not aligned with the coordinate system, a gas parcel's orbit vertically travels through several grid layers: the orbit is below the grid midplane one side and above on the other. This results in an additional numerical friction that influences the simulation result. A similar study was qualitatively mentioned by Fragner & Nelson (2010), who found that the numerical viscosity can drag the disk toward alignment.

3.3.1 Untilted Reference Case

We first modeled the reference case of an untilted disk. We set up a disk with mass $M_{\rm disk} = 0.02\,{\rm M}_\odot$ around a Solar-like star with a viscosity of $\alpha_{\rm t} = 10^{-3}$. The surface density parameter was set to $\Sigma_0 = 209.2\,{\rm g/cm^2}$ with a power law exponent of $p = 1$. We note that in FARGO3D, the set-up is scalable so that the results also apply to different mass and length scales. The disk ranges from $r_{\rm in} = 2.6\,{\rm au}$ to $r_{\rm out} = 26\,{\rm au}$. We chose an aspect ratio at R_0 of $h_0 = 0.05$, along with a flaring index of $i_{\rm fl} = 0.5$, and we set the temperature structure accordingly. In Figure 3.2, we present the aspect ratio of the initial set-up, with both the analytical calculation according to Equation 3.5 (black dashed line) and a fit from our simulation data (pink solid line).

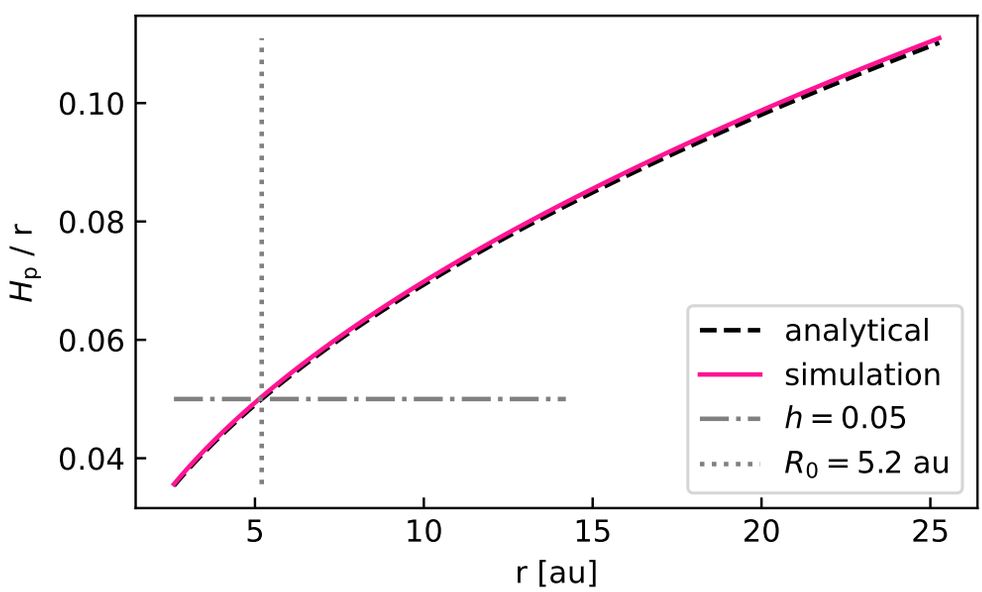

Figure 3.2: Aspect ratio (i.e., pressure scaleheight scaled with radius) $h(r) = H_{\rm p}(r)/r$ of our initial set-up. The black dashed line is the analytical calculation according to Equation 3.5, the pink solid line shows the Gaussian fit from the initial set-up in our simulation. Gray dotted and dashed lines indicate the reference radius $R_0 = 5.2\,{\rm au}$ and the corresponding reference aspect ratio $h_0 = 0.05$, respectively.

For the fit of the aspect ratio, we used a Gaussian function to fit the vertical density profile at each radius according to:

$$\rho(z) = \rho_0 \exp\left(-\frac{z^2}{2H_p^2}\right), \tag{3.7}$$

where ρ_0 is the midplane density, z the height above the midplane, and H_p the pressure scaleheight of the disk. We note that for simplicity, we used the radial shells of the grid instead of extrapolated cylindrical radii to fit the Gaussian profiles. This means that the fitted (pink) curve is only an approximation, however, it is sufficient for the purpose of double-checking our initial set-up. The parameters we chose, namely, the flaring index of $i_{fl} = 0.5$, result in a globally isothermal disk.

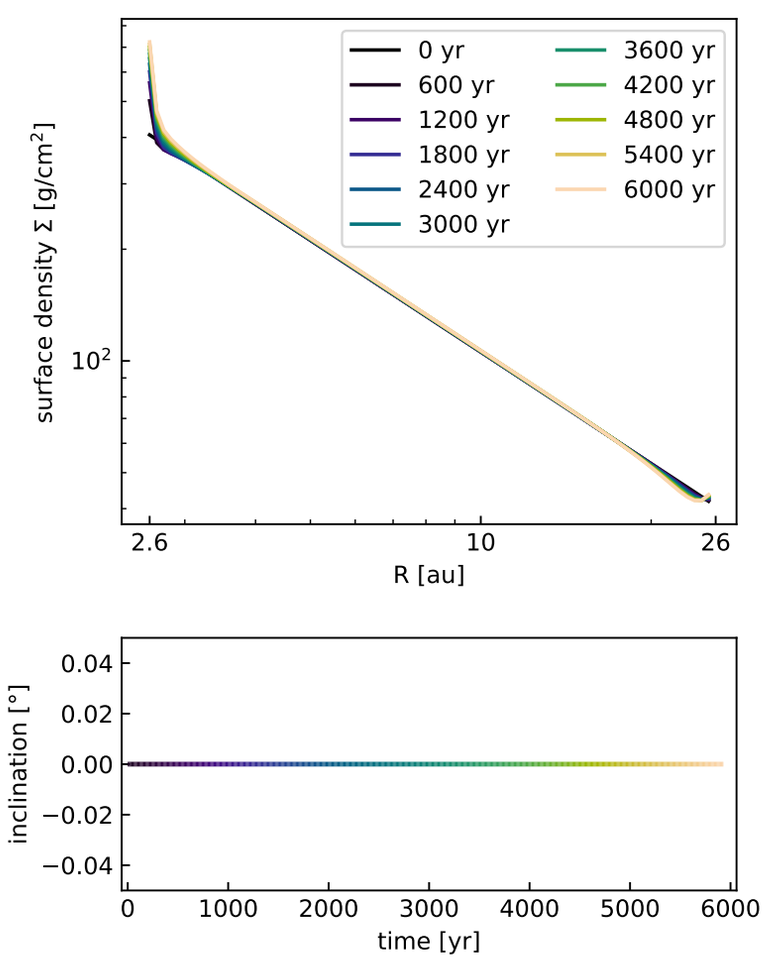

Figure 3.3: Surface density (top panel) and inclination (bottom panel) evolution of a disk aligned to the grid midplane. The color in the bottom panel highlights the time. The simulation covers a time span of 6000 years, which are 500 orbits at the reference radius, $R_0 = 5.2$ au.

We ran the tilted disk simulations for 500 orbits at $R_0 = 5.2\,\mathrm{au}$, which translates to $t_{\mathrm{tot}} = 6,000\,\mathrm{yr}$ with one orbit being $t_{\mathrm{orbit}} = 12\,\mathrm{yr}$[1]. For now, we set the resolution of 80 cells in r-direction with the grid logarithmically spaced in r, 100 cells in azimuthal φ-direction and 40 cells in vertical θ-direction with a range of $-25.8^\circ < \theta < 25.8^\circ$.

From the 3D simulations, we compute the surface density using:

$$\Sigma(r) = \int_0^\pi \rho_\varphi(r,\theta)\; r\; \sin(\theta)\; \mathrm{d}\theta, \tag{3.8}$$

where $\rho_\varphi(r,\theta)$ is the azimuthally averaged density of the disk. Figure 3.3 shows the time evolution of the surface density (top panel) and the inclination (bottom panel), defined as the angle between the angular momentum vector and the z-axis. A detailed description of how we retrieve the inclination can be found in Section 3.3.2.

As expected, the inclination remains zero throughout the whole simulation which means the disk stays aligned to the grid midplane. The surface density stays constant on our timescales, except for some deviations at the grid inner and outer edge, due to the rigid boundary conditions. Because this is merely a reference case, we did not investigate the deviations in detail.

3.3.2 Tilted disk

Next, we tilted the disk by ten degrees with respect to the grid midplane. In a first test, we used the same resolution as in the reference case aligned to the midplane. We set up the tilt in x-direction, meaning that the total angular momentum vector of the disk points in direction of the x-axis, which means a rotation of the disk around the y-axis. Figure 3.4 shows a cross-section of this set-up.

To retrieve the inclination angle, we determine the total angular momentum vector for each radial shell $\vec{L}_r$. To achieve this, we transformed the cell coordinates, as well as the gas velocities, from spherical to Cartesian coordinates. We were then able to calculate the angular momentum vector of each shell using:

$$\vec{L}_r = \int \rho(r,\theta,\phi)\; \vec{r} \times \vec{v}\; r^2 \sin(\theta) \mathrm{d}\theta \mathrm{d}\phi, \tag{3.9}$$

where $\vec{v}$ is the gas velocity. We note that the resulting $\vec{L}_r$ is given in Cartesian coordinates as well. By normalizing $\vec{L}_r$, we get the direction of angular momentum,

[1] Note: one actual orbit at 5.2 au is 11.858 yr, which we round up to 12 yr for simplicity.

$\vec{l}_r$, which we used to compute the inclination angle i using

$$i = \arccos\left(\vec{l} \cdot \vec{l}_z\right), \tag{3.10}$$

where $\vec{l}_z$ is the unit vector of the z-axis with $(0, 0, 1)$.

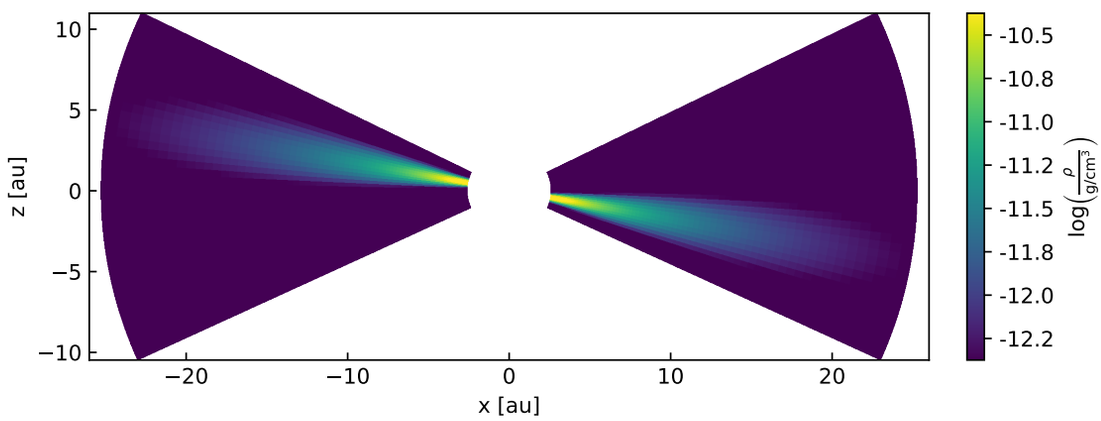

Figure 3.4: Cross-section through the initial tilted disk along the x-axis.

In addition to the inclination, we investigate the precession angle, which we define as the clockwise angle between angular momentum vector projected onto the x-y-plane and the x-axis. This definition gives an initial precession angle of $0°$.

Figure 3.5 shows the surface density evolution, as well as the evolution of inclination and precession angle. The surface density shows a stronger pile-up at the inner boundary and an adjacent density deficit, which we attribute to effects caused by the reflective (rigid) boundary. We investigated this by running two more simulations of the same tilted disk set-up, but using the outflow boundary conditions at the inner edge in radial direction (as shown in Figure 3.6). Apart from the boundary condtitons, one simulation has the exact same initial conditions, while the other is set up with an exponential cut-off at the inner and outer disk edges. In this comparison, we indeed see that the pile-up at the inner edge is caused by the rigid boundary conditions and does not occur in the simulations with inner outflow conditions. However, we observe that the inner region of the disk shows a density deficit in comparison to the initial state ranging up to 5 au. Interestingly, this seems to occur in all three simulations, which suggests that this is not an effect caused by the inner boundary. We suspect that this effect could be caused by an unphysical warp that we find in the simulation, which we discuss later in this section. As we are mainly interested in the alignment with the grid, we do not go into more detail here. We merely note that special care should be taken when looking at the surface density evolution of the inner region in our simulations.

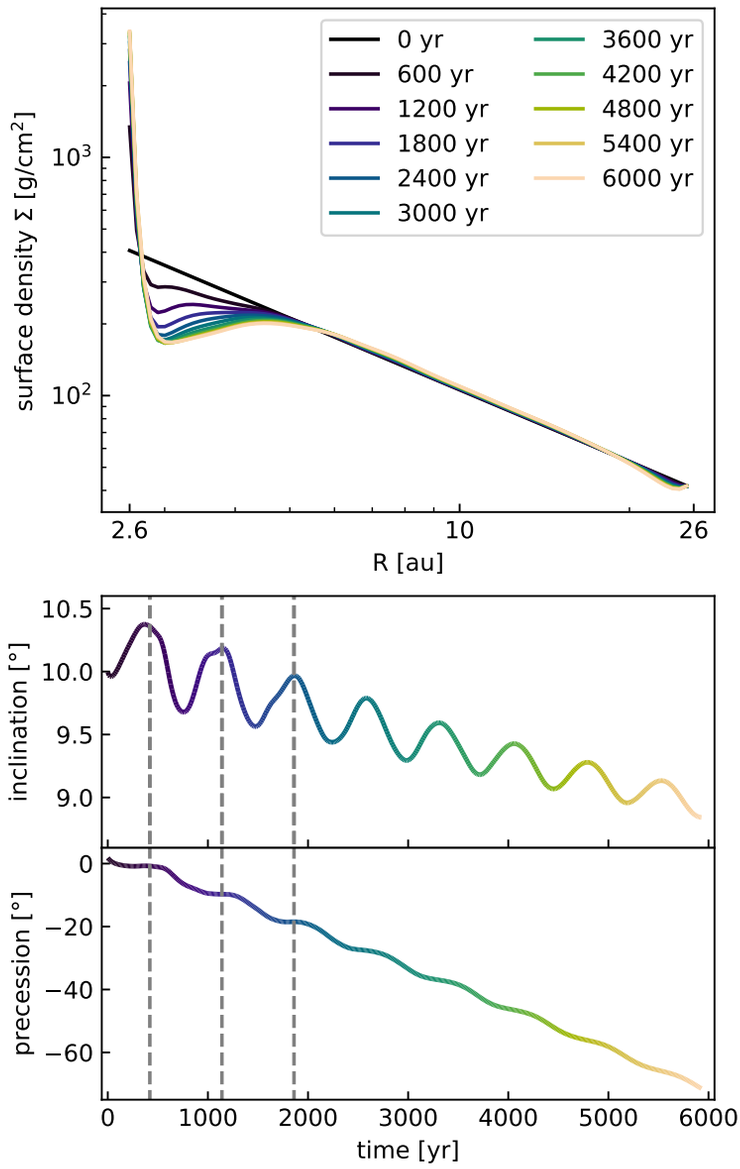

Figure 3.5: Similar to Figure 3.3, but for the a disk tilted by 10° with respect to the grid midplane. The additional panel at the bottom shows the precession angle of the disk. The grey dashed lines indicate the inclination oscillation periods investigated in Figure 3.7.

In an ideal set-up, the inclination and precession angle should stay constant. In our simulation (Figure 3.5), we see that the inclination decreases over time. This means the disk is dragged by numerical effects toward an alignment with the grid geometry. However, considering a total decrease of less than 1.5 degrees over a time span of 6000 years, the result is surprisingly good.

The precession angle, however, shows a much stronger trend. During the simulated period of 6000 years, the disk precesses by approximately 75° in a counterclockwise motion (negative precession angle). Physically, the disk should not precess; therefore, this is clearly an effect caused by the grid. The reason for the

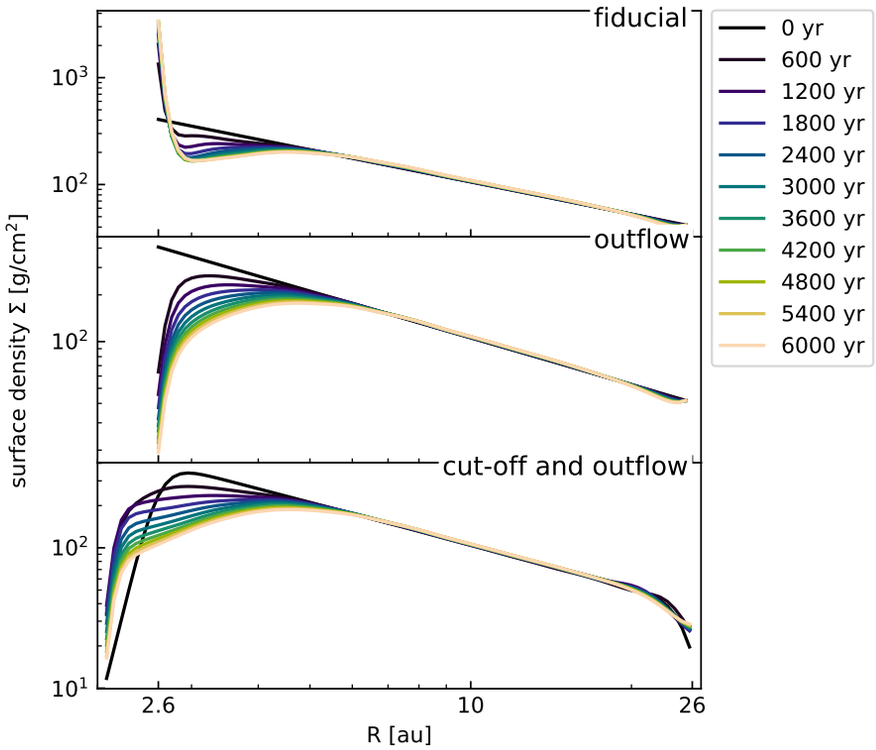

Figure 3.6: Surface density evolution of a tilted disk by 10° in simulations with different boundary conditions. The top panel shows our fiducial set-up with rigid boundaries, the middle is the same set-up, but with the outflow boundary conditions at the inner edge, and the bottom panel has an exponential cutoff at outer and inner edge, in addition to inner outflow boundary conditions.

effect could be numerical friction a gas particle experiences when traveling from one cell to another. Because the disk is tilted, a gas parcel has to not only travel through all cells in φ-direction within one orbit, but additionally through several layers in θ-direction. This increases the amount of numerical friction and might cause the gas parcel to be slightly delayed in its motion through the θ-layers. Therefore, a gas parcel arrives later at its original θ-height and the whole disk shows a precession motion in the same direction as the orbital rotation; that is, in our simulation, the orbital direction of the disk is counter-clockwise, as well as the precession. This can indeed be explained by a delay in θ: The vertical motion of the gas parcels in a tilted disk during one orbit can be considered like shifting a Gaussian function up and down, similar to an advection. For advection schemes, Icke (1991) investigated the phase-shift P due to numerical friction (see their Equation 3.10). For $P > 0$, the phase is lagging, which means that the transported function is trailing behind the true solution. Icke (1991) found that the investigated higher-order advection schemes resulted in this phase-lag, namely, $P > 0$. Even though FARGO3D uses a different advection algorithm, it is likely

this algorithm has the same problem when the resolution is too low. Our findings agree with this hypothesis, that is, we are able to explain the precession we find in our simulation with a phase-lag caused by numerical friction. Because the numerical friction decreases when the resolution is increased, we expect the precession effect to be reduced in higher resolutions. We describe how we tested this aspect in Section 3.3.3.

In Figure 3.5, in addition to the decrease of inclination, we can also observe an oscillation pattern. To investigate its cause, we took a look at the inclination profiles in different time steps. We chose the first and second period from maximum to maximum, which is indicated by the grey dashed lines in Figure 3.5, bottom panel. The first period roughly extends from 420 to 1140 years, the second from 1140 to 1860 years.

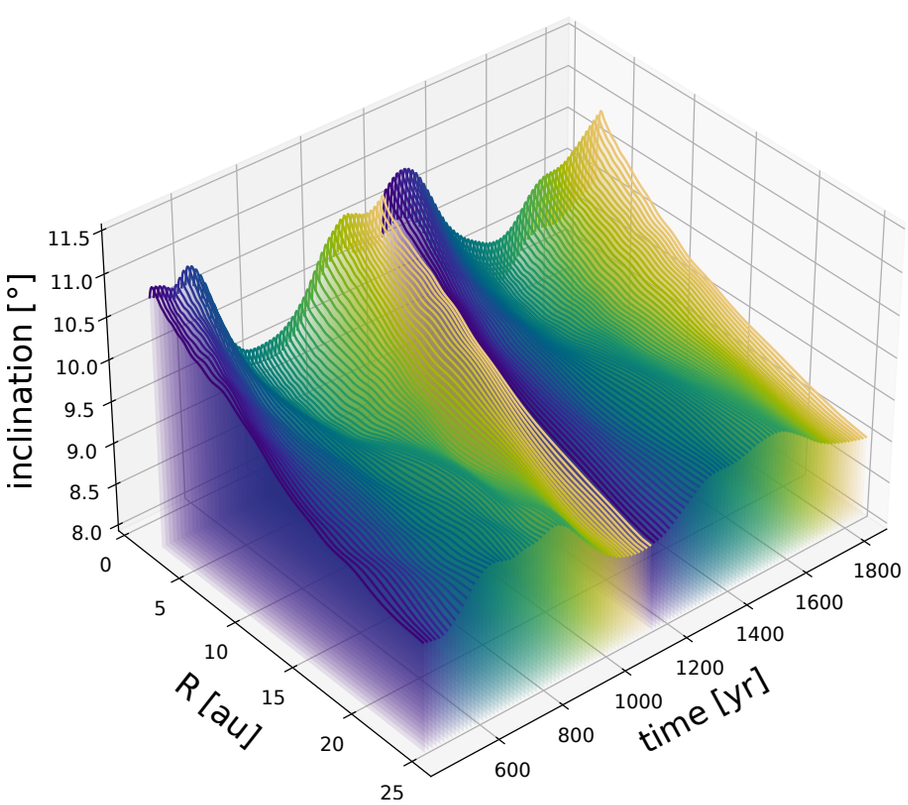

Figure 3.7: Inclination profile evolution during the first and second periods of the inclination oscillation. Each period is indicated by the color scale from blue to yellow. The first period extends from 420 to 1140 years, the second from 1140 to 1860 years.

Figure 3.7 shows the evolution of the inclination profile during these two periods with the time axis as a third dimension, where the color scheme from blue to yellow indicates one period. We find that the inclination profile varies periodically, which can explain the oscillations in the averaged inclination angle for the total disk. We find that the disk is not perfectly planar which would have a con-

stant inclination profile with radius. This means that the disk in our simulation is slightly warped and evolves in a typical wave-like warp evolution. We note that the warping is modest and not caused by a physical effect but results from numerical grid effects. The warp might arise due to the grid effects not having the same strength at all radii. Because the orbital period is shorter at smaller radii, the inner disk experiences more numerical friction than the outer disk in a given time. As this is not a physical effect, we do not further investigate the evolution of the warp. Additionally, it is rather modest and does not strongly interfere with our evaluation of the grid effects. However, it can explain the oscillations in the mean inclination of the total disk. We additionally suspect this to influence the evolution of the surface density, as mentioned earlier in this section.

3.3.3 Different resolutions

In this section, we investigate the grid effects in different resolutions. We aim to probe the influence of resolution in the three directions and therefore set up three simulations: one with resolution doubled only in r-direction (we call this simulation `r_resolution`), a second one with resolution doubled in φ-direction (called `phi_resolution`), and a third one doubling only the θ resolution (`theta_resolution`). In a fourth simulation (`high_resolution`), we used a higher resolution in all three directions: 160 cells in r, 200 cells in φ, and 160 cells in θ. An overview over the simulation resolutions is presented in Table 3.1.

Table 3.1: Resolutions in different simulations

Simulation name	Cells in r	Cells in φ	Cells in θ
Fiducial (from Section 3.3.2)	80	100	40
cells-per-scaleheight (cps) at $r = 5.2$ au	1.7 cps	0.7 cps	2.2 cps
`r_resolution`	160	100	40
`phi_resolution`	80	200	40
`theta_resolution`	80	100	80
`high_resolution`	160	200	160

Figure 3.8 shows the inclination and precession in the simulations with varying resolutions. Looking at the inclination evolution, we find that the decrease of inclination is weakest for the simulation `high_resolution`: Comparing the three simulations with increase of resolution in one direction each, we find that the grid effects are especially sensitive for resolution in θ-direction. The inclination

oscillations become weaker and the overall decrease is less steep. Resolution in the r-direction, however, shows no significant improvements, compared to the fiducial set-up from Section 3.3.2.

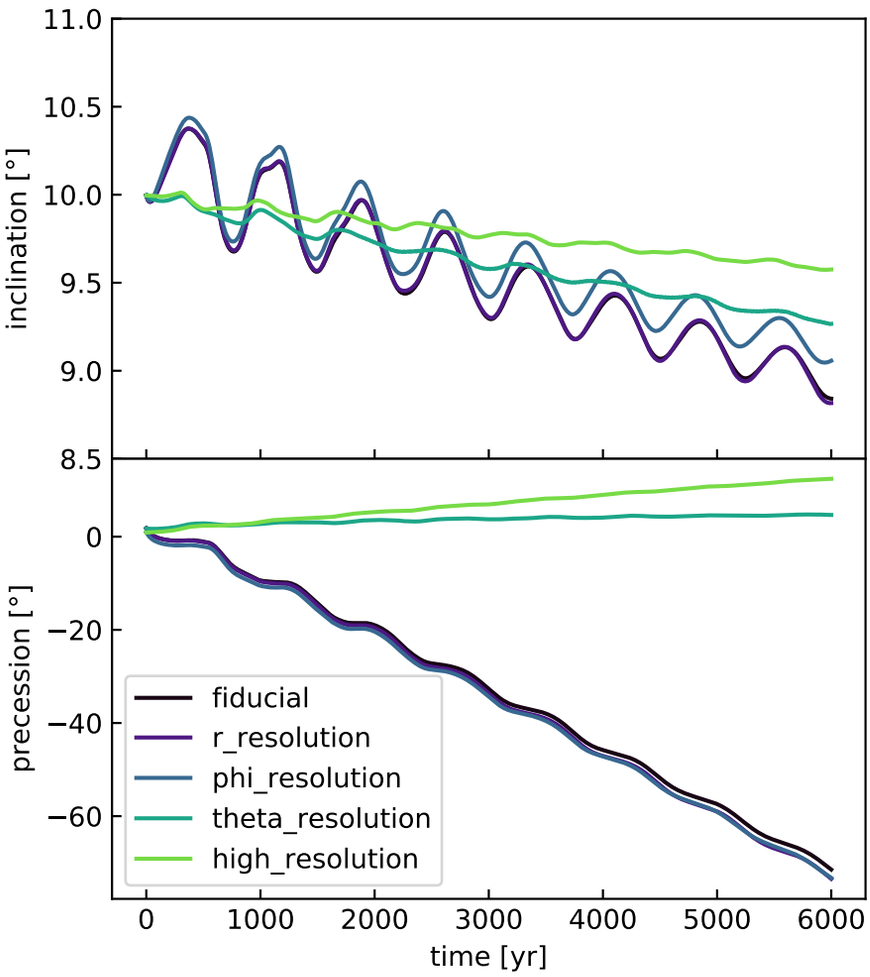

Figure 3.8: Inclination (top panel) and precession angle (bottom panel) in simulations with varying resolutions in a disk tilted by 10° with respect to the grid midplane.

We find that resolution in r and φ do not influence the precession motion. However, higher resolution in θ makes a large difference for the precession, as we have already suspected in Section 3.3.2. In simulation `theta_resolution`, there is almost no precession of the disk. This indeed confirms our suspicion that the precession is mainly caused by friction of gas parcels that have to travel through several θ-layers because of the tilt. We note that simulation `high_resolution` is slightly precessing in the other direction. However, this precession is still small compared to the fiducial resolution.

Overall, we find that the grid effects get weaker for higher resolution, as expected. The oscillation of the inclination and precession angle we investigated in Figure 3.7 becomes much weaker when increasing the θ-resolution. Higher reso-

lution can severely increase the computation time. Doubling the resolution in all three directions prolongs the computation by a factor of 16 ($2^3 = 8$ for the three directions and an additional factor of two due to the decreased time step). However, the simulations we are investigating in this work are still feasible, because we can take the advantage of multi-node GPU parallelization. For our purposes, we find the grid effects of simulation `theta_resolution` to be sufficiently small. Therefore we continued using this resolution for our investigations of a warped disk, described in Section 3.4.

3.3.4 Dependence on viscosity

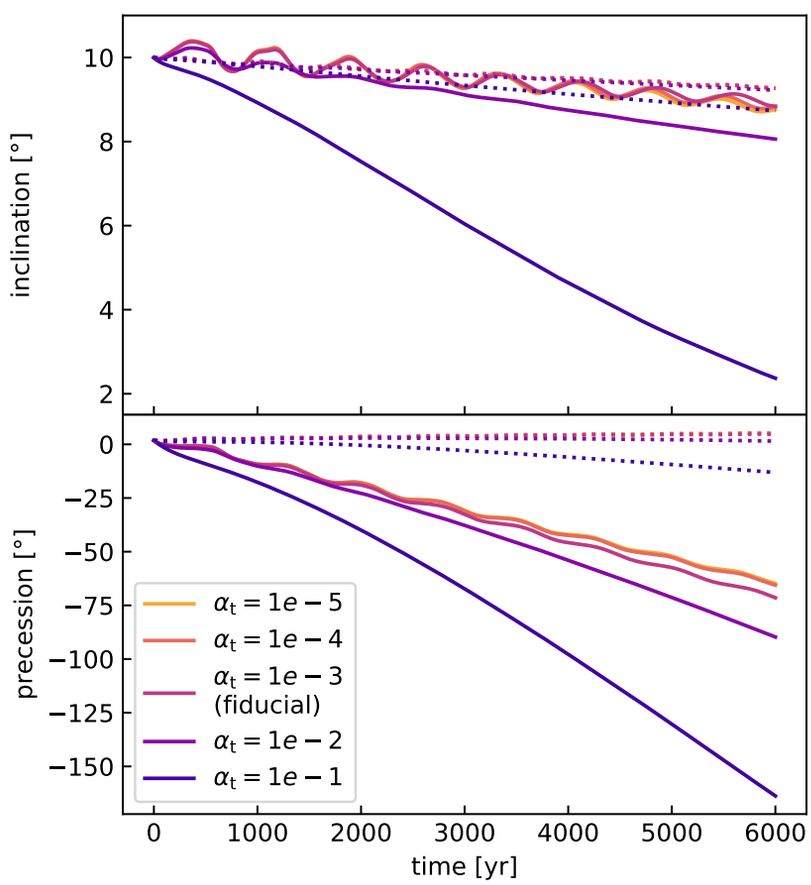

Figure 3.9: Same as Figure 3.8, but for simulations using varying viscosities. The disks are still tilted by 10° with respect to the grid midplane. The dotted lines show the same simulations with higher resolution in θ-direction (corresponding to `theta_resolution` in Table 3.1).

To investigate the role of viscosity for the grid effects, we perform four further simulations varying the viscosity parameter α_t. For these simulations, we use the initial low resolution (see Section 3.3.2). We keep the set-up exactly the same except for the viscosity, which we set to $[\alpha_t = 10^{-5}]$, $\alpha_t = 10^{-4}$, $\alpha_t = 10^{-2}$,

and $\alpha_t = 10^{-1}$. The fiducial simulation investigated in previous sections has a viscosity of $\alpha_t = 10^{-3}$.

Figure 3.9 shows the evolution of the inclination and the disk precession in those simulations. The simulations with $\alpha_t = 10^{-5}$, $\alpha_t = 10^{-4}$, and $\alpha_t = 10^{-3}$ show a very similar behaviour with almost the same amount of decrease in inclination and precession angle. For higher viscosities, however, the grid effects seem to be much stronger. We investigated the same simulations in higher resolution (corresponding to `theta_resolution`) and find that the grid effects significantly decrease for all viscosities (dotted lines in Figure 3.9). However, the simulation with the highest viscosity, $\alpha_t = 10^{-1}$, still shows slightly stronger numerical effects than the other simulations. This means that in order to accurately model higher viscosities, it is even more important to consider a higher resolution. In this work, we are mainly interested in viscosities of $\alpha_t = 10^{-3}$ and lower and therefore do not go into more detail here. It should, however, be kept in mind for future projects.

3.3.5 Higher inclination

In order to study the grid effects for a different tilt inclination, we perform a simulation of a disk tilted by 30° with respect to the grid midplane. For this, we decided to use a higher resolution, namely, it is the same as in `simulation high_resolution`. Since our disk is more inclined, we need to extend the computation domain in θ-direction. In order to achieve the same resolution in θ for this case, we need more grid cells in θ. Table 3.2 shows the resolution comparison between the two simulations. We kept the cell amounts in r and φ the same.

Table 3.2: Resolution comparison between different inclinations

Simulation name	θ_{min}	θ_{max}	Cells in θ	Degree per cell
`high_resolution`	-25.8°	25.8°	160	0.322°/cell
`30deg`	-43.0°	43.0°	264	0.326°/cell

Figure 3.10 shows that the inclination decreases by about two degrees over a time span of 6000 years. We can roughly estimate the decay rate $\lambda = -1/i \, \mathrm{d}i/\mathrm{d}t$, resulting in $\lambda = -2°/30° \; 1/(6000\,\mathrm{yr}) = -1.1 \times 10^{-5}\,\mathrm{yr}^{-1}$. When comparing this to the simulation `high_resolution` with $\lambda = -0.5°/10° \; 1/(6000\,\mathrm{yr})$, which are $-8.3 \times 10^{-6}\,\mathrm{yr}^{-1}$, we see that the decay rate for higher inclinations is higher. We therefore expect the inclination decay not to be perfectly linear. For future projects investigating higher inclinations, we keep in mind that more tests should

be made. The precession of the disk varies a little, but the change stays within a few degrees.

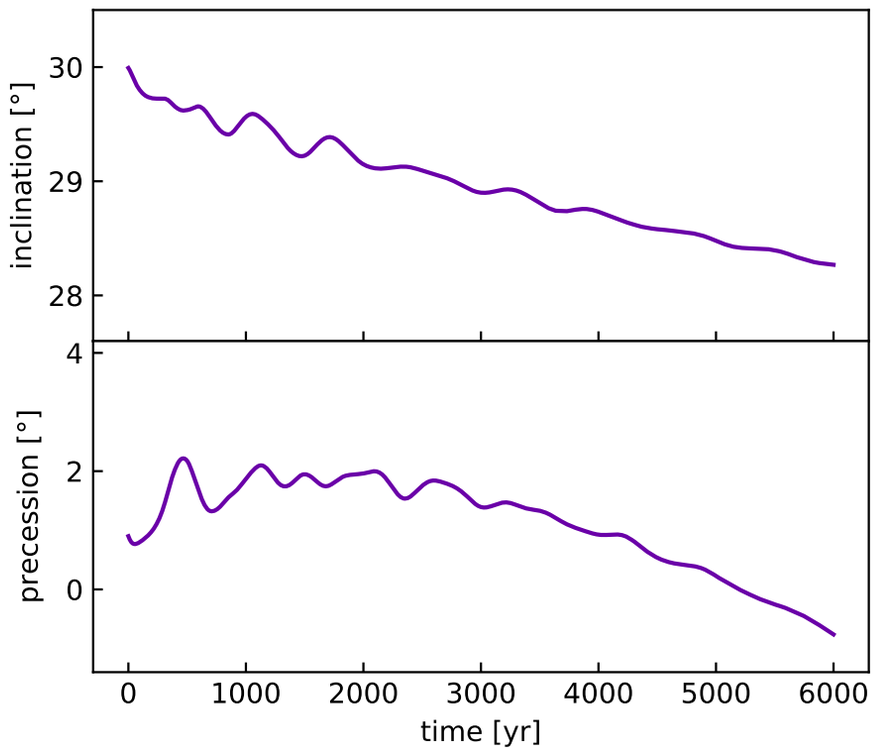

Figure 3.10: Inclination (top panel) and precession (bottom panel) evolution of a disk tilted by 30° with respect to the grid midplane.

All in all, we find that the grid effects can be negligible for a high enough resolution. The resolution we find is still feasible for full 3D hydrodynamic simulations. We therefore conclude that it is possible to simulate disks with out-of-plane features using a grid-based method, when keeping in mind that grid effects might play a role under certain conditions.

3.4 Warped disk

To investigate the warp evolution in 3D hydrodynamics, we set up an initially warped disk around a single central star. We note that the shape of the warp is not physically motivated by any formation scenario, as we are interested in the evolution from that point on. The initial warp is given in Equation 3.6. Since we did not include a misaligned binary or companion or any other external component, the warp is not driven and will smooth out according to the warp evolution. The initial maximum warp is $i_{\max} = 10°$. We locate the warp to $r_{\text{warp}} = 10.4\,\text{au}$ with a width of $r_{\text{width}} = 2.6\,\text{au}$. For the resolution, we chose 80 cells in r, 100 cells in φ, and 134 cells in θ with an extend of $-43° < \theta < 43°$, which keeps the

cells-per-scaleheight ratio the same (i.e., 4.4 cps at $r = 5.2$ au) as in the simulation `theta_resolution` in Section 3.3.2. We chose this to keep the computational time short so we can perform multiple simulations. We performed one high-resolution simulation doubling the resolution in all three directions and find that the qualitative results are the same. Our evaluation of this high resolution simulation can be found in Appendix 3.A.

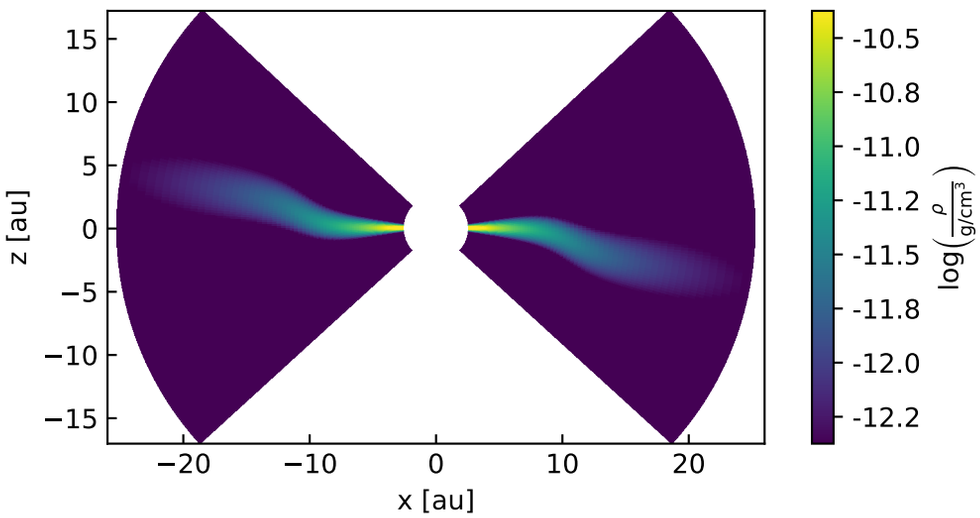

Figure 3.11: Cross-section of the initial warped disk along the x-axis.

Figure 3.11 shows a cross-section of this initial set-up. Except for the warping of the disk, all parameters are the same as in our previous simulations (see Section 3.3.1). We again chose a turbulence parameter of $\alpha_t = 10^{-3}$ and therefore expected a wave-like evolution of the warp, as $h > \alpha_t$. In the following sections, we investigate the evolution of the inclination profile, as well as the precession profile (=twist) of the disk. We expected the profiles to depend on the radius, therefore, we do not consider at the radially averaged inclination and precession angle.

3.4.1 Inclination profile

We first investigated the evolution of the inclination profile in detail. In Figure 3.12, we show its evolution. In this figure, the wave-like behavior is evident and is visible as a standing wave of the global bending modes superimposed on a global mean tilt of the disk. This mean tilt of the disk does not visibly decay, although we expect it to decay slowly due to numerical effects. The warp amplitude is dampened over time. Over the first 6000 years (500 orbits at R_0), the disk does not reach the planar state.

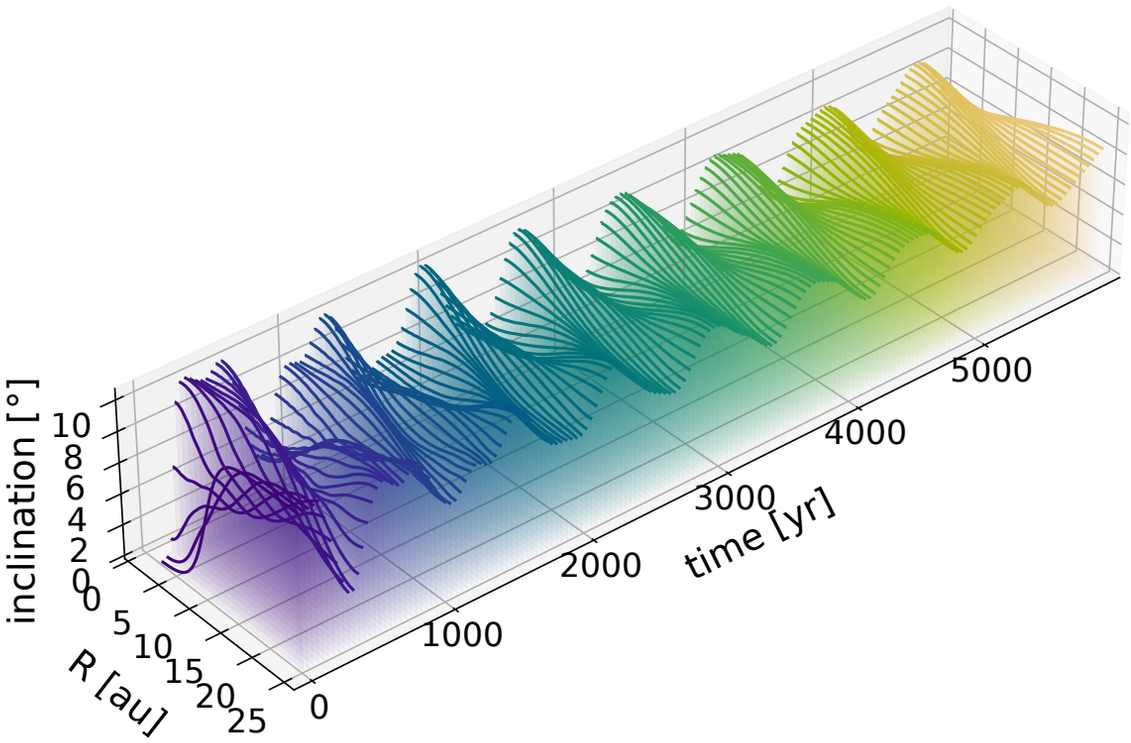

Figure 3.12: Evolution of the inclination profile in the warped disk simulation. The color simply highlights the time.

To investigate the damping of the warp, we continued running the simulation up to 2.4×10^4 yr (2000 orbits at R_0). Figure 3.13 shows this long-term evolution. The warp is dampened so that we end up with a nearly planar, but spatially tilted disk.

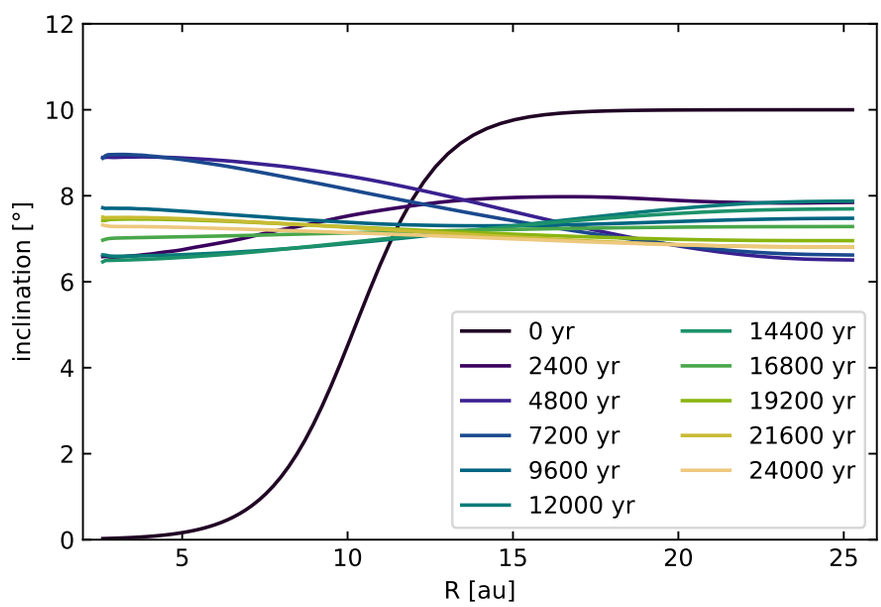

Figure 3.13: Long-term evolution of the inclination profile in the warped disk simulation.

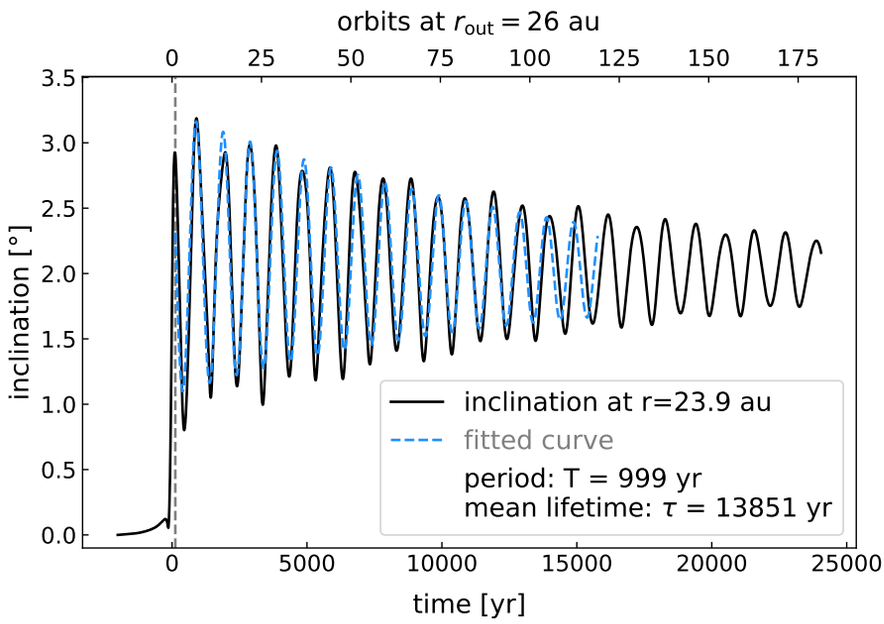

Figure 3.14: Decay of inclination in the warped disk simulation. We chose to evaluate the inclination close to the outer edge at a radius of 22.5 au. The black line shows the simulation data, the blue dashed line the fit. The grey dashed line indicates the starting point of the fit.

In Figure 3.14, we investigate the warp wave period and inclination damping in more detail. We chose a radius close to the outer edge of the disk at $r = 22.5\,\mathrm{au}$ and fit the inclination evolution at this point with an exponentially decaying cosine function of the form:

$$f(t) = A\cos(\omega t - b)\ \exp(-\lambda t) + c + d\,t, \tag{3.11}$$

with amplitude parameter, A, frequency, ω, and decay rate, λ. We allow for a phase shift, b, in the cosine function, an offset c, and a linear damping in overall inclination with d.

Our fit gives a wave frequency of $\omega = 0.008\,\mathrm{yr}^{-1}$, which leads to a warp wave period of

$$P = \frac{2\pi}{\omega} = 757\,\mathrm{yr}. \tag{3.12}$$

We can make an estimate of the period from linear theory in the following way. The wave speed of the warp wave is approximately half the sound speed in the disk $v_\mathrm{w} = c_\mathrm{s}/2$ (Lubow & Ogilvie, 2000). Because we are investigating a globally isothermal set-up for now, the sound speed is $c_\mathrm{s} = 653\,\mathrm{m/s}$ everywhere in the disk. We find that the warp wave behaves similarly to a standing wave, with a wave length of twice our radial disk regime $\lambda_\mathrm{w} = 2\Delta r = 44.8\,\mathrm{au}$. The estimated

period then is

$$P_{\text{linear theory}} = \frac{\lambda_w}{v_w} = \frac{2\Delta r}{2c_s} = 657\,\text{yr}. \tag{3.13}$$

We note that this is the same as the sound-crossing time $t_s = \Delta r / c_s$. This means that the period in our simulation is in agreement with linear theory.

In our fit, we find a decay rate of $\lambda = 8.9 \times 10^{-5}\,\text{yr}^{-1}$, which results in a mean lifetime of the warp of $\tau = 1/\lambda = 1.1 \times 10^4\,\text{yr}$. Linear theory gives a rough estimate of the warp damping timescale with $\tau_{\text{linear theory}} = 1/(\alpha\Omega)$ with Ω as Keplerian frequency. (see e.g., Nixon & King, 2016). If we choose the Keplerian frequency at the outer edge of our disk, this results in $\tau_{\text{linear theory}} = 2.1 \times 10^4\,\text{yr}$, which agrees within a factor of 2 with the findings in our simulation.

From our fit, we also get the mean tilt of the disk (c in Equation 3.11) at our chosen radius, which is 7.7°, and the damping of inclination d, which we find to be $-3 \times 10^{-5}\,\text{yr}^{-1}$, which gives a total inclination loss over the simulated $2.4 \times 10^4\,\text{yr}$ of 0.74°. This loss of mean inclination is a numerical effect as also found in Section 3.3.2. It is also interesting to note the amplitude from the fit, with $A = 1.6°$.

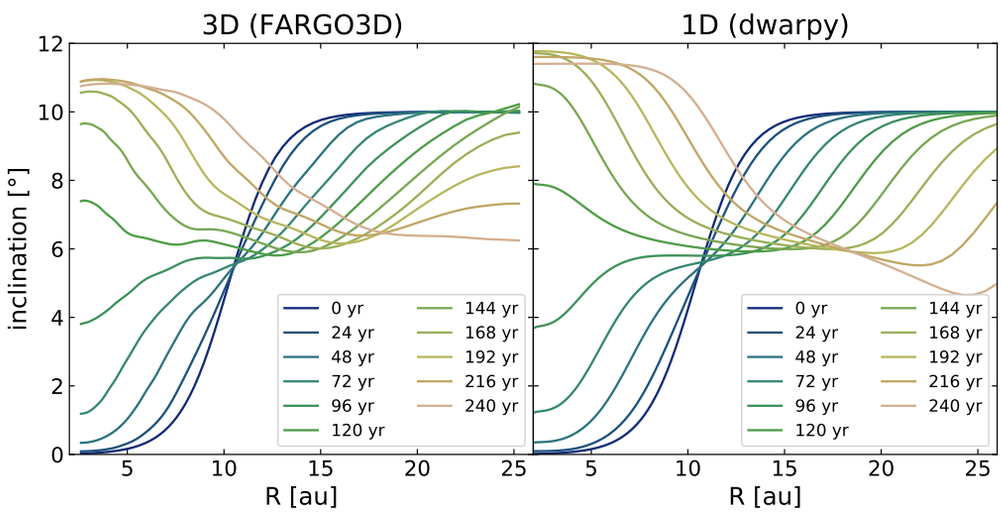

Figure 3.15: Inclination evolution of the warped disk in comparison between the 3D set-up in FARGO3D (left panel) and the 1D set-up in dwarpy (right panel). For comparability, we plot until 240 years of simulated time. Note that the computational domain of the 1D simulation is well beyond the outer edge of the figure.

We went on to compare the 3D hydrodynamic simulations to a 1D model of warped disks. For the 1D model, we split the disk into concentric annuli and assign each annulus an angular momentum vector that determines the orbital plane of the annulus. This way, we have a 1D parametrization for a 3D object. The angular momentum vector can be updated using Equations 3.1–3.3. We set

up the parameters in the 1D model the same parameters as in the 3D model. For this, we use our 1D warped disk evolution code `dwarpy` (Kimmig et al. in prep).

In Figure 3.15, we find a good agreement between 3D and 1D simulations on short timescales. On longer timescales, however, the 1D model shows a larger amplitude of the warp than the 3D simulation, as shown in Figure 3.16. This might be due to boundary conditions, as we used rigid boundaries in the 3D simulation and open boundaries in the 1D model, as `dwarpy` is primarily tested with these conditions. In addition, these open conditions help to avoid a torque from the boundaries acting on the disk. However, the wave-like nature of the inclination evolution is still apparent in the 1D model.

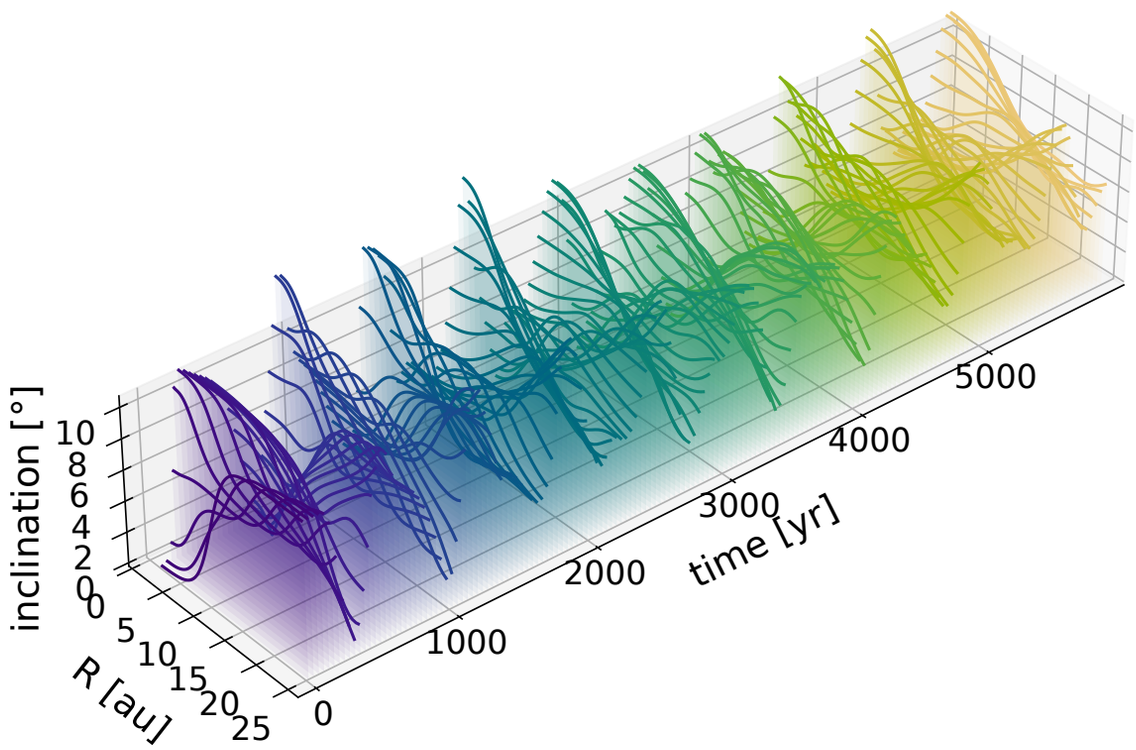

Figure 3.16: Same as Figure 3.12, but for the 1D model with `dwarpy`.

3.4.2 Twisting of the disk

In our 3D simulation, we notice a precession motion within the disk, which does not occur in the 1D model for the wave-like regime. The 3D disk shows a differential precession, meaning that the disk precesses differently depending on the radius, which we call a *twist*. In this section, we investigate the twist in more detail. We aim to find out whether the twist is caused by numerical or physical effects.

At first, we look at the total angular momentum of the disk. We find that its absolute value decreases about 0.5 % in the time span of 6000 yr and 2 % in the

time span of 2.4×10^4 yr. Evaluating the total angular momentum of the planar reference case from Section 3.3.1, we find that the planar disk's absolute angular momentum also decreases by about 0.5 % in the time span of 6000 yr.

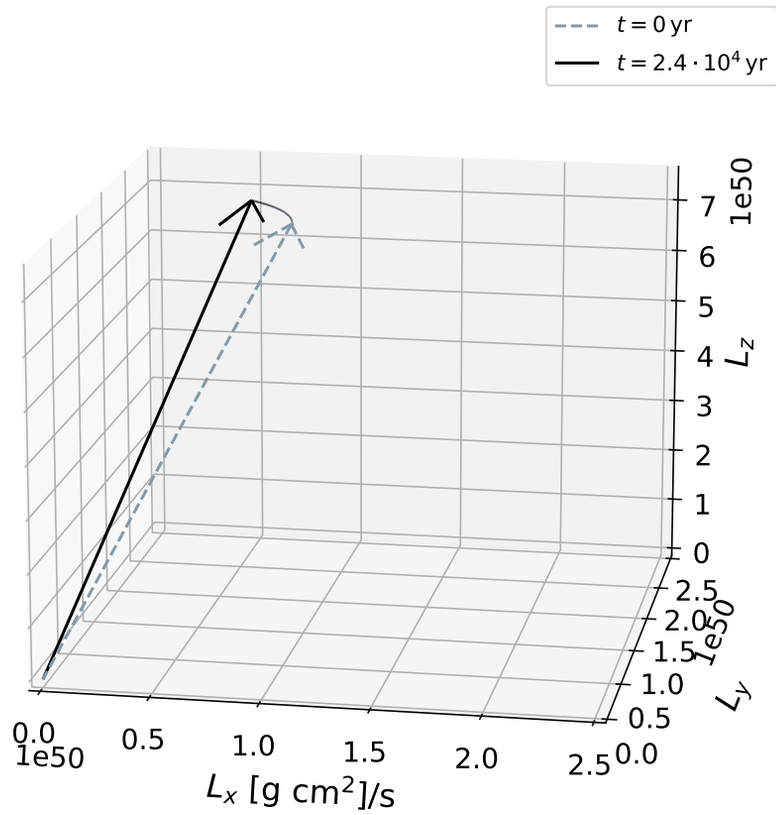

Figure 3.17: Direction of the total angular momentum vector in the beginning of the simulation $t = 0$ yr (grey dashed line) and in the end $t = 2.4 \times 10^4$ yr (solid black line). The line connecting the two arrows indicates the time evolution with darker color the later the time.

Figure 3.17 shows that the direction of the total angular momentum vector slightly changes over a time span of 2.4×10^4 yr, which are 2000 orbits at R_0. The angle between the vectors at the beginning and the end of the simulation is 4.6°. We suspect that the change in direction occurs due to numerical effects. While FARGO3D is programmed such that it conserves azimuthal angular momentum to machine precision, this mainly applies to components perfectly aligned with the grid geometry. We suspect the change in angular momentum we observe in Figure 3.17 to be caused by the fact that the numerical scheme does not account for tilted motions. On a timescale of 6000 yr (inclination evolution in this time span plotted in Figure 3.12), on which we find a significant twisting of the disk, we find the angular momentum vector to change on an angle of only 1.2°. Notably, the total angular momentum vector does not show any oscillatory be-

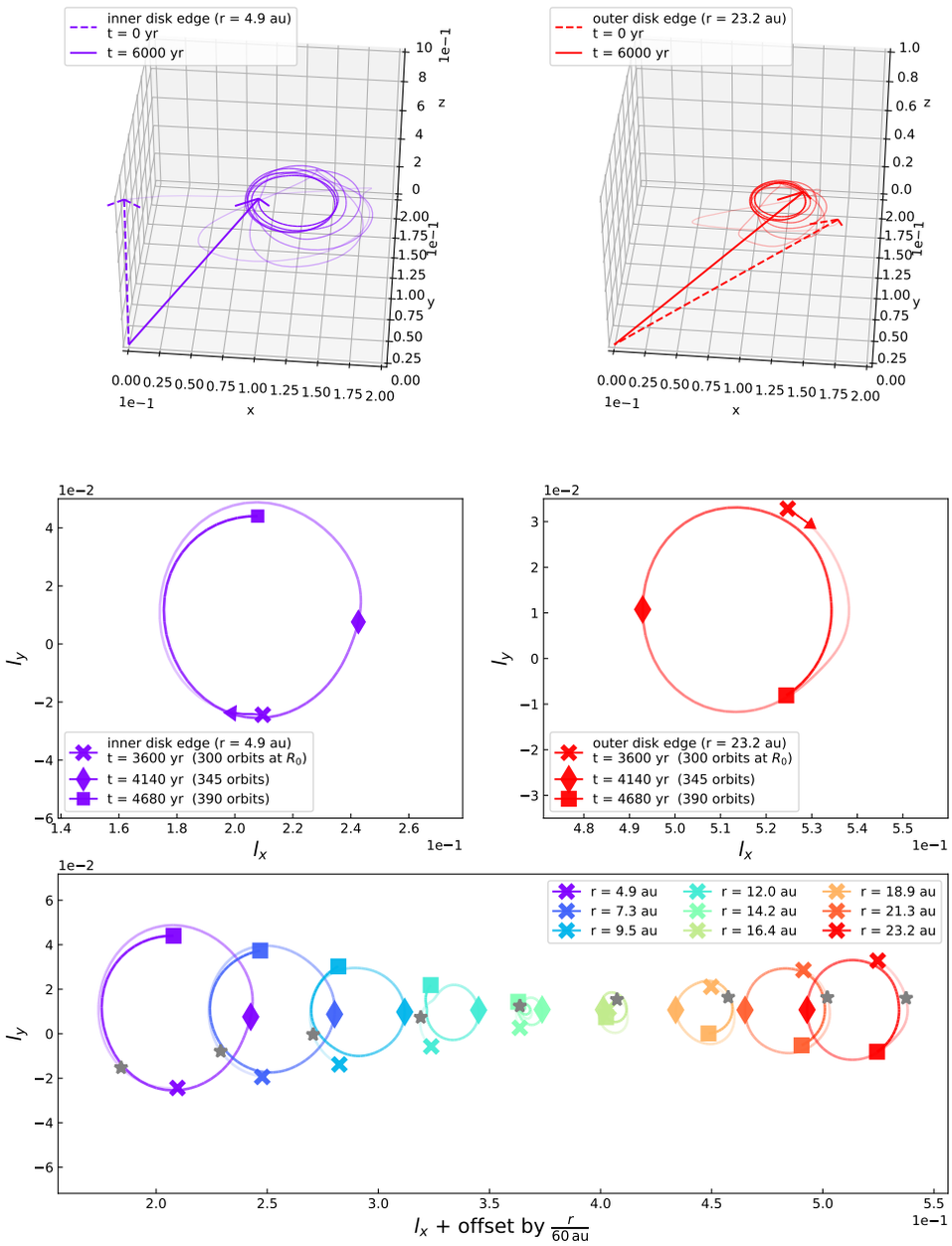

Figure 3.18: Twist motion in the warped disk simulation. **Top row:** Unit angular momentum vectors close to the inner (left panel) and outer (right panel) edge of the disk for the first $t = 6000\,\mathrm{yr}$. Similar to Figure 3.17. **Middle row:** x-y components of the unit angular momentum vector at the same radii as in the top row, but only for the time period between 300-390 orbits at R_0, chosen to roughly show 1.5 precession periods. The direction of the precession is indicated by the arrows. x-markers show the beginning of the plotted time, squares the end. Diamonds indicate the middle of this time period (45 orbits after the x-markers). **Bottom row:** Same as middle row, but for various radii, plotted with an offset of $r/(60\,\mathrm{au})$ in y-direction to disentangle the twist at different radii. The stars show the l_x-l_y components at a snapshot at $t = 3696\,\mathrm{yr}$ (308 orbits at R_0), which shows a twisted state in the time evolution.

haviour. In spite of the slight changes in angular momentum, we can argue that the changes are small and, therefore, the total angular momentum is reasonably well conserved, both in direction and in absolute value.

We plot the twist of the disk by showing the evolution of the unit angular momentum vectors at different radii in Figure 3.18. The angular momentum vectors are extracted from the 3D simulation using Equation 3.9.

A twist occurs when the unit angular momentum vectors point in different directions. In the top row of Figure 3.18, we show the time evolution of the vectors close to the inner disk edge (left) and close to the outer edge (right). We intentionally did not choose the exact disk edges to avoid potential boundary effects. The disk quickly twists and, after some time, the vectors precess in almost perfect circles.

To investigate this motion more closely, we chose a point in time (300 orbits at R_0) at which the circles are already developed and plot in the middle row one and a half periods from that point on. Here, we only plot the x- and y-component of the unit angular momentum vector $\vec{l}_r$. We find the period to be roughly 60 orbits. We see that both the inner and the outer part precess clockwise. However, because the total angular momentum is conserved in direction (as seen in Figure 3.17), the directions counteract, which means that whenever the inner part of the disk points in positive x- and/or y-direction, the outer part points correspondingly in negative x- and/or y-direction. To see this, we indicate a few corresponding times with the symbols in the plot.

In the bottom panel of Figure 3.18, we then plot more radial points in the disk, each radius in a different color. We note that we offset the twist for each radius by a factor of $r/(60\,\mathrm{au})$ in order to disentangle the circles. We chose a linear spacing for the radial evaluation points. At all radii, the disk precesses clockwise, and the counteracting of the directions can be seen in this plot in more detail. One part of the disk always counteracts the precession of another part, so that the total angular momentum is conserved. A clearly twisted state of the disk occurs for example in the snapshot at 308 orbits, which is illustrated with grey stars.

We note that in the long-term evolution of the system, the precession is dampened. This happens on the same timescale as the inclination of the warp is dampened. Additionally, the precession period of the vectors coincides with the inclination wave period.

To explore the origin of the disk's twist — whether it is a numerical or physical effect — we conducted a series of tests, which can be found in Appendix 3.B, and we briefly summarize: The fact that the total angular momentum does not exhibit any oscillatory motion led us to rule out the inner and outer grid boundary as a cause for the twist. To investigate further, we performed a new simulation,

pushing the outer boundary far away from the physical grid edge by applying an exponential cut-off to the disk density. In this scenario, the outer boundary is unlikely to influence the physical outer edge of the disk. However, even in this case, the twist persisted. Furthermore, we performed 1D simulations to explore if the twist might be triggered by the initial conditions in the 3D simulation. However, the 1D model failed to reproduce the twist observed in the 3D model. This strongly suggests that the twist is indeed a 3D phenomenon. Interestingly, a similar effect can be seen in SPH simulations of warped disks (R. Martin, priv. comm.).

While we cannot be completely sure at this point, our tests indicate that the twist likely arises from a physical cause rather than being a numerical artefact. We suspect that specific terms neglected in the linearization process in deriving the 1D equations play a role in why the 1D model cannot reproduce the twist.

3.4.3 Investigating a differently flared disk

In order to relax the assumption of a globally isothermal disk, we ran an additionally simulation with a locally isothermal disk using a flaring index of $i_{\mathrm{fl}} = 0.25$ (see Equation 3.5) and setting the temperature structure accordingly. We keep all other parameters the same. A cross-section of the initial set-up is shown in Figure 3.19.

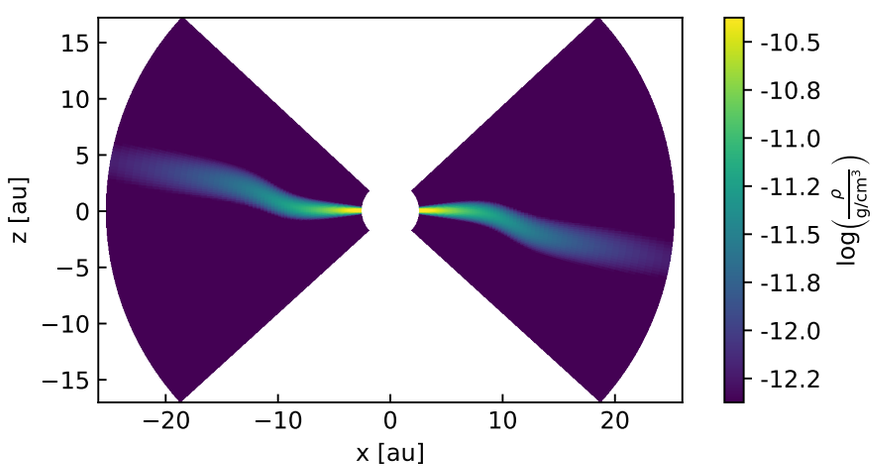

Figure 3.19: Cross-section along the x-axis of the locally isothermal warped disk.

Investigating the inclination evolution, we find the expected wave-like behavior, as shown in Figure 3.20.

The overall behavior is similar to the globally isothermal disk. However, there seems to be an amplitude modulation with a period of about 4000 yr, which can also be seen when we look at the inclination evolution at a specific radius (we

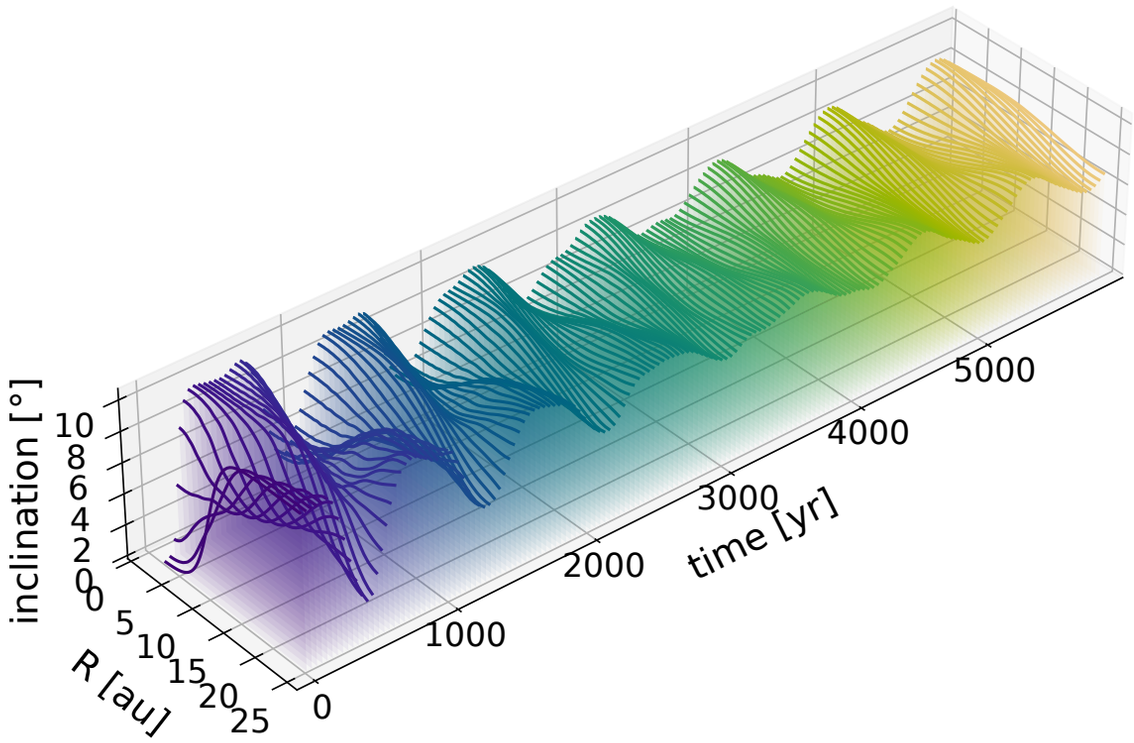

Figure 3.20: Evolution of the inclination profile in the locally isothermal warped disk. Like Figure 3.12.

chose $r = 22.5\,\mathrm{au}$) as shown in Figure 3.21 (black line). This could be either a numerical or a physical effect, which would require further investigation. This would go beyond the scope of this work, thus we simply mention this observation at this point.

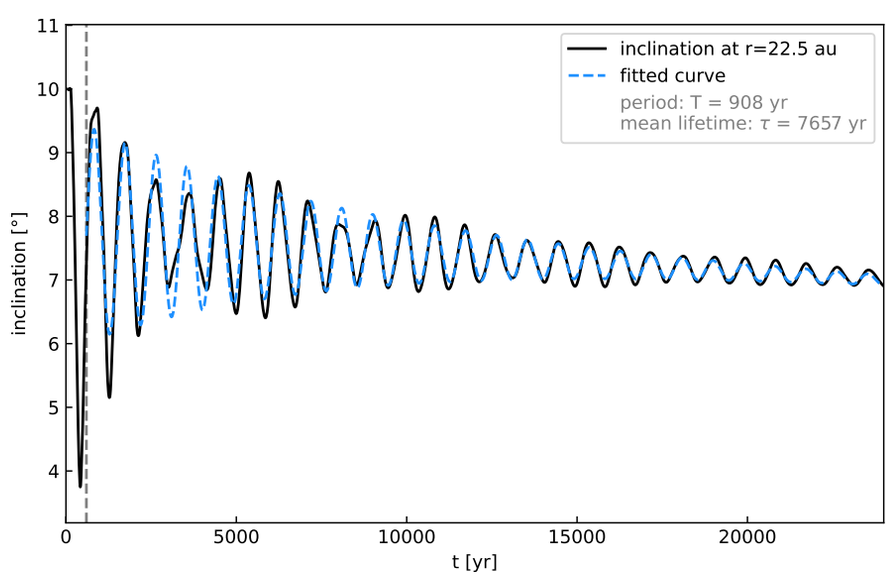

Figure 3.21: Like Figure 3.14, but for the locally isothermal disk.

In Figure 3.21, we investigate the inclination decay rate according to Equa-

tion 3.11 and find a decay rate of $\lambda = 1.3 \times 10^{-4}\,\mathrm{yr}^{-1}$, which gives a mean lifetime of $\tau = 1/\lambda = 7.7 \times 10^3\,\mathrm{yr}$. This is slightly shorter than the fitted mean lifetime of the globally isothermal disk. For reference, linear theory gives an estimation of $\tau_{\text{linear theory}} = 1/(\alpha\Omega) = 2 \times 10^4\,\mathrm{yr}$, which does not depend on the disk's vertical structure. In future work, the influence of the vertical structure on the warp lifetime could be investigated in more detail.

In Appendix 3.B, we investigate the twist of the locally isothermal disk. We find that it still occurs, but the twist behavior appears to be more complicated than in the globally isothermal case.

3.4.4 Different viscosities

We further test the dependence of the warp and twist on viscosity and perform two additional simulations, using the same initial set-up but varying the original $\alpha_t = 10^{-3}$ to lower ($\alpha_t = 10^{-5}$) and higher viscosity ($\alpha_t = 10^{-2}$).

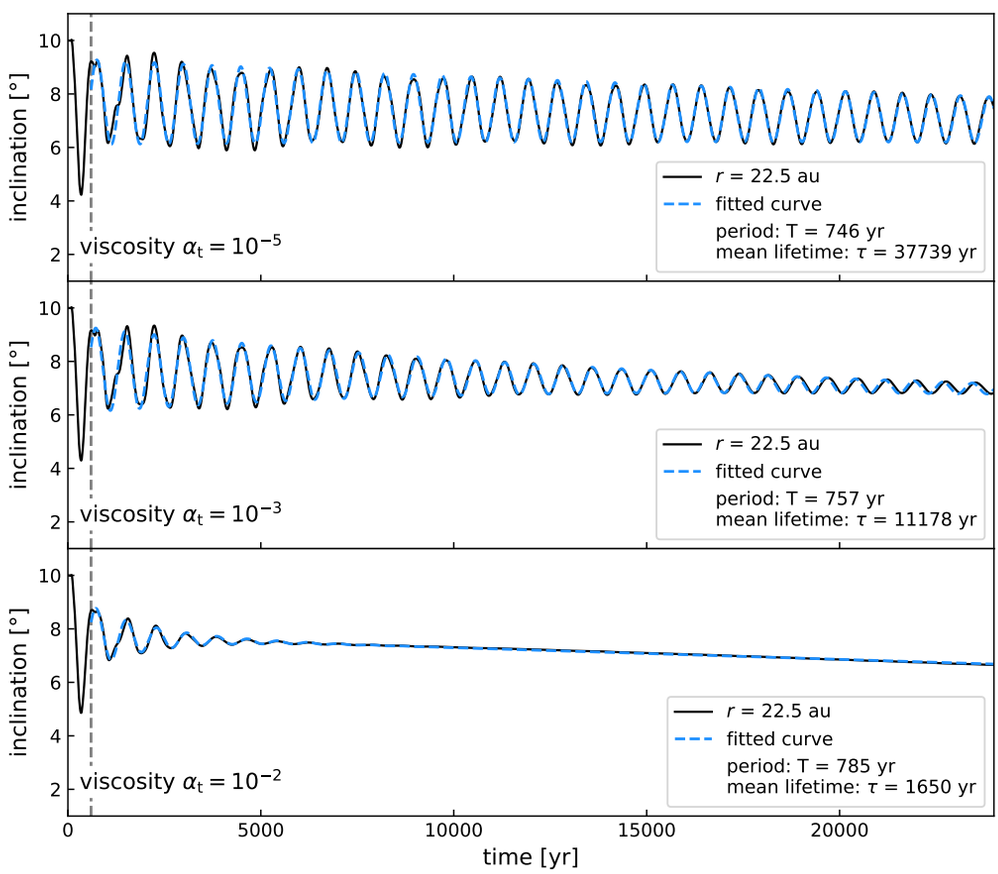

Figure 3.22: Inclination evolution at radius $r = 22.5\,\mathrm{au}$ (black solid lines) in simulations with different disk viscosities. The blue dashed lines indicate the fit according to Equation 3.11. The middle panel corresponds to the fiducial simulation and is the same as Figure 3.14.

We plot the inclination evolution at a radius $r = 22.5\,\mathrm{au}$ (close to the outer edge) of the simulations with varying viscosities in Figure 3.22 to investigate the warp decay rates. We find that for a ten times higher viscosity (bottom panel), the warp is dampened roughly ten times faster than in our fiducial simulation, as expected by linear theory (recall $\tau_{\text{linear theory}} = 1/(\alpha\Omega)$). For the low viscosity simulation (top panel), the mean lifetime is longer than the fiducial simulation, as expected. However, instead of the factor 100 predicted by linear theory, we find a factor of roughly 4. This could mean that the simulation is influenced by numerical viscosity and grid effects, or that additional effects play a role in dampening the warp that are not taken into account in the derivation of the timescale estimation. Investigating the reason here in detail would go beyond the scope of this work.

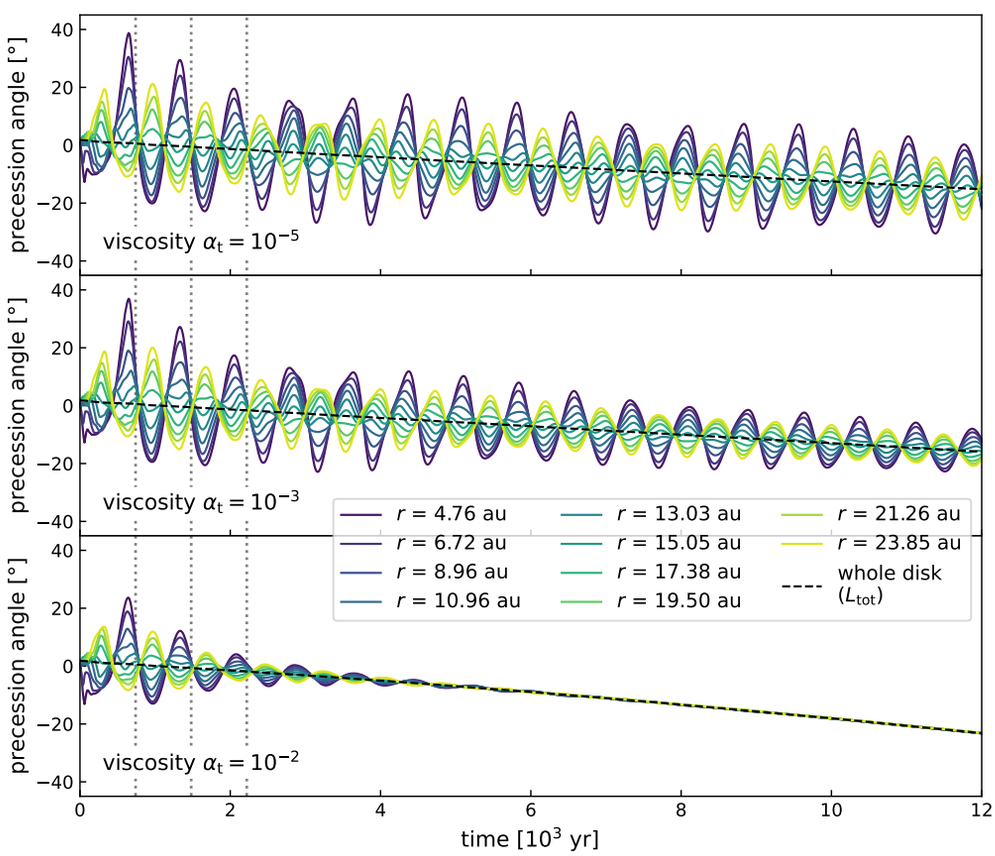

Figure 3.23: Precession angles for different radii (colored lines) in simulations with different disk viscosities. The black dashed line in each panel shows the precession angle of the angular momentum vector, $\vec{L}_{\text{tot}}$, of the whole disk. The grey dotted lines indicate precession periods of roughly 740 yr.

In Figure 3.23, we plot the precession angle over time for the three different viscosities. Recall that we define the precession angle as the clockwise angle between x-axis and angular momentum vector projected onto the x-y-plane, giving

an initial precession angle of 0° at all radii. We plot the precession angle at different radii (colored lines). As a reference, we additionally plot the precession angle of the total angular momentum vector (black dashed line) and note that it does not oscillate.

In all cases, we find that the total angular momentum vector changes direction in time, which means that the disk overall precesses. This overall precession is more pronounced in the high viscosity case, $\alpha = 10^{-2}$. This is not a physical effect, but a result from grid effects, as explored in Section 3.3.4. A higher resolution would help keep the direction of the angular momentum conserved for a longer time period. However, since we were mainly interested in the differential precession, namely, the twist, we did not perform additional simulations in higher resolution at this point.

In all cases, we found a twist, which is dampened much faster for high viscosity. The precession period is similar for all viscosities, as indicated with the grey dotted lines in Figure 3.23, and roughly equals 740 yr. Despite the fact that parts of the disk clearly precess, the total angular momentum direction does not oscillate. We take this as another indication that the twisting behaviour is physical, although the reason for it is not clear yet.

3.5 Internal dynamics of the warped disk and origin of the torques

3.5.1 Sloshing motions and internal torques

The internal torque responsible for the propagation of a warp through the disk is primarily due to resonant horizontal internal gas motions (Papaloizou & Pringle, 1983; Papaloizou & Lin, 1995; Lubow & Ogilvie, 2000). We refer to these as "sloshing motions" because they are caused by sideways pressure gradients due to the warp (see Figure 5 of Ogilvie & Latter, 2013a), and behave very similar to a layer of water on a tilted tray. For any snapshot of a 3D warped disk model, the internal torque can be calculated as shown in Appendix 3.C.

A description of how these internal sloshing motions are driven, how they behave, and how they give rise to an internal torque, was given in DKZ22. There, the authors used a variant of the local shearing box approach of Ogilvie & Latter (2013a). After employing two linearization steps, they derived the solutions for the sloshing motions, and from those obtained a generalized set of 1D warped disk equations. With our 3D model, we can investigate how good these approximate solutions for the sloshing motions are, as we can directly analyze the mo-

tions of the gas inside the 3D disk and compare them to the predictions of DKZ22.

Of course, we are not the first to compare 3D warped disk models to 1D models. For instance, Nelson & Papaloizou (1999) performed 3D SPH simulations of warped disks in both the wavelike and diffusive regime, and compared the results to 1D models. They also see the sloshing motions in their 3D models. In our FARGO3D model in spherical coordinates, we have the advantage compared to SPH models that we can study the disk many scale heights above the midplane, where the densities are orders of magnitude lower than at the midplane. While these regions do not contribute significantly to the internal torque, they may contribute to observations of the disk.

3.5.2 Sloshing and breathing motions in the 3D model

To compare the internal dynamics of our 3D warped disk model with the local shearing box approach of DKZ22, we chose a single annulus of the disk, namely, we chose a radius, r, at which we performed the comparison. In DKZ22, the global disk is assumed to be oriented such that the $\vec{l}$ vector (the unit vector perpendicular to the disk annulus) at this radius points into the global positive z-direction (see Figure 2 of DKZ22). Furthermore, the disk is oriented such that the local warp vector $\vec{\psi} = \mathrm{d}\vec{l}/\mathrm{d}\ln r$ points in the positive x-direction. To compare our 3D disk model, at radius r, with the local shearing box description of DKZ22, we therefore need to rotate it to this configuration.

There is, however, a small numerical subtlety. The first rotation, putting $\vec{l}$ into the positive z-direction, is a straightforward rotation around the $\vec{l} \times \vec{e}_z$ axis, where $\vec{e}_z$ is the unit vector in the global z-direction. In our 3D model we perform this rotation as a coordinate mapping using linear interpolation, and, of course, we also rotate the velocity vectors accordingly. The second rotation, however, which is the rotation around the z-axis such that $\vec{\psi}$ points into positive x-direction, can cause numerical difficulties. This is because numerical noise can make the direction of the warp vector $\vec{\psi}$ wiggle wildly at radii for which $|\vec{\psi}| \ll 1$; for instance, around radii where it flips sign. As long as we only study a single annulus of the disk this is not a problem. However, when comparing the results of neighbouring annuli, we might find major differences simply due to large differences in horizontal (x-y) orientation. This is purely an artefact of the choice of horizontal orientation. Since our disk model is initiated with a warp purely in the x-z-plane, we chose, for this section, to omit the second rotation. The global orientation of the model is close enough to the DKZ22 choice that we can perform our analysis.

We analyzed our model at time of $t = 120\,\mathrm{yr}$ (10 orbits at R_0) at a radius of $r = 8.3\,\mathrm{au}$. We chose this point in time because the disk already had some time

to relax and the internal torques are fully developed, but the disk system did not have time yet to change much. At this moment, this disk annulus is inclined with respect to the coordinate system by $-3.8°$. If we display the density in the unrotated angular coordinates θ, ϕ, this leads to the image Figure 3.24-left, where the annulus looks wavy. If we remap this into a new, rotated, coordinate system, the disk annulus becomes straight (Figure 3.24-right). We can see that the density at the disk midplane has moderate maxima and minima. They are caused by the vertical expansion and compression motion, called "breathing motion" by Ogilvie & Latter (2013a).

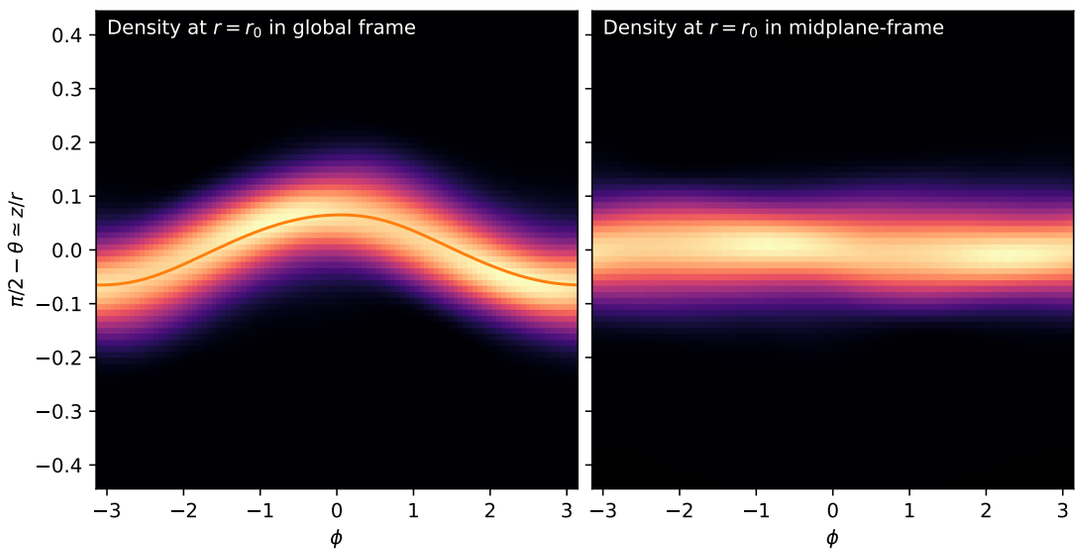

Figure 3.24: Gas density of the disk annulus at $r = 8.3\,\mathrm{au}$ at time $t = 120\,\mathrm{yr}$. The map is a standard (ϕ, θ) projection of the sphere of constant distance to the star. The color scale is linear. Left: in unrotated coordinates. Right: in rotated coordinates such that the disk annulus lies in the equatorial plane.

In this new rotated frame, we can analyze the radial velocity $v_r(\theta, \phi)$, namely, the sloshing motion, and the vertical velocity $v_z(\theta, \phi)$, namely, the breathing motion. These are shown in Figure 3.25. The Keplerian motion of the gas flows from left to right (toward increasing ϕ), which can therefore be regarded as kind of a time axis, even though these figures show one snapshot in time. In the left panel it can be seen that, as expected, the radial velocity $v_r(z, \phi)$ has consistently opposite sign above/below the disk midplane. This is the sloshing motion that produces the internal torque. Far from the midplane, this sloshing motion becomes supersonic. However, most of the torque is produced below about one scale height (root-mean-square height of the disk above the disk's midplane); that is, the grey dot-dashed line in the figure, where the motions are subsonic, so that the torque is presumably not much affected by the supersonic motions higher up. The grey

lines in Figure 3.25 mark the vertical extend of the disk, that is, the root-mean-square widths of the vertical Gaussian density profile. The lines become slightly wavy due to the breathing motion causing the vertical compression and expansion in the disk.

The right panel shows the vertical motion of the gas. In this figure, the sign flips at the disk midplane as well, meaning that the motion is either expanding or compressing the disk vertically (i.e., the breathing motions). These motions are much weaker than the sideways sloshing motions, but they also become supersonic far above the disk midplane, leading to the formation of shocks where the upward (blue) motion hits the downward (red) motion.

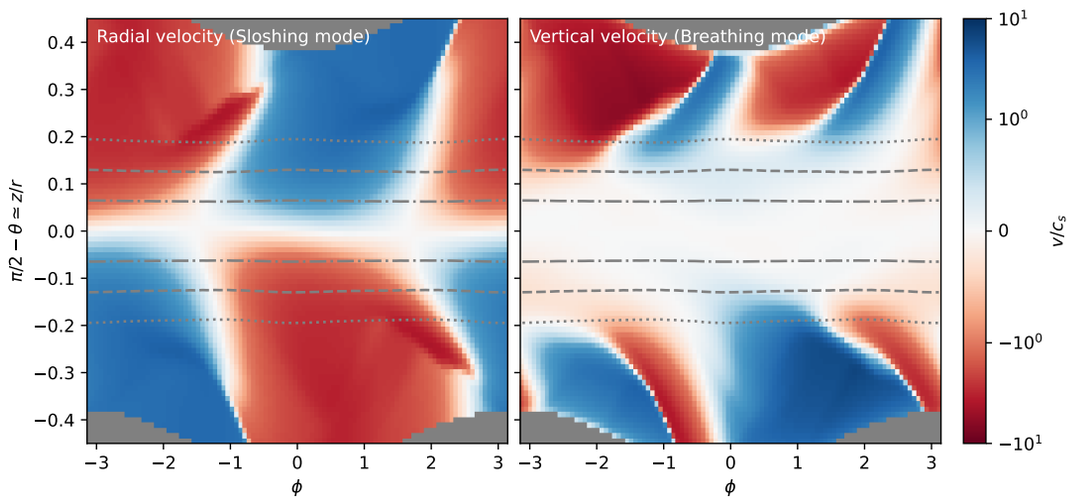

Figure 3.25: Gas velocity components in units of the local isothermal sound speed at $r = 8.3\,\mathrm{au}$ at time $t = 120\,\mathrm{yr}$, in the rotated frame (as in Figure 3.24-right). The colors are linear between -1 and 1, and logarithmic for $|v/c_s| > 1$. Note: the isothermal sound speed c_s is constant at $0.66\,\mathrm{km/s}$ throughout each panel, consistent with a disk aspect ratio of $h_p/r = 0.064$. Left: Radial velocity (sloshing motion). Right: Vertical velocity (breathing motion). The dot-dashed, dashed and dotted grey lines mark the rms vertical extend of the disk (which would relate to the pressure scale height in a steady-state disk), twice that, and three times that. The grey areas below and above are the regions outside the model grid.

These results show that the sloshing and breathing motions predicted from the linearized shearing box model (Ogilvie & Latter, 2013a, DKZ22) are indeed occurring in the 3D warped disk model. And these velocities can be quite large, close to or exceeding the sound speed, especially at two or more scale heights above the disk surface. This may have relevant consequences for kinematic observations (using molecular lines) of warped protoplanetary disks.

In Figure 3.26 we show a vertical slice of Figure 3.25-left, at azimuth $\phi = 1.29$. The figure shows that the linear approximation of the sloshing motion $v_r(r, z, t) = V_r(r, t)\Omega z$, which stands at the basis of all 1D warped disk models, appears to be

a good approximation up to several scale heights at this radius and time. Deviations do occur at some other radii and times, but overall they are minor.

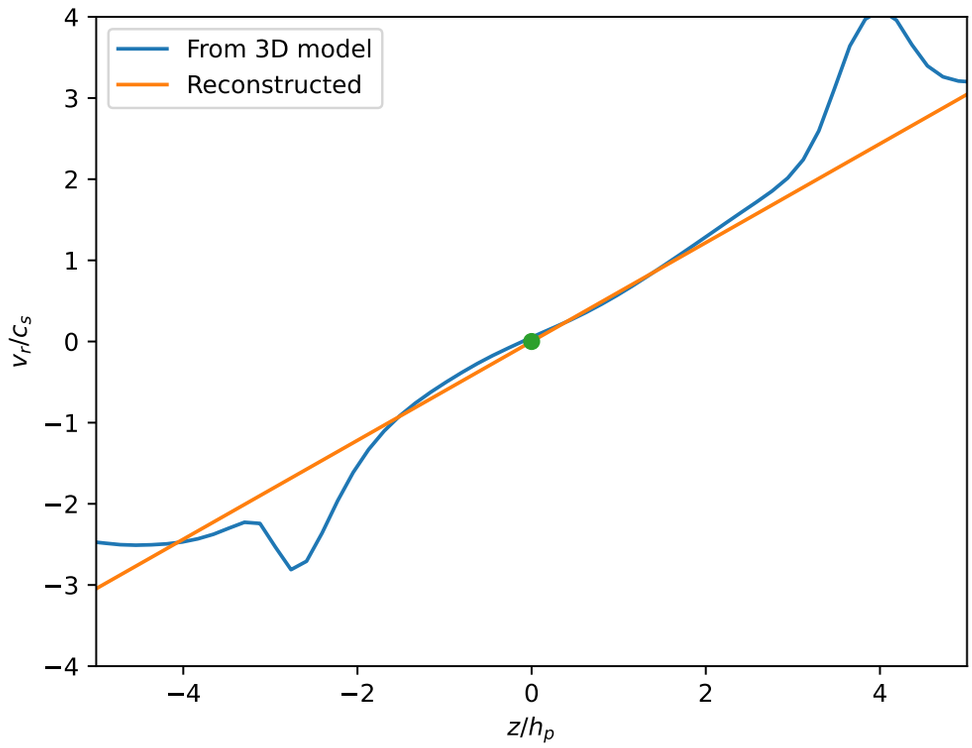

Figure 3.26: Radial gas velocity in units of the local isothermal sound speed, at the same radius and time as in Figure 3.25, at azimuth $\phi = 1.29$, i.e., a vertical slice of that figure. The blue curve shows the data from the 3D model, the orange curve a linear reconstruction using a slope computed as in Appendix 3.D.

3.6 Conclusion

We performed 3D simulations of misaligned disks using FARGO3D (Benítez-Llambay & Masset, 2016). To study the applicability of the grid-based code to misaligned features, we set up a disk that is planar, but tilted with respect to the grid midplane and compared the result to a planar disk aligned to the grid midplane. The latter case has been studied extensively in previous works, therefore, we used it as our reference case. Physically, the tilted case should lead to the same results, meaning all deviations in the simulation result from grid effects, namely, numerical friction. We find that grid-based methods can simulate misaligned features surprisingly well, given a high enough resolution. We find the vertical resolution (in θ) to be most important in terms of avoiding grid effects. Addition-

ally, the minimum required resolution to accurately model misaligned features depends on disk viscosity: for higher viscosity, a higher resolution is needed. For future studies using high viscosities in grid-based methods, we recommend performing resolution studies in these specific cases.

We set up an initially warped disk around a single star and we did not include any component driving the warp. Evaluating the warp evolution in this isolated system, we find the evolution to take on a wave-like character, as expected. Comparing the evolution to a 1D ring code model, we find good agreement in inclination evolution. Looking at the twist of the disk, however, we find a significant twisting in the 3D model, which is not seen in the 1D model. The absence of this effect in the 1D model does not necessarily mean that it is an unphysical effect. Looking at the total angular momentum of the whole disk, it does not precess and, in fact, is conserved in both absolute value and direction, which indicates the twist not to be caused by grid effects. Further tests, including a comparison to 1D models and decreasing the importance of the outer boundary by moving it away from the disk edge point to the same conclusion. For higher viscosity, we observe a less pronounced twisting with a faster damping of the precession motion. We suspect the twist to be a physical effect in the 3D warp evolution. The reason why it is not seen in 1D models could be that the effect was neglected in the linearization process.

Evaluating the internal dynamics in our simulation in detail, we find a sloshing and breathing motion, as predicted in the local shearing box approach in DKZ22. These motions are mainly responsible for the warp evolution and lead to the generation of the internal torque. We find that the sloshing and breathing velocities can become supersonic in the upper layers of the disk. Although the upper layers do not significantly influence the warp evolution, since the internal torque is produced close to the midplane, it may have a significant influence on kinematic observations of warped disks.

Appendices to Chapter 3

3.A High-resolution simulation of a warped disk

To check the dependency on resolution, we performed a simulation of our fiducial warped disk set-up with a higher resolution. For this simulation, we doubled the resolution in all three directions, which means 160 cells in r-direction (3.4 cells-per-scaleheight at $r = 5.2\,\mathrm{au}$), 200 cells in ϕ-direction (1.6 cps at $r = 5.2\,\mathrm{au}$), and 264 cells[2] (8.2 cps at $r = 5.2\,\mathrm{au}$) in θ-direction.

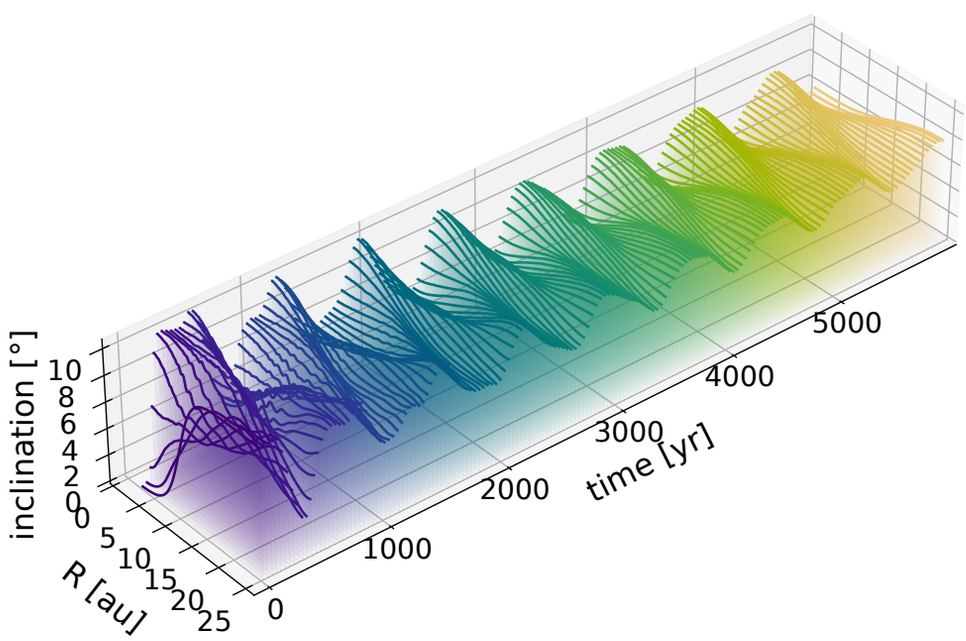

Figure 3.A.1: Evolution of the inclination profile in the high-resolution warped disk simulation. The color highlights the time. Similar to Figure 3.12.

[2]The resolution in θ should actually have been 268 cells for a doubled resolution, but due to a miscalculation, we set 264. However, we do not expect any significant changes in the result and therefore decided not to run the simulation again.

Figure 3.A.1 shows the wave-like behavior of the simulation. Like in the simulation with lower resolution, we see a global bending mode superimposed on a global tilt. The bending mode appears as standing wave with a wavelength of twice the radial disk regime.

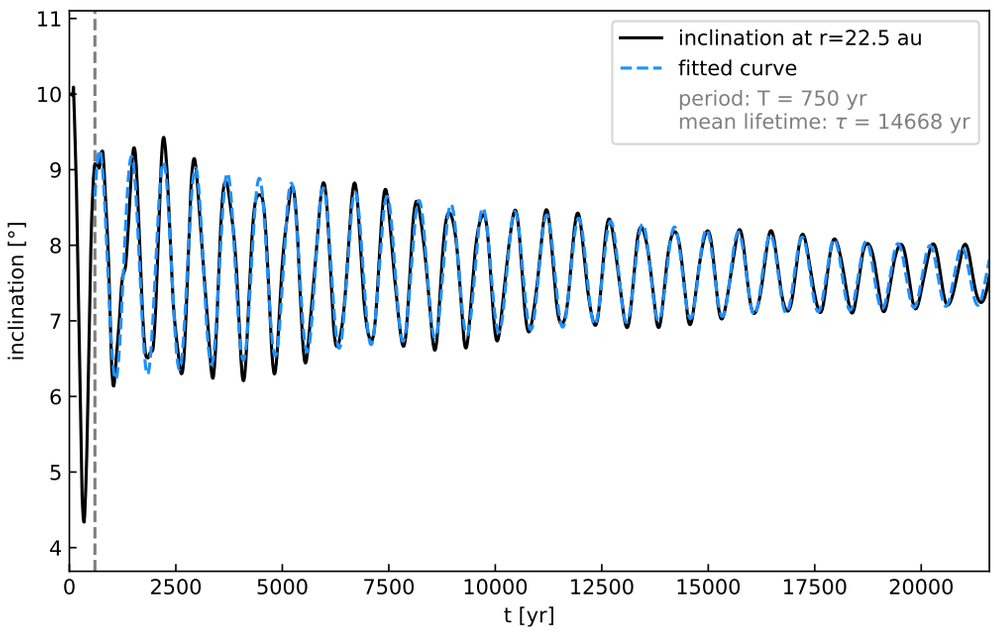

Figure 3.A.2: Decay of inclination in the high resolution warped disk simulation. We evaluate the inclination at $r = 22.5\,\mathrm{au}$. The black line shows the simulation data, the blue dashed line shows the fit. The grey dashed line indicates the starting point of the fit. Similar to Figure 3.14 (note the slightly shorter simulation time).

To evaluate the bending mode in detail, we fit the inclination evolution in the outer part of the disk (i.e., at $r = 22.5\,\mathrm{au}$) with Equation 3.11 (see Figure 3.A.2). The fit parameters give an amplitude $A = 1.6°$, a frequency of $\omega = 0.0083\,\mathrm{yr}^{-1}$, a decay rate of $\lambda = 6.8 \times 10^{-5}\,\mathrm{yr}^{-1}$, a global tilt of $c = 7.7°$, and a global (numerical) inclination loss of $d = -6.8 \times 10^{-6}\,\mathrm{yr}^{-1}$. These parameters indicate a period of $P = 750\,\mathrm{yr}$ and a mean lifetime of $\tau = 1.5 \times 10^{4}\,\mathrm{yr}$.

In comparison to the fiducial resolution simulation, we find a slightly shorter wave period and a slightly lower decay rate leading to a slightly longer mean lifetime of the warp. However, the difference is small (much lower than one order of magnitude) and we can therefore say that the two simulations are in good agreement with each other. Unsurprisingly, we find a much lower inclination loss, d, by one order of magnitude, which supports our assumption that these differences are caused by numerical effects.

Additionally, we briefly evaluate the twisting of the disk in the high resolution simulation, see Figure 3.A.3. For the plot, we chose the same time intervals as for

the fiducial resolution. The twisting behavior of the disk stays the same and does not seem to be strongly influenced by resolution.

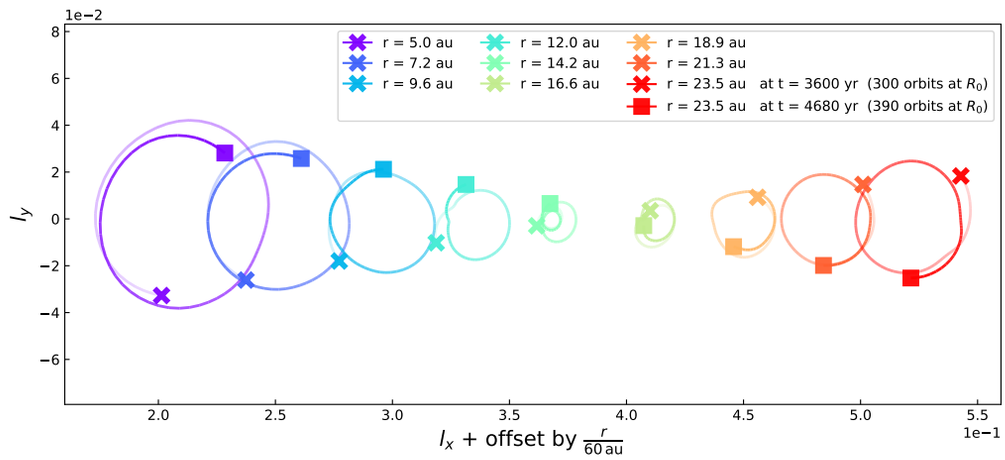

Figure 3.A.3: Twist of the disk in the high resolution simulation (like Figure 3.18, bottom panel).

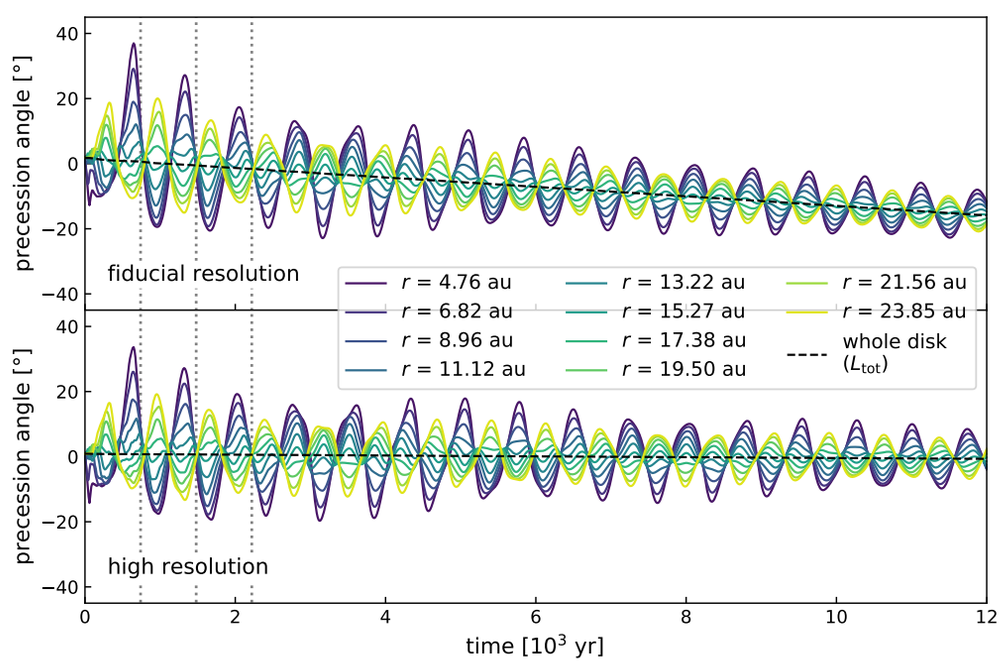

Figure 3.A.4: Precession angles for different radii (colored lines) in simulations with different resolutions. The black dashed line in each panel shows the precession angle of the angular momentum vector $\vec{L}_{\mathrm{tot}}$ of the whole disk. The grey dotted lines indicate precession periods of roughly 740 yr. Similar to Figure 3.23.

Figure 3.A.4 shows the evolution of the precession angles at different radii, as well as the overall precession of the disk in both the fiducial and high resolution simulations. The comparison clearly shows that the overall precession of the whole system (negative slope of the black dashed line for the fiducial resolution)

is an effect caused by numerical effects, as it does not decrease significantly in the high resolution simulation. The twisting motion, however, is very similar in both simulations, suggesting that it is not caused by numerical effects due to too low resolution. The estimated period of the twisting motion of roughly 740 yr (grey dotted lines) coincides with the fitted period of inclination evolution.

3.B Investigation the disk twist

In this section, we describe several tests we carried out to investigate whether the twist we found in the warped disk simulation is a numerical or a physical effect.

3.B.1 Outer boundary

We first performed another 3D simulation where the outer boundary is far away from the disk edge by applying an exponential cut-off to the density profile. In this case, the grid edge is unlikely to influence the simulation.

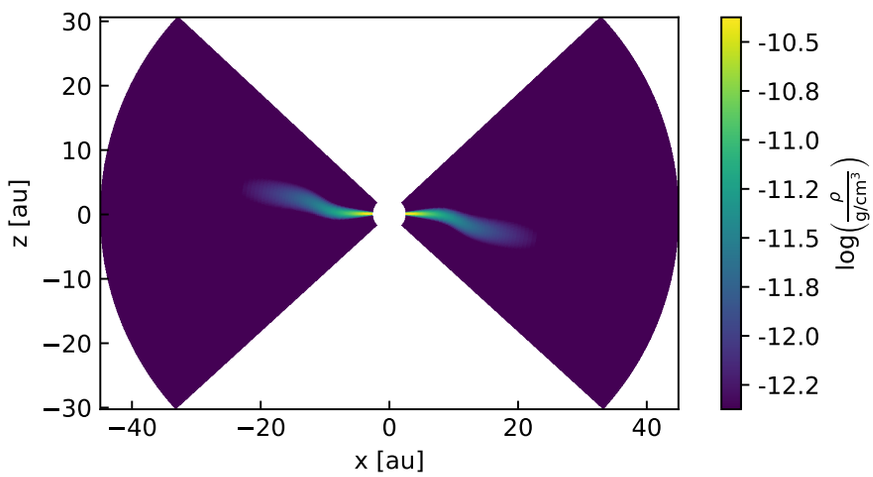

Figure 3.B.1: Set-up of a warped disk with the outer boundary further away from the physical disk edge.

Figure 3.B.1 shows the initial set-up of this simulation. We keep the same initial conditions as in the previous simulation of the warped disk, the only difference being the cut-off at $r = 26$ au in the density profile. As we enlarge the radial space of the grid, we keep the number of cells in the disk domain (within 26 au) the same.

Figure 3.B.2 shows that we also find twisting of the disk. However, the frequency is on a longer timescale than before. Evaluating the inclination evolution of the disk in this set-up, we find that it also takes place on longer timescales, namely, that the warp wave takes longer to travel through the disk. Again, the

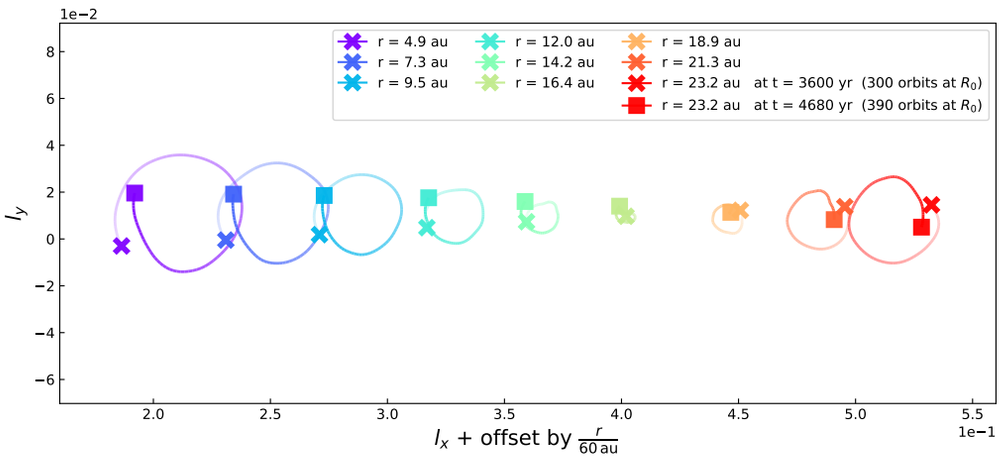

Figure 3.B.2: Twist of a disk with the outer boundary far away from the disk edge, like Figure 3.18, bottom panel.

timescale of the inclination wave corresponds with the timescale of the twist frequency. We find the reason for this to be the cut-off smoothing out on relatively short timescales, as shown in Figure 3.B.3. This leads to the disk being slightly larger, therefore, the timescale of the warp wave is longer. We suspect the reason for this to lie in our initial set-up of the azimuthal velocity, as the smooth-out occurs very quickly. In future work, this could be improved by accounting for the density gradients in the initial set-up.

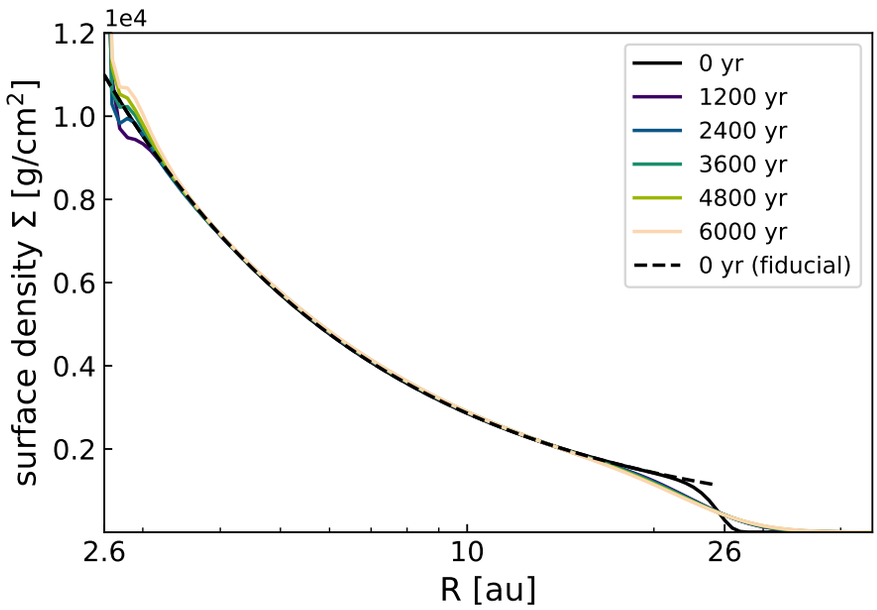

Figure 3.B.3: Surface density of a disk with the outer boundary far away from the disk edge (solid lines). The initial state of the fiducial simulation is plotted as reference (dashed line).

However, the outer boundary is still unlikely to influence the outer disk edge

in this simulation, because the density is very low outside of 26 au. The fact that the twisting persists is an indication that the twist results from a physical process in a warped disk.

3.B.2 1D models

To rule out the notion that the twist is an effect kicked off some time in the beginning of the 3D simulation, we investigated the behaviour of a twist in a 1D model. For this purpose, we take the twisted state at 308 orbits at R_0, which is $t = 3696$ yr and use it as initial condition for a 1D simulation using our code `dwarpy` (Kimmig et al., in prep).

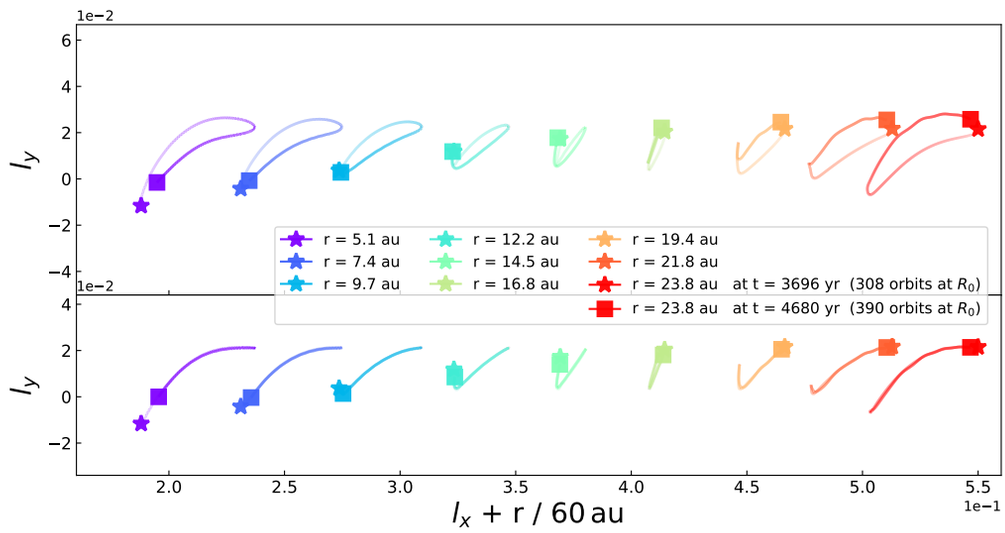

Figure 3.B.4: Evolution of the twisted state in a 1D simulation using `dwarpy` in two different simulations. The initial state of the warp in both simulations is taken from the twisted state in the 3D simulation at $t = 3696$ yr (308 orbits at R_0). The top panel shows the 1D simulation with internal torque $\vec{G}$ extracted from the 3D simulation, the bottom panel shows the same simulation, but internal torque $\vec{G}$ initially set to zero for comparison. Details comparable to Figure 3.18 (bottom panel).

We performed two simulations using this state of the warp. In the first simulation, we used the internal torque extracted from the 3D simulation (see Appendix 3.C). To evaluate the difference it makes, we performed another simulation setting the internal torque values initially to zero and let the 1D equations take care of its evolution. The first case (with extracted internal torque) is shown in Figure 3.B.4, top panel, the latter case (internal torque set to zero) in the bottom panel. In both panels, the stars show the initial state of the unit angular momentum vectors (same as the grey stars in the bottom panel of Figure 3.18). The squares show the state at the end of our simulation time span, which we

chose to be the same as plotted in Figure 3.18.

We find that the 1D model fails to recreate the circular motion of the unit angular momentum vectors. The simulation with the initial torque set to zero (bottom panel of Figure 3.18) shows no circular motion at all, while the simulation with internal torque extracted from the 3D simulations shows deformed ellipses. The latter is the more self-consistent one, which shows a hint of the circular twist motion, but cannot reproduce the full twist seen in the 3D simulation.

From this, we can say that the twisting of the disk seems to be a 3D effect that is not captured in the 1D equations. It might be an effect traced by linear or non-linear terms that were neglected in deriving the equations. We can conclude here that the twist is an effect triggered continuously in the 3D simulation, as opposed to an event kicked-off once.

3.B.3 Keplerianity of the warped disk

In 1D models, an untwisted and perfectly Keplerian disk will not twist. However, if the disk deviates from Keplerianity, a twist can be triggered (second term on left hand side of Equation 3.3). We therefore took a closer look at the azimuthal velocity of the warped disk in the 3D model. Because the orbital plane does not always align with the grid plane, the evaluation of the azimuthal velocity is not straight forward: we need to perform an interpolation. For the interpolation, we use the unit angular momentum vector determining the orbital plane of each grid shell and use the `LinearNDInterpolator` function from `scipy` (Virtanen et al., 2020). This way, we can extract the azimuthal velocity of the disk midplane in each grid shell.

Figure 3.B.5 shows that the azimuthal velocity of the disk deviates from the Kepler velocity as we set up the disk with pressure correction terms. During the simulation, we do not observe strong deviations from our initial set-up, except at the inner and outer boundaries, which means that the warp does not significantly change the azimuthal velocity. The deviation from Keplerian motion results from pressure correction in the initial set-up of the disk. Because the deviation is small, we do not expect this to be the sole reason for the twist. In a future work, this could be investigated using 1D models with an adjusted apsidal frequency.

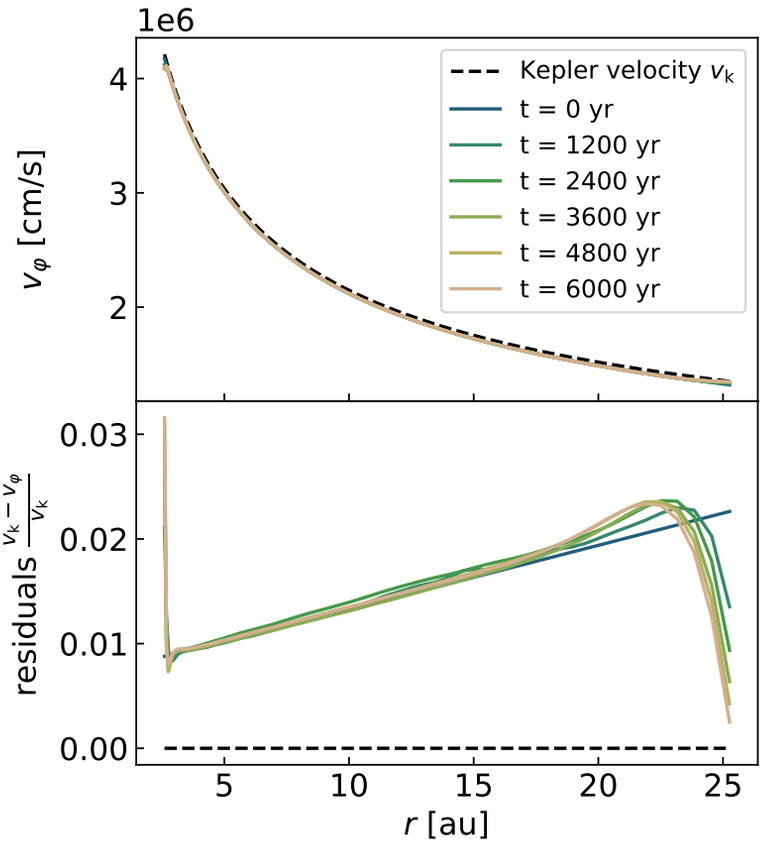

Figure 3.B.5: Azimuthal velocity (top panel) and the residuals from the Kepler velocity (bottom panel). The black dashed line shows the Kepler velocity.

3.B.4 Twist of a differently flared disk

In this section, we investigate the twist behavior of a locally isothermal disk with a flaring index of $i_{\mathrm{fl}} = 0.25$, as described in Section 3.4.3.

Figure 3.B.6 shows the evolution of the unit angular momentum vectors. The top row indicates the time evolution of the vectors. We clearly see that a twist develops in the disk. However, the behavior looks more complicated than in the globally isothermal case (see Figure 3.18). We find that instead of circles, the precession motion takes on an oval or crescent shape, whose orientation also precesses. In the bottom panel, we plot the same time period as plotted in Figure 3.18 in order to see the oval shape of the twisting motion more clearly.

We additionally checked the evolution of the total angular momentum vector in the locally isothermal case. Just like in the globally isothermal case, we find very little loss of absolute value (0.67% within 2.4×10^4 yr) and a slight change in direction (4.2° within 2.4×10^4 yr), which we suspect to occur due to the non-conservative nature of the code for out-of-plane features. Most importantly, we also do not see any precession behavior of the total angular momentum vector,

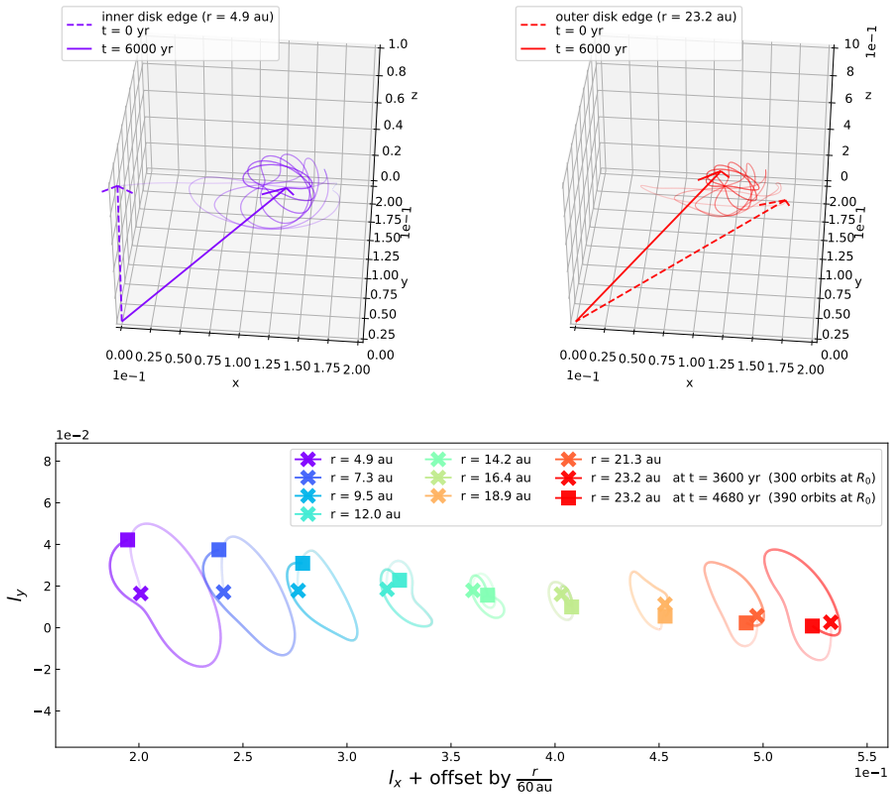

Figure 3.B.6: Twist motion in the locally isothermal disk. **Top:** Unit angular momentum vectors close to the inner (left panel) and outer (right panel) edge of the disk for the first $t = 6000\,\mathrm{yr}$. **Bottom:** x-y-components of the unit angular momentum vector for the time period between 300-390 orbits at R_0 at varying radii, plotted with an offset of $r/(60\,\mathrm{au})$ in y-direction to disentangle the twist at different radii. The x-markers show the beginning of the plotted time, the squares the end. Similar to Figure 3.18.

which means that the twist in the locally isothermal case is also conserving the total angular momentum within the disk.

We take the fact that a twist also occurs in a differently flared disk as another indication that this effect might be physical. In further work, the influence of the vertical disk structure on the warp and twist behavior could be investigated in more detail.

3.C Internal torques in the 3D model

From the 3D simulation of the disk we can, at any given time t, compute the internal torques. We have the variables $\rho(r,\theta,\phi)$ for density, $u_r(r,\theta,\phi)$, $u_\theta(r,\theta,\phi)$, $u_\phi(r,\theta,\phi)$ for the velocities and the isothermal sound speed $c_s(r)$ at our disposal. The velocity components u_ϕ and u_θ contain the Kepler rotation as well. To make the task of computing the internal torque easier, we re-express the velocity in terms of cartesian coordinates X, Y and Z:

$$\begin{pmatrix} u_X \\ u_Y \\ u_Z \end{pmatrix} = \begin{pmatrix} \sin(\theta)\cos(\phi) & \cos(\theta)\cos(\phi) & -\sin(\phi) \\ \sin(\theta)\sin(\phi) & \cos(\theta)\sin(\phi) & \cos(\phi) \\ \cos(\theta) & -\sin(\theta) & 0 \end{pmatrix} \begin{pmatrix} u_r \\ u_\theta \\ u_\phi \end{pmatrix}. \tag{3.14}$$

From this point onward, we will keep the spherical coordinate system (r,θ,ϕ) and the corresponding spherical grid, but express all vector and tensor components in a vector basis tangent to the global cartesian coordinates (X,Y,Z). At any given point (r,θ,ϕ) in our model we can then define the stress tensor:

$$T_{ij} = \rho u_i u_j + p\delta_{ij}, \tag{3.15}$$

where we use the pressure $p = \rho c_s^2$, the Kronecker-delta δ_{ij}, and where we ignore viscosity. Here the indices i and j denote the X, Y or Z direction. We can now compute the local internal torque tensor at every point in our 3D model:

$$g_{ij} = \varepsilon_{ikl} r_k T_{lj} \tag{3.16}$$

(cf. Equation 110 of DKZ22, but now in the global cartesian basis), where ε_{ikl} is the Levi-Civita tensor, and where we use Einstein's summation convention. The symbol r_k is the position vector pointing from the origin (i.e., the star) to the location in the 3D model where we compute g_{ij}. Next we compute the internal torque vector, which is the radial component of this tensor:

$$g_i = g_{ij} r_j / |r| \tag{3.17}$$

(cf. Equations 111-113 of DKZ22), where $|r|$ denotes the length of the position vector r_j. In contrast to DKZ22, we here use the spherically outward component rather than the cylindrically outward component, because in our 3D model we consider the warped disk as a series of spherical shells that mutually exert torques on each other. The differences are, however, marginal.

The local torque vector $g_i(r,\theta,\phi)$ is still a function of all three coordinates. For

the 1D warped disk equations, to which we want to compare our 3D model, we need to compute, at each radius r, the integral of this quantity over the sphere with radius r:

$$G_i(r) = \frac{r}{2\pi} \int_{-\pi}^{\pi} d\phi \int_{-1}^{+1} d\cos(\theta)\, g_i(r, \theta, \phi). \tag{3.18}$$

This is the internal torque vector that we can compare to the internal torque from a 1D warped disk model (e.g., Equation 173 of DKZ22). In Figure 3.C.1 we show these torques in units of $g_0 = \Omega^2 r \Sigma h_p^2$ (see Equation 126 of DKZ22). The results show that the $G_X(r)$ of the 3D and 1D models match well. This is the torque that is primarily responsible for the wavelike propagation of the warp. The torque G_Y is the torque that produces a twist. In the 1D model this is perfectly 0, while in the 3D model it is small, but non-zero. The G_Z torque component in the 3D model is of the same order of magnitude as G_Y, and is rather wiggly. Also in the 1D model it is not perfectly zero, which is due to the fact that the disk is not perfectly aligned with the equatorial $X - Y$ plane.

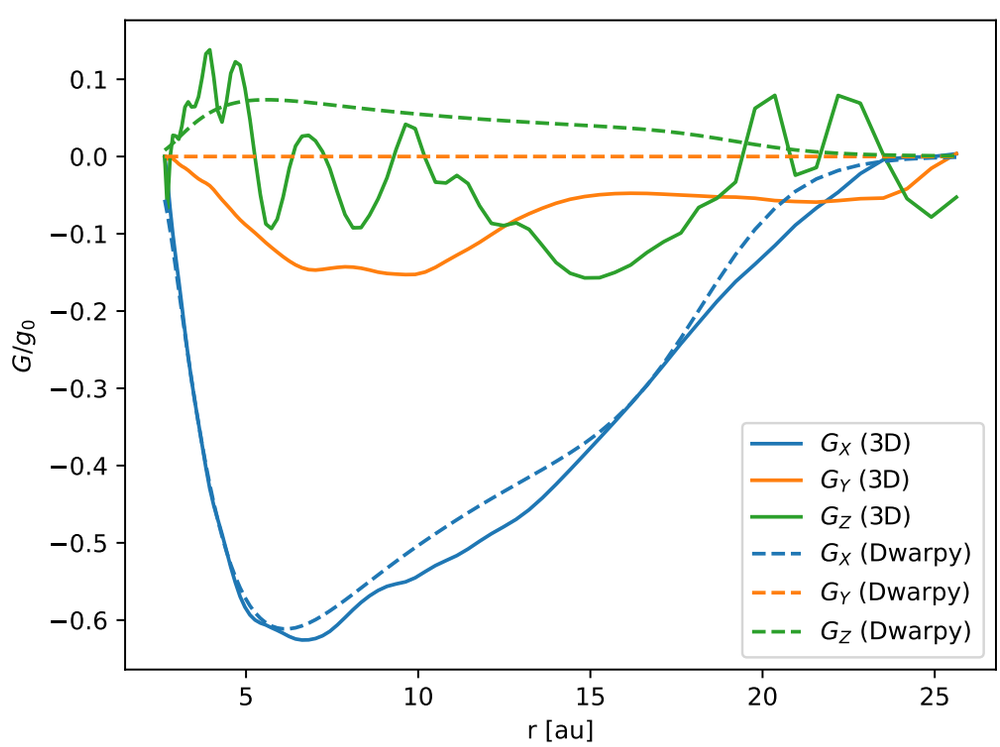

Figure 3.C.1: Internal torques G_x, G_Y and G_Z at time $t = 120\,\mathrm{yr}$ in units of $g_0 = \Omega^2 r \Sigma h_p^2$. Solid lines: From the 3D model. Dashed lines: From the 1D model `dwarpy`.

3.D Extracting V_r, V_ϕ, and V_z from the 3D model

As shown in DKZ22, and following Ogilvie & Latter (2013a), the sloshing motion can be approximated as a linear velocity model

$$v_r = V_r \Omega z, \quad v_\phi = V_\phi \Omega z, \quad v_z = V_z \Omega z, \tag{3.19}$$

where $v_z = -v_\theta$ by convention. In reality, the functions $v_r(z)$, $v_\phi(z)$, and $v_z(z)$ are only approximately linear in z close to the midplane, but strongly deviate from linearity far away from the midplane, as shown for example in Figure 3.26. However, usually the strongest deviation occur well above one scale height, while the strongest effect on the disk dynamics is where the density is the highest. A good estimate of V for a velocity $v(z)$ is:

$$V(r,\phi) = \frac{1}{\Sigma H_p^2 \Omega} \int_{-\infty}^{+\infty} \rho(r,\phi,z) v(r,\phi,z) z dz. \tag{3.20}$$

The $V_r(r,\phi)$ is the key component determining the torque. For each r, it can be well approximated by:

$$V_r(r,\phi) = V_{r0}(r) \cos(\phi - \phi_{r0}(r)), \tag{3.21}$$

where $V_{r0}(r)$ is the amplitude of the sloshing motion, and $\phi_{r0}(r)$ is the phase shift. As shown in DKZ22, for a Keplerian disk in the wavelike regime, the phase shift, at least in the linear theory, is expected to be $\phi_{r0}(r) = 0$ if the warp vector is pointing in the $\phi = 0$ direction. In that case, the warp evolution is entirely along that same direction, and the disk does not acquire a twist. However, if $\phi_{r0}(r) \neq 0$, the disk will acquire a twist, in addition to the wavelike propagation of the warp itself.

From the 3D flattened model we can determine $V_{r0}(r)$ and $\phi_{r0}(r)$ in the following way: First consider, for each given radius, r,

$$V_r(\phi) = A \cos(\phi) + B \sin(\phi). \tag{3.22}$$

We now compute A and B as:

$$A = \int_{-\pi}^{+\pi} V_r(\phi) \cos(\phi) d\phi, \quad B = \int_{-\pi}^{+\pi} V_r(\phi) \sin(\phi) d\phi, \tag{3.23}$$

then

$$V_{r0}(r) = \sqrt{A^2 + B^2}, \quad \phi_{r0}(r) = \tan^{-1}(B/A). \tag{3.24}$$

4

Modeling a stellar fly-by warping the disk around RW Aur A

This chapter will be published in future in a paper by Kimmig, Weber, Rosotti, Facchini, Dullemond, in prep. All simulations presented in this chapter are performed by me. I analyzed the data and created all figures. The text is also written by me. The co-authors provided valuable contributions through comments and discussions.

4.1 Background

Most stars are not born in isolated environments. Usually, they form in large star-forming regions, often in clusters of many thousand stars (Draine, 2011; Krause et al., 2020). Observations show that these star-forming regions are highly dynamic with significant relative velocities between stars (Karnath et al., 2019; Kuhn et al., 2019; Yang et al., 2025). Thus, young stars are likely to encounter other young stars.

As young stars commonly host planet-forming disks, the interactions in a stellar cluster can affect the disk shape and morphology, and in turn influence the process of planet formation. For example, irradiation from nearby stars can cause photoevaporation (Winter & Haworth, 2022), which can influence the disk evolution (e.g., Clarke, 2007; Facchini et al., 2016a; Winter et al., 2018; Keyte & Haworth, 2025; Planet formation environments collaboration et al., 2025). Jets can replenish the interstellar material in these environments, which affects nearby disks accreting this material, for example through streamers (Pineda et al., 2020; Codella et al., 2024; Cacciapuoti et al., 2024).

Furthermore, gravitational interactions in the star-forming region can have a strong impact on the morphology of disks. Numerical simulations found that close encounters with other stars are quite common in star-forming regions (see

e.g. Bate, 2018; Lebreuilly et al., 2021; Rawiraswattana & Goodwin, 2023; Lebreuilly et al., 2024). Pfalzner (2013) argues that there are convincing indications that the early Solar System was shaped by a close encounter (see also Pfalzner & Vincke, 2020), highlighting the importance of these events. Pfalzner (2013) further investigates the statistics of encounters in numerical simulations of solar system birth clusters, where encounters are likely in the first few million years of the cluster's evolutionary stage. Close encounters appear to be equally likely both in high- and low-mass star clusters (Pfalzner & Govind, 2021). The dynamics within these clusters can also lead to multi-star systems (Offner et al., 2023).

Close encounters can occur on both bound and unbound orbits, where the latter is commonly referred to as *stellar fly-bys*. A commonly used definition of a fly-by is an unbound close encounter of two stars with a separation of less than 1000 au (Cuello et al., 2023). The occurrence rate of fly-bys is highest while the objects are still spatially confined to their star-forming region. Therefore, it is likely that at least one of the stars holds a disk when the fly-by occurs. The probability of which disk-hosting stars experience such close gravitational interactions with other stars in their lifetime depends on the stellar density in the star-forming region and can be as high as 70% for stellar densities of at least $500\,\mathrm{pc}^{-3}$ (Winter et al., 2018, see their Fig. 7). Cuello et al. (2023) conclude in their review, that more than half of young stars hosting a disk experience a fly-by with a separation of less than 1000 au.

Stellar fly-bys can have a significant impact on the dynamics and shape of disks around either or both of the fly-by components. One of the first numerical studies of the effect of fly-bys on circumstellar disks was performed by Clarke & Pringle (1993), and the topic has been investigated extensively since. These effects include spiral arms due to tidal perturbations (Ostriker, 1994; Pfalzner, 2003; Cuello et al., 2019; Smallwood et al., 2023), truncation of disk sizes (Breslau et al., 2014; Rosotti et al., 2014; Muñoz et al., 2015; Vincke et al., 2015; Bhandare et al., 2016), ejection and capture of disk material by the fly-by object (Heller, 1995; Jílková et al., 2016; Cuello et al., 2019, 2020; Smallwood et al., 2024), and misalignment and warping of disks (Terquem & Bertout, 1993; Picogna & Marzari, 2014; Xiang-Gruess, 2016; Nealon et al., 2020a). As circumstellar disks are the formation sites of planets, stellar fly-bys can have strong implications on the architecture of planetary systems (Kobayashi & Ida, 2001; Fragner & Nelson, 2009; Thies et al., 2010; Breslau & Pfalzner, 2019; Cuello et al., 2019; Aly & Lodato, 2020; Aly et al., 2021; Longarini et al., 2021).

The resulting shape of the disk depends on the geometry of the fly-by orbit with respect to the disk. Fly-by trajectories are typically classified as either prograde, retrograde, or polar, depening on the direction of the angular momentum

vectors of the orbit and the disk. For prograde fly-bys, both vectors are in the same hemisphere and in retrograde fly-bys in opposite hemispheres. Mutual orientations of these vectors close to 90° are called polar. Prograde orbits are found to be most disruptive (Clarke & Pringle, 1993; Xiang-Gruess, 2016; Winter et al., 2018). In these cases, the spirals caused by the tidal torques are strongest, and the truncation of disks is most effective. For example, Bhandare et al. (2016) find for retrograde orientations that disk sizes after truncation can be twice as large as for prograde fly-bys. A characteristic signature of these retrograde non-coplanar fly-bys is a warp due to the misaligned gravitational torque (Terquem & Bertout, 1993; Xiang-Gruess, 2016; Nealon et al., 2020a; Cuello et al., 2023), although disks can also become warped in inclined prograde fly-bys (see e.g. Larwood, 1997).

Warps in protoplanetary disks have gained importance throughout the recent years, as more and more observations reveal indications that a significant fraction of disks is warped (Ansdell et al., 2020; Kluska et al., 2020; Bohn et al., 2022; Garufi et al., 2022; Benisty et al., 2023). For example, non-axisymmetric shadows can hint at a misaligned inner region of the disk that blocks the light from the star (Marino et al., 2015; Benisty et al., 2017; Debes et al., 2017; Stolker et al., 2017; Muro-Arena et al., 2020; Villenave et al., 2024; Zurlo et al., 2024, and many more). Indications for warps can also be found in kinematic observations (Walsh et al. 2017; Mayama et al. 2018; Phuong et al. 2020; Garg et al. 2021; see also Pinte et al. 2023 for a review).

An inclined stellar fly-by is not the only possible cause for a warped disk. Alternative formation scenarios include misaligned infall of material onto the disk (Thies et al., 2011; Dullemond et al., 2019; Kuffmeier et al., 2021, 2024), misaligned magnetic fields with respect to the disk plane (Foucart & Lai, 2011; Romanova et al., 2021), radiation-induced warping (Pringle, 1996; Maloney et al., 1996; Armitage & Pringle, 1997), misaligned binaries (Facchini et al., 2013, 2014; Foucart & Lai, 2013; Lodato & Facchini, 2013; Deng & Ogilvie, 2022; Rabago et al., 2024), or outer bound companions such as stars or planets (Papaloizou & Lin, 1995; Nealon et al., 2018; Zanazzi & Lai, 2018c; Zhu, 2019).

The evolution of the warp shape after the initial perturbation is controlled by internal torques. These torques arise from pressure gradients and resonant motions that form due to the mutual misalignment of radially adjacent orbits (Ogilvie & Latter, 2013a,b; Dullemond et al., 2022a). In typical conditions of protoplanetary disks, namely thick disks with low viscosity, the warp travels in a wave through the disk (Papaloizou & Lin, 1995; Lubow & Ogilvie, 2000; Nixon & King, 2016; Martin et al., 2019; Kimmig & Dullemond, 2024).

Disk warping as a result of stellar fly-bys is still not fully understood. This is partly because the fly-bys have a large variety of dynamical effects and numer-

ical investigations often focus on other aspects (e.g., Xiang-Gruess (2016) focus on the resulting mean inclination of the disk, Nealon et al. (2020a) focus on misaligning a broken disk with a gap-carving planet, Smallwood et al. (2023) focus on the morphology of the tidal spiral arms). Cuello et al. (2019) studied all effects in both gas and dust extensively, including warping and twisting. However, they do not evaluate the evolution of the warp profile in detail, as they focus mainly on a single snapshot at 2700 yr after the fly-by (see their Fig. 13). Additionally, most numerical studies investigate the effects of fly-bys utilizing Smothed Particle Hydrodynamics (SPH) simulations (see Picogna & Marzari, 2014; Xiang-Gruess, 2016; Cuello et al., 2019; Ménard et al., 2020; Nealon et al., 2020a, etc.), because these simulations do not rely on a specific geometry for the discretization. However, SPH methods usually need to include an artificial viscosity which is often higher than the physical viscosities found in protoplanetary disks (for example by Villenave et al., 2024).

With the recent development to investigate warps in grid-based simulations (Rabago et al., 2023, 2024; Kimmig & Dullemond, 2024), we take the opportunity in this work to focus on the effect of stellar fly-bys in low-viscosity disks. Furthermore, stellar fly-bys provide an ideal laboratory for investigating the evolution of warps. This is because fly-bys create a physically motivated warp shape instead of a parametrized assumption, but only distort the disk once due to their unbound nature. The subsequent warp evolution is then governed by internal processes in the disk, without the influence of external torques.

As an additional motivation for our work, we aim to explore different orientations of trajectories with respect to the disk plane. Recent studies mainly investigate orientations where the trajectory is inclined in such a way that the periastron remains in the same plane as the disk (Cuello et al., 2019; Nealon et al., 2020a; Cuello et al., 2023). This is likely motivated by the fact that Xiang-Gruess (2016) found that for the final mean tilt of the disk, the inclination of the trajectory with respect to the disk is more relevant than the relative position of the periastron. However, the radial inclination *profile* might strongly be affected by the position of the periastron. In young stellar clusters, there is no physical constraint that the periastron should be in the same plane as the disk. In fact, a scenario with the periastron outside the disk plane should be statistically more likely. In the first part of this work, we therefore revisit a limited set of disk-orbit orientations in order to compare the effects on the warping of the disk.

In the second part of this work, we aspire to create links between our numerical models and observations. Observationally, ongoing stellar fly-bys are suspected in quite a few systems, for example in SR 24 (Mayama et al., 2010, 2020; Fernández-López et al., 2017), FU Ori (Takami et al., 2018; Pérez et al., 2020;

Borchert et al., 2022), Z CMa (Dong et al., 2022), UX Tau (Ménard et al., 2020; Zapata et al., 2020), AS 205 (Kurtovic et al., 2018; Weber et al., 2023), and more (see Tab. 1 and Fig. 6 in Cuello et al., 2023). Because a general investigation of observational signatures of fly-bys requires a large parameter space of disk orientations with respect to the observer (which would go beyond the scope of this work), we decided to apply our models to a specific observed system: RW Aur (Ghez et al., 1993).

The RW Aur system is a two-star system, where stars host a disk (Cabrit et al., 2006; Rodriguez et al., 2018; Long et al., 2019; Kurtovic et al., 2024). The system has a distance to the Solar System of 156.1 pc (Gaia Collaboration et al., 2023). Initial mass estimates for the stars by Ghez et al. (1997) and Woitas et al. (2001) found $1.3 - 1.4\,M_\odot$ for star A and $0.7 - 0.9\,M_\odot$ for star B. Fitting Keplerian rotation to the disks' velocity profile, Kurtovic et al. (2024, hereafter Kur24) inferred similar, but slightly different masses of $M_\mathrm{A} = 1.238\,M_\odot$ and $M_\mathrm{B} = 0.995\,M_\odot$. The projected separation between the two stars is about 233 au.

Kur24 present ALMA dust continuum observations with high angular resolution of the two disks around A and B. For the geometry of the disks, they perform MCMC fitting and find disk inclinations of $i_\mathrm{A} = 55°$ and $i_\mathrm{B} = 64°$. Both disks have a position angle of about $\mathrm{PA_B} = 39.5°$, which means that the mutual inclination can be easily determined from the difference of inclinations to be about 9°.

In their analysis of the observations, Kur24 find indications of a warp in the disk around RW Aur A, as they find a peculiar pattern in the residuals between the observations and a planar (unwarped) parametric model. Kur24 are able to minimize the residuals with a model including a misaligned inner disk[1] of 3 au with an inclination of $i_\mathrm{A,inn} = 60.8°$ and a position angle of $\mathrm{PA_{A,inn}} = 35.5°$. This results in a misalignment between inner and outer disk of roughly 6°. A warp in RW Aur A was even suspected prior to this study (Bozhinova et al., 2016; Facchini et al., 2016b), as observations suggested a mismatch between the inclination of the inner and outer disks (inner disk: 77° by Eisner et al. 2007, $> 60°$ by McJunkin et al. 2013; outer disk: $45° - 60°$ by Woitas et al. 2001 and Rodriguez et al. 2013).

Radio observations of CO gas in the system additionally reveal a large-scale structure connecting the two stars (Cabrit et al., 2006) and a chaotic environment (Rodriguez et al., 2018, Kur24). Cabrit et al. (2006) proposed this large-scale structure to be a tidal arm caused by a recent close encounter of star B with the disk around star A, which has later been supported by hydrodynamical simulations

[1] Kur24 fit both the inner and outer disk freely. However, the outer disk inclination and position angle remain almost the same as for their original MCMC fitting.

(Dai et al., 2015).

Kur24 performed a detailed orbital fitting using astrometric data from different epochs and find an eccentricity close to $e \approx 1$, which could either be a highly eccentric bound orbit or a close-to-parabolic unbound orbit. The good observational constraints on the orbit provide a great framework for hydrodynamical simulations of the system. In the orbital analysis by Kur24, bound orbits are slightly favored, which is also proposed by Rodriguez et al. (2018) as explanation for the chaotic environment. However, Cuello et al. (2023) argue that the effect on the disk is similar for highly eccentric binaries and parabolic fly-bys. The difference lies in the repetition of the encounter in the bound case, which can potentially lead to a different disk morphology. However, for our purposes, it is reasonable to assume an unbound parabolic fly-by. We will discuss the orbit geometry in Section 4.4.1.

In our work, we describe our numerical setup in Section 4.2, present the results of our hydrodynamical investigations of different disk-orbit configurations in Section 4.3, and focus on models of the RW Aur system including synthetic observations in Section 4.4. In Section 4.5, we discuss our models and summarize and conclude our work in Section 4.6.

4.2 Numerical method

4.2.1 Hydrodynamic simulations

Fly-bys that are inclined with respect to the disk can pull the disk out of plane, creating a warp. To investigate the dynamical effect of fly-bys on low-viscosity disks, we perform three-dimensional hydrodynamic simulations using the grid-based code FARGO3D (Benítez-Llambay & Masset, 2016), where we include a gravitational perturber on a parabolic orbit. The trajectory of the orbit is modeled with the FARGO orbital advection algorithm (Masset, 2000). We run gas-only simulations and do not make use of the multi-fluid or magnetohydrodynamic features of the code. The capability of the code to model warps and disk planes inclined with respect to the grid geometry was extensively tested in Kimmig & Dullemond (2024).

For the grid to simulate the disk, we use spherical coordinates. Radially, the grid extends from 2.6 au to 41.6 au with 120 logarithmically spaced grid cells. We set the resolution in the azimuthal direction to 100 cells. Vertically, we cap off the poles in order to save computation time and include a range of $\theta_{\mathrm{min}} = 44.2^{\circ}$ to $\theta_{\mathrm{max}} = 135.8^{\circ}$ with 256 vertical grid cells.

We set up an initially planar (unwarped) disk, which is aligned with the grid

midplane. Because we want the outer boundary to have as little influence as possible, we taper the disk such that the computational domain extents farther out than the disk. We therefore adopt for the initial surface density Σ profile

$$\Sigma(r) = \Sigma_0 \left[1 + \exp\left(\frac{r - r_{\rm out}}{0.05 r_{\rm out}}\right)\right]^{-1} \left[1 + \exp\left(\frac{r_{\rm in} - r}{0.05 r_{\rm in}}\right)\right]^{-1}, \tag{4.1}$$

where Σ_0 is the surface density at the reference radius r_0, for which we use $r_0 = 5.2\,\mathrm{au}$. The equation includes exponential cut-offs at both disk edges, where $r_{\rm in}$ and $r_{\rm out}$ are the inner and outer edge of the disk, respectively. To vertically expand the surface density, we use the default setup of the example `p3disof` from FARGO3D.

We assume a locally isothermal model, where we set the temperature structure so that the aspect ratio h takes the form

$$h(r) = h_0 \left(\frac{r}{r_0}\right)^{i_{\rm fl}}, \tag{4.2}$$

with h_0 being the aspect ratio at r_0 and the flaring index $i_{\rm fl}$. For all our models, we use the values $h_0 = 0.05$ and $i_{\rm fl} = 0.25$. The initial azimuthal velocity is set to the Keplerian velocity with a correction for pressure gradients, as described in Appendix 4.A.

In all simulations, we adopt outflow boundaries for the radial direction, where we allow mass to leave the grid domain, but not to enter. This means that the radial velocity is copied from the active domain edge to the ghost cells if positive, but forced to zero if negative. This helps to avoid unphysical influx of gas, which has sometimes been found to occur in fly-by scenarios especially at the inner boundary. We additionally make use of the wave-killing implementation in FARGO3D based on de Val-Borro et al. (2006) and use a width of 10% of the edge radius for our damping zones. Vertically, we set reflective boundaries and azimuthally periodic conditions.

We set the grid origin to the central star hosting the disk. Therefore, we need to account for non-inertial motion of the reference frame due to the fly-by. This is taken care of with the build-in indirect term in FARGO3D. However, we do not treat any non-inertial effects imposed by a possible acceleration from the disk onto the star, for example due to asymmetries in the disk.

Excursion: hyperbolic trajectories

This section provides a reminder on the parameters to describe unbound orbits (hyperbolae) and an overview over the implementation of the initial position and velocity of the star on the fly-by trajectory, called perturber from here on, in our simulations.

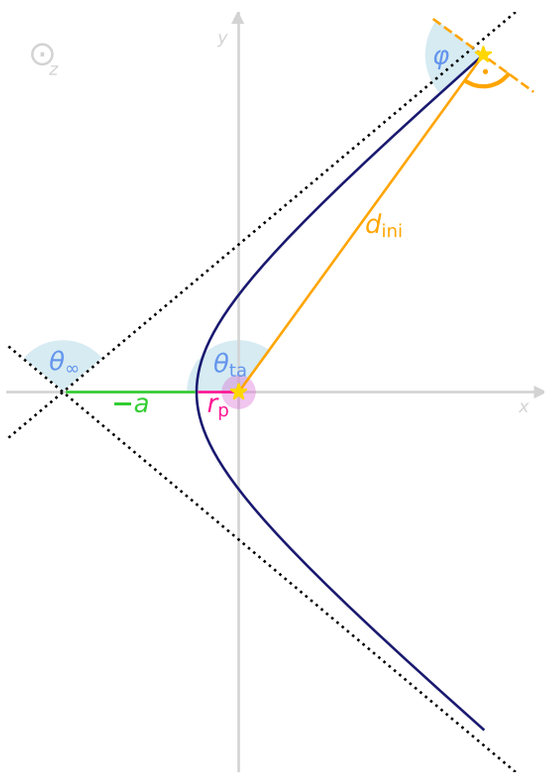

Figure 4.1: Schematics of a hyperbolic trajectory (dark blue line) for a coplanar fly-by viewed from above. The host star with a disk (indicated by the purple circle) is placed at the origin of the coordinate system. Black dotted lines indicate the asymptotes.

The eccentricity of hyperbolic orbits is $e \geq 1$. Orbits with $e = 1$ are called *parabolic*. The eccentricity is related to the external angle between the asymptotes θ_∞ with $e = -1/\cos(\theta_\infty)$. The distance between the periastron (also called periapsis) to the focal point is typically denoted with r_{p}. In the scenario of a fly-by, this distance is often referred to as the distance of closest approach. When eccentricity and the distance of closest approach are given, the semi-major and -minor axes can be calculated as

$$a = -\frac{r_{\mathrm{p}}}{(e-1)} b = -a\sqrt{e^2 - 1}. \tag{4.3}$$

Here, the semi-major axis a is negatively defined, as indicated in Figure 4.1. The

hyperbolic trajectory can be expressed in the form

$$r = \frac{l}{1 - e\ \cos(\theta_{\text{ta}})}, \tag{4.4}$$

where $l = -b^2/a$ is the semi-latus rectum and θ_{ta} is the true anomaly, an angular parameter indicating the current position of the object along the trajectory.

FARGO3D takes the initial position and velocity vector as the fly-by object as input and integrates the trajectory using a fifth-order Runge-Kutta N-body solver. We therefore need to calculate these quantities from the parameters of the hyperbola. For that, we fix the initial distance d_{ini} between the perturber and the disk hosting star (indicated in Figure 4.1).

From this initial distance, we can calculate the initial true anomaly using the hyperbolic trajectory equation

$$\theta_{\text{ta,ini}} = \arccos\left(-\frac{1}{e}\left[\frac{b^2}{a\ d_{\text{ini}}} + 1\right]\right). \tag{4.5}$$

For a coplanar fly-by, the plane of the trajectory coincides with the plane of the disk, which lies in the x-y-plane in our setup. In this case, the initial position can be calculated from the true anomaly with

$$x = -\cos(\theta_{\text{ta}})\ d_{\text{ini}}, y = \sin(\theta_{\text{ta}})\ d_{\text{ini}}, z = 0. \tag{4.6}$$

The velocity vector at the initial position can be calculated as

The initial velocity vector can be determined with the flight path angle φ

$$\tan(\varphi) = \frac{e\ \sin(\theta_{\text{ta}})}{1 + e\ \cos(\theta_{\text{ta}})}, \tag{4.7}$$

leading to the velocity components

$$\begin{aligned} v_x &= -v_{\text{abs}} \cos\left(\varphi - \theta_{\text{ta}} + \pi/2\right) \\ v_y &= -v_{\text{abs}} \sin\left(\varphi - \theta_{\text{ta}} + \pi/2\right) \\ v_z &= 0, \end{aligned} \tag{4.8}$$

where v_{abs} is the absolute value of the velocity. The absolute value can be calculated using the vis-viva equation

$$v_{\text{abs}} = \sqrt{\mu\left(\frac{2}{d_{\text{ini}}} - \frac{1}{a}\right)}, \tag{4.9}$$

where $\mu = GM_{\text{tot}}$ is the standard gravitational parameter with M_{tot} as sum of the

mass of the fly-by object and the mass of the host star.

Inclined fly-by trajectories can then be achieved by rotating the original in-plane hyperbola according to the orbital elements described in the next section.

To test the configuration of the trajectory, we performed a couple of test simulations with different trajectory configurations. Because we were mainly interested in the fly-by trajectory in these tests, we set the disk resolution very low, which speeds up the computation time. This is reasonable, as the N-body integrator of FARGO3D does not depend on the grid resolution for the disk. The resulting trajectory from FARGO3D perfectly matches the analytical solution of the hyperbola in all our test cases, which confirms that our implementation of the initial position and velocity works correctly.

4.2.2 Fly-by geometry

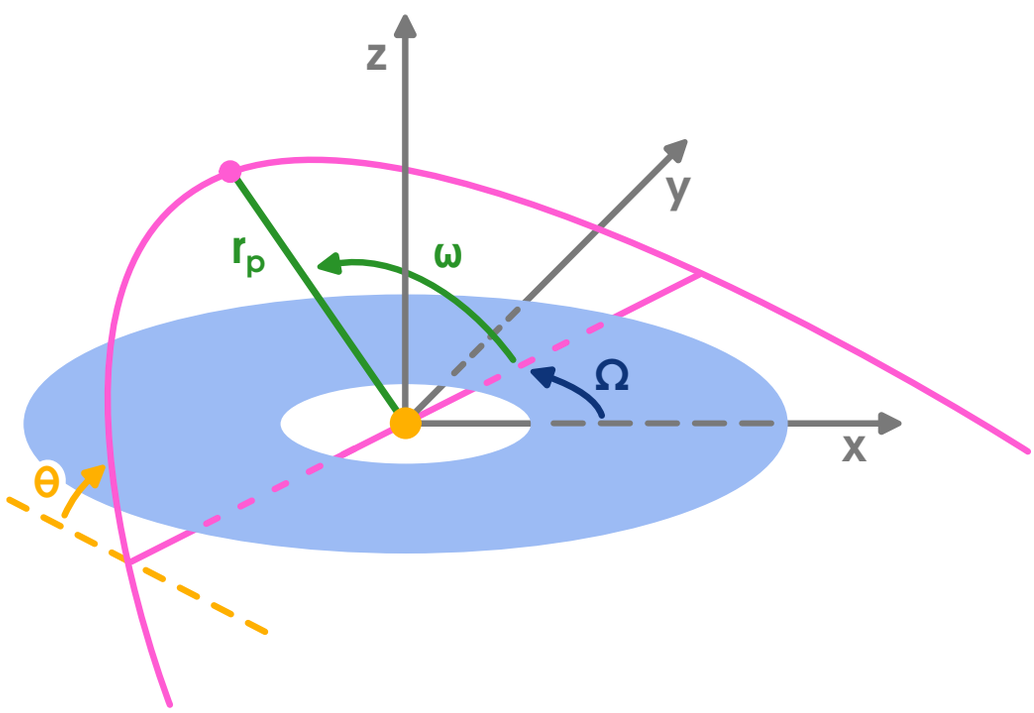

Figure 4.2: Schematics of the definition for the geometry of the fly-by trajectory with respect to the disk plane. Indicated are the inclination of the trajectory θ, the longitude of ascending node Ω, and the argument of periapsis ω. The distance of the closest approach, i.e. the periapsis, is r_p.

For the trajectory of the fly-by with respect to the disk, we define the x-y-plane to coincide with the initial disk midplane. A convenient way to describe the trajectory orientation are the orbital elements, which are the three angles indicated

in Figure 4.2. We call the inclination between trajectory and disk plane θ. The longitude of ascending node Ω is the angle between the x-axis and the intersection line between the plane of the trajectory within the x-y-plane, and the argument of periapsis ω is the angle between the intersection line and the connecting line of origin to periapsis. We note that physically, the longitude of ascending node Ω does not make a difference in our simulations, as the disk is initially axisymmetric, which means that the setup would lead to the same result for different Ω, only rotated.

4.3 Parameter exploration

In this section, we explore a limited set of fly-by configurations. We aim to investigate the dynamical effects of a fly-by on the disk, where we focus on disk warping. We do not intend to cover the full parameter space, nor do we intend to maximize the warp strength of the disk, which would go beyond the scope of this work. Therefore, we choose a set of representative test cases.

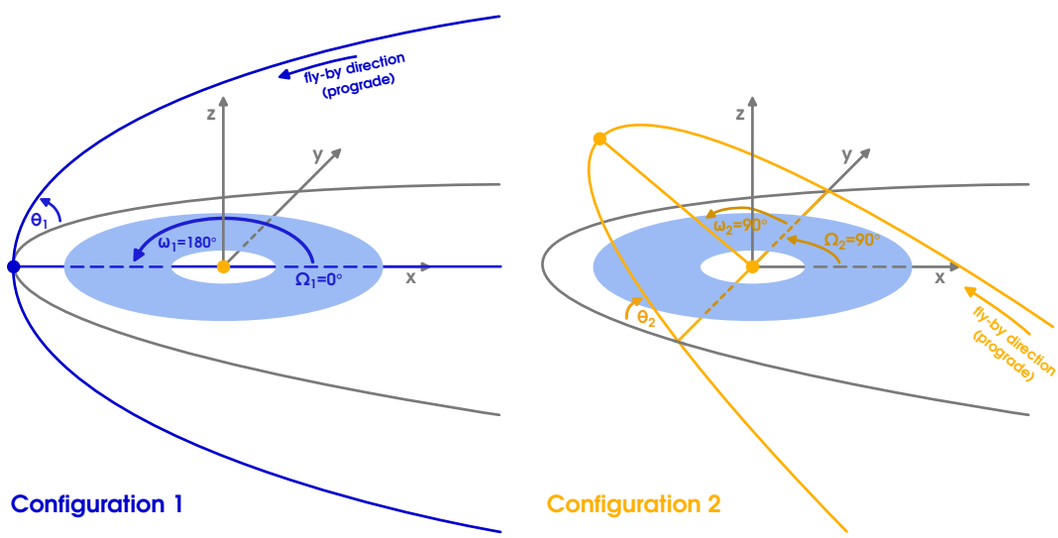

Figure 4.3: Trajectory configurations for our fly-by simulations. The disk lies in the x-y-plane at the origin of the coordinate system with a counterclockwise rotation. Configuration 1 is shown in blue on the left, where the trajectory is rotated about the x-axis with a periapsis in the same plane as the disk. Configuration 2 (orange, right) is rotated about the y-axis with a periapsis out of the disk plane.

Specifically, we decided on two different geometric configurations, depicted in Figure 4.3. For simplicity, we define the trajectories in both configurations such that the perturber comes from the positive x-direction, leading to a periapsis in the negative x-regime. For the first configuration, the periapsis lies in the same plane as the disk and the trajectory is rotated about the x-axis, corresponding to a

longitude of ascending node of $\Omega_1 = 0°$ and an argument of periapsis $\omega_1 = 180°$ (see Figure 4.2 for the definition of these angles). The second configuration is rotated about the y-axis, and therefore $\Omega_2 = 90°$ and $\omega_2 = 90°$. We set the tilt of the trajectories in both cases to $\theta_{1,2} = 30°$.

For both configurations, we perform both a prograde and a retrograde fly-by. Here we note that technically, the definition of the longitude of ascending node Ω would change for the retrograde orbit, as the ascending node flips by 180°. However, for simplicity, we use the same angles to describe both prograde and retrograde orbits and simply flip the starting point of the perturber. For comparison, we additionally perform a co-planar orbit (with $\Omega = 90°$, $\omega = 90°$, and $\theta = 0°$), also both prograde and retrograde.

In all six simulations, we set the distance of the closest approach at the periapsis to $r_p = 104\,\mathrm{au}$. We model parabolic fly-bys with an eccentricity of $e = 1$, and set the initial distance of the perturber from the disk-hosing star to $d_{ini} = 1040\,\mathrm{au}$, so that the disk has enough time to relax from the initial conditions. All six simulations model an equal mass fly-by, where $q = M_{fl}/M_* = 1$. Here, M_* corresponds to the disk-hosting star and M_{fl} to the mass of the perturber. We set $M_* = M_{fl} = 1\,M_\odot$ for both stars.

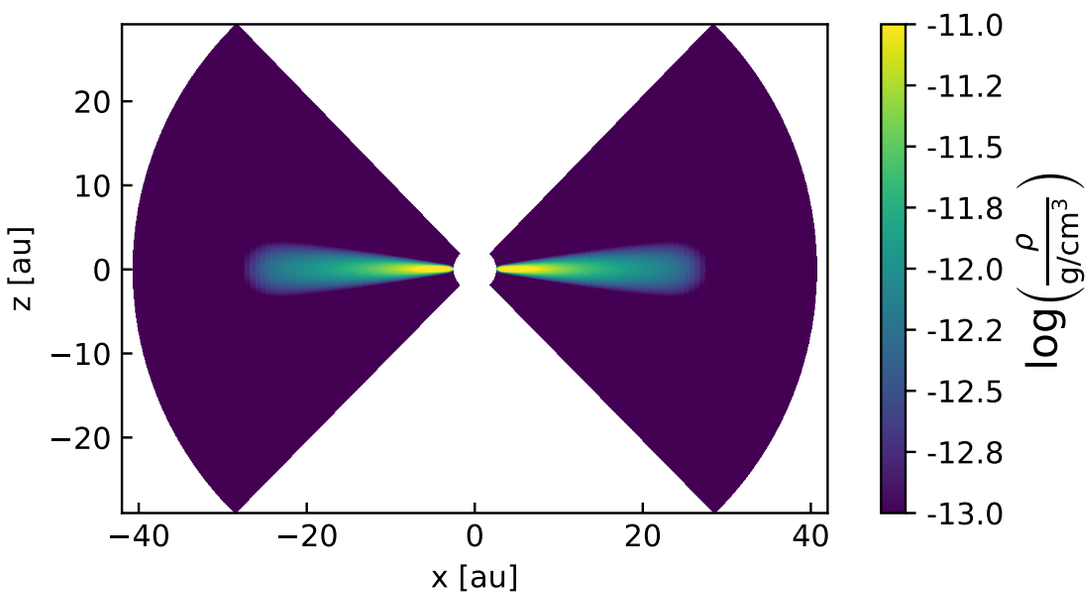

Figure 4.4: Cross-section of the surface density of the initial simulation setup. The computational domain extends further out than the edge of the disk.

A cross-section through the initial disk setup is shown in Figure 4.4. In all six simulations, the disk extends from $r_{in} = 3.12\,\mathrm{au}$ to $r_{out} = 26\,\mathrm{au}$. The surface density follows Equation 4.1 and we set a slope of $p = 1$ a total disk mass of $M_{disk} = 0.02\,M_\odot$, leading to a surface density $\Sigma_0 = 209\,\mathrm{g/cm^2}$ at R_0. The verti-

cal thickness of the disk is determined by the temperature structure and follows Equation 4.2 with $h_0 = 0.05$ at $r_0 = 5.2\,\mathrm{au}$ and $i_{\mathrm{fl}} = 0.25$. For the viscosity, we use an α-viscosity model (Shakura & Sunyaev, 1973) with the dimensionless parameter $\alpha = 10^{-3}$.

4.3.1 Disk warping

We can investigate the warping of the disk with the evolution of the inclination profile. Analogously to Kimmig & Dullemond (2024), we compute the angular momentum vector of each radial shell of the grid and compute the inclination at each radius as the angle between the local angular momentum vector and the z-axis. In the following evaluation of the simulations, we define $t = 0$ to be the moment of the closest approach between the two stars. We initialize our simulations at $t = -2012\,\mathrm{yr}$, which allows for about 15 orbits at the outer disk edge ($r = 26\,\mathrm{au}$) before the closest approach. Most simulations end at $t = 1995\,\mathrm{yr}$, when the perturber has roughly reached the same distance as in the beginning.

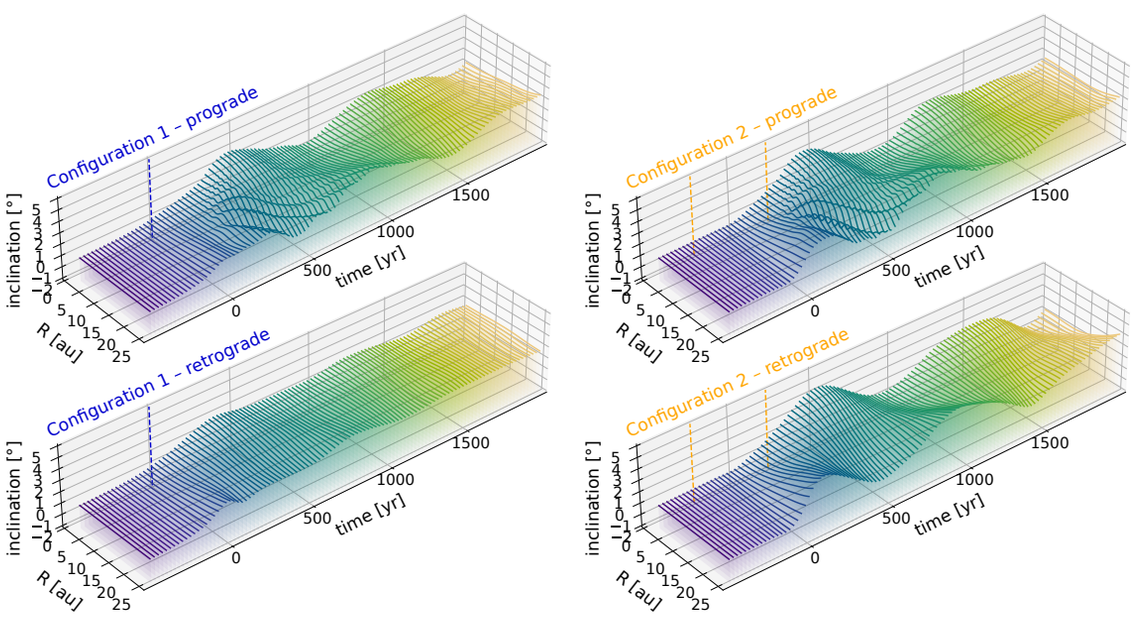

Figure 4.5: Inclination evolution of the fly-by simulations with prograde and retrograde fly-by of Configuration 1 (periastron in the same plane as the disk) in the top two panels and Configuration 2 (periastron out of disk plane) in the bottom 2 panels. The time axis is scaled so that $t = 0$ indicates the moment of closest approach of the fly-by object. Color indicates the time, the vertical blue and orange dashed lines indicate the times when the perturber crosses the (initial) disk midplane. We note that we only plot the inclination profile up to the outer radius of the disk $r_{\mathrm{out}} = 26\,\mathrm{au}$, but the computational domain extends further out.

Figure 4.5 shows the inclination evolution for both configurations for pro- and retrograde orbits. We checked that the inclination of the disk for a co-planar fly-

by does not change, which means that the disk does not warp in these cases, as expected.

Fly-bys on an inclined trajectory, however, all induce a change of the disk inclination with a small warp in most cases. Only the retrograde case for Configuration 1, where the trajectory is tilted about the x-axis (but the periastron is in the disk's midplane), inhibits almost no warp. Here, the disk tilts rigidly by about 2°. In the other three simulations, the disk becomes warped, and the warp travels in a wave through the disk. This wave shows the typical standing wave behavior of the global bending modes with a wavelength of $2\,r_{\text{out}}$.

Both prograde simulations show features in addition to the warp wave which are excited around the time of closest approach. These features move outward and dissipate quickly and are likely linked to the spiral arms that are excited more strongly in prograde fly-bys. We will take a closer look at the spiral arms in Section 4.3.2.

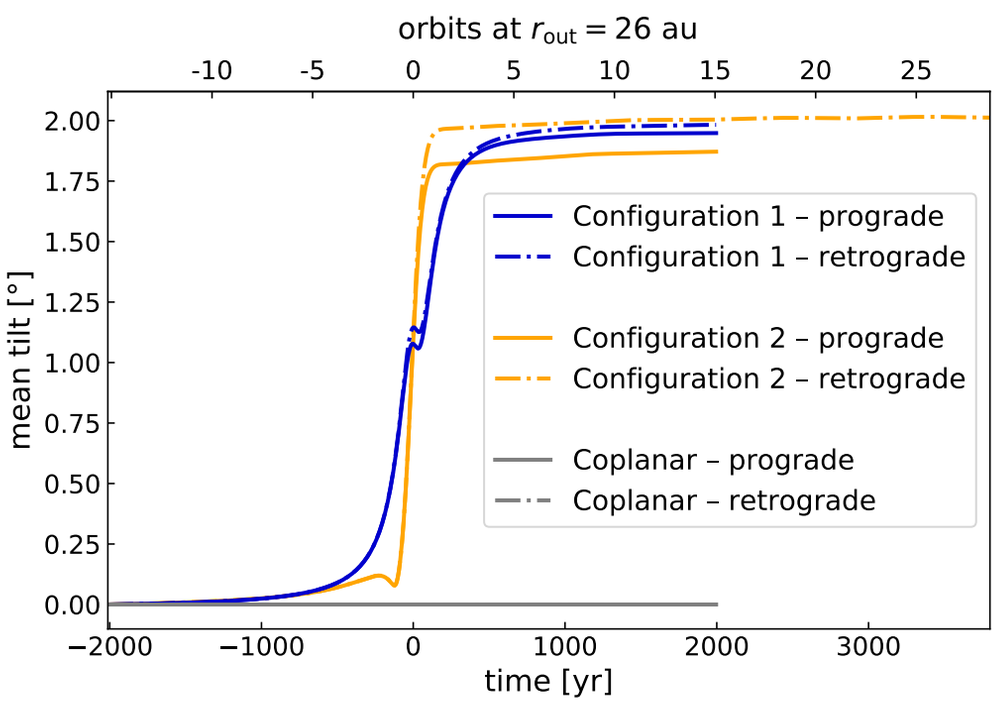

Figure 4.6: Mean tilt defined as the angle between the total angular momentum vector of the disk and the z-axis for all six trajectory configurations.

To investigate the mean tilt of the disk due to the fly-by, we evaluate the mean inclination in each simulation by computing the angle of the total angular momentum vector with respect to the z-axis. Figure 4.6 shows the evolution of the mean tilt for all simulations. All inclined fly-bys induce a mean tilt of close to 2°, irrespective of the exact geometry of the trajectory. This is consistent with the results by Xiang-Gruess (2016), who find that the absolute value of the inclination θ

of the orbit with respect to the disk is the decisive quantity determining the final mean tilt of the disk. Looking at the inclination profiles, we find, however, that the warping of the disk very well depends on the exact orientation of the trajectory. In particular, the warp is stronger for the retrograde case in Configuration 2, where the periapsis does not lie in the same plane as the disk. Because the warp is strongest in this simulation (a maximum misalignment of about 4°), we decided to investigate this simulation on longer timescales. This way, we can study the decay of the warp after the perturber has left the system. Figure 4.7 shows the evolution of the orbital plane inclination at $r = 23.9$ au, which is close to the outer edge of the disk.

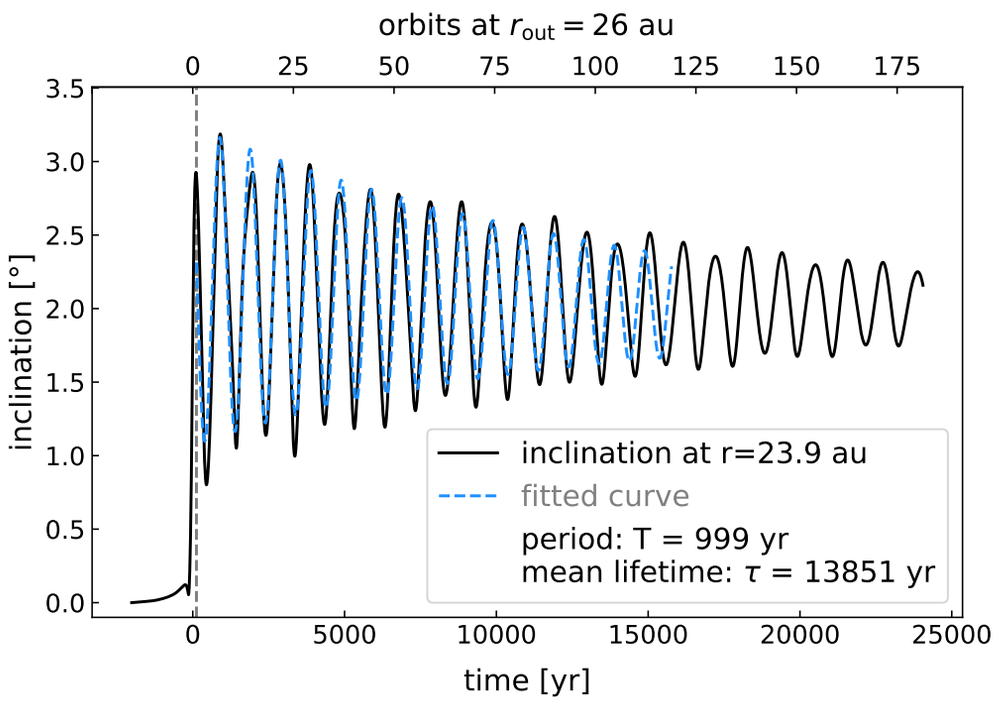

Figure 4.7: Evolution of the orbital plane at $r = 23.9$ au in the retrograde simulation in Configuration 2 (see Figure 4.3, right). We start the fit according to Equation 4.10 (blue dashed line) at the first maximum of the curve (grey dashed line) and stop the fit at $t = 1.58 \times 10^4$ yr, where the period seems to change. We note that this figure shows the evolution over a longer time than Figure 4.5.

We can estimate the decay of the warp by fitting

$$f(t) = A\cos(\omega t - b) \times \exp(-\lambda_d t) + c + d\,t, \tag{4.10}$$

where A is the amplitude parameter, ω the frequency, λ_d the decay rate, b a possible phase shift, c an offset which corresponds to the mean tilt, and d a linear damping in overall inclination. The latter parameter is included for possible inclination damping due to the grid, as found in Kimmig & Dullemond (2024).

However, in our simulations with such a low warp amplitude, we find almost no damping, that is, $d = 10^{-5}\,\mathrm{deg\ yr^{-1}}$. For the fit, we use the `scipy`-function `curve_fit` (Virtanen et al., 2020).

We find that some level of warping is still present after the perturber is already long gone. The mean lifetime of the warp is around $\tau = 1/\lambda_\mathrm{d} \approx 1.4 \times 10^4\,\mathrm{yr}$ and the period of the warp wave about $T = 10^3\,\mathrm{yr}$. This aligns with theoretical estimates, as the damping of the warp can be approximated with linear theory $\tau_{\text{liner theory}} = 1/(\alpha\Omega_\mathrm{out}) \approx 2 \times 10^4\,\mathrm{yr}$, where Ω_out is the Keplerian frequency evaluated at the outer edge of the disk (Lubow & Ogilvie, 2000). The period of the warp can be estimated with the wave speed of the warp $\tau_{\text{warp wave}} = \Delta r / v_\mathrm{warp}$, resulting in approximately 700 yr, where $\Delta r = r_\mathrm{out} - r_\mathrm{in}$ and $v_\mathrm{warp} = c_\mathrm{s}/2$ with c_s as the sound speed (e.g., Nixon & King, 2016).

Additionally, we notice a period change after about $1.6 \times 10^4\,\mathrm{yr}$. This is likely a numerical effect, since this is not physically expected in the evolution of an undriven warp (see e.g. Kimmig & Dullemond, 2024). We therefore stop the fit of the warp decay at that time.

In addition to a warp, the disk can twist, a differential precession described analogously to Kimmig & Dullemond (2024) by the angle between the angular momentum vector of a disk annulus, projected to the x-y-plane, and the x-axis. Twists have been found to occur in fly-by scenarios, for example in Cuello et al. (2019). Figure 4.8 shows the time evolution of the precession angle p, which we calculate as the angle between the x-axis from the projection of the angular momentum vector to the x-y-plane

$$p = \arctan\left(L_y, L_x\right), \tag{4.11}$$

where $L_{x,y}$ are the x, y-components of the angular momentum vector.

We find a differential precession, i.e., a twist, after the disk is warped, consistent with Kimmig & Dullemond (2024). This twist likely occurs due to pressure forces in the disk that influence the warp evolution. This is currently under investigation (Aly et al., in prep.). We note that the differential precession of the disk occurs on a full circular motion, even though Figure 4.8 may suggest a motion rocking back and forth. This is due to our definition of the precession angle with respect to the static coordinate system instead of the precession axis. However, as the precession axis changes over time, there is no unambiguous definition for the precession motion, and we therefore decided to stay consistent with the definition of Kimmig & Dullemond (2024). Both prograde fly-bys show a more complicated pattern in the time between $0 - 500\,\mathrm{yr}$, which is likely due to the spirals. If we compare Configuration 1 (with a periastron in plane) to Config-

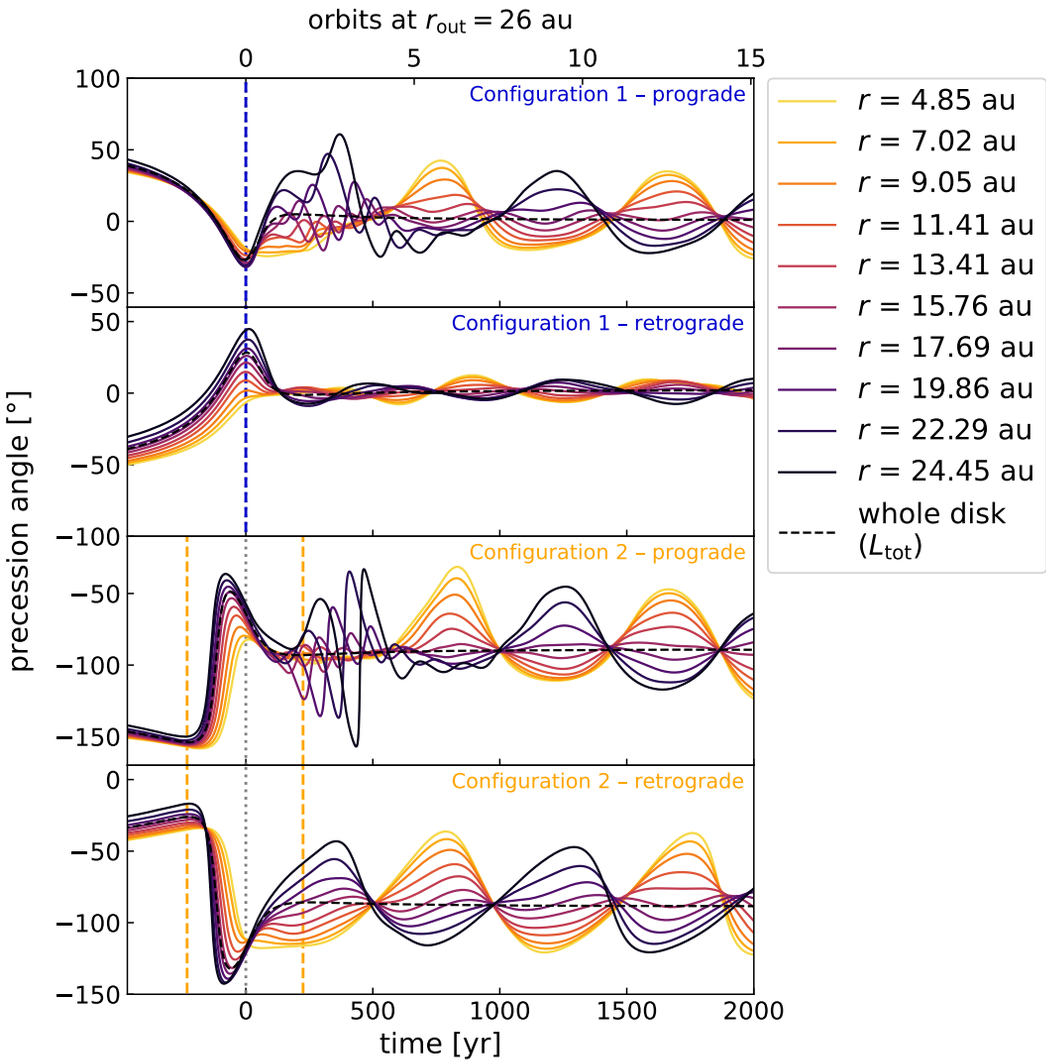

Figure 4.8: Precession angles for different radii in all four inclined simulations. The black dashed line indicates the precession angle for the total angular momentum vector of the disk. We only show times for where the inclination is $\leq 0.1°$, as the precession angle is undefined otherwise. The blue and orange dashed lines highlight the times when the perturber crosses the initial disk midplane. For a good comparison, the range of the y-axis is the same in all panels.

uration 2, we see that the twist occurs slightly earlier for Configuration 2. This likely occurs because the perturber crosses the disk plane already prior to the periastron. To highlight this, we included the blue and orange dashed lines in Figure 4.8. At these times, the gravitational force in vertical direction changes sign, leading to a strong perturbation. The twisting is strongest for the retrograde case of Configuration 2, where the warp is also strongest.

In summary, inclined fly-bys can excite warps and twists that remain even after the perturber has reached a distance > 1000 au. This can mean for observations that for warps triggered by a fly-by, the fly-by object is not necessarily

associated with the perturbed system. We find moderate warp strengths of $\leq 4°$. However, the warp can be stronger for different fly-by parameters, i.e. a shorter distance of closest approach, a more massive fly-by object, or more inclined trajectories. Although it would be interesting to find parameters to maximize the excited warp, it is not the focus of this study.

4.3.2 Spirals

Fly-bys are known to create spirals due to tidal effects (Clarke & Pringle, 1993; Ostriker, 1994). Figure 4.9 shows snapshots of the vertically integrated density (per radial shell) before, during, and after the close encounter of the prograde simulation in Configuration 2. We show further snapshots of the 2D structure in Appendix 4.B, Figure 4.B.1.

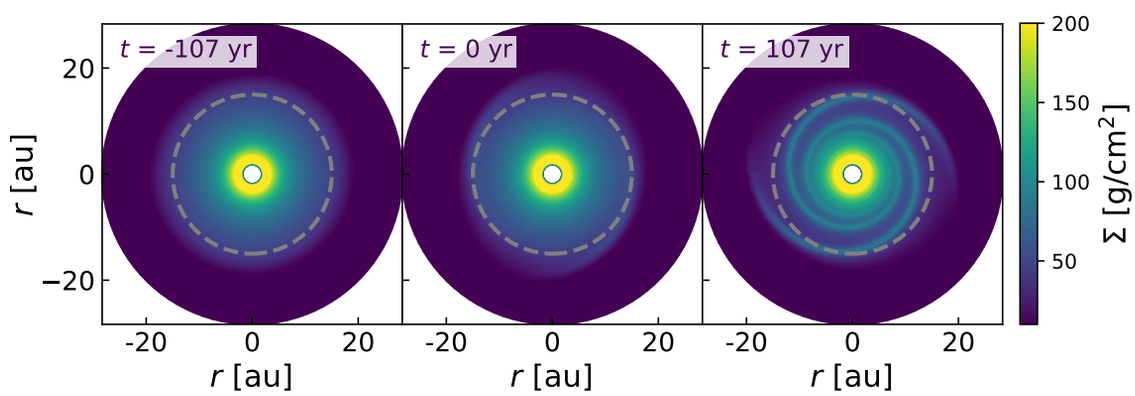

Figure 4.9: Surface density snapshots of the prograde fly-by in Configuration 2. Time $t = 0$ yr is the point of closest approach. The grey dashed circle indicates a radius of 15 au, where we perform further analysis of the spirals.

We investigate the spirals in more detail by measuring the strength of the spirals in all six different setups. For that, we extract the maximum value of the surface density Σ_{peak} at a single radial location over time, analogous to Smallwood et al. (2023), and scale it with the mean surface density Σ_{mean} at that radius. Figure 4.10 shows the evolution of this peak surface density, which indicates the strength of the spirals, in all of our simulations at $r = 15$ au.

We find that strong spirals occur for all three prograde setups. The retrograde simulations, on the other hand, show little or no spirals, consistent with previous findings (e.g. Clarke & Pringle, 1993; Cuello et al., 2019, 2023). We thus focus on the prograde simulations for the further evaluation in this section.

The strongest spirals occur for the coplanar prograde orbit. The simulation with the orbit tilted with respect to the x-axis (Configuration 1), where the periastron is in-plane, follows with the second strongest spirals. Configuration 2,

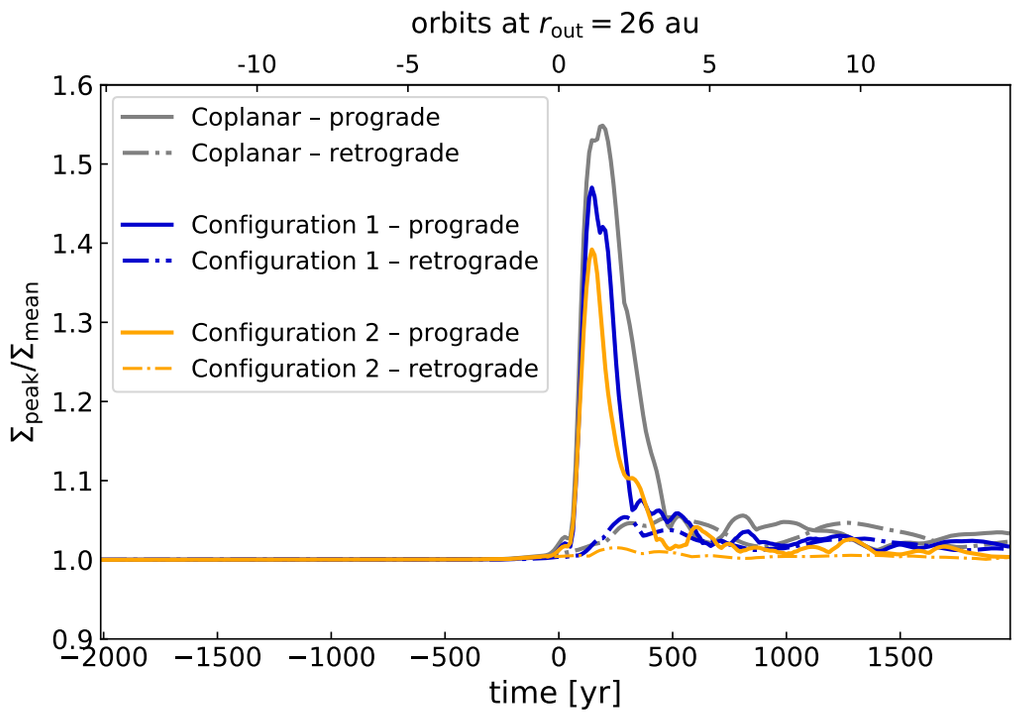

Figure 4.10: Time evolution of the peak surface density at $r = 15$ au in all six simulations. Prograde simulations are shown with solid lines, while retrograde simulations are indicated with dash-dotted lines.

with a periastron outside of the disk plane, shows the weakest of the three prograde fly-bys. This is consistent with the findings of Smallwood et al. (2023), see their Figure 14 (but we note that their setup is defined rotated by 90°, so that their rotation about the x-axis corresponds to the case with the periastron out-of plane).

We then investigate the azimuthal evolution of the spirals in Figure 4.11, where we plot an azimuthal cut at the same radius, $r = 15$ au, over time. In all simulations, the spirals are extremely short-lived and only last about 500 yr. At the time where the spirals dissolve, the perturber is located at a distance of about 370 au from the disk-hosting star, which are roughly $3.6\, r_{\rm p}$.

In comparison to Smallwood et al. (2023), the spirals in our simulations dissolve faster on physical timescales. As the disk in their simulations has properties different from our setup, we perform a quick analysis of timescale estimations here. Smallwood et al. (2023) find a lifetime of about 5000 yr for a disk ranging from $10 - 100$ au. The outer disk has an orbital time scale of about 1000 yr, which means that the outer disk performs about 5 orbits during the lifetime of the spirals. In our simulations, the spirals live roughly 500 yr in a disk ranging from $2 - 26$ au, leading to an orbital period of 130 yr at the outer disk edge, which are slightly less than 4 orbits during the spiral lifetime. This compares well with the 5 orbits found by Smallwood et al. (2023). In this context, we want to point out

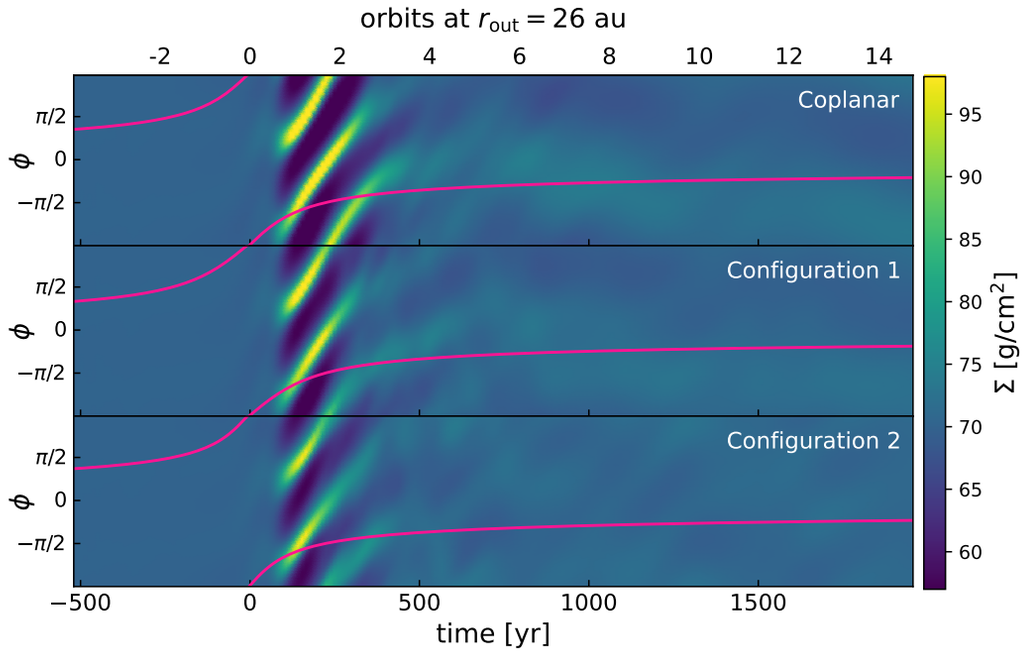

Figure 4.11: Azimuthal cut of the vertically integrated surface density at $r = 15$ au for all three prograde simulations. The pink line indicates the angle to the perturber projected to the x-y-plane. The time axis is scaled such that $t = 0$ yr indicates the point of closest approach.

that the fact that the spirals live longer than the longest orbital timescale in the disk indicates that the spirals are not simply a shear of a density wave.

Additional differences between our simulations and Smallwood et al. (2023) are the disk viscosity, which is smaller by at least a factor of 2 in our simulations, the disk mass, which is about 20 times higher in our simulations, and the flaring of the disk. Smallwood et al. (2023) set up an unflared (often called flat) disk with a constant aspect ratio of $H_p/r = 0.05$, whereas we set our temperature structure such that the disk is flared with an index of 0.25. These factors could also have an impact on the lifetime of the spirals. Furthermore, Smallwood et al. (2023) focus on less massive perturbers than we do, but for the lifetime of the spirals they do not find any strong dependency on the perturber mass.

The lifetime of the spirals in our simulations coincides with the lifetime of the additional features in the inclination profile for the prograde simulations (as seen in Figure 4.5). If the spirals are warped, they could cast shadows. As the spirals significantly change on observable timescales, this could possibly lead to an evolution of shadow features on short timescales, as observed in a few disks, for example in TW Hya (Debes et al., 2017), HD 135344B (Stolker et al., 2017), or MWC 758 (Ren et al., 2020).

4.3.3 Disk truncation

Fly-bys are known to truncate the disk. We therefore briefly discuss this phenomenon in our simulations. Breslau et al. (2014) find an empirical relation of final disk sizes after a fly-by

$$r_{\text{final}} \approx 0.28\, q^{-0.32}\, r_{\text{peri}}, \tag{4.12}$$

where q is the mass ratio between the two stars and r_{peri} the distance of the closest approach. Disks experiencing a prograde fly-by are affected more strongly than retrograde fly-bys, where disks can be up to twice as large (Bhandare et al., 2016; Cuello et al., 2019).

In our simulations, $q = 1$ and $r_{\text{peri}} = 104\,\text{au}$ and therefore we would expect a disk size of 29 au. However, our disks are already compact from the beginning, with 26 au and we therefore do not expect the fly-by to affect the size of the disk.

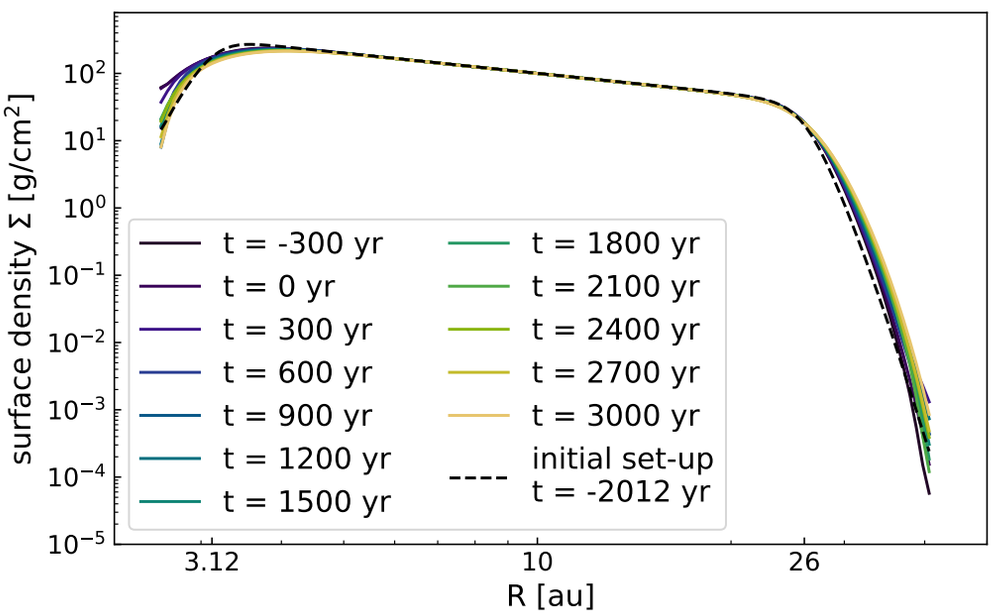

Figure 4.12: Evolution of the surface density in the retrograde simulation in Configuration 2. The time $t = 0\,\text{yr}$ corresponds to the time of closest approach. The black dashed line indicates the initial surface density setup according to Equation 4.1.

Figure 4.12 shows the surface density evolution for the retrograde Configuration 2 as an example. Indeed, the disk does not show truncation effects and only spreads slightly due to viscous evolution. We find this behavior in all of our simulations. This allows us to keep the main focus on the warp evolution of the disks discussed above.

4.4 Models of RW Aur

We aim to apply our hydrodynamic models to RW Aur, a two-star system which recently underwent a close encounter and where both stars host a disk. Our motivation for this system is the recent indication by Kur24 that the disk around star A might be warped. Kur24 additionally performed a detailed analysis of the star's orbit. They found that the system is either in a highly eccentric bound orbit, or a fly-by. In either case, the eccentricity is found to be close to $e \approx 1$ and the periastron occurred only recently, about 300 yr ago. In the frame of this work, we choose to model an unbound trajectory. Additionally, we focus on the disk around RW Aur A and neglect the disk of star B.

4.4.1 Hydrodynamic models

Model setup

In this section, we present hydrodynamic models as described in Section 4.2. For the disk around RW Aur A, we set up an initially planar disk with a range from $1.2 - 20$ au. We therefore extend the grid domain inward to 1 au. In order to keep the resolution consistent with the simulations in Section 4.3, we increase the number of radial cells to 160. The chosen disk size is motivated by the size of the observed dust disk at $\lambda = 1.3$ mm in the system (Kur24), as we aim for radiative transfer models in the millimeter wavelength range tracing the dust continuum. We note that observations suggest that the disk extends to an inner edge at 0.1 au, while our inner radius is set to 1.2 au. However, smaller cavities become computationally costly in grid-based simulations, which is why we settled for a larger inner radius.

For the masses of the stars, we use the fit of the dynamical mass by Kur24 with $M_A = 1.238\,M_\odot$ and $M_B = 0.995\,M_\odot$ of star A and B, respectively. This leads to a mass ratio of $q = M_B/M_A = 0.8037$. The orbital period at the outer edge of the disk is 80 yr. For the gas disk mass, we assume $M_{gas} = 0.01\,M_A$. We keep the slope of the surface density and the temperature structure (and hence the vertical shape of the disk) the same as in our previous models. This gives a surface density of $\Sigma_0 = 179\,g/cm^2$ at the reference radius of $r_0 = 5.2$ au. As in the previous models, we set the disk viscosity to $\alpha = 10^{-3}$.

Kur24 find that the inner and outer disk are likely misaligned with respect to each other. They find for the outer disk plane an inclination of $i_{d,\,out} = 54.8$ deg and a position angle of $PA_{d,\,out} = 39.4°$, and for the inner disk an inclination of $i_{d\,in} = 60.8$ deg and a position angle of $PA_{d,\,in} = 35.6°$. Additionally, Kur24 fit the orbit of RW Aur B in the reference frame of star A. Their best fit gives a dis-

tance of closest approach $r_p = 55\,\mathrm{au}$, an orbit inclination in the plane of the sky of $i_o = 129.8°$, a position angle of $\Omega_o = 73.8°$, and an argument of periapsis of $\omega_o = 42.3°$. They report an eccentricity of e= 0.787 for their best fit. However, unbound orbits are not ruled out. Because we model an unbound orbit, we set the eccentricity to $e = 1$. For the other orbital parameters, we use the best-fit values. Because we do not expect a mean disk tilt of more than a few degrees, we set up the models such that the disk initially lies in the plane of the observed outer disk. The exploration of different initial disk planes is left for future work.

The orbital parameters and the disk orientation by Kur24 are given in the reference frame of the sky. For the grid-based hydrodynamical simulations, however, it is best for the disk to initially lie in the x-y-plane. We therefore need to compute the respective geometry of the orbital parameters with respect to the disk plane. The detailed steps for the calculation of the angles can be found in Appendix 4.C. We note that due to the definition of the angles as shown in Figure 4.2, we need to take the inclination $\theta_{\mathrm{d,\ calc}} = 180° - \theta_{\mathrm{d,\ measured}}$ to calculate the mutual angles.

We find a mutual inclination between the orbit and the outer disk plane to be $\theta_{\mathrm{mut}} = -27.5°$, where the minus sign indicates that the periastron is below the disk plane in our simulations. This value for the mutual inclination is also reported by Kur24. For the argument of periastron with respect to the disk plane, we find $\omega_{\mathrm{mut}} = 86.3°$. At this point, we can arbitrarily set the longitude of ascending node arbitrarily, as the disk is initially axisymmetric. However, this angle will become important for the radiative transfer simulations, where we need to project the model to the sky plane in order to calculate synthetic observations.

Warping of the disk

Figure 4.13 shows the evolution of the inclination profile for the simulation adapted to RW Aur. The disk develops a warp with a maximum misalignment of about 5°. As expected, the warp travels as a wave through the disk. We find a final mean inclination (defined as the angle between the total angular momentum vector and the z-axis) of 2.6°. In the dust continuum observations, Kur24 find indications of a warp in the disk around RW Aur A. By minimizing the residuals between the observation and a Keplerian model of a broken disk with a misaligned inner disk, they find a misalignment of around 6° between inner and outer disk, which aligns nicely with the expected warp from our simulation.

Compared to Figure 4.5, the warp is slightly stronger and the wave evolves on shorter timescales. Although the geometry of the fly-by trajectory is similar to Configuration 2 in the previous part of this work, there are some important

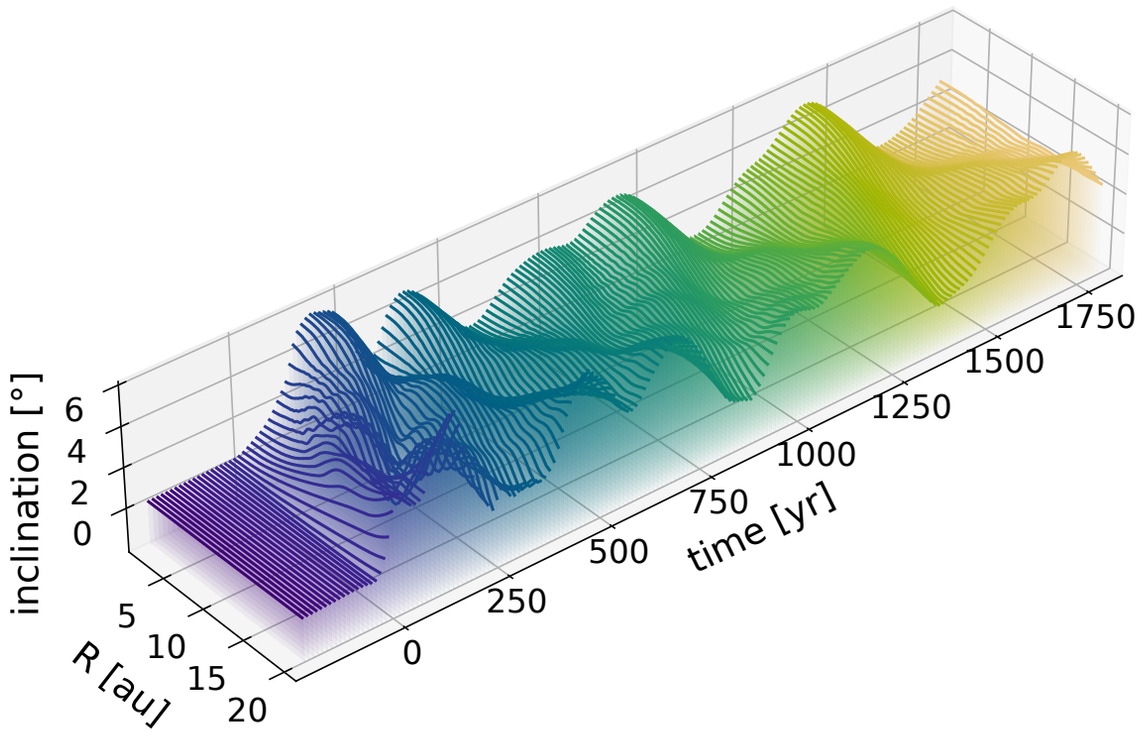

Figure 4.13: Evolution of the inclination profile for the simulation of the disk around RW Aur A. Color indicates the time, time $t = 0$ indicates the point of closest approach.

differences. First, the disk is smaller in size, with an outer radius of $r_{\text{out}} = 20\,\text{au}$ instead of 26 au. This for example influences the warp timescale, which is sensitive to the disk size because of the reflection of the warp wave at the disk edges. Further, the host star has a larger mass, whereas the perturber has a lower mass than in the previous simulations. The distance of closest approach is shorter with $r_{\text{p}} = 55\,\text{au}$ instead of 104 au.

In Figure 4.13, the evolution of the inclination profile shows a pattern that suggests that multiple superimposed bending waves are present. Although this behavior is of interest for theoretical warps, we decided to leave a detailed investigation of this phenomenon for future work, as our focus is the comparison to observations of the RW Aur system.

Spirals

As the fly-by in the RW Aur system is prograde, we expect the excitation of spiral arms. Figure 4.14 shows the peak surface density (top), as well as the azimuthal density evolution (bottom) in the disk at a radius of $r = 15\,\text{au}$.

We see that clear spirals are excited roughly at the point of closest approach. As before, the spirals are short-lived. They disappear after roughly 200 yr, which corresponds to 2.5 orbits at the outer disk edge. At this time, the perturber is

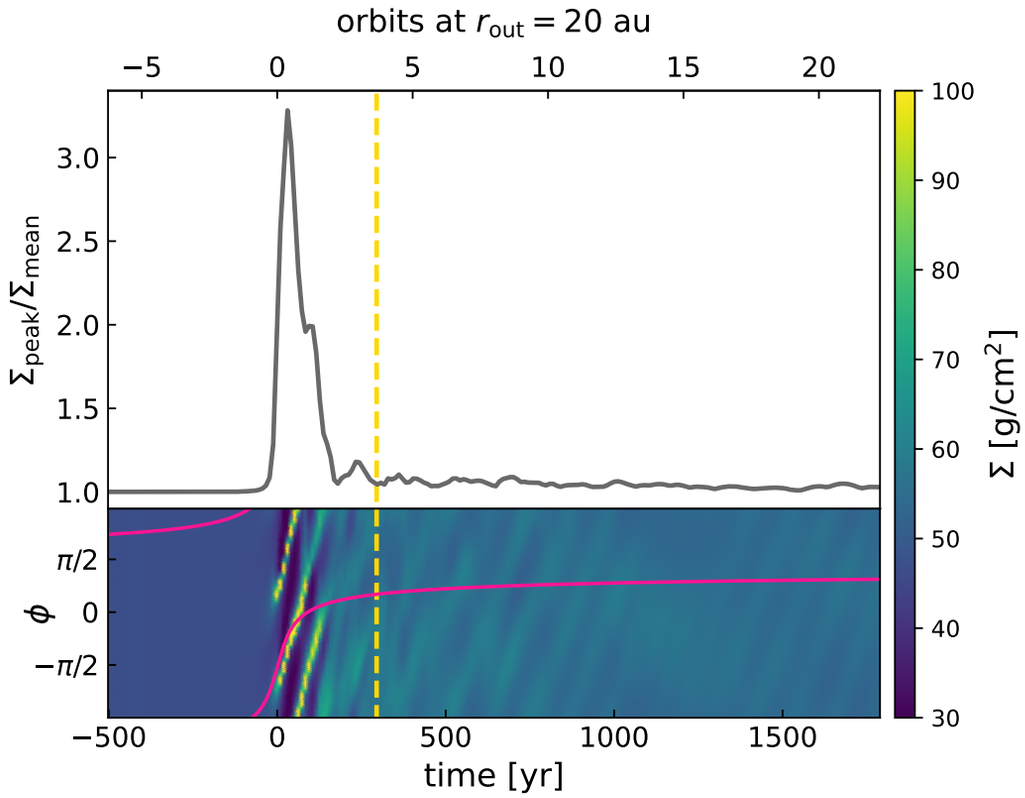

Figure 4.14: Peak surface density (top panel) and azimuthal profile evolution (bottom panel) of the RW Aur simulation at $r = 15$ au. As in Figure 4.11, the pink line indicates the angle to the perturber. The yellow dashed line highlights the current point of time at $t = 295$ yr after periastron.

about 200 au away from the disk-hosting star. This is slightly shorter than the four orbits of the outer disk edge we found in Figure 4.11. The likely reason for this are the aforementioned differences in the model setup of disk size, disk and stellar masses, and trajectory parameters. About the absolute strength of the spirals in the top panel, it is not trivial to compare to the previous simulations, because we chose the same plotting radius of $r = 15$ au for both parts, but the disk size differs. Investigating the effect of disk and fly-by properties on the lifetime of the spirals would be interesting in future work.

4.4.2 Different disk viscosities

Because spirals might have different lifetimes for different disk viscosities, we investigate the hydrodynamical results in one simulation with a larger $(\alpha = 10^{-2})$ and one with a lower disk viscosity $(\alpha = 10^{-4})$. All other parameters, including the trajectory of the fly-by, remain exactly the same.

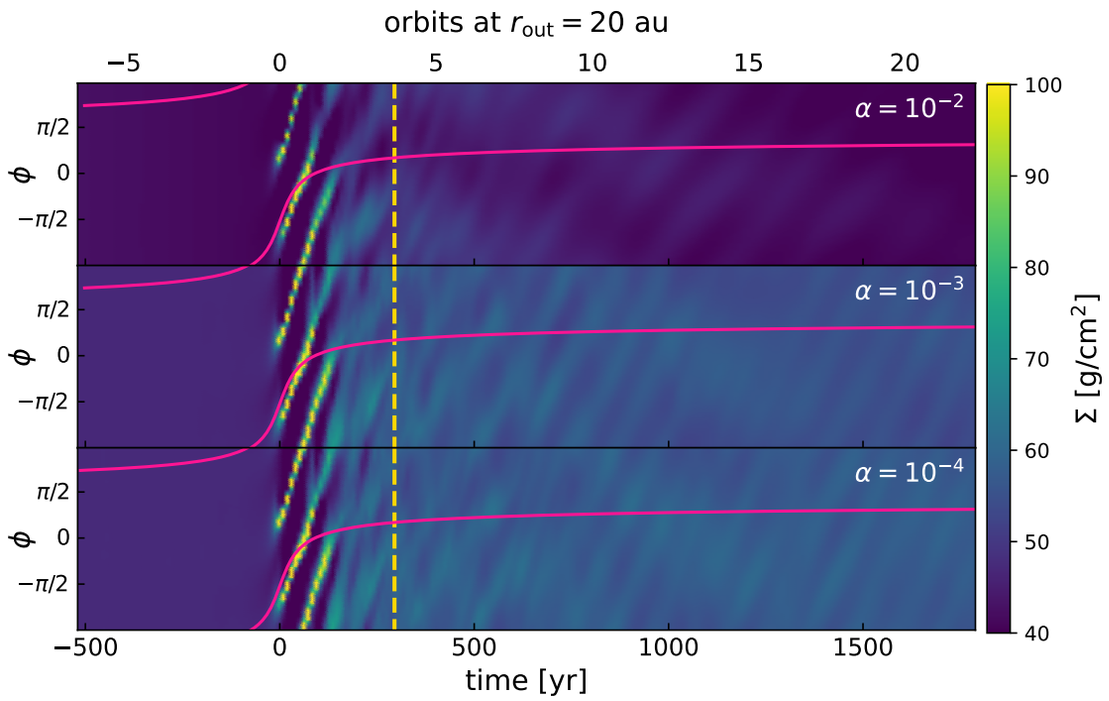

Figure 4.15: Azimuthal surface density profile evolution at $r = 15$ au for the simulations with different disk viscosities. The yellow dashed line indicates the current time and the pink line indicates the angle to the perturber.

Figure 4.15 shows the evolution of the azimuthal profile at $r = 15$ au for the simulations with different viscosities. The middle panel here shows the fiducial simulation presented before. Surprisingly, the lifetime of the spirals does not depend strongly on the viscosity. As expected, the spirals dissolve slightly faster for higher viscosity. However, for lower viscosity, no significant difference in spiral lifetime is visible. This means that we do not expect to see strong spirals at the current time of observations, even if different assumptions on viscosity are taken. The lifetime of the spirals could, however, be dependent on other disk properties, such as initial disk size and vertical density structure (inter alia, flaring).

Investigating the warp in these simulations in Figure 4.16, we find that the amplitude of the excited warp also does not depend on the disk viscosity. However, the viscosity influences the evolution of the warp after the fly-by. This is

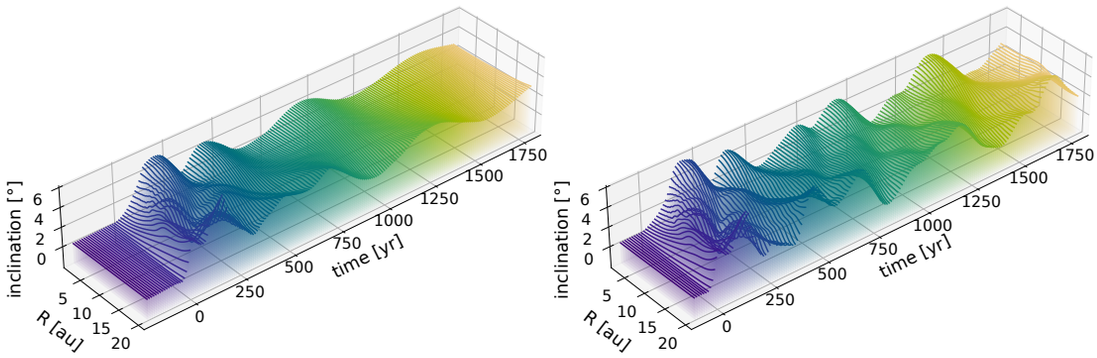

Figure 4.16: Evolution of the inclination profile in the simulation with $\alpha = 10^{-2}$ (left) and $\alpha = 10^{-4}$ (right).

especially visible for the largest viscosity simulation as the warp is dampened rapidly. The two low-viscosity simulations show no strong differences on the short simulated timescales. However, in the context of the results by Kimmig & Dullemond (2024), we expect a longer lifetime of the warp for the lowest viscosity.

Comparison to other work

Hydrodynamic models of a fly-by in the RW Aur system were performed a decade ago by Dai et al. (2015) using SPH. Their focus was the observed large-scale tidal arm that seems to link star A and B. One of their main results was that a prograde encounter was necessary in order to produce such a tidal arm, which aligns very well with the findings of the astrometric orbit fitting by Kur24. In order to produce the tidal arm, they set up an initially larger disk of 60 au, which is then truncated by the fly-by. When comparing the orbital parameters, their best model is similar to the result of the astrometric fit, and therefore to the setup in our work, as shown in Table 4.1. The good match of the orbital parameters is not a given, as Dai et al. (2015) fitted the orbital parameters so that their model matched the observed large-scale tidal arm.

Comparing the hydrodynamic results of the disk in detail is difficult, as the disk properties differ strongly, also shown in Table 4.1. A similarity we find are the excited spirals, which is not surprising given the prograde nature of both fly-by setups. Looking at their Figure 4, the spirals also seem to be short-lived and seem to dissolve within 200 yr after periastron passage.

A direct comparison of the warping is not possible, as they did not explicitly analyze the warp. However, the warp evolution would differ for models of different viscosity (see e.g. Kimmig & Dullemond, 2024). In the simulations by Dai et al. (2015), the viscosity is larger by a factor of 100.

However, the fact that the trajectory parameters are similar might indicate that we could reproduce a similar large-scale tidal structure in our simulations if our

Table 4.1: Comparison of simulation setups

	this work (and Kurtovic et al., 2024)	Dai et al. (2015)
fly-by parameters		
stellar mass M_A	$1.238\,M_\odot$	$1.4\,M_\odot$
stellar mass M_B	$0.995\,M_\odot$	$0.9\,M_\odot$
eccentricity e	1	1
closest approach r_p	55 au	70au
mutual inclination θ	27°	18°
arg. of periastron ω	89°	80°
disk parameters		
initial disk size	20 au	60 au
viscosity α	10^{-3}	10^{-1}
initial disk mass	$1.238 \times 10^{-2}\,M_\odot$	$1.6 \times 10^{-3}\,M_\odot$

initial disk size (and the computational domain) was larger. This may be worth investigating in more detail in combination with warps in future work.

4.4.3 Radiative transfer models of the dust continuum

In this section, we aim to compare our models of a fly-by in the RW Aur system with observations. For this, we run Monte Carlo simulations using the radiative transfer code RADMC-3D (Dullemond et al., 2012). The dust temperature is calculated consistently with the radiative transfer model using the Monte Carlo Bjorkman & Wood (2001) method implemented in RADMC-3D, where we use the modified random walk option (Fleck & Canfield, 1984). We use 10^8 photon packages to compute the temperature. We then compute the sky model of the system with ray-tracing (also 10^8 photon packages) and produce synthetic images by convolving the fluxes with a two-dimensional Gaussian imitating the corresponding telescope's finite resolution. We note that to remain consistent with the observations by Kur24, we use a value of 154 pc for the distance to RW Aur A (Gaia Collaboration et al., 2016, 2021), instead of the 156.1 pc found in the Gaia Data Release 3 (Gaia Collaboration et al., 2023).

We compare the simulation with the ALMA dust continuum observation. For the composition of the dust, we assume the DIANA standard composition of 87% carbon and 13% pyroxene, where the pyroxene is composed of molecule bonds with 70% magnesium and 30% iron. The porosity is set to 25% (Woitke

et al., 2016). We compute the dust opacity and scattering matrices with `optool` (Dominik et al., 2021).

Since the hydrodynamic simulation only models gas, we need to assume a spatial dust distribution in the disk. Because the behavior of larger dust particles in warping disks is not well known yet, we assume small dust grains of a singular size $a = 1\,\mu$m that are perfectly coupled to the gas. The choice of a singular dust size in contrast to a dust size distribution is motivated by the lack of good observational constraints on the actual size distribution. Additionally, it allows us to ensure that the dust follows the dynamics of the gas.

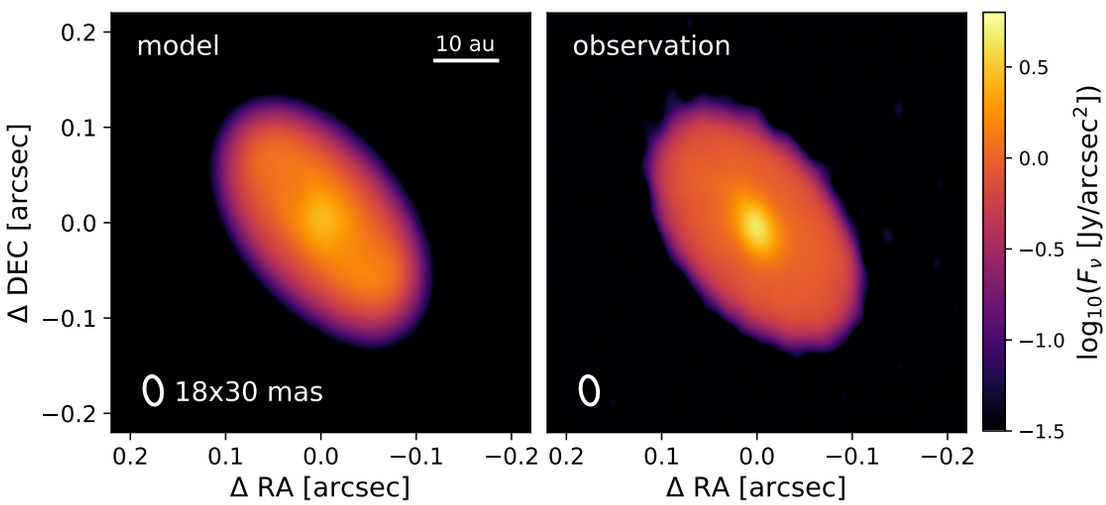

Figure 4.17: Synthetic observation of our hydrodynamic simulation at $t = 259$ yr after periastron at a wavelength of $\lambda = 1.3$ mm (left panel) next to the ALMA Band 6 observation of RW Aur (right panel, Kurtovic et al., 2024), also at $\lambda = 1.3$ mm. The ellipse in the bottom left corner indicates the beam and is the same for both images.

For the dust-to-gas ratio, we aim to match the total flux of the observation, which Kur24 reported to be 34.5 mJy. With a dust-to-gas ratio of 10^{-2} (and a distance of 154 pc to the source), our radiative transfer models result in a total flux of 31.5 mJy, and we therefore adopt this dust-to-gas ratio. However, we note that our choice of a single grain size of small dust could underestimate the flux in dust continuum wavelengths. We also note that the dust-to-gas ratio is somewhat flexible, as the total gas disk mass in our hydrodynamic simulations is scalable, as we are not treating self-gravity, nor the indirect term from the disk onto the star. This means that the same total flux can also be reached when the gas disk mass and dust-to-gas ratio are scaled differently. For a comparison with the observational image, we convolve the radiative transfer image with a beam of 18×30 mas and a position angle of 8.186, as reported for the observational data.

According to the fit by Kur24, the time of observation was $t = 259$ yr after the

periastron. We confirmed in our simulation that the position of the perturber matches the observed position of RW Aur B. Figure 4.17 shows a comparison of the model next to the observation by Kur24. Both images are observed at a wavelength of $\lambda = 1.3\,\mathrm{mm}$. Overall, the images compare well. In the observation, the central emission is slightly stronger, which could be because of our choice of a larger cavity in the simulation for reasons of computation time. We present the comparison between the convolved and unconvolved model in Appendix 4.D, which shows that a few spiral features close to the inner edge are visible, which are then hidden by the beam resolution. A fine-tuned quantitative match is out of the scope of this work, as many parameters, such as disk characteristics, fly-by trajectory and dust models, have an impact on the result of the model.

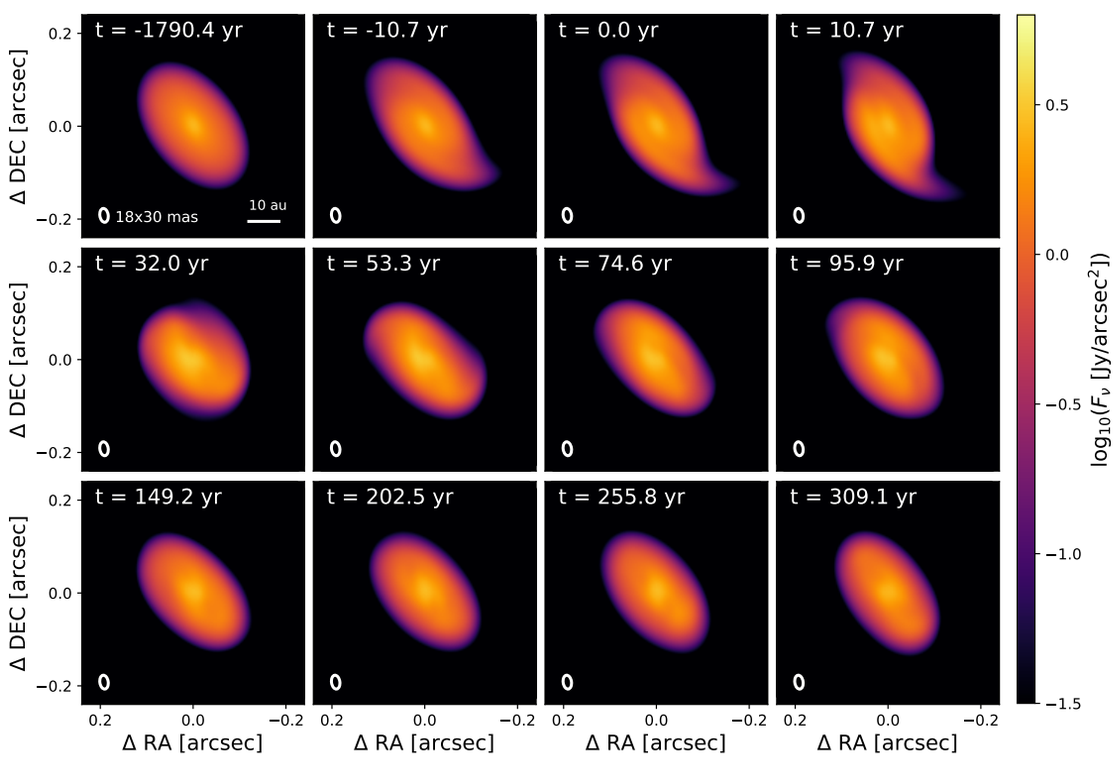

Figure 4.18: Synthetic observations at $\lambda = 1.3\,\mathrm{mm}$ of the RW Aur A simulation at different times. The first panel shows the initial setup of the simulation, time $t = 0\,\mathrm{yr}$ is the time of the closest approach, and the current time step lies between the second last and last panels. The images are convolved with the same beam as Figure 4.17.

In Figure 4.18, we present radiative transfer simulations at different times of the hydrodynamic simulation. During the point of closest approach ($t = 0\,\mathrm{yr}$), the spiral structure excited by the fly-by is indeed visible, but quickly disappears. The system is (synthetically) observed from the same location at each time, which corresponds to inclination and position angle of the initial setup of the simulation. The warp only changes the disk plane by a few degrees throughout the simula-

tion, and therefore the observed inclination of the disk does not vary strongly. However, a slight variation of the inclination and position angle on a time scale of a few tens of years could be observable.

One of the objectives of the comparison between the simulations and the real observation is whether the spiral structures produced by the fly-by should be observable with state-of-the-art instruments. At $t = 259\,\mathrm{yr}$ in our simulations, the strongest spirals have already dissolved, as we show in Figure 4.14. In the simulations by Dai et al. (2015), the spirals seem to be weak as well at the time of comparison. However, some weak spiral structures are still residue in our simulations, also seen in the unconvolved image in Figure 4.D.1. After the convolution (Figure 4.17), however, we find that these structures are not discernible, leading to the good match between model and observation.

A next step is to evaluate the gas kinematics in observations of molecular lines, which is planned for the near future. Observational data of gas kinematics in the RW Aur system are currently lacking good spatial resolution, but we are hoping that this will change in the upcoming years.

4.5 Discussion

In this work, we have studied the dynamical effects of fly-bys on protoplanetary disks, with a special focus on disk warping. In this section, we discuss the limitations of our study.

First and foremost, we present only a limited set of fly-by configurations. We do not study the effect of changing the distance of closest approach, nor the mass ratio of the two stars. We expect stronger warps for closer approaches and higher mass ratios of fly-by mass to host star mass. Additionally, different inclinations of the trajectory, similar to the studies by Xiang-Gruess (2016) and Cuello et al. (2019) could be investigated with a stronger focus on disk warping. Different disk properties, such as viscosity or temperature influencing the vertical structure (flaring), can also lead to a different warping behavior. In this work, we investigated the warp behavior in a few example configurations, and we leave a further exploration of the parameter space for future work.

We performed our models in the rest frame of the disk hosting star. Because a fly-by accelerates the host star, we need to account for non-inertial motion of the simulation. This is usually done in the form of indirect terms. While we take into account the acceleration of the host star by the fly-by object, we neglect the acceleration of the host star due to potential asymmetric distribution of the gas in the disk. As disks in fly-bys can become very asymmetric due to the spirals and the warping, this can potentially have an effect on the host star and in term a back-

reaction onto the disk. However, the physics and the correct implementation of this indirect term is still under investigation (Jordan & Rometsch, 2025, Crida et al. 2025a,b, subm.), which is why we decided to neglect this effect for now. The extent of the influence of this indirect term could be investigated in future work.

We want to mention that the radiation from the perturber onto the disk could influence the results of the hydrodynamic simulations, which is currently neglected in our models. Shadows in the disk due to the warp can influence the disk dynamics, as well as the temperature structure of the disk (Su & Bai, 2024; Zhang & Zhu, 2024; Ziampras et al., 2024). If the perturber is massive, it can emit strong radiation in the UV regime that influences the disk (Guarcello et al., 2023).

Fly-bys can induce gravitational instability in massive disks (Thies et al., 2010). However, since the typical disk-to-star mass ratio for this effect lies around 0.5, this is not relevant for our models.

For the RW Aur system, Kurtovic et al. (2024) find that bound orbits are likelier by a factor of 0.28. However, in our models, we assume an unbound fly-by trajectory. In general, the effect of highly eccentric orbits is expected to be similar to that of unbound orbits (Cuello et al., 2023). We can perform a quick timescale estimation: The best fit of Kurtovic et al. (2024) includes an eccentricity of $e = 0.78$ and leads to an orbital period of approximately 2800 yr. In our simulations, the excited warp is expected to be still present after this time, which means that a repeated encounter due to the bound nature of the orbit could create a different warp structure than a single fly-by. However, unbound orbits can not be ruled out observationally for this system.

Another factor that should be kept in mind when interpreting our RW Aur models is that the evolution of the warp also depends on disk properties, of which not all are well constrained. We oriented the size of the disk in our models to the size of the observed dust disk. However, the extent of the gas disk of RW Aur A seems to be larger roughly by a factor of 2. Additionally, because of computational restrictions we had to set the size of the inner disk cavity to about 1 au, although observations indicate a much smaller cavity of likely 0.1 au. However, modeling such a small cavity is computationally expensive in grid-based models and we decided to make a trade-off between cavity size and computation time. In our models, we neglect the disk around RW Aur B, since we are mainly interested in the warping of the disk around star A.

Our hydrodynamic models of the system only contain gas. For the radiative transfer simulations, we then assume a dust-to-gas ratio and that the dust is perfectly coupled to the gas. This is why we only assume small dust particles. In reality, however, larger dust is likely to have an influence on the appearance of the disk in observations. A more consistent way would be to model the behav-

ior of dust in the hydrodynamics simulations. However, simulating the dust in hydrodynamic simulations of a warped disk has not been tested very well in FARGO3D up-to-date. Since we obtain disks that are misaligned with respect to the grid geometry, we avoid including dust in the hydrodynamics without further tests. However, our assumptions on dust grain size and composition might influence the results of our radiative transfer dust continuum models.

Different assumptions for the dust could also influence the visibility of the spirals. The spatial distribution of large dust grains does not result from the hydrodynamical model and might not be captured by the assumption that dust grains are tightly coupled to the gas. Larger dust is likely to be present and add to the continuum emission. As larger dust could be less coupled to the gas, the spirals would appear weaker. In this case, the spirals should remain unobservable at $t = 259$ yr even for a more refined treatment of the dust.

Interestingly, a jet is observed in the RW Aur system (Hirth et al., 1994; Alencar et al., 2005; Melnikov et al., 2009). Jets are thought to be linked to magnetic fields and could indicate MHD winds launched from the disk. Magnetic fields likely influence the dynamics of warped disks. So far, warping of protoplanetary disks under the influence of magnetic fields has not been well studied.

An interesting fact worth mentioning is that RW Aur A is found to have an unusually high accretion rate of about $10^{-7}\,M_\odot/\mathrm{yr}$ (Hartigan et al., 1995). Cabrit et al. (2006) suggested the recent fly-by as possible explanation, as fly-bys could be able to trigger episodes of increased accretion (so-called FU Orionis events Bonnell & Bastien, 1992; Pfalzner, 2008; Forgan & Rice, 2010). Even though strictly speaking RW Aur A is not an FU Orionis object in the definition (Connelley & Reipurth, 2018, see e.g.), accretion episodes could still play a role for the star and disk. Additionally, several dimming events have been observed for RW Aur A (Rodriguez et al., 2013, 2016; Antipin et al., 2015; Petrov et al., 2015) which have been suggested to be caused by surrounding disrupted material (Rodriguez et al., 2013; Dodin et al., 2019) or a warp in the disk (Bozhinova et al., 2016; Facchini et al., 2016b).

4.6 Conclusion

In this work, we performed simulations of inclined fly-bys passing a protoplanetary disk, where we put the focus on the warping of the disk. In our simulations, we chose to model parabolic orbits ($e = 1$), where the velocity at the periastron is lowest in comparison to other unbound orbits. This means that parabolic fly-bys are expected to have the largest influence on the disk. We find that inclined fly-bys can trigger a warp of a few degrees, which evolves in a wave-like manner through the disk, lasting much longer than the fly-by itself. This means that a warp triggered by a fly-by could still be observed when the fly-by object is long out of sight. The warping is most prominent in fly-bys where the periastron is not in the same plane as the disk, especially in a retrograde fly-by. This is particularly interesting, as the warping in such fly-by configurations has not been studied well before. A known signature of prograde stellar fly-bys are spiral structures, which we also see in our simulations. The spiral structure is relatively short-lived, lasting only about four orbits of the outer disk.

We applied the stellar fly-by scenario to the RW Aur system, where a recent (about 300 yr ago) close encounter between two stars hosting a disk is suspected. Recent orbital fitting by Kurtovic et al. (2024) gives good constraints on the mutual geometry of the fly-by trajectory with respect to the disk, which we can use to set up our simulations. We find that the trajectory of RW Aur B around the RW Aur A is likely to induce a warp of around 5° in the disk around star A, consistent with observational indications of a misalignment between inner and outer disk regions of 6°.

We use radiative transfer simulations of our hydrodynamic model to compare the results to the observations. We find that in dust continuum wavelengths ($\lambda = 1.3$ mm) the disk in our model looks smooth and the spirals are not visible. This compares well to the observation of the dust continuum of RW Aur A. Synthetic kinematic observations could possibly give insight into the observability of a warp. These remain to be evaluated in the near future.

In summary, this work shows that fly-bys might be able to explain frequently observed shadow features in protoplanetary disks. Depending on disk properties, the warp can remain present for longer timescales, so that the perturber might not always be observable. Investigating the ongoing fly-by in the RW Aur system in hydrodynamic simulations can give insight into the dynamics of the system.

Appendices to Chapter 4

4.A Initial azimuthal velocity in the hydrodynamical simulations

The initial azimuthal velocity follows a Keplerian profile with a correction for pressure gradients. Because of the exponential cut-offs in the density, we need to adjust the implementation of the azimuthal velocity in FARGO3D, as the cut-offs introduce additional pressure gradients that are not accounted for in the default implementation. For that, we set the initial azimuthal velocity to

$$v_\phi(r) = v_\mathrm{k} \left(\frac{r}{r_\mathrm{cyl}} \right)^{i_\mathrm{fl}} + \frac{r_\mathrm{cyl}}{\rho} \frac{\partial\, p(r_\mathrm{cyl}, z)}{\partial r_\mathrm{cyl}}, \tag{4.13}$$

where $v_\mathrm{k} = \sqrt{GM_*/r}$ is the Keplerian velocity, r the spherical radius and r_cyl the cylindrical radius in the coordinate system where the central star is at the origin, ρ the density, and p the pressure. As in Dullemond et al. (2020), Equation C.6, we use the cylindrical radius in this pressure gradient correction. We solve the differential quotient in the initial setup numerically with the first-order midpoint method on a fine grid. Without this adjustment for the azimuthal velocity, the disk would spread and quickly smooth out the surface density cut-off especially at the outer disk edge, as the material would possess too much angular momentum. This effect can be seen in Kimmig & Dullemond (2024), Figure B.3, where the pressure gradient due to the cut-off had not yet been accounted for.

4.B Spirals

Here, we present the spiral structure excited by the stellar fly-by in the prograde simulation of Configuration 2. In Figure 4.B.1, we show the 2D surface density, which we obtain by vertically integrating the density in each radial shell. We show different snapshots within the lifetime of the spirals of about 500 yr, as suggested by Figure 4.11.

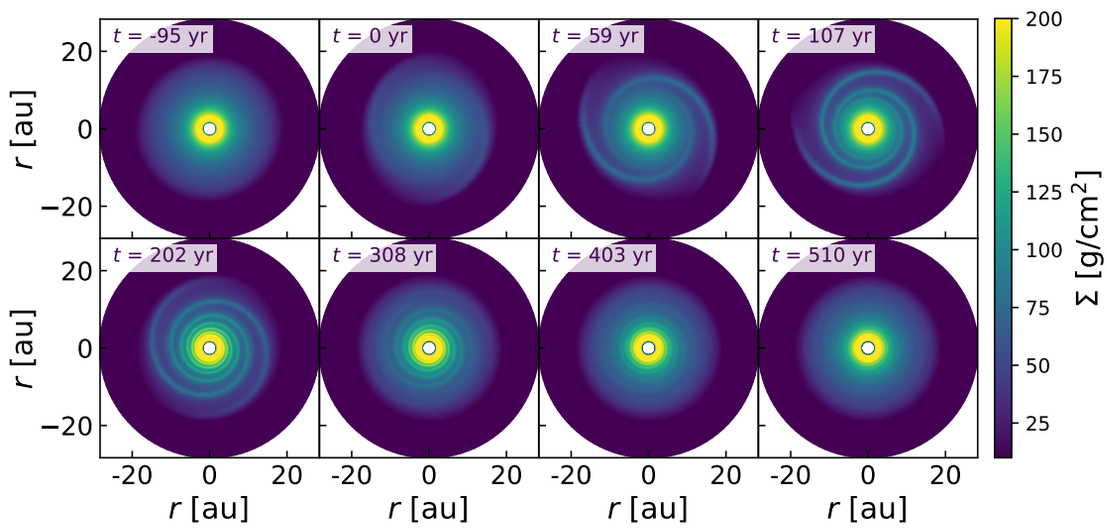

Figure 4.B.1: Snapshots of the simulation with an inclined prograde fly-by in Configuration 2 (periastron out of the disk plane). The closest approach occurs at $t = 0$ yr. The color scale for the surface density is linear, which highlights the spirals better than a logarithmic scale.

In agreement with Smallwood et al. (2023), the pitch angle decreases over time as the spirals wind up. A detailed measurement of pitch angle and pattern speed is not trivial and would go beyond the scope of this work.

4.C Calculation of the mutual geometry between orbit and disk

In this section, we derive the equations to find the mutual geometry of disk and orbit, in the case that the geometry of the disk plane and the orbit is given in the reference frame of the sky. We performed this consideration on the basis of the RW Aur geometry system, which is why we chose some definitions that are convenient for this specific case. However, this geometry consideration can be applied to other systems if careful attention is brought on these definitions.

We define a left-handed coordinate system for the sky frame[2], with the z^{sky}-axis pointing away along the line of sight, as shown in Figure 4.C.1.

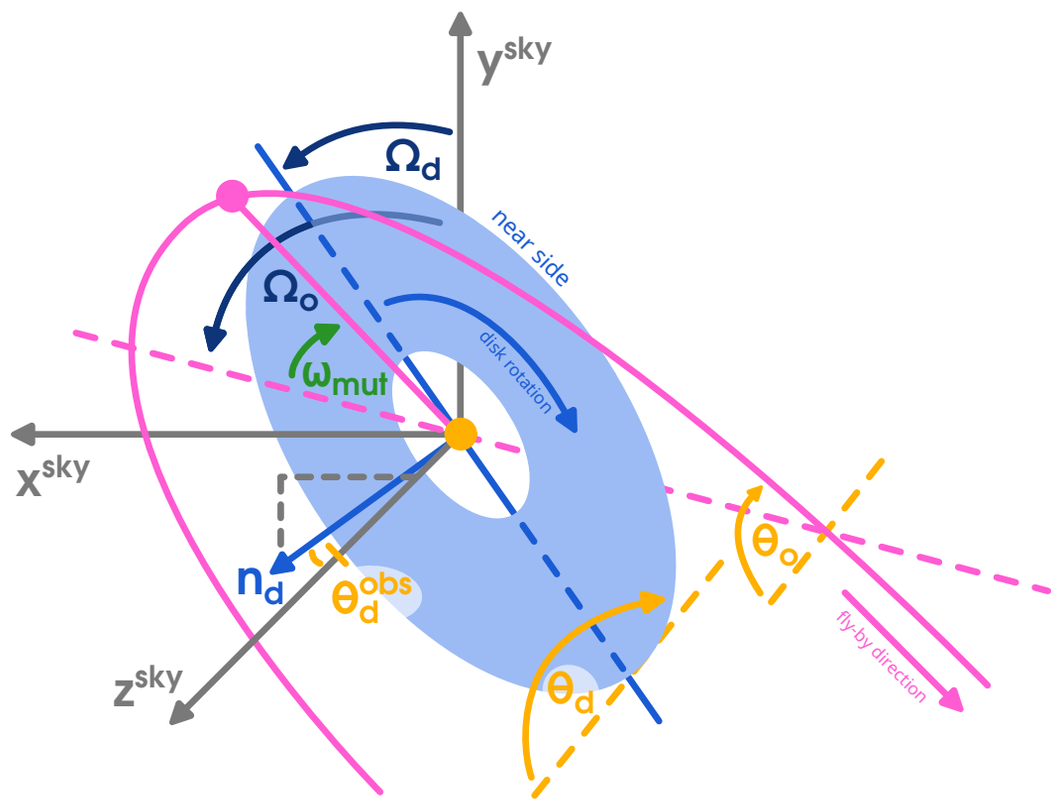

Figure 4.C.1: Geometry of the disk and fly-by orbit of the RW Aur system in the reference frame of the sky. Light blue indicates the disk, pink indicates the orbit, where the pink dashed line shows the crossing line of the plane of the orbit with the x-y-plane and the periastron (pink dot) is "in front", meaning closer to us than the x-y-plane. The position angles $\Omega_{\text{d,o}}$, inclinations $\theta_{\text{d,o}}$ and the argument of the periapsis of the orbit ω_{o} are defined consistently with our definition in Figure 4.2. Note that this coordinate system is left-handed.

An observed disk is characterized by a position angle Ω_{d}, which corresponds to the longitude of ascending node in the plane of the sky, and an inclination θ_{d} with respect to the sky plane. From these angles, we can construct the normal vector of the disk in the reference frame of the sky

$$\vec{n_{\text{d}}} = \begin{pmatrix} -\sin(\theta_{\text{d}})\cos(\Omega_{\text{d}}) \\ -\sin(\theta_{\text{d}})\sin(\Omega_{\text{d}}) \\ \cos(\theta_{\text{d}}) \end{pmatrix}, \tag{4.14}$$

[2]This left-handed coordinate system is motivated by the fact that East and West are typically flipped in observational coordinate systems.

where Ω_d is the longitude of ascending node of the disk, corresponding to the crossing line of the disk with the plane of the sky. This angle is defined from North, or positive y-axis, as indicated in Figure 4.C.1.

It is important to note that according to the geometry definition of trajectory to disk in Figure 4.2, the inclination angle θ_d is not the same angle as the inclination typically given in observations θ_d^{obs}. This θ_d^{obs} is defined as the angle between the normal vector and the part of the line of sight pointing toward us (see Figure 4.C.1). By this definition, $\theta_d = \pi - \theta_d^{obs}$. When we plug this into the normal vector in Equation 4.14, with $\sin(\pi - \theta) = \sin(\theta)$ and $\cos(\pi - \theta) = -\cos(\theta)$ we see that the third component is negative for $|\theta_d^{obs}| < \pi$. This aligns with our definition of a left-handed coordinate system.

The orbit is characterized by a position angle Ω_o, an inclination θ_o, and an argument of periapsis ω_o. Here, the definition of inclination extracted from observations usually aligns with the inclination definition in Figure 4.2, which is why we can use the value from observations directly. The normal vector of the plane can be described analogous to the disk's normal vector

$$\vec{n_o} = \begin{pmatrix} -\sin(\theta_o)\cos(\Omega_o) \\ -\sin(\theta_o)\sin(\Omega_o) \\ \cos(\theta_o) \end{pmatrix}. \tag{4.15}$$

4.C.1 Mutual inclination

The mutual inclination between the disk plane and the orbital plane then simply corresponds to the angle between the two normal vectors $\vec{n}_d$ and $\vec{n}_o$. This can be calculated by

$$\cos(\theta_{mut}) = \frac{\vec{n}_d \cdot \vec{n}_o}{|\vec{n}_d|\,|\vec{n}_o|} = \vec{n}_d \cdot \vec{n}_o, \tag{4.16}$$

where the last term holds true because both vectors are unit vectors. This results in

$$\cos(\theta_{mut}) = \sin(\theta_d)\sin(\theta_o)\cos(\Omega_d - \Omega_o) + \cos(\theta_d)\cos(\theta_o). \tag{4.17}$$

The same expression can for example be found in van der Plas et al. (2019), their Equation 4 or Gonzalez et al. (2020), their Equation 2.

4.C.2 Argument of periapsis of the orbit with respect to the disk plane

Finding the argument of periapsis with respect to the disk plane is not trivial. Gonzalez et al. (2020) consider a similar geometric problem in the disk of

HD 100453. However, in their SPH simulations, they were able to measure this angle. Here, we aim to derive an expression to calculate the angle from the given orientations of disk and orbit on the sky.

To derive the equation for this, we construct a vector along the longitude of ascending node of the orbit along the disk plane in the frame of the sky coordinate system, and a vector pointing to the periapsis. The argument of periapsis of the orbit with respect to the disk plane (which we will call *mutual argument of periapsis* in the following) then corresponds to the angle between those two constructed vectors.

First, we construct the vector along the longitude of ascending node of the orbit within the disk plane in the coordinate system of the sky. We call this vector $\vec{d}$ and calculate it with the cross product of the two normal vectors

$$\vec{d}^{\,\mathrm{sky}} = \vec{n}_\mathrm{d} \times \vec{n}_\mathrm{o}, \tag{4.18}$$

which results in

$$\vec{d} = \begin{pmatrix} -\sin(\theta_\mathrm{d})\sin(\Omega_\mathrm{d})\cos(\theta_\mathrm{o}) + \cos(\theta_\mathrm{d})\sin(\theta_\mathrm{o})\sin(\Omega_\mathrm{o}) \\ -\cos(\theta_\mathrm{d})\sin(\theta_\mathrm{o})\cos(\Omega_\mathrm{o}) + \sin(\theta_\mathrm{d})\cos(\Omega_\mathrm{d})\cos(\theta_\mathrm{o}) \\ \sin(\theta_\mathrm{d})\sin(\theta_\mathrm{o})\sin(\Omega_\mathrm{o} - \Omega_\mathrm{d}) \end{pmatrix}. \tag{4.19}$$

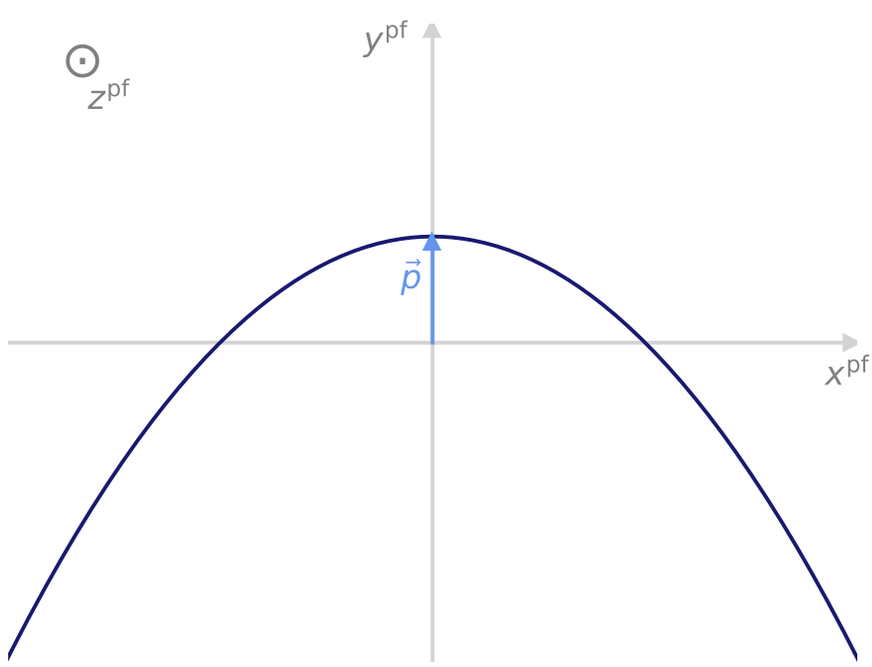

Figure 4.C.2: Our definition of the perifocal frame, which lies in the plane of the orbit.

Second, we need to construct the vector pointing to the periapsis. For this, we define a new coordinate system in the plane of the orbit. We define it such that the periapsis lies on the y_{pf}-axis. We use the index pf for this coordinate system, as it is sometimes called *perifocal frame* (see Figure 4.C.2).

In this perifocal frame, the coordinates of the unit vector pointing to the periapsis are trivial: $\vec{p}^{\mathrm{pf}} = (0,1,0)$. To construct the coordinates of this vector in the reference frame of the sky, we need to rotate the coordinate system along all three angles that characterize the orientation of the orbit. As these characterizing angles are defined counter-clockwise, we need to rotate the coordinate system clockwise in order to find the correct coordinates. In a left-handed coordinate system, the following rotation matrices describe clockwise rotations

$$R_\omega = \begin{pmatrix} \cos(\omega_\mathrm{o}) & -\sin(\omega_\mathrm{o}) & 0 \\ \sin(\omega_\mathrm{o}) & \cos(\omega_\mathrm{o}) & 0 \\ 0 & 0 & 0 \end{pmatrix}, \tag{4.20}$$

$$R_\theta = \begin{pmatrix} \cos(\theta_\mathrm{o}) & 0 & \sin(\theta_\mathrm{o}) \\ 0 & 1 & 0 \\ -\sin(\theta_\mathrm{o}) & 0 & \cos(\theta_\mathrm{o}) \end{pmatrix}, \text{ and} \tag{4.21}$$

$$R_\Omega = \begin{pmatrix} \cos(\Omega_\mathrm{o}) & -\sin(\Omega_\mathrm{o}) & 0 \\ \sin(\Omega_\mathrm{o}) & \cos(\Omega_\mathrm{o}) & 0 \\ 0 & 0 & 0 \end{pmatrix}. \tag{4.22}$$

Using these matrices, we can determine the coordinates of $\vec{p}$ in the frame of the sky

$$\vec{p}^{\mathrm{sky}} = R_\Omega \, R_\theta \, R_\omega \, \vec{p}^{\mathrm{pf}}, \tag{4.23}$$

which gives

$$\vec{p}^{\mathrm{sky}} = \begin{pmatrix} -\cos(\Omega_\mathrm{o})\cos(\theta_\mathrm{o})\sin(\omega_\mathrm{o}) - \sin(\Omega_\mathrm{o})\cos(\omega_\mathrm{o}) \\ -\sin(\Omega_\mathrm{o})\cos(\theta_\mathrm{o})\sin(\omega_\mathrm{o}) + \cos(\Omega_\mathrm{o})\cos(\omega_\mathrm{o}) \\ \sin(\theta_\mathrm{o})\sin(\omega_\mathrm{o}) \end{pmatrix}. \tag{4.24}$$

We note that the rotations do not change the length of this vector, meaning that it still is a unit vector. With this, we can finally calculate the angle between

$\vec{d}^{\,\mathrm{sky}}$ and $\vec{p}^{\,\mathrm{sky}}$, which gives the mutual argument of periapsis

$$\begin{aligned}\cos(\omega_{\mathrm{mut}}) =& \vec{d}^{\,\mathrm{sky}} \cdot \vec{p}^{\,\mathrm{sky}} \\ =& \sin(\omega_{\mathrm{o}}) \sin(\theta_{\mathrm{d}}) \cos(2\theta_{\mathrm{o}}) \sin(\Omega_{\mathrm{d}} - \Omega_{\mathrm{o}}) \\ &+ \cos(\omega_{\mathrm{o}}) \left[\sin(\theta_{\mathrm{d}}) \cos(\theta_{\mathrm{o}}) \cos(\Omega_{\mathrm{o}} - \Omega_{\mathrm{d}}) \right. \\ &\left. - \cos(\theta_{\mathrm{d}}) \sin(\theta_{\mathrm{o}})\right].\end{aligned} \tag{4.25}$$

4.D Unconvolved radiative transfer data

Figure 4.D.1 shows the convolved and unconvolved radiative transfer simulation in comparison to each other. In the unconvolved image, weak spiral structures close to the inner edge of the disk are visible. However, they disappear with the convolution.

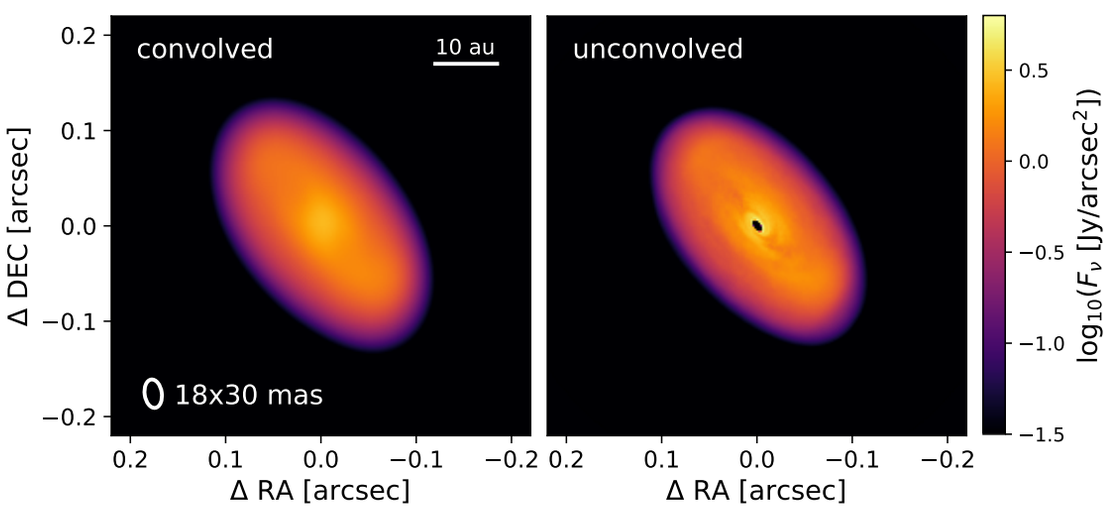

Figure 4.D.1: Like Figure 4.17, but both panels are the radiative transfer model. The left panel is convolved with a Gaussian beam, the right panel shows the unconvolved, raw output from the radiative transfer model.

5

Asymmetric signatures of warps in edge-on disks

This chapter is based on the paper Kimmig & Villenave (2025), accepted by Astronomy & Astrophysics. I performed all simulations presented in this chapter. The main text is written by me with valuable comments from my collaborator Marion Villenave. Only for Sections 5.2.3 (including Figure 5.3) and 5.4 (including Figure 5.10), the base text was written by my collaborator Marion Villenave with contributions from me. The evaluation of the flux ratios and asymmetries (Figures 5.6, 5.7, 5.9, 5.C.2, and 5.C.3) was done by Marion Villenave. The idea for this project originated at the ERC Conference on Planet Formation in Varenna, Italy in June 2024 in connection with the presentation of my research.

5.1 Background

Understanding the physical structure of protoplanetary disks is of critical importance to understand planet formation. Historically, protoplanetary disks have been assumed to be axi-symmetric with all material distributed along the same plane. However, a growing number of observations is revealing the presence of asymmetric features, such as spirals, shadows, and other lateral asymmetries (e.g., reviews by Benisty et al., 2023; Bae et al., 2023). Some of these asymmetries can be indications of a misaligned inner region or warp casting a shadow onto the outer part of the disk. Misalignments or warps might in fact be fairly common in protoplanetary disks. A local misalignment (i.e., broken disk) or warp (i.e., smooth misalignment) will locally perturb the planet formation process and can be a cause for the diversity of planets.

Warps can be formed in many different scenarios. One scenario is a bound companion object, either a planet (Facchini et al., 2014) or a binary companion which is inclined with respect to the disk plane. This could either be an outer companion (Zanazzi & Lai, 2018a), a system with a circumbinary disk (Facchini

et al., 2013; Lodato & Facchini, 2013; Zanazzi & Lai, 2018b; Deng & Ogilvie, 2022; Rabago et al., 2023; Young et al., 2023), or any combination of both. This companion object exerts a gravitational torque on the disk. This torque causes concentric rings within the disk to precess. Because the torque highly depends on the distance to the gravitational perturber, the concentric rings precess on different timescales. This produces the warp shape. The same principle applies to a flyby of a massive object inclined with respect to the disk (Picogna & Marzari, 2014; Dai et al., 2015; Xiang-Gruess, 2016; Cuello et al., 2019, 2023, Kimmig et al., in prep.). Such fly-bys can be common, especially in the early phases of star and disk formation (Pfalzner & Govind, 2021). A further formation scenario is late infall of material, which can add angular momentum in a different direction and thus distort the disk (Dullemond et al., 2019; Ginski et al., 2021; Kuffmeier et al., 2021; Krieger et al., 2024). Finally, a change in the rotation axis during the formation process due to a magnetic field is also suggested to cause misalignments (AA Tau; Bouvier et al., 1999).

The diversity of formation scenarios already hints at the variety of appearances of misalignments in observations. Additionally, warps are highly dynamic (Papaloizou & Pringle, 1983; Papaloizou & Lin, 1995). Once the warp is formed through one of the formation scenarios, internal torques come into play. These internal torques arise due to the misalignment of neighboring orbits, which leads to pressure gradients in the disk. The pressure gradients then cause resonant motions of the gas, called sloshing motions (Dullemond, Kimmig, & Zanazzi, 2022a), and vertical breathing modes (Held & Ogilvie, 2024). These motions exert a torque on the different orbital planes within the disk and hence change the orientation of the orbits. Thus, the net effect of the internal torque and pressure gradients is the evolution of the warp shape.

In typical conditions of a protoplanetary disk (especially low viscosity), the warp travels as a wave through the disk, often referred to as the wave-like regime (Lubow & Ogilvie, 2000; Gammie et al., 2000; Ogilvie & Latter, 2013a,b). Its wave speed is related to the sound speed in the disk (Nixon & King, 2016). The wave is dampened over time, mainly by viscosity, on a damping time scale that can be estimated by $t_{\rm damp} \approx 1/(\alpha\Omega_{\rm K})$, with $\Omega_{\rm K}$ as Kepler frequency evaluated at the outer regime of the disk (Lubow & Ogilvie, 2000). Here, α is the Shakura-Sunyaev viscosity parameter (Shakura & Sunyaev, 1973). This time scale typically ranges from 10^3 to 10^5 years (Foucart & Lai, 2014; Poon et al., 2021; Rowther et al., 2022; Kimmig & Dullemond, 2024). During their evolution, warps may also break into separate disks under certain conditions (Nixon et al., 2013; Doğan et al., 2023; Young et al., 2023; Rabago et al., 2024).

Because of their dynamic evolution, warps can take on various shapes leading

to a plethora of disk misalignment observations. Indeed, asymmetric observations linked to shadows due to warps are recurrent in scattered light imaging of low to mid-inclination protoplanetary disks (e.g., Garufi et al., 2018, 2022; Benisty et al., 2023). Low-inclination systems can show narrow dark lanes (Benisty et al., 2017; Pinilla et al., 2018; Keppler et al., 2020), broad dark regions (Garufi et al., 2016; Debes et al., 2017; Muro-Arena et al., 2020; Kraus et al., 2020; Hashimoto et al., 2024), or a combination of both (Stolker et al., 2016; Benisty et al., 2018). Furthermore, the sensitivity and spectral resolution of ALMA are now allowing to reveal a larger number of warped disks, for example via gas kinematic observations (e.g., Casassus et al., 2015; Loomis et al., 2017; van der Plas et al., 2017; Pérez et al., 2018; Sakai et al., 2019; Yamato et al., 2023).

In parallel, more and more studies also aim to directly compare the orientation of the inner and the outer regions of protoplanetary disks. Francis & van der Marel (2020) compared the inclination and position angle of the inner disk ($\lesssim$ 20au) and main ring of 14 transition disks observed at high angular resolution with ALMA, finding that 8 of them are significantly misaligned. Ansdell et al. (2020) instead analysed a sample of 24 dipper stars, for which the inner disk is believed to have an inclination close to edge-on, and found that the outer disks follow a random distribution of orientations, indicative of significant misalignment for these systems. Bohn et al. (2022) compared the inclination of the outer disk, based on ALMA observations, with that of the inner disk, obtained using VLT/Gravity for a subsample of 20 transition disks. They identify 6/20 disks with clear evidence of misalignments, all of which showing shadows on their outer disks at scattered light wavelengths, compatible with the derived inner disk geometry. Kluska et al. (2020) use reconstructed images of near-infrared interferometry observations to evaluate the symmetry of the innermost region of 15 protoplanetary disks around Herbig AeBe stars. They find evidence of non-axisymmetric emission that can be linked to warps in 5/15 disks.

A key to interpreting the plethora of misalignment observations are models for identifying signatures of warped disks. Such models are able to provide kinematic insight (Casassus et al., 2015; Young et al., 2022; Zuleta et al., 2024) or chemical signatures (Young et al., 2021) in disks containing warps. Shadows can be investigated in synthetic observations in scattered light (Nealon et al., 2019; Juhász & Facchini, 2017). Facchini et al. (2018) investigated shadow signatures of broken disks in intermediate inclination disks and were able to reproduce both dark lanes for strong misalignments, and broad regions for low to moderate misalignments. The location of observed shadows can be used to constrain the geometry of the inner, misaligned disk (Min et al., 2017). The shadows can be variable, e.g. for precessing broken disks (Nealon et al., 2020b).

Asymmetries can also occur in disks observed edge-on (Villenave et al., 2024). Edge-on disks typically appear in scattered light observations as two nebulae separated by a dark line (e.g., Burrows et al., 1996; Stapelfeldt et al., 1998). Those two nebulae correspond to the surface regions of the disk, while the dark line occurs because the material close to the midplane obscures the light from the host star. Thus, the characteristics of the dark line highly depend on properties and vertical distribution of the dust contained in the disk (Watson et al., 2007). On the other hand, the surfaces of the disk are less dense and therefore multiple scattering events allow photons to escape the disk and reach the observer, thus leading to the two bright nebulae. In a perfectly planar, unwarped disk, viewed perfectly edge-on, the nebulae would appear entirely symmetric. Even though observing such a disk with a slight inclination variation would lead to one of the nebulae being brighter due to forward scattering, the extent of both nebulae along their major axis would still be symmetric. However, observations show that a large fraction of edge-on protoplanetary disks at scattered light wavelengths display a shift or lateral asymmetry of their nebulae (15/20 disks analyzed by Villenave et al. 2024, see also Berghea et al. 2024). A misalignment of the inner disk region is proposed to explain this asymmetry, as reproduced in some models (Facchini et al., 2018; Nealon et al., 2019; Villenave et al., 2024).

In this work, we specifically target the scattered light appearance of edge-on and almost edge-on disks containing a warp. We aim to investigate how the asymmetry of the two nebulae changes depending on the warp morphology and to find limits of observability. In addition, we also evaluate the warp geometry that can lead to a switch in the brightest nebula with wavelength, which has been observed in a few systems (Grosso et al., 2003; Villenave et al., 2024). We present our models in Section 5.2 and the results in Section 5.3. In Section 5.4, we link our results to observations by evaluating the misalignment between the outer regions of edge-on disks and jets presumably linked to the inner region. We conclude our work in Section 5.5.

5.2 Methods

To study the appearance of warped edge-on protoplanetary disks, we perform radiative transfer simulations using RADMC-3D (Dullemond et al., 2012). We create most models in a wavelength of $\lambda = 0.8\,\mu$m, but extend it to $\lambda = 2\,\mu$m, $12\,\mu$m, and $21\,\mu$m for some parameter sets. Images in this near- to mid-infrared regime are often called *scattered light images*, as scattered light usually dominates the appearance of disks in these wavelengths. In the longer, mid-infrared regime wavelengths thermal emission can contribute to the radiation from disks, and

we include the thermal emission in all of our models. However, even with the thermal emission, the scattered light scattered light dominates the outcome of the images. The images are scaled by 2.28 au per pixel, and for the evaluation using spine fitting, we assume a distance of 140 pc.

5.2.1 Model set-up

We set up an initial gas density structure, where the surface density profile follows a power law with an exponential cut-off both at the inner and outer disk edge, according to

$$\Sigma(r) = \Sigma_0 \left(\frac{r}{R_0}\right)^{-p} \left(\frac{1}{1+\exp(\frac{r-r_{\rm out}}{0.05\, r_{\rm out}})}\right) \left(\frac{1}{1+\exp(\frac{r_{\rm in}-r}{0.05\, r_{\rm in}})}\right), \tag{5.1}$$

with $r_{\rm in}$ and $r_{\rm out}$ as inner and outer disk edge, respectively, and Σ_0 as surface density at the reference radius R_0, which we set to $R_0 = 5.2$ au. According to typical temperature structures in protoplanetary disks, the vertical extent can be described by

$$h(r) = \frac{H_{\rm p}}{r} = h_0 \left(\frac{r}{R_0}\right)^{i_{\rm fl}}, \tag{5.2}$$

where h_0 is the aspect ratio at the reference radius R_0 and $i_{\rm fl}$ is the flaring index. To parametrize the warp, we implement a tilt profile inspired by Martin et al. (2019) of

$$i(r) = i_{\rm max} \left[\frac{1}{2} \tanh\left(\frac{r - r_{\rm warp}}{r_{\rm width}}\right) - \frac{1}{2}\right], \tag{5.3}$$

with $i_{\rm max}$ as maximum warp tilt, $r_{\rm warp}$ the warp location, and $r_{\rm width}$ is the width of the warp transition. This setup is identical to Kimmig & Dullemond (2024), with adjusted parameters.

In all our models, the disk ranges from $r_{\rm in} = 2$ au to $r_{\rm out} = 200$ au, while the grid extends from 0.5 au to 260 au in the radial direction. We use a full spherical grid, i.e., the vertical extent is set from 0 to π. For the resolution, we chose 250 grid cells in the radial direction, 100 cells in the azimuthal direction and 250 cells in the vertical direction. We set the aspect ratio to $h_0 = 0.1$ and use a flaring disk geometry with $i_{\rm fl} = 0.1$. Similar parameters have been obtained from the modeling of scattered light images of several disks (e.g., Muro-Arena et al. 2018; Sturm et al. 2023, see also Angelo et al. 2023).

We choose for the properties of the star a mass of $M_* = 2.5\, M_\odot$, a radius of $R_* = 1.8\, R_\odot$, and an effective temperature of $T = 10500\, K$. For the gas distribution, we set a slope of $p = 1$ and $\Sigma_0 = 34.3\, {\rm g/cm^2}$ at the reference radius of $R = 5.2$ au, resulting in a gas disk mass of $M_{\rm gas} = 0.01\, M_*$.

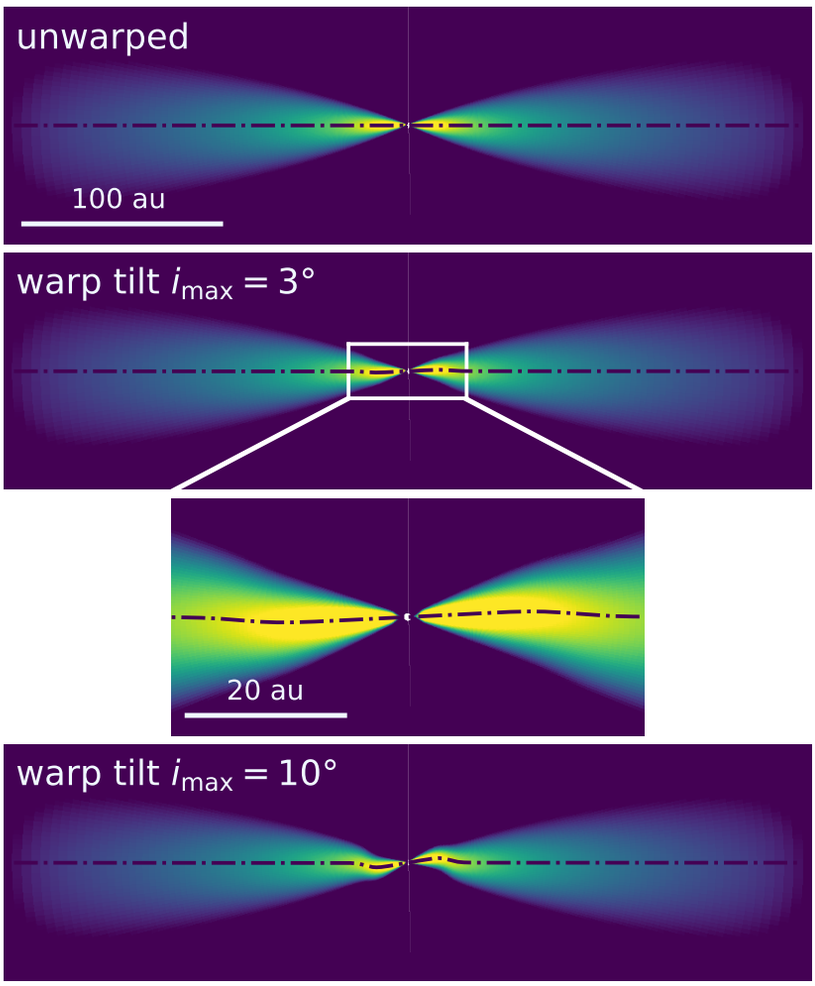

Figure 5.1: Vertical cross-section of the gas density set-up for an unwarped disk, a warp of 3°, and a warp of 10°. The dash-dotted line indicates the disk midplane.

In order to investigate the effect of differently warped disks, we vary the warp tilt i_{max} from 0° to 10° in steps of 1°. For the location of the warp, we set a fiducial value of $r_{warp} = 20\,\text{au}$, but vary the location of the warp for a warp tilt of 3° to $r_{warp} \in \{5\,\text{au}, 50\,\text{au}, 100\,\text{au}\}$. To get a smooth warp transition at all locations, we scale the warp width with the location of the warp using $r_{width} = 0.25\,r_{warp}$. We can measure the warp strength in each case by evaluating the maximal displacement of the disk midplane in terms of the pressure scale height at the location of the warp. Equation 5.3 shows that the tilt angle between the disk midplane at the warp location r_{warp} with respect to the inner (as well as outer) disk midplane is $i_{max}/2$. We can then calculate the displacement w from the height of the midplane $z_{mid}(r_{warp})$ with respect to the midplane of the inner (or outer) disk in terms of

the local pressure scale height at the warp location

$$w = \frac{z_{\mathrm{mid}}(r_{\mathrm{warp}})}{H_{\mathrm{p}}(r_{\mathrm{warp}})} = \frac{r_{\mathrm{warp}} \tan\left(\frac{i_{\mathrm{max}}}{2}\right)}{H_{\mathrm{p}}(r_{\mathrm{warp}})}. \tag{5.4}$$

The numbers of w for the cases in our investigation are given in Table 5.1 and Figure 5.1 shows vertical cross-sections through the gas density for three example cases with different warp tilts (for $r_{\mathrm{warp}} = 20\,\mathrm{au}$).

Table 5.1: Overview over the warp strength w in our disk set-ups

r_{warp} \ i_{max}	1°	2°	3°	4°	5°	6°	7°	8°	9°	10°
5 au			0.26							
20 au	0.08	0.15	0.23	0.31	0.38	0.46	0.53	0.61	0.69	0.76
50 au			0.21							
100 au			0.19							

5.2.2 Radiative transfer

For the radiative transfer simulations, we need to include dust in our models. We assume small dust particles, which are perfectly coupled to the gas and well-mixed, which means that the structure of the dust perfectly follows the structure of the gas disk. Then, we chose a dust-to-gas ratio of 10^{-3}, leading to a total dust mass of $M_{\mathrm{dust}} = 10^{-5} M_*$. We note that this dust-to-gas ratio is slightly lower than typically assumed, because small dust particles likely only make up a fraction of the total dust mass in protoplanetary disks. Despite recent studies on the behavior of larger dust particles in warped disks (Cuello et al., 2019; Aly et al., 2021, 2024), many aspects remain unexplored, which is why we decided to only consider a single grain size of $a = 10\,\mu\mathrm{m}$. This is the simplest possible description, in contrast to a dust size distribution, as such distributions are not yet well constrained for protoplanetary disks. The assumption that dust of this size is well coupled to the gas is supported by observations, at least in some systems (Pontoppidan et al., 2007; Sturm et al., 2023; Duchêne et al., 2024; Villenave et al., 2024). We set a composition of carbon and silicate (pyroxene with 70% magnesium and 30% iron) with a mass ratio of carbon to pyroxene of 0.87/0.13, and a porosity of 25%, according to the DIANA standard dust model (Woitke et al., 2016). We create the corresponding opacity using optool (Dominik et al., 2021). The resulting scattering and absorption opacities are shown in Figure 5.A.1 in the appendix.

To make sure that the qualitative results still hold for a different choice of dust grain sizes, we explored grain sizes of $a = 0.5\,\mu$m and $1\,\mu$m, as well as a dust size distribution in Appendix 5.C. Overall, we find similar results for the lateral asymmetries and flux ratios in all of these models.

The scattering phase functions in our set-up are very forward-peaked, especially for wavelengths up to a few micron. This can lead to very expensive simulations. However, we can use a technique to save computation time, called chopping. In this technique, we chop off a few degrees of the scattering phase function and treat rays within that cone as if they were not interacting with the scattering particle. This technique helps to avoid bright spots that appear in the radiative transfer models if not enough scattering photons are used. We carefully checked the applicability of this technique in our case in Appendix 5.A. For the Monte Carlo temperature calculations, we use 10^8 photon packages. For the near-/mid-infrared radiative transfer images, we use 10^9 scattering photon packages for all images in the wavelengths of $0.8\,\mu$m, $2\,\mu$m, and $21\,\mu$m. We found that at $12\,\mu$m, the same amount of photon packages leads to noisy images, which is why we use twice as much photon packages for this wavelength.

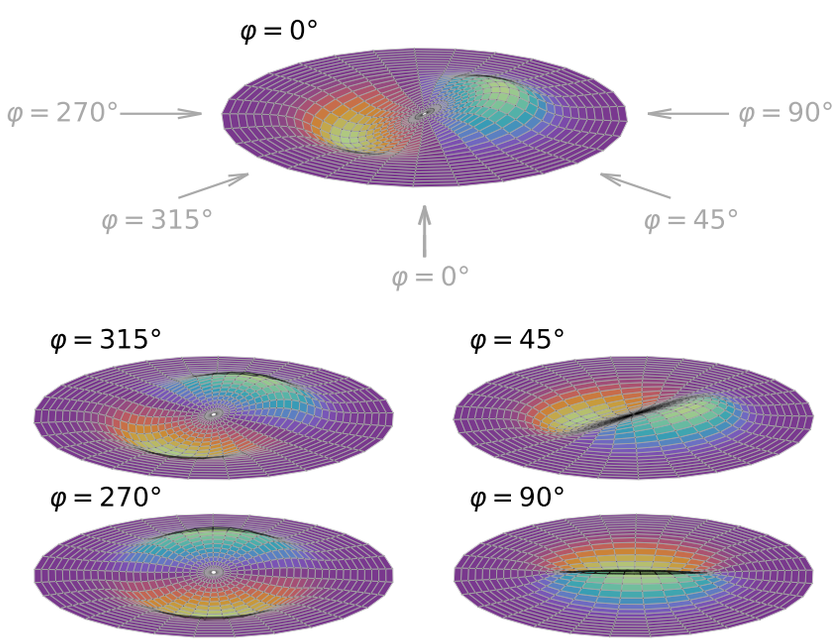

Figure 5.2: Definition of the azimuthal φ-angles. Colors represent the height above the x-y-plane: purple is in plane, blue-green above and red-yellow below. If the outer disk is viewed perfectly edge-on, the quadrant of 270°–0° is identical to the quadrant 0°–90°, only flipped upside down. The sector 90°–270° is identical to the points of sector 270°–90° appropriately rotated and flipped. We chose this definition of φ to be consistent with Villenave et al. (2024).

Because warped disks are not axisymmetric, we need to synthetically observe the disk from different directions. For that, we define an angle φ, so that $\varphi = 0°$ looks at the warp tilt from the side, as illustrated in Figure 5.2. We can exploit some symmetries in the disk, as the disks in our models are untwisted. Therefore, we only need to consider a quarter of the φ-space if the outer disk is viewed perfectly edge-on (inclination of exactly $i = 90°$). The remaining regime of φ can then be achieved by appropriate rotations of the images. In some models, we chose to look at the outer disk slightly inclined ($i = 85°$). In this case, we need to cover half of the azimuthal regime, as a part of the symmetry is broken.

5.2.3 Analysis

Images of edge-on protoplanetary disks in the mid- to near-infrared wavelength regime typically show two nebulae separated by an elongated dark lane. In the presence of a tilted or warped inner region, the illumination of the upper disk surfaces does not follow spherical symmetry and depends on the viewing orientation. This can lead to changes in the flux ratio between the two nebulae and/or to lateral asymmetries.

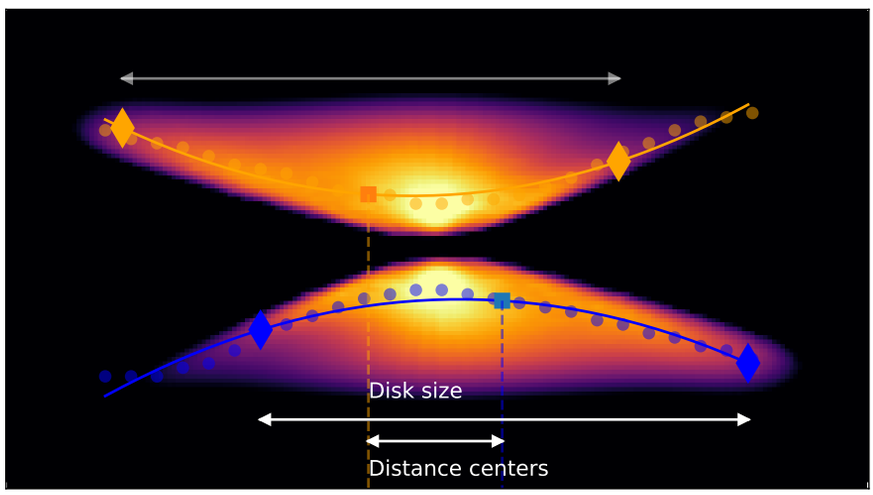

Figure 5.3: Schematic representation of the spine fitting. The light circles show the location of the maxima after a high order polynomial fit of the minor axis profiles. The solid lines represent the final spines after fitting the maxima by a polynomial of order 2. The diamond represent the locations where the flux reaches 10% with respect to the maximum of the spine, and the squares are the center of the spine, i.e., the midpoint of these two points. The lateral asymmetry is the ratio between the distance of the centers to averaged disk size.

To quantify the lateral asymmetry and flux ratio in relation to different warp parameters, we follow the methodology employed by Duchêne et al. (2024) and

following works on JWST observations. This method identifies a "spine" for each of the two scattering nebulae[1]. To do so, the method first estimates the location of the two maxima along the minor axis profiles for every location along the nebulae. The minor axis profiles, averaged to a resolution of 0.1″ or 0.2″ (for a disk model at a distance of 140 pc), are fitted by a polynomial function of order 6 or 8, which is used to assess the location of the two maxima. Those are then fitted by a polynomial function of second order to determine the two spines. On both spines, we then identify the two points on each side of its maximum where the flux reaches 10% with respect to the maximum. We define the midpoint of these two points as the center of the spine, and define the distance between them as the disk size. Finally, following Villenave et al. (2024), we define the lateral asymmetry $\delta_{\rm spine}$ as the distance between the center of both spines in the direction along the nebulae's major axis, divided by the averaged disk size. The procedure described above is repeated multiple times for different radial extents on the scattering nebulae, between 0.9″ and 1.6″ with steps of 0.1″, and for other parameters (averaged resolution, polynomial order) in order to estimate an error on the measurement of the lateral asymmetry. A schematic representation of the spine fitting is shown in Fig. 5.3.

In addition, independent of the spine fitting, we estimate the integrated flux ratio between the top and bottom nebulae. We do this by taking the ratio of the total flux included in the top nebula divided by the total flux of the bottom nebula. We notice that this definition is the inverse of that of Villenave et al. (2024). Therefore the flux ratio in our unwarped models is greater than one for a disk inclined at 85°, in contrast to theirs being smaller than one.

5.3 Results

Protoplanetary disks in near-/mid-infrared show, if they are viewed edge-on (at an observer inclination close to 90°), two nebulae separated by a dark lane. In the following section (Section 5.3.1), we present the near-infrared images[2] at $\lambda = 0.8\,\mu$m for different warp morphologies, as well as our analysis of the lateral asymmetry and the flux ratio between the two nebulae. In Section 5.3.2, we will discuss images at multiple wavelengths. In Appendix 5.B, we additionally show the models of an unwarped reference case, both perfectly edge-on and slightly inclined (85°).

[1] We note that we call it spine due to the arc-like shape. It is not identical to the mathematical spline-fitting method.

[2] We note that we do not show all images of all models we created, but a select sample. However, every dot in Figures 5.6, 5.7, and 5.9 is a full near-/mid-infrared radiative transfer simulation.

5.3.1 Near-infrared images at a single wavelength

We present near-infrared images at $\lambda = 0.8\,\mu$m of different warp amplitudes (characterized by $i_{\max}$) in Figure 5.4, top two rows. The bottom row in this figure shows models with different locations of the warp, or in other words different sizes of the misaligned inner region. All disks in this figure are viewed perfectly edge-on and at an azimuthal angle of $\varphi = 0°$, meaning that the warp tilt is viewed from the side (see Figure 5.2). For this viewing angle, the lateral asymmetry is maximal, as the shadowed regions of both nebulae are the most opposite.

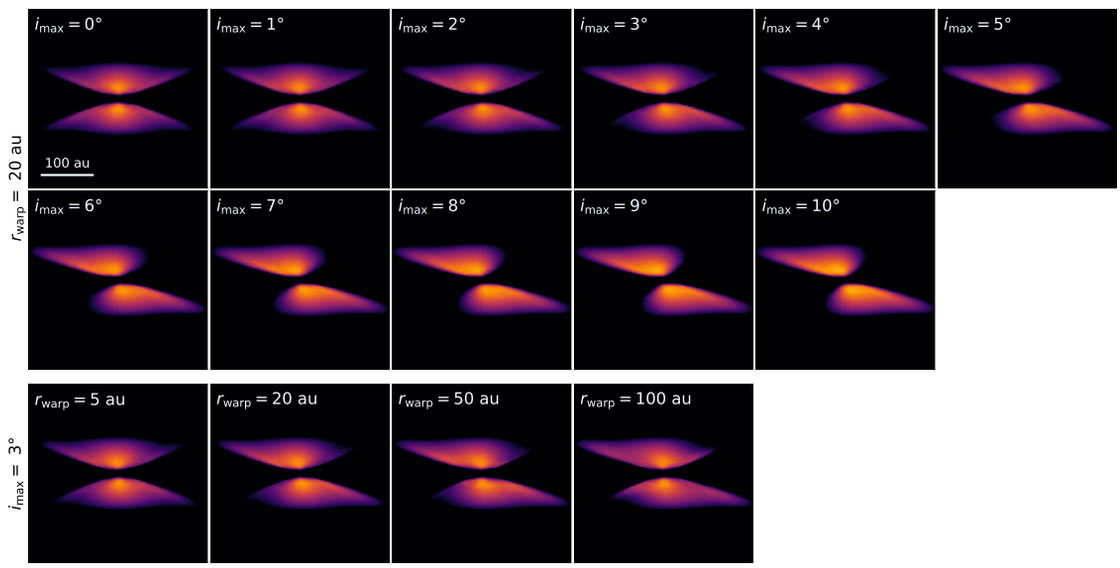

Figure 5.4: Near-infrared radiative transfer models of disks with different amplitude warps defined by $i_{\max}$, observed at $\lambda = 0.8\,\mu$m at $\varphi = 0°$ (top two rows). The bottom row shows models with a varying warp location or in other words a varying size of the misaligned inner region. For the color, we use a logarithmic scale.

The orientation of the warped disk with respect to the observer has a large effect on the visibility of the asymmetry. In Figure 5.5, we show how this picture changes for different azimuthal orientations in the model with a misalignment between inner and outer disk of $i_{\max} = 3°$. The top row shows the perfectly edge-on view (inclination of 90°), while the bottom row presents a disk inclined by 85°. The figure shows that the lateral asymmetry vanishes for azimuthal viewing angles shifted by 90° from zero, as the misaligned inner region is viewed face-on in these cases (see Figure 5.2, bottom row).

To quantify the results of the near-infrared images, we evaluate the lateral asymmetry, as well as the flux ratio between the two nebulae as described in Section 5.2.3. Figures 5.6 and 5.7 present both quantities for our models with varying warp amplitude and warp location, respectively. In all those models, the outer disk is viewed perfectly edge-on. By eye, we define a lateral asymmetry of $\geq 10\%$

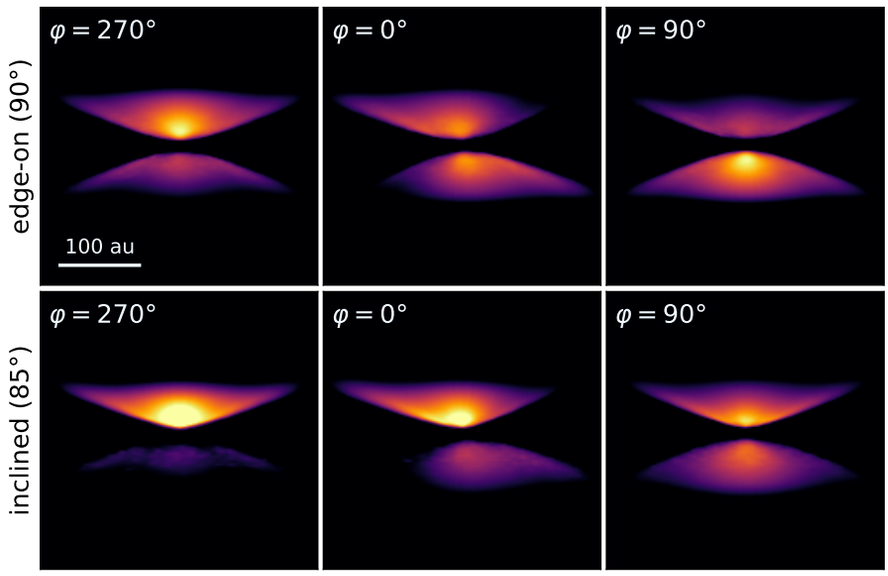

Figure 5.5: Near-infrared radiative transfer models ($\lambda = 0.8\,\mu$m) of a disk with tilt $i_{\max} = 3°$ observed from different azimuthal angles φ (color in log-scale). The top row shows a perfectly edge-on view, while the bottom row shows the disk observed at an inclination of 85°. We note that for symmetry reasons, we do not need to simulate $\varphi = 90°$. The image shown in this figure is the simulation of $\varphi = 270°$ flipped upside down.

to be visible and note that this is a somewhat arbitrary definition, but motivated by previously published work (see Villenave et al., 2024). The pink shaded region in Figures 5.6 and 5.7 indicates the region below this visible threshold.

We find that the stronger the warp (higher $i_{\max}$), the stronger the lateral asymmetry. This result is expected, since stronger misalignments can cast larger shadows. In Figure 5.4, we see that the lateral asymmetry of a warped disk can be visible in scattered light with a misalignment of only 2°. This means that even slight warps can in principle be observable. However, we note that this is only the case for the best azimuthal viewing angle. For viewing angles within 30° around $\varphi = 270°$ (and $\varphi = 90°$, respectively), even a stronger warp of 10° misalignment can not produce a significant lateral asymmetry (see Figure 5.6).

The difference in flux between the two nebulae, on the other hand, is maximal for a viewing angle of $\varphi = 270°$ and, for an edge-on view on the outer disk, equals one if the warp is viewed directly from the side ($\varphi = 0°$). In observations, the flux ratio by itself is not a unique indication of a warp or misalignment, since slightly inclined planar disks also exhibit a difference in flux between the two nebulae. However, the variation of the flux ratio with wavelength can be a strong indicator of warps, which we will explore in Section 5.3.2.

When changing the location of the warp (bottom row in Figure 5.4), we can see a similar effect: the further out the warp, the stronger the asymmetry in the

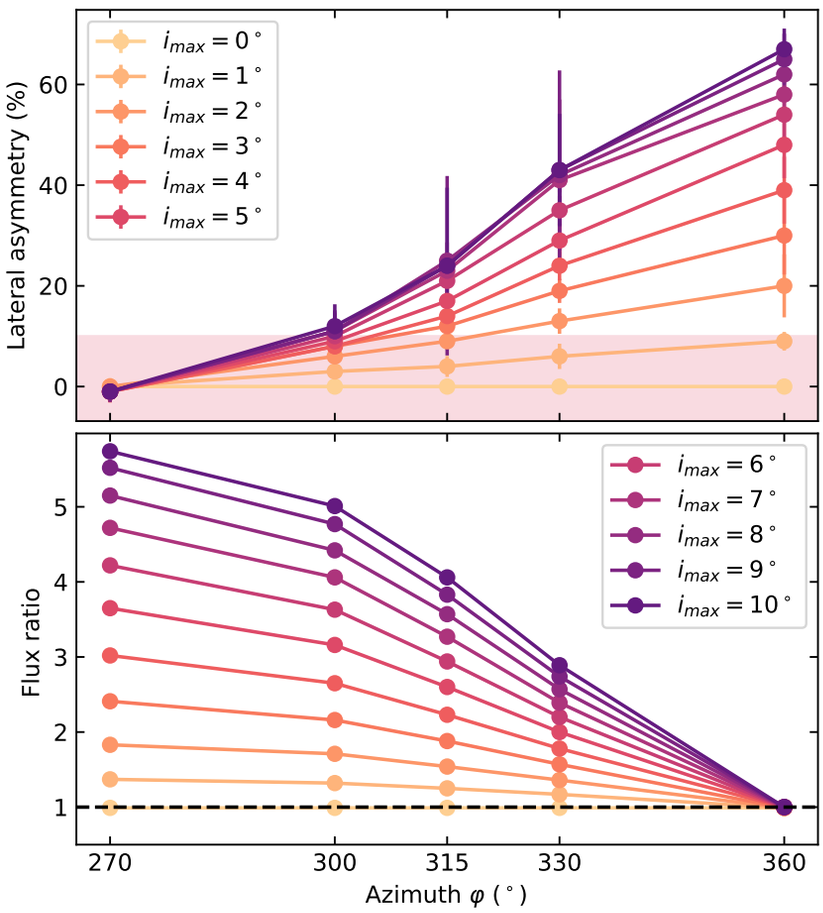

Figure 5.6: Lateral asymmetry (top) and flux ratios (bottom) for warped disk models of different warp tilts $i_{\max}$ (at $\lambda = 0.8\,\mu$m). The outer disk is viewed perfectly edge-on (meaning an inclination of 90°). For symmetry reasons, we only need to model a quarter of the azimuthal regime in this configuration. The curves can be extended to the remaining regime by flipping the curves appropriately. The pink shaded region in the top panel corresponds to a lateral asymmetry of $< 10\%$, which is what we assume not to be visible by eye.

near-infrared images. However, this only holds true up to a certain point, as a warp location of 100 au shows slightly less asymmetry than a warp location of 50 au, see bottom row of Figure 5.4 and Figure 5.7. We suspect this to occur because of the way we set up the warp shape, as we scale width of the warp with the warp location. This description is the most natural, because it is coherent in logarithmic space. However, considered linearly, the warp transition is wider for warps located further out, leading to a less steep warp curve where more light can pass. This reduces the size of the shadowed region and causes less lateral asymmetry.

Additionally, we find the flux ratio for the case of $r_{\text{warp}} = 100$ au to be smaller than for some warps closer in at all azimuthal angles. This could again be linked

to the set-up of the warp: Because the warp is close to the outer edge, the outer disk is small compared to the other models, which could influence both lateral asymmetry and flux ratio.

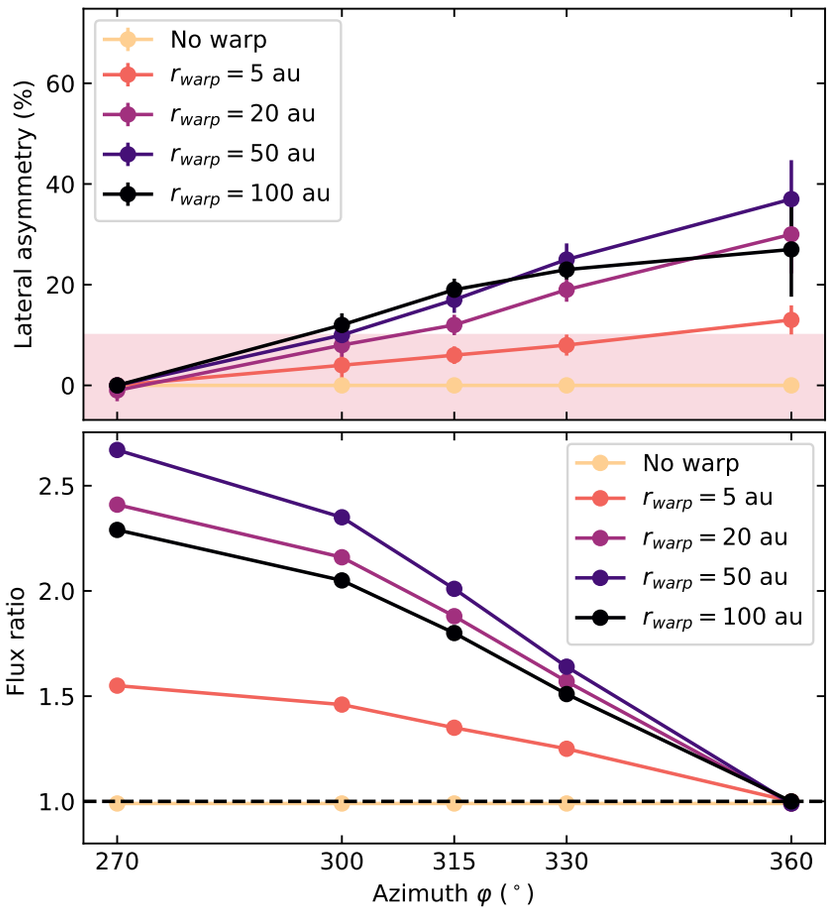

Figure 5.7: Same as Figure 5.6, but for different warp locations r_{warp} for a warp amplitude characterized by $i_{\mathrm{max}} = 3°$. Again due to symmetry reasons, the curves can be extended to the whole azimuthal regime. As in Figure 5.6, the pink shaded region highlights the lateral asymmetry we assume not to be visible by eye.

An interesting fact is that the image of the warped disk at $\varphi = 270°$ with the outer disk viewed perfectly edge-on (top left image in Figure 5.5) looks very similar to an unwarped disk which is inclined with respect to the observer, see Figure 5.B.1 in Appendix 5.B, bottom left panel. For observations, this means that it can be difficult to distinguish between an inclined planar disk and a perfectly edge-on warped system. We notice that in our models, the near-infrared image of the inclined planar disk is more strongly peaked toward the star. However, this is unlikely to serve as distinction for observations, since the disk parameters are usually not known precisely.

5.3.2 Near-/mid-infrared radiative transfer models in multiple wavelengths

A few observations of protoplanetary disks show a swap of the brightest nebula with wavelength: in shorter wavelengths one nebula appears brighter, while the other nebula appears brighter in longer wavelengths. This phenomenon is rare, so far it has only been observed in three disks: IRAS04302+2247, HH30, and 2MASS J16281370-2431391 (Flying Saucer). The swap does not occur at the same wavelength for the observed disks. In IRAS04302+2247, the swap occurs between $\lambda = 12.8\,\mu$m and $21\,\mu$m (Villenave et al., 2024), while the switch for the Flying Saucer occurs between $\lambda = 1.3\,\mu$m and $2.2\,\mu$m (Grosso et al., 2003). Finally, Tazaki et al. (2025) identified a change in the brightest nebula of HH30 between $7.7\,\mu$m and $12.8\,\mu$m. They mentioned intrinsic flux variability between epochs as a potential origin for a wavelength swap. However, with their observations being observed consecutively within 3h, they ruled out this possibility for this system. On the other hand, Villenave et al. (2024) were able to recreate this phenomenon in a broken disk with a misaligned inner region. In this work, we aim to investigate if a continuously warped disk exhibits a similar behavior

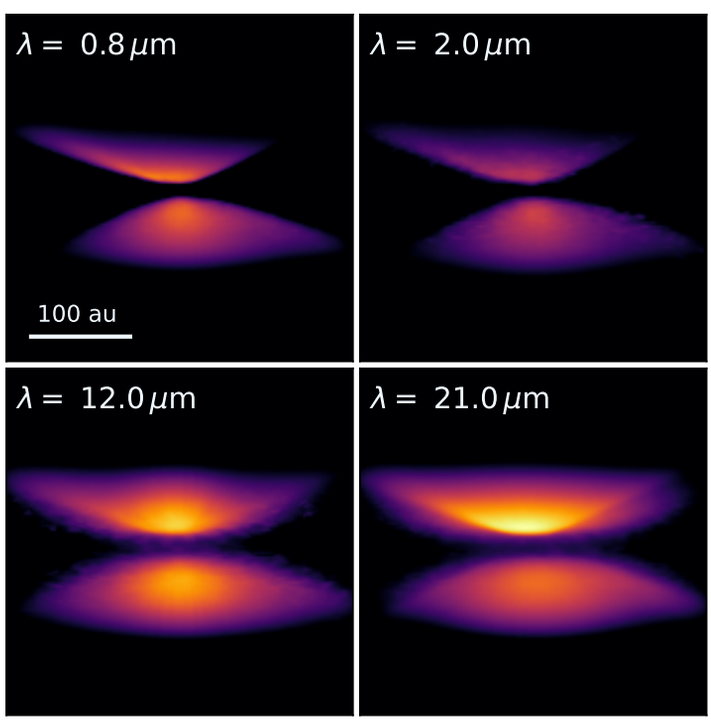

Figure 5.8: Near-/mid-infrared radiative transfer models of a disk with tilt $i_{\max} = 10°$ at $\varphi = 60°$ with an inclination of 85° observed in different wavelengths (color in log-scale). Considering the integrated flux, the bottom nebula is brighter than the top at shorter wavelengths, but at $\lambda = 21\,\mu$m, the top nebula is brighter.

For that, we present radiative transfer simulations in four different wavelengths: $\lambda = 0.8\,\mu$m, $2\,\mu$m, $12\,\mu$m, and $21\,\mu$m. We test the multi-wavelength behavior for two different warp tilts $i_{\max} = 3°$ and $10°$. In these models, the outer disk is viewed at an inclination of 85°, because the phenomenon only occurs for slightly inclined disks, as discussed later in this section. We indeed find a swap in brightest nebula in specific cases. Figure 5.8 shows an example of such a case, in especially, a warp tilt of 10° and an azimuthal viewing angle of $\varphi = 60°$. For the shortest wavelength, $\lambda = 0.8\,\mu$m, the bottom nebula is brighter, while for $\lambda = 21\,\mu$m, the top nebula clearly appears brighter.

The phenomenon of the switch between brightest nebula can be explained by the shadow from the misaligned inner region. First, we need to understand that in a general disk that is slightly inclined with respect to the line of sight, one of the nebulae appears brighter than the other. This is because forward scattering is dominant over backward scattering (see e.g. Benisty et al., 2023, their Figure 2), which makes the nebula closest to the observer brighter. Now, an inclined warped disk could be oriented in such a way that this brighter nebula is actually shadowed by the misalignment. In this case, the nebula actually appears darker. However, in longer wavelengths, the disk could be able to emit more thermal radiation and therefore the shadow would be less pronounced. Thus, the nebula can again appear brighter. To test the hypothesis, we performed additional radiative transfer simulations with the scattering switched off (option `scattering_mode_max=0` in RADMC-3D). We indeed find almost no emission for $\lambda = 0.8\,\mu$m and $2\,\mu$m, indicating that the light in the scattering simulations indeed results purely from scattered light. In contrast, we find thermal emission in these test simulations in the wavelengths $\lambda = 12\,\mu$m and $21\,\mu$m, where it is more significant for the latter. However, we want to point out that the scattered light still dominates the appearance of the disks at both of these wavelengths. In summary, the fact that the thermal emission becomes more significant for longer wavelengths means that the shadows in the scattered light become less pronounced, which enables the swap in brightest nebula with wavelength.

Evaluating the flux ratios quantitatively in Figure 5.9, we see that for a φ-regime of between 30° and 90° (and due to symmetry also up to 120°), a flux ratio swap between wavelengths can be possible. This only occurs for the stronger warp of $i_{\max} = 10°$ in our models. For the moderate warp of $i_{\max} = 3°$, the variation of the flux ratio with azimuthal angle is less strong at all wavelengths, so that the ratio never drops below one.

Concentrating on the disk containing a stronger warp, we see that the shape of the flux ratio curve differs with wavelength. Generally, for shorter wavelength the curve is steeper and there is a stronger variation of the flux ratios with az-

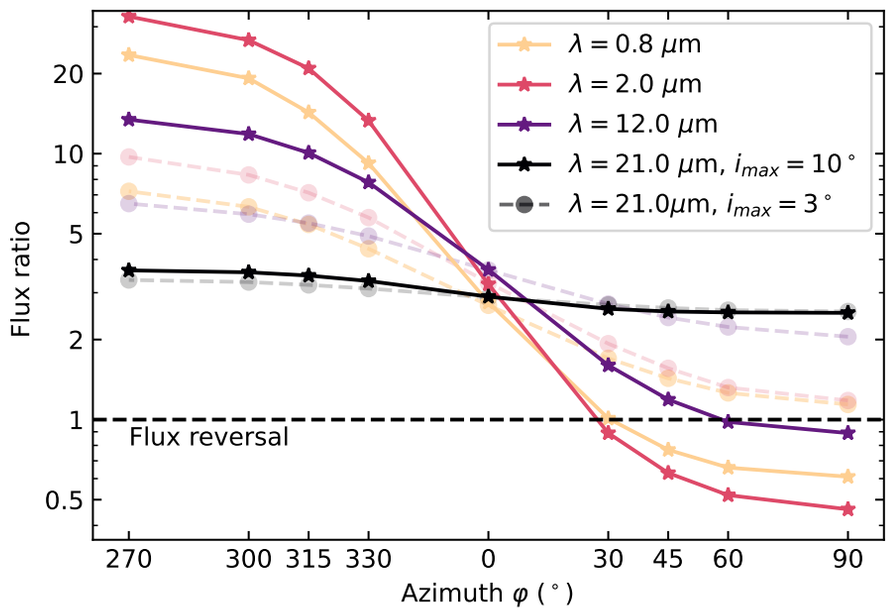

Figure 5.9: Flux ratios for models of warped disks with a warp tilt of 10° (solid lines) and of 3° (light dashed lines) in four different wavelengths. The outer disk is oriented with an inclination of 85°. In this case, we need to calculate the models for half of the φ-regime, the other half is symmetric. The dashed black line indicates the line where the flux ratio equals one (where both nebulae have the same brightness). We note that the y-axis is plotted in log-scale.

imuth. Interestingly, a wavelength of $\lambda = 2\,\mu$m shows more variation than $\lambda = 0.8\,\mu$m. This could be due to a difference in the chopped scattering opacity and consequently a difference in albedo (see Figure 5.A.1). The flux ratio curve for $\lambda = 21\,\mu$m is shallowest, leading to a flux ratio always above one. At the shorter wavelengths, the flux ratio drops below one for orientations where the misalignment is shadowing the otherwise brighter nebula. We see that this swap of brightest nebula can occur at different wavelengths, depending on the azimuthal orientation of the disk. Recall that we evaluate the flux ratio by using the integrated flux in our models. We additionally checked the flux ratios when considering only the peak intensity and found that the curves are qualitatively the same, but slightly noisier and shifted, so that only the curve of $\lambda = 2\,\mu$m drops below one. However, the swap still occurs and with slightly different parameters, such as a different inclination of the outer disk, a similar result can be achieved in peak intensity flux ratios.

In our models, we notice that the azimuthal curve at 21 μm follows the same qualitative shape as the shorter wavelengths, with their maximum at $\varphi = 270°$ and their minimum at $\varphi = 90°$ (see Figure 5.9). On the other hand, Villenave et al. (2024) find that the 21 μm curve is flipped with respect to the shorter wave-

lengths. This difference could lie in the different opacities and geometry of the models. Specifically, Villenave et al. (2024) investigated a broken disk, while we investigate a continuously warped disk. In a broken disk, the inner edge of the outer disk and the outer edge of the inner disk could thermally radiate onto the outer disk in longer wavelengths and therefore leading to the inversion of the curve. Because in the models of this work, there are no gap edges, we expect this thermal emission to be less strong.

At this point, we want to note that we expect the phenomenon of the swap in brightest nebula with wavelength to occur rarely, because a very specific orientation of the observed disk is required. In especially, the outer disk needs to be slightly inclined with respect to the observer, and the azimuthal viewing orientation of the system is restricted to a specific regime with respect to the orientation of the misalignment. This expectation connects to the fact that as of now, only three disks have been observed to exhibit this phenomenon. However, if observed, a change in the brightest nebula with wavelength can be a strong indicator of a misalignment between inner and outer disk.

5.3.3 Caveats

The findings in this work provide valuable insight, although they should be considered within their limitations, which we discuss in this section.

Most importantly, the results significantly depend on the disk model. The vertical thickness and flaring of the disk influence the extent of the shadows. In thinner disks with a lower aspect ratio, we expect a stronger lateral asymmetry, because a larger part of the outer disk's surface can be hidden behind the misalignment. In thicker disks, on the other hand, the outer disk can be puffed up enough to bulge out of the shadow. A similar argument applies when considering differently flared disks, which occurs for different temperature structures. With more flaring, the surface can bulge out more, leading to less lateral asymmetry. In the same line of arguments, the size of the disk, in especially with respect to the location of the warp, can also influence the lateral asymmetry. Additionally, the warp parametrization has a strong impact on the shadowed region. As it is not well constrained yet, we studied one of simplest warp shapes in this work: a warp that is only tilted in one direction. In general, there can be more complicated shapes, for example twisted disks or multiply warped/twisted disks, leading to more complex shadow signatures. Since the overall parameter space for disk and warp shapes is extremely large, a further exploration would go beyond the scope of this work.

Another factor influencing the results of the near-/mid-infrared images is the

scattering opacity, which depends on the dust properties and total dust mass (Watson et al., 2007). A higher dust mass would lead to a higher opacity and we therefore expect the dark lane between the nebulae to be wider, possibly influencing the lateral asymmetry. Different dust sizes or a size distribution can also strongly affect the opacity. In our models, we only consider small dust grains that are perfectly coupled with the gas. Although it is likely that larger dust particles are present in protoplanetary disks, we do not expect them to have a strong effect, as they are likely settled to the midplane (e.g. Villenave et al., 2020). We additionally recall our use of the so-called chopping mechanism of 2° to calculate the scattering matrix due to the forward peaked phase functions at small wavelengths. Although we thoroughly tested the applicability of this mechanism to our case in Appendix 5.A, it remains an approximation. We notice that we slightly overestimate the total flux by a few percent when using the chopping mechanism. Since we are mainly interested in the lateral asymmetry and flux ratios, this does not have a large effect on the results in this work.

We also note that the near-/mid-infrared images presented in this study are not convolved to a specific instrument resolution, in order to keep this study general as convolution may depend on specific telescope settings. As the images are fairly smooth, we do not expect a convolution to significantly change the results.

Lastly, we mention that our definition of the lateral asymmetry is somewhat arbitrary. We lean the definition on previously published work, but it can be defined differently, which could have an impact on the results. Our fitting method strongly depends on the parameters chosen, namely the radial range of the spines, the radial and vertical averaging of the minor axis profiles, the order of the polynomial function fitting the minor axis profiles, the assumed location for the center of the dark lane. In this work we explored how varying these parameters will impact the results, reaching to error bars between a few percents to tens of percents (see Fig. 5.6 and Fig. 5.7). However, due to the limited parameter space explored, the relative comparison between models are likely more robust than the absolute values of the lateral asymmetries.

5.4 Occurrence of warps in protoplanetary disks

In Section 5.3, we investigated the level of lateral asymmetry that can be expected for different warp amplitudes and locations, under our fiducial assumptions for dust opacities and warp geometry. Here, we aim to link these predictions to direct observations of edge-on protoplanetary disks. We compare the outer disk and jet orientation of four previously published edge-on disks observed at scattered light wavelengths. Our goal is to look for misalignment between the very inner regions

of the disks, where the jet is launched, and the outer disk seen in scattered light or at millimeter wavelengths. Then, we compare apparent misalignments with the observed lateral asymmetry to assess the potential geometry of the systems.

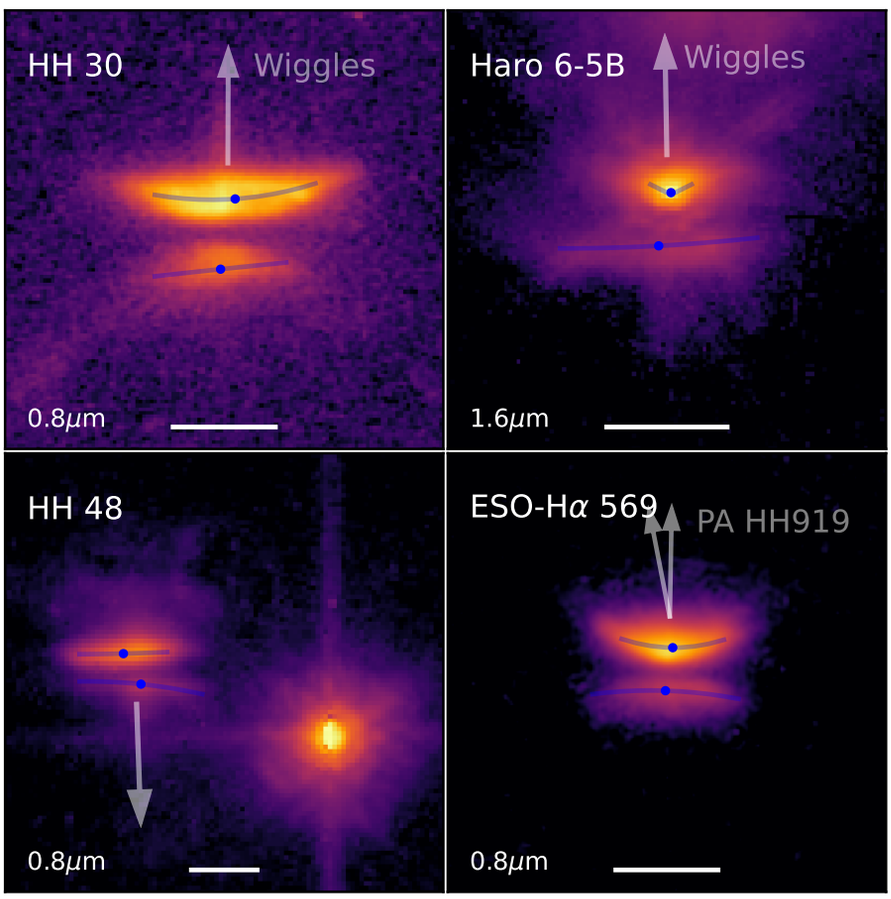

Figure 5.10: Scattered light observations of four edge-on disks in log-scale, where we estimate the level of lateral asymmetry (blue spines) and indicate the estimated direction of the jet (white lines). A 0.5" horizontal line is indicated in the bottom left corner of the images.

We selected the disks based on the recent study of Villenave et al. (2024), who found that 15 out of the 20 systems that they analyzed display strong lateral asymmetries. Seven sources of this sample display clear jet features, among which we identified four sources with a published value for the position angle (PA) of their jets from high angular resolution observations in the literature (with the other three disks, HV Tau C, Tau042021, and ESO Hα-574 having a jet whose PA is not explicitly characterized in the literature; Stapelfeldt et al. 2003; Duchêne et al. 2014, 2024). We report the values for the jet position angle in Table 5.2. We note however that the published jet PA of HH48, reported by Stapelfeldt et al. (2014), suffered from image distortion in the HST Advanced Camera instrument (K. Stapelfeldt, priv. comm.). In Table 5.2, we report our visual estimate of the jet PA on the distortion corrected image, leaving a more precise measurement for

future work. All disks have been observed and well characterized at millimeter (with ALMA) or scattered light wavelengths (with HST), so we additionally report the outer disk position angle in Table 5.2. If no misalignment is present, we expect the position angle of the jet to be exactly perpendicular to that of the disk's major axis. The scattered light images together with the corresponding jet orientation are displayed in Fig. 5.10.

Table 5.2: Comparison between outer disk position angle (PA_{out}) and jet position angle (PA_{jet})

Disk	HH30	HH48	Haro6-5B	ESO Hα-569
PA_{out} (°)	$121^{(1)}$	$75^{(1)}$	$145^{(1)}$	$155^{(9)}$
PA_{jet} (°)	$31^{(2,3,4)}$	$\leq 13^{(5)}$	$56^{(6,7,8)}$	$60-75^{(10)}$
ϑ (°)	0	$0-2$	1	$0-10$
δ_{spine} (%)	$5-9$	$8-15$	$10-36$	$3-5$
Notes jet/disk	Bending, wiggling	Perturbed nebulae	Wiggling	Assuming jet is HH919 filament

Notes. $\vartheta = |[PA_{out} - 90] - PA_{jet}|$ characterizes the misalignment between the jet (inner disk) and the outer disk. The lateral asymmetry δ_{spine} is fitted using the same method as in the models (see Sect. 5.2.3).
References. (1) Villenave et al. (2020); (2) Burrows et al. (1996); (3) Anglada et al. (2007); (4) Estalella et al. (2012); (5) this work; (6) Eislöffel & Mundt (1998); (7) Krist et al. (1998); (8) Woitas et al. (2002); (9) Wolff et al. (2017); (10) Bally et al. (2006)

All four systems show hints towards small levels of misalignment of their inner disk. In the case of HH48, we find a misalignment between jet and disk bottom nebula of about 2°, while no misalignment with the top nebula is identified. Indeed, HH48 displays an apparent misalignment between its top and bottom nebulae, hinting toward a distorted morphology. A somewhat similar misalignment can also be found in some of our models due to illumination effects, such as in Figure 5.8, top two panels. However, for a good comparison, the current observational constraints on the dust and gas morphology of HH48 are not sufficient. In ESO Hα-569, the jet visible in the scattered light image does not have a published PA, but is thought to be launching the HH919 jet, which could be consistent with either being aligned, or misaligned to the outer disk by up to 10°. Finally, even though the jet and disk of HH30 and Haro6-5B are consistent with no misalignment, the jet of both sources wiggles at large distances. This can be explained in case of varying orientation of the accreted material, suggesting a precession of the inner disk (Terquem et al. 1999; of order of $\sim 1°$ for HH30,

Louvet et al. 2018). Alternatively, interaction with a non uniform environment may lead jets to bend. Regular wiggles as observed in these systems are however not necessarily expected in that case.

Following the methodology previously described (Sect. 5.2.3, Villenave et al. 2024), we estimated the lateral asymmetry in these disks, as represented on Figure 5.10 and indicated in Table 5.2. The strongest lateral asymmetry is found around Haro6-5B ($10-30\%$), while ESO Hα-569 is barely asymmetric ($3-5\%$). HH48 and HH30 show intermediate levels of asymmetries of order 10%.

HH48 shows the most convincing case for a distorted morphology and hints to a misalignment between the jet and the disk plane of up to 2°. Further, the disk presents a significant lateral asymmetry. Within the modeling presented in Sect. 5.3, we found that lateral asymmetry around 10% could be obtained for a warped disk with a misalignment between inner and outer disk of $i_{max} = 1-2^\circ$ if viewed with the optimal orientation ($\varphi \sim 360^\circ$), or for stronger warps, up to $i_{max} = 10^\circ$, for less favorable viewing angles ($\varphi \to 270^\circ$), which would be consistent with the apparent jet/disk misalignment observed. Both the significant lateral asymmetry and the locally aligned but wiggling jets of HH30 and Haro6-5B suggest that these systems could also possess warps, which are, however, weak or not viewed in a favorable orientation. Lastly, ESO Hα 569 could be consistent with either no misalignment or an unfavorable warp orientation.

Finally, we also mention that a local change in the disk scale height, leading to asymmetric shadowing of the outer disk, or variation in the stellar illumination (e.g., spots; Stapelfeldt et al., 1999) could also lead to lateral asymmetries. Dedicated imaging campaigns would be needed to determine the timescale of the variability of the lateral asymmetry and disentangle the mechanisms.

5.5 Conclusion

In this work, we present various near-/mid-infrared images from radiative transfer simulations of edge-on protoplanetary disks containing a warp. Edge-on disks in scattered light typically show two nebulae separated by a dark lane. These nebulae correspond to the two surfaces of the disk, whereas the dark lane corresponds to the optically thick midplane. Warped disks contain a misaligned inner region casting a shadow onto the outer disk, leading to visible asymmetries between the two nebulae. We quantify this asymmetry by fitting a spine curve for each nebula individually and call this relative distance in between the nebula centers "lateral asymmetry". We investigate the visibility of the lateral asymmetry for different warp parameters, especially the warp amplitude and the location of the steepest warp transition, or in other words different sizes of

the misaligned inner region. Additionally, we evaluate the flux ratio between the two nebulae. Because warped disks are not axisymmetric, we performed radiative transfer simulations for images viewed from different azimuthal angles. Most of our simulations are performed at a wavelength of $\lambda = 0.8\,\mu$m, but we extend the simulations to $\lambda = 2\,\mu$m, $12\,\mu$m, and $21\,\mu$m in specific cases.

We find that a warp can be visible in edge-on disks for warp tilts as low as $i_{\max} = 2^\circ$ in optimal azimuthal viewing angles. The larger the warp tilt, the stronger the lateral asymmetry. Additionally, the location of the warp within the disk influences the asymmetry as well. If the warp is located further out, the asymmetry is stronger. This means that in edge-on disks, warps close to the inner edge of the disk are harder to detect. However, our models show a point where the asymmetry decreases for even further warp locations. We suspect this to occur due to the warp transition width which is scaling with radius. This leads to a shallower warp curve, and consequently more light can pass, causing smaller shadows and therefore less lateral asymmetry.

The flux ratio between the two nebulae can also indicate a warp in specific cases. In unwarped and perfectly edge-on disk, the two nebulae have the same brightness. Due to the shadows in warped disks, the flux ratio can vary depending on the azimuthal angle. By itself, the flux ratio is not a strong indicator of a warp, since the relative brightness of the two nebulae also varies in an unwarped disk when it is not oriented perfectly edge-on. Nevertheless, we find that in some rare occasions, the flux ratio can be an indication of warps in observations after all, when observing the disk in multiple wavelengths. For this scenario, the outer edge of the warped disk should be slightly inclined (not perfectly edge-on; we chose an inclination of 85° in our models). If the disk is additionally oriented azimuthally, such that the nebula that would be brighter if unwarped is now shadowed by the misalignment, this nebula appears darker in the near-infrared. At slightly longer wavelength ($12 - 21\,\mu$m in our models), however, the disk's thermal emission is large enough so that this nebula can appear brighter, as the shadow is less prominent, leading to a swap in brightest nebula with wavelength. We confirm this swap in brightest nebula with wavelength if the warp is strong enough, in our models $i_{\max} = 10^\circ$. For small warps ($i_{\max} = 3^\circ$), we can not reproduce this switch even at the best viewing angle.

In observations, such a swap is found in three edge-on disks so far: IRAS04302 +2247, HH30, and Flying Saucer. As expected, this phenomenon is rare, as it requires a very specific orientation of the disk with respect to the observer. However, when it occurs, it is a strong indicator for a misalignment. In observations, the inclination of an observed disk is often inferred from the flux ratio. If the observed disk contains a misalignment, it could lead to a mismatch of inclina-

tions inferred from different wavelengths. Such a mismatch is indeed found for example in Tazaki et al. (2025). We want to point out that observed disk inclinations usually have large uncertainties. However, if a swap with wavelength is observed, it can be a good indication that the disk is inclined and warped.

Additionally, we analyzed the relative position angle between optical jets and the outer disk plane in four previously published edge-on protoplanetary disks. We specifically targeted disks showing some level of lateral asymmetry in previous scattered light observations. In our investigation, we find that all systems show hints to slight misalignments. We use our models to make a rough estimation of the amplitude of misalignment in those disks. For HH48, we find that depending on azimuthal orientation, a warp between $1 - 10^{\circ}$ could be present, consistent with the measurement of jet and bottom disk surface misalignment ($\lesssim 2^{\circ}$). In the other systems, the misalignments of a few degrees could be consistent with the apparent wiggling of the jet and the lateral asymmetries in the nebulae. In summary, the weak or lack of misalignments between the jets and outer disks could indicate that warps in protoplanetary disks are typically only of a few degrees. However, more observed systems are needed in order to draw strong conclusions.

Lateral asymmetries in edge-on observations can point to the presence of a warp, and with additional information about the vertical structure of the disk, it can be possible to make estimations about the warp parameters. As always, these results must be interpreted within their limitations, which we elaborated in Section 5.3.3. Although it is hard to infer the exact warp parameters from observations at this point, this study takes the first step in quantifying the asymmetry and trying to match the warp strength to the observed asymmetry. However, the parameter space of different warp shapes is too large to cover in one single work, and we therefore have to leave further explorations for future studies.

Appendices to Chapter 5

5.A On the forward scattering peak

For this work, we needed to perform a large amount of simulation runs, as each viewing angle φ in each wavelength requires its own radiative transfer simulation. In order to keep the computation time feasible for this study, each simulations should not take too long to run. One of the main factors for computation time in radiative transfer simulations is the amount of scattering photon packages used. The more photon packages are used, the closer the result gets to reality, but also the longer the simulation takes.

A commonly used technique to get away with fewer photon packages, but still end up with a smooth result, is called angular chopping (see e.g. documentation of `optool`, Dominik et al., 2021). This technique makes use of the fact that light, which is scattered within only a few degrees around the forward scattering direction, can be approximated as unscattered. This means that these photon packages, that would be scattered within this forward peaked regime, can be treated as if they did not interact with the scattering particle. Internally, `optool` uses the chopping angle (option `-chop` in `optool`) to set the values of the scattering matrix within the cone of the set angle to the value at the cone edge. The tool compensates for the chopping in order to ensure energy conservation by adjusting the scattering cross-section, which leads to a slightly altered opacity for wavelengths with a significant forward peak in the phase function. Figure 5.A.1 shows the comparison of the scattering opacity with and without chopping.

Clearly, chopping is especially important if the scattering phase function is extremely forward peaked – meaning that most photons are scattered within only a few degrees from the original direction. Indeed, for short wavelengths, where the forward scattering peak in the phase function is extreme, Figure 5.A.1 shows that the chopping mechanism reduces the opacity in this regime, while it

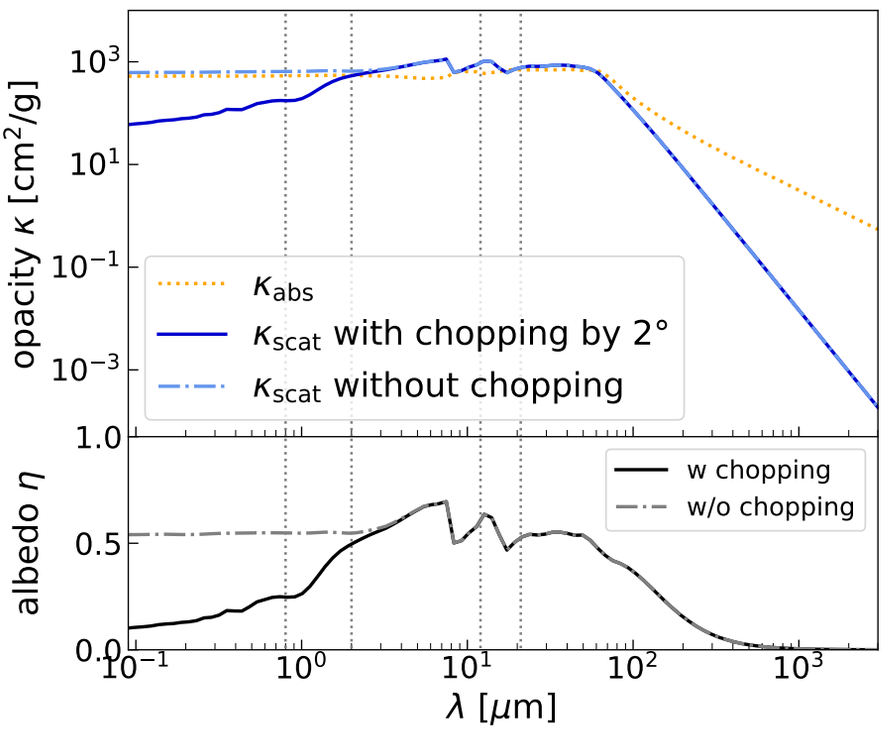

Figure 5.A.1: Scattering opacity (mass-weighted) with chopping of 2° (solid) and without chopping (dash-dotted) for the DIANA standard model, as used in this work. The mass-weighted absorption opacity is indicated with the orange dotted line. The lower panel shows the albedo $\eta = \kappa_{\rm scat}/(\kappa_{\rm abs} + \kappa_{\rm scat})$. The gray dotted lines indicate the wavelengths investigated in this work.

does not influence the longer wavelengths, where the phase function is not as strongly forward-peaked. Without the chopping mechanism, radiative transfer codes can have difficulty to deal with such an extreme forward peak, leading to bright spots in the resulting image, if too few scattering photons are used. These bright spots can indeed be avoided by using an enormous amount of scattering photons. However, this would lead to long computation times[3].

By looking at the phase function for our dust set up, we see that at the wavelength of 0.8 μm, the phase function indeed is extremely forward peaked. In Figure 5.A.2, we plot the Z_{11}-component of the scattering matrix, whose integral determines the total scattering cross-section $\sigma_{\rm scat}$ with (e.g. Dullemond et al., 2012)

$$\sigma_{\rm scat} = \int_0^{\pi} \sin\theta {\rm d}\theta \int_0^{2\pi} {\rm d}\phi \; Z_{11}(\theta, \phi). \tag{5.5}$$

Since we consider three additional wavelengths in the main part of the paper, we

[3]On our machine with our settings, an image simulation with RADMC-3D using 10^9 scattering photons takes less than one hour, while a simulation with 3×10^{10} scattering photons takes more than a day. This would be unfeasible for a project like this work.

additionally checked the scattering phase function for them. At 2 μm, we also find a strong forward peak, but it is less strong than for $\lambda = 0.8\,\mu$m by several orders of magnitude. For the longer wavelengths of 12 μm and 21 μm, there is only a very weak forward-scattering peak, which means that a consideration at these wavelengths does not require the chopping mechanism. However, the chopping mechanism also does not have a large effect on the results in these wavelengths. For simplicity, we therefore treat all simulations in the main part using the same opacity set-up with chopping of 2°.

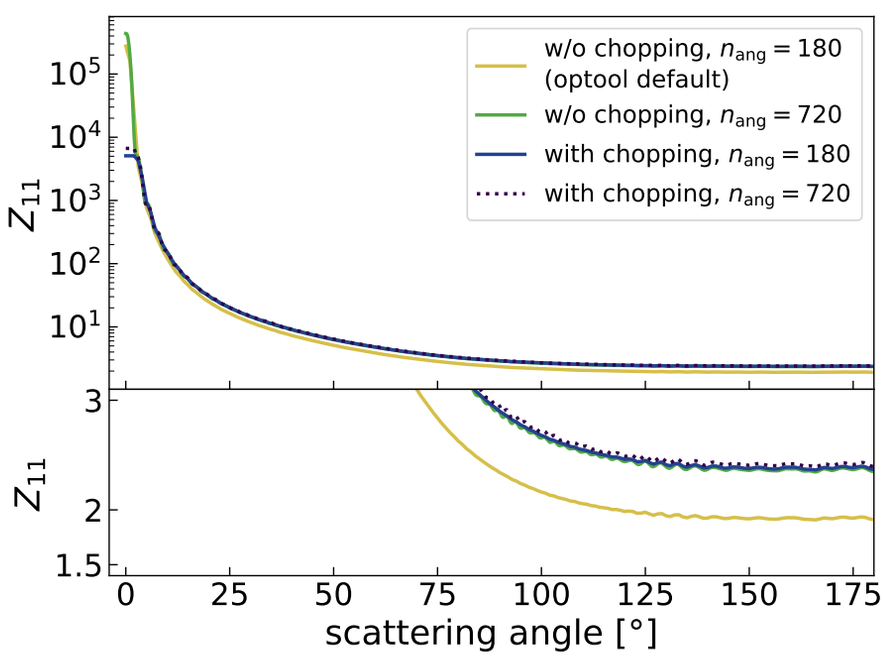

Figure 5.A.2: Phase function, i.e. Z_{11}-component of the scattering matrices, for the DIANA standard model in the wavelength $\lambda = 0.8\mu$m without the chopping mechanism and with chopping by 2°, using varying internal resolutions (n_{ang}) in `optool`. The bottom panel shows the same curves as the top panel, but with the y-axis linear and stretched so that the difference for larger scattering angles becomes visible. Except for the cut by 2° at the forward peak, the phase function is nearly the same for the case without chopping and high internal resolution (green line) and with chopping for the default internal resolution (blue solid line).

Interestingly, we noticed that for such extreme forward scattering peaks like in our case, the default internal angular resolution[4] of `optool` is not enough to accurately determine the scattering phase function. We initially noticed a discrepancy between the phase functions with and without chopping using the default angular resolution $n_{ang} = 180$ of `optool`, see yellow and blue lines in Figure 5.A.2. We found that this difference in the scattering phase function leads to a relative difference of intensity in the images of about 30%. We suspected the reason for this

[4]The internal angular resolution n_{ang} can be set using the option `-s <n_ang>` in `optool`.

difference between the phase functions with and without chopping to be linked to the extreme forward scattering peak. The tool `optool` normalizes the scattering matrix to produce the correct integral. As the forward-scattering peak has a strong contribution to the integral, a slight inaccuracy within the peak could lead to strong inaccuracies for larger scattering angles. Therefore, a higher internal angular resolution ensures an accurate calculation of the forward scattering peak, leading to a more accurate determination of the normalized values for high scattering angles. On the other hand, if the extreme forward peak is cut off using the chopping mechanism, the normalization can be more accurate for high scattering angles in this case as well. Indeed, using a higher internal angular resolution for the scattering phase function gets rid of this difference, as shown in Figure 5.A.2 in the green line, which almost perfectly aligns with the blue line in the regime of higher scattering angles. Changing the internal angular resolution for the phase function with the chopping mechanism does indeed not significantly change the phase function (dotted line), as the normalization integral is sensitive to slight deviations when the peak is chopped. We therefore conclude that it is not necessary to use the higher angular resolution for simulations when using a chopped phase function.

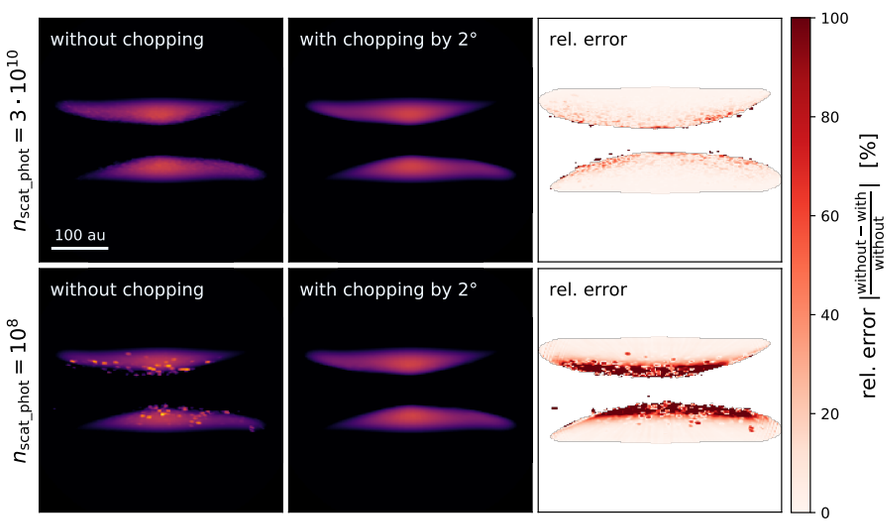

Figure 5.A.3: Comparison of the RADMC-3D images between cases with chopping by 2° and without chopping for 3×10^{10} scattering photons (top row) and 10^8 scattering photons (bottom row). These models are calculated at the wavelength $\lambda = 0.8\,\mu$m. The right column shows the relative error in percent. Here, we ignored intensity values of the images that are smaller than 10^{-17} in order to avoid artifacts.

In order to ensure that the chopping does not change the correctness of the result, we ran comparison simulations using different amounts of scattering photons in a test case. Because we performed this test in an early stage of this project,

our test case has slightly different disk parameters. We used a warped disk with a disk tilt of $i_{\max} = 10°$ at a warp location of $r_{\text{warp}} = 20\,\text{au}$. The range of the disk and the coordinate system are the same as for the simulations in the main part of this work, but the aspect ratio of the disk is $h_0 = 0.05$ at the reference radius $R_0 = 5.2\,\text{au}$ and the flaring index is $i_{\text{fl}} = 0.25$. Additionally, we used a higher dust mass than in our main models, i.e. $M_{\text{dust}} = 10^{-4} M_*$, which leads to a different shape and separation width of the top and bottom nebula.

In total, we ran four simulations for this test: one set using $n_{\text{scat\_phot}} = 3 \times 10^{10}$ scattering photons, and one set with $n_{\text{scat\_phot}} = 10^8$, each set both without chopping and with chopping of 2°. For the simulations without chopping, we used an internal angular resolution of the phase functions of $n_{\text{ang}} = 720$, while for the simulations with chopping, we kept the default resolution of $n_{\text{ang}} = 180$, since we were aiming at performing the final simulations using this default resolution.

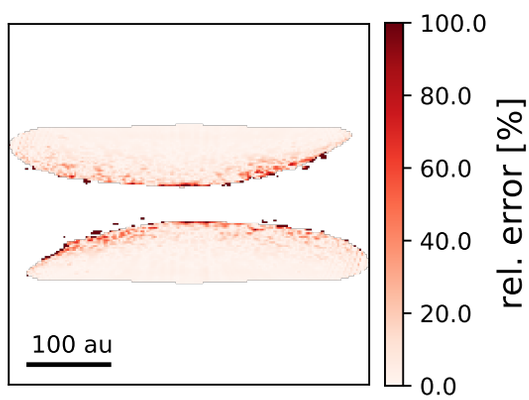

Figure 5.A.4: Relative error between the model closest to reality ($n_{\text{phot\_scat}} = 3 \times 10^{10}$ without chopping, top left panel in Fig. 5.A.3) and the computationally least expensive model ($n_{\text{phot\_scat}} = 10^8$ with chopping by 2°, bottom middle panel in Fig. 5.A.3).

Figure 5.A.3 shows the image results for all four simulations, and in addition the relative error of the resulting intensities $\delta = \left| \frac{I_{\text{without chopping}} - I_{\text{with chopping}}}{I_{\text{without chopping}}} \right|$ for both sets. In order to avoid artifacts in the residuals due to very small values in the images, we ignored the areas with intensity values lower than 10^{-17}. The bottom left panel of Figure 5.A.3 shows the bright spots if too few scattering photon packages are used in the case without the chopping mechanism. The bright spots especially occur in the transition regimes between the optically thick and optically thin part of the disk. They are unphysical artifacts due to the strong forward scattering peak at this wavelength. As expected, there are two ways to avoid these bright spots. One way is to use more scattering photons (top left panel), which is physically closer to reality, but has the problem of long computation time. The other way is to use the chopping mechanism (middle column), where we achieve

a similarly good result at lower computational cost.

In Figure 5.A.4, we show the relative error between the model closest to reality and the trade-off model with low computational cost. The median of the relative error is 2.7%, and we therefore conclude that it is safe to use a chopping of the phase function of 2° in order to save computation time for our final models.

5.B Unwarped disk

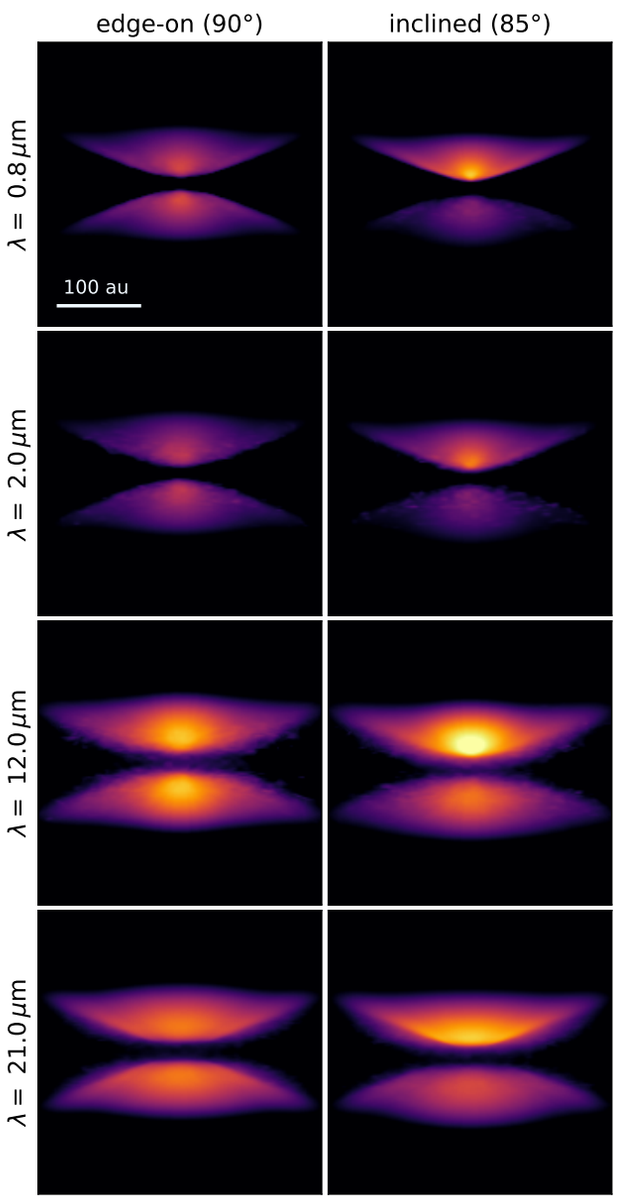

Figure 5.B.1: Synthetic near-/mid-infrared radiative transfer images in log-scale in different wavelengths of an unwarped disk. The left column shows the disk observed perfectly edge-on, the right column viewed at an inclination of 85°.

As a reference case for the models of warped disks, we investigate a planar, untilted disk in near-/mid-infrared. As described in Section 5.2, our disk contains dust of grain size $a = 10\,\mu$m. Because this model is perfectly axisymmetric, we do not need to consider different viewing angles.

For an observer viewing the disk perfectly edge-on (inclination of 90°), top and bottom nebulae are perfectly symmetric across multiple wavelengths, as shown in Figure 5.B.1, top row. Here, nebulae have the same shape and brightness. Looking at the disk at a slight inclination of 85°, the top nebula appears brighter in all wavelengths (see bottom row of Figure 5.B.1). This occurs mainly due to forward scattering, but backward scattered light from the far side of the disk contributes as well.

5.C Testing smaller grain sizes

In this section, we explore the lateral asymmetry and flux ratio in models with smaller dust grain sizes in the example of a misalignment of $i_{\max} = 3°$ and a warp location of $r_{\rm warp} = 20\,$au. In the main part, we focused on a single dust grain size of $a = 10\,\mu$m. Here, we extend our investigations to $a = 1\,\mu$m and $0.5\,\mu$m, as well as a dust size distribution for comparison. For the dust size distribution, we chose dust sizes from $a = 0.1\,\mu\text{m} - 10\,\mu$m, distributed in a commonly assumed power-law distribution according to $n(a)\text{d}a \propto a^{-3.5}\text{d}a$. All other parameters remain the same as in the main part of this work.

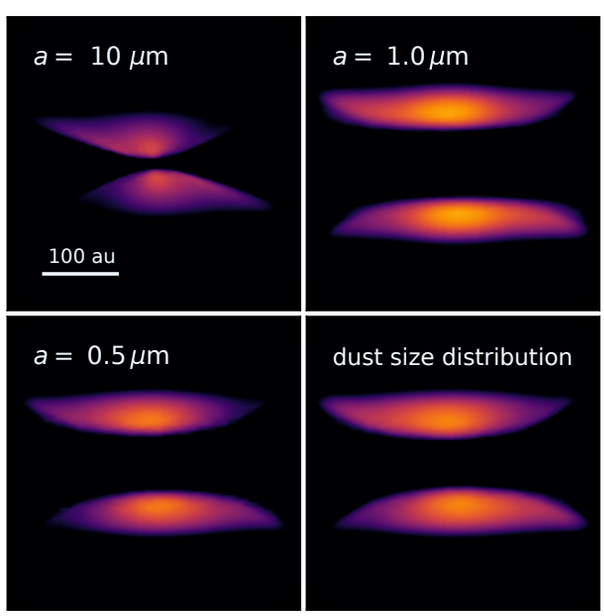

Figure 5.C.1: Radiative transfer simulations of the model with a misalignment of 3° at a location of 20 au, viewed from $\varphi = 0°$, for different dust sizes. Images are shown for $\lambda = 0.8\,\mu$m.

We find that the appearance of the disk nebulae in the radiative transfer images differs between the models of different dust sizes, as shown in Figure 5.C.1. In especially, the shape of the nebulae is less rounded and the separation between the nebulae is wider for the smaller dust grain sizes. This is because of the different opacities due to the different models of dust grain sizes. However, when comparing the lateral asymmetry and flux ratio, we find the same trend as in our main models, as shown in Figure 5.C.2. This good agreement between the different assumptions on the dust indicates that the results of this work in terms of lateral asymmetry and flux ratio can be applied in a more general way.

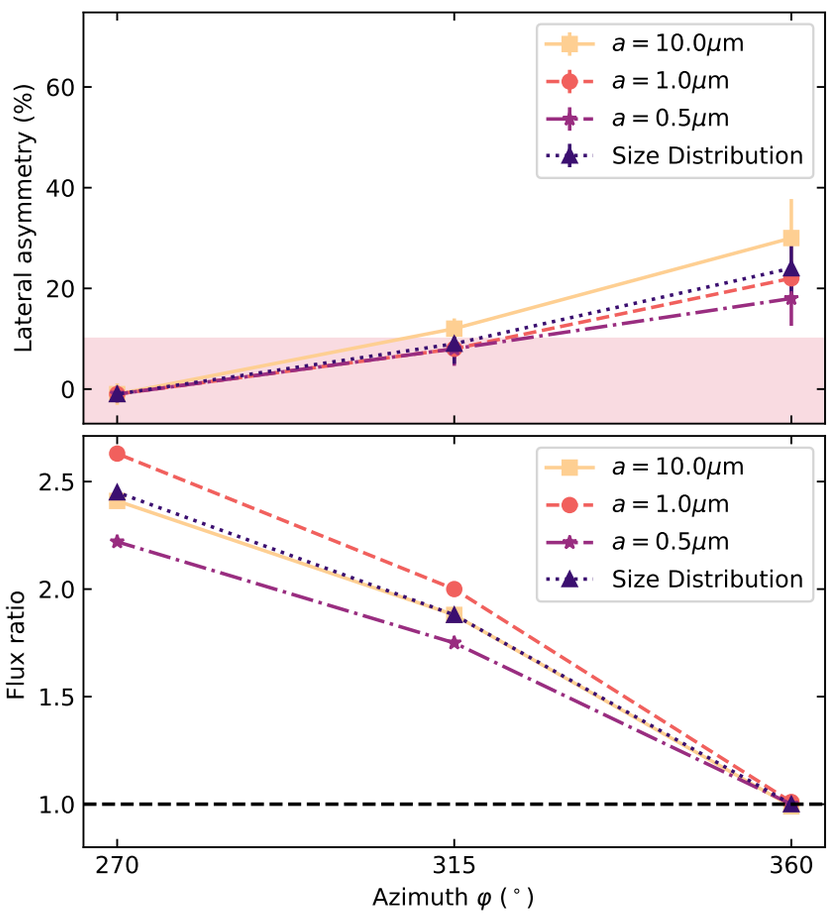

Figure 5.C.2: Same as Figure 5.6, but for a misalignment of $i_{\max} = 3^\circ$ and different assumptions on the dust size in the models. All data points are for radiative transfer models at the wavelength $\lambda = 0.8\,\mu$m.

We further checked for the different dust size models, if the swap in flux ratio with wavelength (see Sect 5.3.2) can be reproduced for smaller grains. Figure 5.C.3 shows that all three dust size models can reproduce the swap in the brightest nebula with wavelength. In particular, for all alternative dust models explored in this section, the flux ratio swap occurs at shorter wavelength than in the case of our fiducial model with $a = 10\mu$m, which is noticeable at 12μm in-

stead of 21μm. We show in Figure 5.C.4 the images at the different wavelengths for a dust size of $a = 1\,\mu$m.

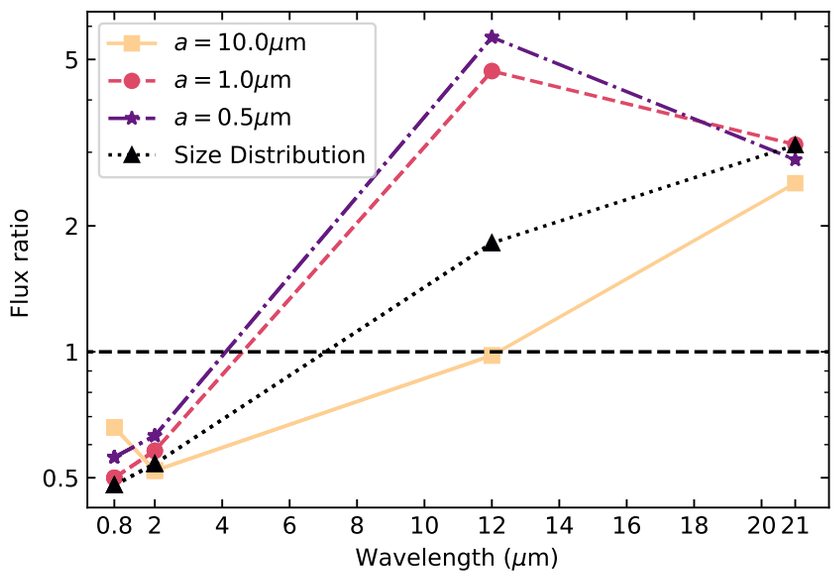

Figure 5.C.3: Flux ratio as a function of wavelengths for models of warped disks with a warp tilt of 10° and different dust properties. The models are simulated with $\varphi = 60°$, and the y-axis is plotted in log-scale.

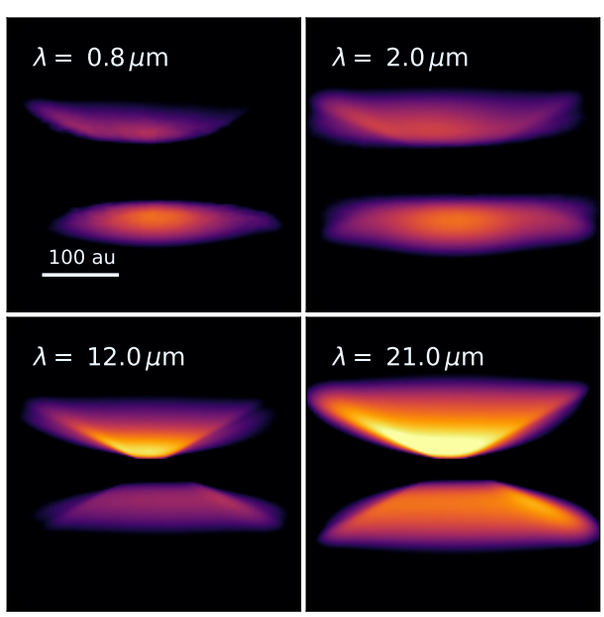

Figure 5.C.4: Same as Figure 5.8, but for the models with a dust grain size of $a = 1\,\mu$m instead of 10 μm.

We note that for our chosen fiducial dust size of $a = 10\,\mu$m, the silicate feature in the absorption opacity at roughly $\lambda = 10\,\mu$m is weak. However, the other models shown here have a stronger silicate feature because of the smaller grains. Checking the appearance of the images for wavelengths around $\lambda = 9 - 12\,\mu$m, we found that the silicate feature does not have a strong effect on the lateral asymmetry.

6 Conclusions and outlook

Protoplanetary disks are the key for understanding the formation and evolution of planets. While the research field has experienced giant leaps of advancement in the recent decades, a lot of important conditions are still unconstrained. To solve this gap of knowledge, a synergy between the observational and theoretical research in this field is crucial. Observations give insight into the conditions in disks, which helps to set constraints for theoretical models. At the same time, theoretical models can aid in the interpretation of observational data. In fact, theoretical models rely on the confirmation from observations, otherwise they are just an idea. This synergy comes to life in scientific collaborations, bringing us closer to the holistic understanding of planet formation.

This thesis contributes to the knowledge and understanding of planets' birthplaces. While the work itself is situated in the theoretical field, I continue to follow this synergy in the research field through close collaborations with observational researchers and by investigating synthetic observations of my models. I am committed to sustaining and strengthening the link between observations and theory.

6.1 Summary

This thesis is dedicated to the thorough investigation of warped disks in three-dimensional hydrodynamic simulations, as well as their appearance in synthetic observations. Warped disks gained relevance throughout the past decade, as an increasing amount of observations suggests indications of warps in protoplanetary disks. These indications are commonly non-axisymmetric shadows, such as narrow lanes or broad dark regions, that are cast from an inner region which is misaligned with respect to the outer region. Because warped disks evolve in a characteristic manner, constantly changing their orbital planes, warps can have strong implications on the process of planet formation. Understanding the for-

mation and evolution of warps is therefore an important aspect in the objective to understand how planets are born.

Chapter 1 provides an introduction on protoplanetary disks from both the observational and the theoretical perspective. The focus of this chapter are the main processes leading to planet formation. Chapter 2 then introduces the basic concepts of warped disks, including their formation and evolution. The nature of the warp evolution depends on the properties of the disk, mainly the viscosity in comparison to the vertical extend of the disk. For viscous, thin disks, the warp evolves diffusively, where it dissipates into a planar, unwarped disk. In thick disks with low viscosity, on the other hand, the warp travels as a wave through the disk.

Chapter 3: Warped disks in grid-based simulations

The aim of Chapter 3 is to understand the evolution behavior in three dimensions. For that, I used grid-based hydrodynamical simulations to investigate the dynamical effects of warps. Grid-based simulations are a valuable tool to study protoplanetary disks, as they can model low-viscosity disks more accurately in comparison to Smoothed Particle Hydrodynamics (SPH) methods as alternatives. However, because the grid contains an intrinsic geometry, grid-based methods are optimal for simulating planar disks where the disk midplane is aligned with the grid midplane. For warped disks, this is no longer the case. Therefore, I dedicated the first part of this chapter to assess the impact of a misalignment between disk and grid. I found that the resolution in the vertical direction is the most important. If this is not large enough, the geometry of the grid has a strong, unphysical effect on the disk plane, causing the disk to align with the grid plane and precess around the z-axis. However, for an appropriate vertical resolution, these unphysical effects can be minimized.

Using this result, I simulated an initially warped disk in grid-based simulations with appropriate vertical resolution. These simulations clearly show the wave-like evolution of the warp and compare well to one-dimensional models in terms of evolution of the inclination profile. Surprisingly, I found that in addition to the warp, the disk is twisting in the three-dimensional simulation, which is not reproduced in the one-dimensional model I use for the comparison. In this twisting motion, different regions of the disk precess differently. However, during this twist, the total angular momentum of the disk stays the same and does not change direction. I performed a series of tests in order to determine if this twist occurs physically or numerically. All tests indicate that the twisting is a physical effect which is captured in the three-dimensional dynamics, but ignored in one-dimensional models of a perfectly Keplerian disk.

In collaboration with my co-author, we evaluated the internal dynamics to investigate the sloshing and breathing motions that are predicted to occur in warped disks in linearized shearing box models. These motions generate the internal torque of the disk, which is the main driver of warp evolution. My simulations show that these motions indeed occur in three-dimensional simulations and become supersonic in the upper layers of the disk. While the upper layers do not have a great influence on the overall warp evolution, this phenomenon can have great implications for kinematic observations of warps. Overall, we were able to recreate the warp evolution with an additional simulation method while additionally gaining an understanding of the importance of gas pressure support for the warp evolution.

Chapter 4: Modeling a stellar fly-by warping the disk around RW Aur A

Using this powerful tool explored in the previous chapter, I investigated stellar fly-bys as formation scenario of warps in Chapter 4. Stellar fly-bys are common in the early, disk-hosting stage of planet formation, and can have drastic impacts on the shapes and sizes of protoplanetary disks. This chapter particularly focuses on the warping excited by fly-bys, which can now be accurately studied for low-viscosity disks in grid-based simulations. I found that fly-bys can indeed create warps of a few degrees, and the resulting warp depends on the specifics of the fly-by. The geometry of the trajectory with respect to the disk has a large influence on the warping. I explored both a geometry with a periastron in the disk plane, and a geometry where the periastron is not in the same plane as the disk. In addition, the direction of the fly-by in comparison to the rotational direction (called prograde for the same direction and retrograde for opposite directions) also influences the warping. Within the explored parameters, a retrograde fly-by with an out-of-disk-plane periastron produces the strongest warp, a warp with a maximum misalignment of about $4 - 5°$. In contrast, the retrograde fly-by with a periastron in the same plane as the disk showed the least amount of warping of less than $1°$. This shows that the strength of the excited warp does not only depend on the mutual inclination between orbit and disk planes, but also the specifics of the trajectory.

In the simulation of the strongest warp, the lifetime of the warp is much longer than the fly-by itself. This means that signatures of warps produced by fly-bys can be observed even if the perturber is far away such that it is not traceable anymore. In contrast to that, my simulations show that spiral arms, which are a characteristic signature of pro-grade fly-bys, are extremely short-lived and only last a few orbits at the outer edge of the disk. This is in alignment with previ-

ously found results, and implies that the perturber should be observed for disks containing spirals caused by fly-bys.

In the second part of Chapter 4, I conducted a case study of a system called RW Aur, which consists of two disk-hosting stars that recently experienced a close encounter. Astrometric data reveals that the trajectory is either bound on a highly eccentric orbit, or unbound close to a parabolic trajectory. In the frame of this project, I assumed an unbound parabolic fly-by. Modeling this system provides insight into the mechanics shaping the disks in this system. I focused on the disk around RW Aur A and my simulation shows that a warp of about 5° can be expected. Indeed, observations suggest a misalignment between inner and outer disk region of around 6°. The warping in this system shows a complex behavior with indications of multiple superimposed warp waves.

The aim of this case study was the comparison of synthetic observations of the model to real observations of the system. I thus performed radiative transfer simulations to create images of the dust continuum. For the dust, I assumed only small dust, since that is expected to be coupled to the gas and follow the warping movement. Because the trajectory is prograde for RW Aur A, spirals are expected to appear in the disk. However, the observation of the dust continuum appears completely smooth with no visible spirals. In my simulation, the spirals indeed occur, but dissolve fast before the current time of the observation. Therefore, the synthetic dust continuum image of the current point of observation also appears smooth and compares well with the observation. The lifetime of the spirals could depend on disk properties, which is why I performed additional hydrodynamic simulations for different disk viscosities. However, the lifetime of the spirals did not change for a lower viscosity, and was only slightly shorter for a larger viscosity. For the excited warp, the amplitude is similar for the different viscosities. A difference, however, is seen in the evolution of the warp.

All in all, this chapter shows that fly-bys have a strong influence on the morphology of disks. Because fly-bys are common in young stellar systems, they might have a large impact on the architecture of planetary systems.

Chapter 5: Asymmetric signatures of warps in edge-on disks

In Chapter 5, I investigated the appearance of warps in disks observed edge-on with synthetic observations in a systematic approach. Protoplanetary disks observed edge-on in near-/mid-infrared wavelengths show two bright regions separated by a dark lane. This lane corresponds to the midplane of the disk, which appears dark because it is optically thick and hides the light from the star. The bright regions correspond to the surfaces of the disk, where light from the star

is scattered toward the observer. Many disks observed edge-on show asymmetries between the two surfaces. These asymmetries can be caused by shadows from an inner region which is misaligned with respect to the outer region. In this chapter, I investigated whether parameters of the warp could be inferred from the observed asymmetries.

For that, I performed radiative transfer simulations of warped disks with different misalignments between inner and outer disk, as well as different locations, meaning radii of steepest inclination change, of the warp. In collaboration with my co-author, we evaluated the asymmetry between disk surfaces, called lateral asymmetry, in a quantitative way. In addition, we evaluated the flux ratio between the disk surfaces. The simulations show that two quantities depend on the warp parameters, but also on the orientation of the disk with respect to the observer. For an optimal orientation, subtle warps of only 2° misalignment can lead to a noticeable lateral asymmetry. However, for unfortunate orientations, even larger misalignments do not produce observable asymmetries.

In these more unfortunate orientations, one surface appears brighter than the other one, as one of the surfaces is shadowed by the warp. In an unwarped disk observed perfectly edge-on, both surfaces would have the same brightness. However, this difference in flux between the surfaces can also appear in an unwarped disk, if the disk is tilted slightly away from edge-on. This makes it hard to distinguish between a warped disk viewed perfectly edge-on and an unwarped, slightly tilted disk, as they appear very similar.

In some cases, a solution to this degeneracy exists if the disk is observed in multiple wavelengths. In a warped disk, the flux ratio can flip depending on wavelength, meaning that for shorter wavelengths, one surface appears brighter than the other, whereas in longer wavelengths, the other surface appears brighter. This can occur if the warped disk is observed slightly tilted and the warp is oriented in such a way that the warp shadows the disk surface that would be brighter in an unwarped disk with the same tilt. This way, the surface actually appears darker. However, in longer wavelengths, thermal emission becomes more important so that the shadow is less pronounced, and the surface appears brighter again. This phenomenon is observed in a few edge-on disks, and since there is no other explanation for it up-to-date, it is a strong indication that a warp is present in these disks. However, it is expected to be rare in observations, as it requires a specific viewing orientation.

Even though it is challenging to infer exact parameters of the warp from the observations of asymmetries and flux ratios without knowing the exact viewing orientation of disks, this chapter provides a valuable insight into the appearance of warped disks viewed edge-on. By understanding the asymmetric signatures,

it is possible to tackle the question of how common warped disks are and learn more about their properties.

6.2 Outlook

Warped disks become more and more relevant as highly resolved images indicate their existence and thus, their formation, evolution, and interaction with the environment gain focus within the research community. Understanding their dynamical behavior as well as investigating their appearance in observations is important to comprehend their role in the formation of planets. The grid-based methodology that I investigated in this thesis to model warped disks opens the door for many future projects following up on this. This work provides valuable insights into the dynamics of warps, a possible formation scenario, and observational signatures in synthetic observations. Nevertheless, there are many questions about their complex dynamics and appearance that remain unanswered.

For example, all my simulations have been performed in the assumption of locally isothermal disks, where the temperature does not change in time. Realistically, however, the temperature is changing throughout the lifetime of disks. Taking this into account in simulations requires the treatment of realistic heating and cooling mechanisms within disks. Because the temperature is a main factor for the vertical structure of disks, a changing temperature also means an evolution of the disk thickness. The warp evolution is driven by internal torques arising from sloshing and breathing modes in the disk which means that a change of the vertical disk structure due to an evolving temperature can influence the evolution of warps. Additionally, irradiation and shadowing because of the warped shape can play a significant role for the temperature of the disk. Thus, modeling warp evolution with more attention to the temperature is an important future step and will provide more insight into the realistic behavior of warps.

With regard to the formation of planets in warped disks, one of the obvious next steps is the consistent treatment of dust in hydrodynamical models. The hydrodynamical simulations in this thesis model pure gas disks. Understanding the behavior of dust grains in warped disks is highly important, as the dust distribution has implications on both observations and the process of planet formation. Because the reaction of dust grains to a changing orbital plane is not well studied yet, there is a lot of work to be done.

The physics behind warps is detailed and complex, and plays a significant role in the evolution of protoplanetary disks, which poses many further research questions. In the following, I outline a few concrete ideas for follow-up projects, which are partially already in progress.

Kinematics in RW Aur A

In Chapter 4, I investigated the appearance of RW Aur in radiative transfer simulations of the dust continuum. An important next step is to investigate the kinematics in molecular lines. Warps could have a strong impact on the kinematics, since the sloshing motions found in the hydrodynamic simulation in Chapter 3 show supersonic flows at the disk surfaces. I plan to investigate the velocity channel maps of CO-lines in synthetic observations of my hydrodynamic model of RW Aur A. This will give insight into the chances of observing of a warp in the kinematics of this system.

Additionally, I aim to investigate observational signatures of warps and spirals in detail. As my models in the first part of Chapter 4 include both spirals in an unwarped disk for the prograde co-planar simulation and warped spirals in the inclined simulations, I am planning to look for distinctions to make it easier to identify warps in observations.

Twisting in 3D models

My findings in Chapter 3 on the twisting of an undriven warped disk sparked a new collaboration led by Hossam Aly to investigate this effect in more detail. Within the collaboration, we are able to reproduce the twist behavior in different numerical codes, both grid-based like FARGO3D and ATHENA++, as well as Smoothed Particle Hydrodynamics (SPH) codes such as PLUTO. This supports my hypothesis that the twisting is a physical effect intrinsic to the warp dynamics.

In the frame of this collaboration, we will investigate the origin of the torque leading to the twist. For this, we aim to check whether pressure gradients in the disk, that lead to a deviation of the azimuthal velocity from Keplerianity, can be responsible for the twist. As a part of this collaboration, I will investigate this hypothesis with both one-dimensional and three-dimensional models. Further members of the collaboration are Rebecca Nealon, Giuseppe Lodato, Sijme-Jan Paardekooper, Callum Fairbairn, and Ian Rabago.

Precession of observed jets

A further idea for a project is the investigation of observed disk jets. Such jets often show an oscillating behavior, or often called *wiggles*. Since jets are launched from the inner region of the disk, this wiggling could be a tracer of a precessional motion of the inner disk, possibly linked to the twisting of a warped disk. Observations of jets and their velocities can give insight into the precession period of the inner disk, which might help to constrain disk and warp parameters. Therefore, an investigation from the theoretical point of view on the dependency

of time scales on different parameters of the disk, like disk size and warp amplitude, will be a good first step, potentially leading to an international collaboration with researchers on the observational side in order to constrain parameters from observations of wiggling jets.

The idea for this project was sparked at the Italian National Conference on Star and Planet Formation in Sexten, Italy (lead organizer Francesca Bacciotti), which took place in January 2025, through my presentation on the work of Chapter 5, as well as presentations especially by Alessio Caratti o Garatti and Sam Federmann on their observations of wiggling jets and detailed measurements of jet velocities.

Prevalence of warps in protoplanetary disks

Even though observations of non-axisymmetric features indicating warps become more and more common, the prevalence of warps in protoplanetary disks is still an open question. Following up on the work of Chapter 5 and extending the investigation of observational signatures of warps will help shed light on this question. In this frame, kinematics will also play a key role. This is one of the goals of my post-doc position in the field of protoplanetary disks with Giovanni Rosotti at the Università degli Studi in Milan, Italy.

Warped disks around black holes

The physics behind the dynamics of warps can not only be applied to protoplanetary disks, but more generally for other accretion disks as well. For example, accretion disks around spinning black holes can develop a warp if the spin axis of the black hole is misaligned with the rotational axis of the disk. In this scenario, the black hole acts a torque on the disk, referred to as Lense-Thirring effect.

Observations of some black holes reveal so-called Quasi-Periodic Oscillations (QPOs), which are X-ray frequency regimes that show a higher intensity in their Fourier analysis of the spectrum. These QPOs seem to be linked to the presence of accretion disks. Although their origin is still unknown, they are thought to originate in the very inner region of accretion disks around massive objects. One hypothesis is that they could be linked to the Lense-Thirring effect.

In a collaboration led by Guglielmo Mastroserio, we aim to investigate warped accretion disks around stellar mass black holes and their possible connection to QPOs. For that, we are using my one-dimensional warp evolution code `dwarpy`, which I developed prior to this dissertation during my Master's project at Heidelberg University, and the insights on warp evolution gained from this work. Further members of this collaboration are Giuseppe Lodato, Giovanni Rosotti, and Alessia Franchini.

Other ideas

The area of warped disks and their non-axisymmetric features in observations is rich of further research questions. The possibilities for projects range from an analysis of the warp dynamics of disks that for example contain substructures to the further investigation of observational signatures.

Directly following the work of Chapter 4, a closer analysis of the lifetime of spirals in stellar fly-bys would be interesting. Here, the question is which factors, including disk parameters and warp strength, influence the lifetime of the spirals. Another interesting follow-up question is the amplitude of the excited warp and on which parameters it depends. What is the largest amplitude we can excite through a fly-by event? Furthermore, since kinematics of disks gain more and more importance, distinguishing the signatures from spirals and warps will become important. Or going a step further, can we distinguish planar, unwarped spirals from warped spirals in disk kinematics?

Another important direction for future work are magnetic fields and their influence on the dynamics of warps. An indication that magnetic fields can be present in warped disks are the observations of wiggling jets. As mentioned before, the oscillation of the jets could indicate a precession of the inner disk region due to a warp. However, the main mechanism to launch a jet from the disk is thought to be linked to magnetic fields. These magnetic fields can act a torque on the orbital plane of a disk and thus influence the dynamic behavior of warps. Magnetic effects in warp dynamics are not studied well so far, as the dynamics of warps without magnetic fields is already quite complex. Investigating these under the influence of magnetohydrodynamcis is challenging with the current computational resources. However, I think it will be an exciting research direction in future.

Investigating these and further research questions will contribute to a comprehensive understanding of warped disks and their role in the field of planet formation.

6.3 Conclusions

Warps play a significant role in the field of protoplanetary disks, as they appear to be common and influence the dynamical evolution of disks. The variety of formation scenarios and possible warp shapes indicate their diverse influence on the formation process of planets. My work in the frame of this thesis, together with the current research in the area of warped disks, is pushing us closer to a complete understanding of their gas dynamics.

However, as we gain knowledge and our understanding becomes deeper, new research questions arise, which require successive investigation. The grid-based method, which I explored in this work, has proven to be a robust and versatile tool to tackle some of these research questions. My work demonstrates the applicability of grid-based methods to the formation and evolution of warped disks. The grid-based simulations provide a deeper insight into the detailed and complex dynamics of warps, as well as the warp formation in a specific scenario. Additionally, I strengthen the link between theoretical models and observations, using radiative transfer simulations.

As the research field of protoplanetary disks is active, new theoretical and observational findings are constantly changing our picture of disk evolution and planet formation. Despite this progress, many observed phenomena remain unexplained, and key physical processes governing these systems have yet to be fully uncovered. Curiosity and the drive to explore will be essential as we keep pushing the boundaries of knowledge in the area of warped disks.

Acknowledgements

My PhD has been a transformative experience, helping me to grow into an independent researcher. I owe special thanks to my advisor, Kees Dullemond, for his consistent support and encouragement, insightful guidance, and the many lessons that have shaped my PhD experience and will stay with me throughout my career.

I am also deeply grateful to my other advisors, whose expertise and inspiration have been invaluable in shaping my research and academic development. Their advice and mentorship have played a crucial role in my journey, and I'm thankful for the support and perspectives they shared along the way. I am also especially thankful to my examiners for their time and willingness to engage with this work.

To the research groups both in Heidelberg and Milan, thank you for all the inspiring discussions, the shared passion for science, and the open-minded atmosphere. Beyond the science, I am grateful for the laughs and many moments we shared during lunches, on hikes, and many other occasions. I am proud to be a part of such thoughtful and inspiring teams.

I am truly grateful to my co-authors and collaborators for the opportunity to work together throughout this thesis. These collaborations have not only enriched my research, but have also been a genuine source of motivation and joy. I also sincerely appreciate those who contributed their expertise and knowledge to my simulations and models. Working with these dedicated, open-minded, and encouraging colleagues has been one of the most rewarding aspects of my PhD, and I'm excited to continue these connections in the future.

I am extremely thankful for the opportunity to attend various international conferences, where I was able to share my work, learn from others, and connect with researchers from around the world. These experiences contributed to my growth as a scientist and led to meaningful collaborations and friendships. I am

grateful for every conversation, bit of advice, and spark of inspiration that came from those meetings.

I would like to thank all those who took the time to read and comment on my manuscript. Your thoughtful feedback and suggestions helped to improve the clarity and structure of the writing, and enhanced the overall quality of this work. I truly appreciate your time and support.

I would also like to thank Heidelberg University and the IMPRS and HGSFP graduate programms for providing the resources and environment that made this research possible.

To my family and friends, thank you for being there through every step of this journey. Your love, support, and understanding made all the difference, and I'm incredibly lucky to have you by my side.

I wish to remember and honor Willy Kley, who sadly passed away in 2021. As one of my advisors, he would have played an important role in this thesis, and his absence is deeply felt. I feel fortunate to have experienced his deep knowledge, kindness, and thoughtful guidance. His legacy continues to inspire my work, and everything I learned from him will remain with me as I continue my research career.

Funding and software acknowledgements

This work has been funded by the DFG research group FOR 2634 "Planet Formation Witnesses and Probes: Transition Disks" under grants DU 414/23-2 and KL 650/29-1, 650/29-2, 650/30-1. Additionally, I acknowledge support by the High Performance and Cloud Computing Group at the Zentrum für Datenverarbeitung of the University of Tübingen, the state of Baden-Württemberg through bwHPC and the German Research Foundation (DFG) through grant INST 37/935-1 FUGG. I also acknowledge support from the European Union (ERC Starting Grant DiscEvol, project number 101039651) and from Fondazione Cariplo, grant No. 2022-1217. Views and opinions expressed are, however, those of the author(s) only and do not necessarily reflect those of the European Union or the European Research Council. Neither the European Union nor the granting authority can be held responsible for them. I gained great benefit for this work from Core2disk-III, which is supported by the LABEX P2IO, the PCMI, PNPS, and PNP programs, and the OSU Paris-Saclay. This work makes use of the following ALMA data: ADS/JAO.ALMA#2018.1.00973.S ALMA is a partnership of ESO (representing its member states), NSF (USA) and NINS (Japan), together with NRC (Canada), MOST and ASIAA (Taiwan), and KASI (Republic of Korea), in cooperation with the Republic of Chile. The Joint ALMA Observatory is operated by ESO, AUI/NRAO and NAOJ.

Some images and plots in this work were made with the Python (Van Rossum & Drake, 2009) library `matplotlib` (Hunter, 2007). We acknowledge also the usage of `numpy` (Harris et al., 2020), `scipy` (Virtanen et al., 2020), and `astropy` (Astropy Collaboration et al., 2022). Additional software was used for computer-assisted language editing.

List of Figures

List of Tables

List of Publications

Publications included in this work

Kimmig, C. N. & Dullemond, C. P. 2024, Warped disk evolution in grid-based simulations, Astronomy and Astrophysics, 689, A45, doi:10.1051/0004-6361/-202348660

Kimmig, C. N. & Villenave, M. 2025, Asymmetric Signatures of Warps in Edge-on Disks, arXiv e-prints, arXiv:2504.05399, doi:10.48550/arXiv.2504.05399, accepted to Astronomy and Astrophysics

Kimmig, C. N., Weber, P., Rosotti, G. P., Facchini, S., & Dullemond, C. P., in prep., Modeling a stellar fly-by warping the disk around RW Aur A

Publications not included in this work

Kimmig, C. N., Dullemond, C. P., & Kley, W. 2020, Effect of wind-driven accretion on planetary migration, Astronomy and Astrophysics, 633, A4, doi:10.1051/0004-6361/201936412

Dullemond, C. P., Kimmig, C. N., & Zanazzi, J. J. 2022, On the equations of warped disc dynamics, Monthly Notices of the Royal Astronomical Society, 511, 2925–2947, doi:10.1093/mnras/stab2791

Kurtovic, N. T., Facchini, S., Benisty, M., Pinilla, P., Cabrit, S., Jensen, E. L. N., Dougados, C., Booth, R., Kimmig, C. N., Manara, C. F., & Rodriguez, J. E., 2024, Binary orbit and disks properties of the RW Aur system using ALMA observations, Astronomy and Astrophysics, 511, 2925–2947, doi:10.1051/0004-6361/202347583

References

Agertz, O., Moore, B., Stadel, J., et al. 2007, Fundamental differences between SPH and grid methods, Monthly Notices of the Royal Astronomical Society, 380, 963–978. doi:10.1111/j.1365-2966.2007.12183.x

Alencar, S. H. P., Basri, G., Hartmann, L., & Calvet, N. 2005, The extreme T Tauri star RW Aur: accretion and outflow variability, Astronomy and Astrophysics, 440, 595–608. doi:10.1051/0004-6361:20053315

Alexander, R., Pascucci, I., Andrews, S., Armitage, P., & Cieza, L. 2014, The Dispersal of Protoplanetary Disks, in Protostars and Planets VI, ed. H. Beuther, R. S. Klessen, C. P. Dullemond, & T. Henning, 475–496. doi:10.2458/azu_uapress_9780816531240-ch021

Aly, H., Gonzalez, J.-F., Nealon, R., et al. 2021, Dust traffic jams in inclined circumbinary protoplanetary discs - I. Morphology and formation theory, Monthly Notices of the Royal Astronomical Society, 508, 2743–2757. doi:10.1093/mnras/stab2794

Aly, H. & Lodato, G. 2020, Efficient dust ring formation in misaligned circumbinary discs, Monthly Notices of the Royal Astronomical Society, 492, 3306–3315. doi:10.1093/mnras/stz3633

Aly, H., Nealon, R., & Gonzalez, J.-F. 2024, WInDI: a Warp-Induced Dust Instability in protoplanetary discs, Monthly Notices of the Royal Astronomical Society, 527, 4777–4789. doi:10.1093/mnras/stad3494

Andrews, S. M. 2020, Observations of Protoplanetary Disk Structures, Annual Review of Astronomy and Astrophysics, 58, 483–528. doi:10.1146/annurev-astro-031220-010302

Andrews, S. M., Huang, J., Pérez, L. M., et al. 2018, The Disk Substructures at High Angular Resolution Project (DSHARP). I. Motivation, Sample, Calibration, and Overview, Astrophysical Journal, Letters, 869, L41. doi:10.3847/2041-8213/aaf741

Andrews, S. M., Wilner, D. J., Hughes, A. M., Qi, C., & Dullemond, C. P. 2009, Protoplanetary Disk Structures in Ophiuchus, Astrophysical Journal, 700, 1502–1523. doi:10.1088/0004-637X/700/2/1502

Angelo, I., Duchene, G., Stapelfeldt, K., et al. 2023, Demographics of Protoplanetary Disks: A Simulated Population of Edge-on Systems, Astrophysical Journal, 945, 130. doi:10.3847/1538-4357/acbb01

Anglada, G., López, R., Estalella, R., et al. 2007, Proper Motions of the Jets in the Region of HH 30 and HL/XZ Tau: Evidence for a Binary Exciting Source of the HH 30 Jet, Astronomical Journal, 133, 2799–2814. doi:10.1086/517493

Ansdell, M., Gaidos, E., Hedges, C., et al. 2020, Are inner disc misalignments common? ALMA reveals an isotropic outer disc inclination distribution for young dipper stars, Monthly Notices of the Royal Astronomical Society, 492, 572–588. doi:10.1093/mnras/stz3361

Antipin, S., Belinski, A., Cherepashchuk, A., et al. 2015, Resolved photometry of the binary components of RW Aur, Information Bulletin on Variable Stars, 6126, 1. doi:10.48550/arXiv.1412.7661

Armitage, P. J. 2007, Lecture notes on the formation and early evolution of planetary systems, arXiv e-prints, astro–ph/0701485. doi:10.48550/arXiv.astro-ph/0701485

Armitage, P. J. 2022, Lecture notes on accretion disk physics, arXiv e-prints, arXiv:2201.07262. doi:10.48550/arXiv.2201.07262

Armitage, P. J. & Kley, W. 2019, From Protoplanetary Disks to Planet Formation, From Protoplanetary Disks to Planet Formation: Saas-Fee Advanced Course 45. Swiss Society for Astrophysics and Astronomy. doi:10.1007/978-3-662-58687-7

Armitage, P. J. & Pringle, J. E. 1997, Radiation-induced Warping of Protostellar Accretions Disks, Astrophysical Journal, Letters, 488, L47–L50. doi:10.1086/310907

Astropy Collaboration, Price-Whelan, A. M., Lim, P. L., et al. 2022, The Astropy Project: Sustaining and Growing a Community-oriented Open-source Project

and the Latest Major Release (v5.0) of the Core Package, Astrophysical Journal, 935, 167. doi:10.3847/1538-4357/ac7c74

Avenhaus, H., Quanz, S. P., Garufi, A., et al. 2018, Disks around T Tauri Stars with SPHERE (DARTTS-S). I. SPHERE/IRDIS Polarimetric Imaging of Eight Prominent T Tauri Disks, Astrophysical Journal, 863, 44. doi:10.3847/1538-4357/aab846

Avenhaus, H., Quanz, S. P., Schmid, H. M., et al. 2017, Exploring Dust around HD 142527 down to 0.025″ (4 au) Using SPHERE/ZIMPOL, Astronomical Journal, 154, 33. doi:10.3847/1538-3881/aa7560

Bae, J., Isella, A., Zhu, Z., et al. 2023, Structured Distributions of Gas and Solids in Protoplanetary Disks, in Protostars and Planets VII, ed. S. Inutsuka, Y. Aikawa, T. Muto, K. Tomida, & M. Tamura, 423. doi:10.48550/arXiv.2210.13314

Balbus, S. A. 2009, Magnetohydrodynamics of Protostellar Disks, arXiv e-prints, arXiv:0906.0854. doi:10.48550/arXiv.0906.0854

Balbus, S. A. & Hawley, J. F. 1998, Instability, turbulence, and enhanced transport in accretion disks, Reviews of Modern Physics, 70, 1–53. doi:10.1103/RevModPhys.70.1

Bally, J., Walawender, J., Luhman, K. L., & Fazio, G. 2006, Deep Imaging Surveys of Star-forming Clouds. IV. The Meek and the Mighty: Outflows from Young Stars in Chamaeleon I, Astronomical Journal, 132, 1923–1937. doi:10.1086/507523

Bate, M. R. 2018, On the diversity and statistical properties of protostellar discs, Monthly Notices of the Royal Astronomical Society, 475, 5618–5658. doi:10.1093/mnras/sty169

Benisty, M., Dominik, C., Follette, K., et al. 2023, Optical and Near-infrared View of Planet-forming Disks and Protoplanets, in Protostars and Planets VII, ed. S. Inutsuka, Y. Aikawa, T. Muto, K. Tomida, & M. Tamura, 605. doi:10.48550/arXiv.2203.09991

Benisty, M., Juhasz, A., Boccaletti, A., et al. 2015, Asymmetric features in the protoplanetary disk MWC 758, Astronomy and Astrophysics, 578, L6. doi:10.1051/0004-6361/201526011

Benisty, M., Juhász, A., Facchini, S., et al. 2018, Shadows and asymmetries in the T Tauri disk HD 143006: evidence for a misaligned inner disk, Astronomy and Astrophysics, 619, A171. doi:10.1051/0004-6361/201833913

Benisty, M., Stolker, T., Pohl, A., et al. 2017, Shadows and spirals in the protoplanetary disk HD 100453, Astronomy and Astrophysics, 597, A42. doi:10.1051/0004-6361/201629798

Benítez-Llambay, P. & Masset, F. S. 2016, FARGO3D: A New GPU-oriented MHD Code, APJS, 223, 11. doi:10.3847/0067-0049/223/1/11

Berghea, C. T., Bayyari, A., Sitko, M. L., et al. 2024, Dracula's Chivito: Discovery of a Large Edge-on Protoplanetary Disk with Pan-STARRS, Astrophysical Journal, Letters, 967, L3. doi:10.3847/2041-8213/ad43e3

Béthune, W., Lesur, G., & Ferreira, J. 2017, Global simulations of protoplanetary disks with net magnetic flux. I. Non-ideal MHD case, Astronomy and Astrophysics, 600, A75. doi:10.1051/0004-6361/201630056

Bhandare, A., Breslau, A., & Pfalzner, S. 2016, Effects of inclined star-disk encounter on protoplanetary disk size, Astronomy and Astrophysics, 594, A53. doi:10.1051/0004-6361/201628086

Bjorkman, J. E. & Wood, K. 2001, Radiative Equilibrium and Temperature Correction in Monte Carlo Radiation Transfer, Astrophysical Journal, 554, 615–623. doi:10.1086/321336

Blandford, R. D. & Payne, D. G. 1982, Hydromagnetic flows from accretion disks and the production of radio jets., Monthly Notices of the Royal Astronomical Society, 199, 883–903. doi:10.1093/mnras/199.4.883

Blum, J. & Wurm, G. 2008, The growth mechanisms of macroscopic bodies in protoplanetary disks., Annual Review of Astronomy and Astrophysics, 46, 21–56. doi:10.1146/annurev.astro.46.060407.145152

Bodenheimer, P., Laughlin, G. P., Rozyczka, M., Yorke, H. W., & Plewa, T. 2006, Numerical methods in astrophysics, Series in Astronomy and Astrophysics, Boca Raton, FL: CRC Press. doi:10.1201/9781420011869

Bohn, A. J., Benisty, M., Perraut, K., et al. 2022, Probing inner and outer disk misalignments in transition disks. Constraints from VLTI/GRAVITY and ALMA observations, Astronomy and Astrophysics, 658, A183. doi:10.1051/0004-6361/202142070

Bohn, A. J., Kenworthy, M. A., Ginski, C., et al. 2019, Discovery of a directly imaged disk in scattered light around the Sco-Cen member Wray 15-788, Astronomy and Astrophysics, 624, A87. doi:10.1051/0004-6361/201834523

Bohren, C. F. & Huffman, D. R. 1983, Absorption and Scattering of Light by Small Particles, Wiley

Bonnell, I. & Bastien, P. 1992, A Binary Origin for FU Orionis Stars, Astrophysical Journal, Letters, 401, L31. doi:10.1086/186663

Borchert, E. M. A., Price, D. J., Pinte, C., & Cuello, N. 2022, On the rise times in FU Orionis events, Monthly Notices of the Royal Astronomical Society, 510, L37–L41. doi:10.1093/mnrasl/slab123

Bouvier, J., Chelli, A., Allain, S., et al. 1999, Magnetospheric accretion onto the T Tauri star AA Tauri. I. Constraints from multisite spectrophotometric monitoring, Astronomy and Astrophysics, 349, 619–635

Bozhinova, I., Scholz, A., Costigan, G., et al. 2016, The disappearing act: a dusty wind eclipsing RW Aur, Monthly Notices of the Royal Astronomical Society, 463, 4459–4468. doi:10.1093/mnras/stw2327

Breslau, A. & Pfalzner, S. 2019, Creating retrogradely orbiting planets by prograde stellar fly-bys, Astronomy and Astrophysics, 621, A101. doi:10.1051/0004-6361/201833729

Breslau, A., Steinhausen, M., Vincke, K., & Pfalzner, S. 2014, Sizes of protoplanetary discs after star-disc encounters, Astronomy and Astrophysics, 565, A130. doi:10.1051/0004-6361/201323043

Burrows, C. J., Stapelfeldt, K. R., Watson, A. M., et al. 1996, Hubble Space Telescope Observations of the Disk and Jet of HH 30, Astrophysical Journal, 473, 437. doi:10.1086/178156

Cabrit, S., Pety, J., Pesenti, N., & Dougados, C. 2006, Tidal stripping and disk kinematics in the RW Aurigae system, Astronomy and Astrophysics, 452, 897–906. doi:10.1051/0004-6361:20054047

Cacciapuoti, L., Macias, E., Gupta, A., et al. 2024, A dusty streamer infalling onto the disk of a class I protostar. ALMA dual-band constraints on grain properties and the mass-infall rate, Astronomy and Astrophysics, 682, A61. doi:10.1051/0004-6361/202347486

Calvet, N., D'Alessio, P., Hartmann, L., et al. 2002, Evidence for a Developing Gap in a 10 Myr Old Protoplanetary Disk, Astrophysical Journal, 568, 1008–1016. doi:10.1086/339061

Cannon, C. J. 1973, Frequency-Quadrature Perturbations in Radiative-Transfer Theory, Astrophysical Journal, 185, 621–630. doi:10.1086/152442

Casassus, S., Avenhaus, H., Pérez, S., et al. 2018, An inner warp in the DoAr 44 T Tauri transition disc, Monthly Notices of the Royal Astronomical Society, 477, 5104–5114. doi:10.1093/mnras/sty894

Casassus, S., Marino, S., Pérez, S., et al. 2015, Accretion Kinematics through the Warped Transition Disk in HD142527 from Resolved CO(6-5) Observations, Astrophysical Journal, 811, 92. doi:10.1088/0004-637X/811/2/92

Cassan, A., Kubas, D., Beaulieu, J. P., et al. 2012, One or more bound planets per Milky Way star from microlensing observations, Nature, 481, 167–169. doi:10.1038/nature10684

Cazzoletti, P., van Dishoeck, E. F., Pinilla, P., et al. 2018, Evidence for a massive dust-trapping vortex connected to spirals. Multi-wavelength analysis of the HD 135344B protoplanetary disk, Astronomy and Astrophysics, 619, A161. doi:10.1051/0004-6361/201834006

Chang, E. & Youdin, A. N. 2024, "Halfway to Rayleigh" and Other Insights into the Rossby Wave Instability, Astrophysical Journal, 976, 100. doi:10.3847/1538-4357/ad81f6

Charbonneau, D., Brown, T. M., Latham, D. W., & Mayor, M. 2000, Detection of Planetary Transits Across a Sun-like Star, Astrophysical Journal, Letters, 529, L45–L48. doi:10.1086/312457

Chiang, E. I. & Goldreich, P. 1997, Spectral Energy Distributions of T Tauri Stars with Passive Circumstellar Disks, Astrophysical Journal, 490, 368–376. doi:10.1086/304869

Chromey, F. R. 2010, To Measure the Sky, Cambridge University Press, 135 et seq. doi:10.1017/CBO9781316424117

Clarke, C. & Carswell, B. 2007, Principles of Astrophysical Fluid Dynamics, Cambridge University Press. doi:10.1017/CBO9780511813450

Clarke, C. J. 2007, The photoevaporation of discs around young stars in massive clusters, Monthly Notices of the Royal Astronomical Society, 376, 1350–1356. doi:10.1111/j.1365-2966.2007.11547.x

Clarke, C. J. & Pringle, J. E. 1993, Accretion disc response to a stellar fly-by, Monthly Notices of the Royal Astronomical Society, 261, 190–202. doi:10.1093/mnras/261.1.190

Codella, C., Podio, L., De Simone, M., et al. 2024, FAUST XII. Accretion streamers and jets in the VLA 1623-2417 protocluster, Monthly Notices of the Royal Astronomical Society, 528, 7383–7396. doi:10.1093/mnras/stae472

Connelley, M. S. & Reipurth, B. 2018, A Near-infrared Spectroscopic Survey of FU Orionis Objects, Astrophysical Journal, 861, 145. doi:10.3847/1538-4357/aaba7b

Cuello, N., Dipierro, G., Mentiplay, D., et al. 2019, Flybys in protoplanetary discs: I. Gas and dust dynamics, Monthly Notices of the Royal Astronomical Society, 483, 4114–4139. doi:10.1093/mnras/sty3325

Cuello, N., Louvet, F., Mentiplay, D., et al. 2020, Flybys in protoplanetary discs - II. Observational signatures, Monthly Notices of the Royal Astronomical Society, 491, 504–514. doi:10.1093/mnras/stz2938

Cuello, N., Ménard, F., & Price, D. J. 2023, Close encounters: How stellar flybys shape planet-forming discs, European Physical Journal Plus, 138, 11. doi:10.1140/epjp/s13360-022-03602-w

Cui, C., Gerbig, K., Li, Y.-P., et al. 2025, Dust Growth in ALMA Rings: II. Dusty Rossby Wave Instability, arXiv e-prints, arXiv:2504.05095. doi:10.48550/arXiv.2504.05095

Dai, F., Facchini, S., Clarke, C. J., & Haworth, T. J. 2015, A tidal encounter caught in the act: modelling a star-disc fly-by in the young RW Aurigae system, Monthly Notices of the Royal Astronomical Society, 449, 1996–2009. doi:10.1093/mnras/stv403

D'Angelo, G. & Lubow, S. H. 2010, Three-dimensional Disk-Planet Torques in a Locally Isothermal Disk, Astrophysical Journal, 724, 730–747. doi:10.1088/0004-637X/724/1/730

de Val-Borro, M., Edgar, R. G., Artymowicz, P., et al. 2006, A comparative study of disc-planet interaction, Monthly Notices of the Royal Astronomical Society, 370, 529–558. doi:10.1111/j.1365-2966.2006.10488.x

Debes, J. H., Poteet, C. A., Jang-Condell, H., et al. 2017, Chasing Shadows: Rotation of the Azimuthal Asymmetry in the TW Hya Disk, Astrophysical Journal, 835, 205. doi:10.3847/1538-4357/835/2/205

Demianski, M. & Ivanov, P. B. 1997, The dynamics of twisted accretion disc around a Kerr black hole., Astronomy and Astrophysics, 324, 829–834

Deng, H. & Ogilvie, G. I. 2022, Non-linear behaviour of warped discs around a central object with a quadrupole moment, Monthly Notices of the Royal Astronomical Society, 512, 6078–6092. doi:10.1093/mnras/stac858

Dodin, A., Grankin, K., Lamzin, S., et al. 2019, Analysis of colour and polarimetric variability of RW Aur A in 2010-2018, Monthly Notices of the Royal Astronomical Society, 482, 5524–5541. doi:10.1093/mnras/sty2988

Dominik, C., Min, M., & Tazaki, R. 2021, OpTool: Command-line driven tool for creating complex dust opacities, Astrophysics Source Code Library, record ascl:2104.010

Dong, R., Liu, H. B., Cuello, N., et al. 2022, A likely flyby of binary protostar Z CMa caught in action, Nature Astronomy, 6, 331–338. doi:10.1038/s41550-021-01558-y

Doğan, S., Nixon, C., King, A., & Price, D. J. 2015, Tearing up a misaligned accretion disc with a binary companion, Monthly Notices of the Royal Astronomical Society, 449, 1251–1258. doi:10.1093/mnras/stv347

Doğan, S., Nixon, C. J., King, A. R., Pringle, J. E., & Price, D. 2023, Hydrodynamical Simulations of Misaligned Accretion Discs in Binary Systems: Companions tear discs, in The Predictive Power of Computational Astrophysics as a Discover Tool, ed. D. Bisikalo, D. Wiebe, & C. Boily, 177–183. doi:10.1017/S1743921322001387

Draine, B. T. 2011, Physics of the Interstellar and Intergalactic Medium, Princeton University Press. doi:10.1515/9781400839087

Drążkowska, J., Bitsch, B., Lambrechts, M., et al. 2023, Planet Formation Theory in the Era of ALMA and Kepler: from Pebbles to Exoplanets, in Protostars and Planets VII, ed. S. Inutsuka, Y. Aikawa, T. Muto, K. Tomida, & M. Tamura, 717. doi:10.48550/arXiv.2203.09759

Duchêne, G., Ménard, F., Stapelfeldt, K. R., et al. 2024, JWST Imaging of Edge-on Protoplanetary Disks. I. Fully Vertically Mixed 10 μm Grains in the Outer Regions of a 1000 au Disk, Astronomical Journal, 167, 77. doi:10.3847/1538-3881/acf9a7

Duchêne, G., Stapelfeldt, K., Isella, A., et al. 2014, Panchromatic imaging and modeling of SSTtau J042021+281349: A new prototypical edge-on protoplanetary disk, in Exploring the Formation and Evolution of Planetary Systems, ed. M. Booth, B. C. Matthews, & J. R. Graham, 111–112. doi:10.1017/S174392131300803X

Dullemond, C. P. 2012, Lecture notes on Radiative Transfer in Astrophysics – Theory, Numerical Methods and Applications, https://www.ita.uni-heidelberg.de/~dullemond/lectures/radtrans_2012/index.shtml, accessed: 2025-02-20

Dullemond, C. P., Isella, A., Andrews, S. M., Skobleva, I., & Dzyurkevich, N. 2020, Midplane temperature and outer edge of the protoplanetary disk around HD 163296, Astronomy and Astrophysics, 633, A137. doi:10.1051/0004-6361/201936438

Dullemond, C. P., Juhasz, A., Pohl, A., et al. 2012, RADMC-3D: A multi-purpose radiative transfer tool, Astrophysics Source Code Library, record ascl:1202.015

Dullemond, C. P., Kimmig, C. N., & Zanazzi, J. J. 2022a, On the equations of warped disc dynamics, Monthly Notices of the Royal Astronomical Society, 511, 2925–2947. doi:10.1093/mnras/stab2791

Dullemond, C. P., Küffmeier, M., Goicovic, F., et al. 2019, Cloudlet capture by transitional disk and FU Orionis stars, Astronomy and Astrophysics, 628, A20. doi:10.1051/0004-6361/201832632

Dullemond, C. P., Ziampras, A., Ostertag, D., & Dominik, C. 2022b, Razor-thin dust layers in protoplanetary disks: Limits on the vertical shear instability, Astronomy and Astrophysics, 668, A105. doi:10.1051/0004-6361/202244218

Dutrey, A., Semenov, D., Chapillon, E., et al. 2014, Physical and Chemical Structure of Planet-Forming Disks Probed by Millimeter Observations and Modeling, in Protostars and Planets VI, ed. H. Beuther, R. S. Klessen, C. P. Dullemond, & T. Henning, 317–338. doi:10.2458/azu_uapress_9780816531240-ch014

Eckhardt, B., Schneider, T. M., Hof, B., & Westerweel, J. 2007, Turbulence Transition in Pipe Flow, Annual Review of Fluid Mechanics, 39, 447–468. doi:10.1146/annurev.fluid.39.050905.110308

Eislöffel, J. & Mundt, R. 1998, Imaging and Kinematic Studies of Young Stellar Object Jets in Taurus, Astronomical Journal, 115, 1554–1575. doi:10.1086/300282

Eisner, J. A., Hillenbrand, L. A., White, R. J., et al. 2007, Near-Infrared Interferometric, Spectroscopic, and Photometric Monitoring of T Tauri Inner Disks, Astrophysical Journal, 669, 1072–1084. doi:10.1086/521874

Espaillat, C., Muzerolle, J., Najita, J., et al. 2014, An Observational Perspective of Transitional Disks, in Protostars and Planets VI, ed.

H. Beuther, R. S. Klessen, C. P. Dullemond, & T. Henning, 497–520. doi:10.2458/azu_uapress_9780816531240-ch022

Estalella, R., López, R., Anglada, G., et al. 2012, The Counterjet of HH 30: New Light on Its Binary Driving Source, Astronomical Journal, 144, 61. doi:10.1088/0004-6256/144/2/61

Facchini, S., Clarke, C. J., & Bisbas, T. G. 2016a, External photoevaporation of protoplanetary discs in sparse stellar groups: the impact of dust growth, Monthly Notices of the Royal Astronomical Society, 457, 3593–3610. doi:10.1093/mnras/stw240

Facchini, S., Juhász, A., & Lodato, G. 2018, Signatures of broken protoplanetary discs in scattered light and in sub-millimetre observations, Monthly Notices of the Royal Astronomical Society, 473, 4459–4475. doi:10.1093/mnras/stx2523

Facchini, S., Lodato, G., & Price, D. J. 2013, Wave-like warp propagation in circumbinary discs - I. Analytic theory and numerical simulations, Monthly Notices of the Royal Astronomical Society, 433, 2142–2156. doi:10.1093/mnras/stt877

Facchini, S., Manara, C. F., Schneider, P. C., et al. 2016b, Violent environment of the inner disk of RW Aurigae A probed by the 2010 and 2015 dimming events, Astronomy and Astrophysics, 596, A38. doi:10.1051/0004-6361/201629607

Facchini, S., Ricci, L., & Lodato, G. 2014, Probing the presence of planets in transition discs' cavities via warps: the case of TW Hya, Monthly Notices of the Royal Astronomical Society, 442, 3700–3710. doi:10.1093/mnras/stu1149

Fairbairn, C. W. & Ogilvie, G. I. 2021a, Non-linear dynamics of hydrodynamic tori as a model of oscillations and bending waves in astrophysical discs, Monthly Notices of the Royal Astronomical Society, 505, 4906–4919. doi:10.1093/mnras/stab1554

Fairbairn, C. W. & Ogilvie, G. I. 2021b, Non-linear resonant torus oscillations as a model of Keplerian disc warp dynamics, Monthly Notices of the Royal Astronomical Society, 508, 2426–2446. doi:10.1093/mnras/stab2717

Fairbairn, C. W. & Ogilvie, G. I. 2023, Parametric instability in warped astrophysical discs: growth, saturation, and feedback, Monthly Notices of the Royal Astronomical Society, 520, 1022–1043. doi:10.1093/mnras/stad211

Feautrier, P. 1964, Sur la resolution numerique de l'equation de transfert., Comptes Rendus Academie des Sciences (serie non specifiee), 258, 3189

Fernández-López, M., Zapata, L. A., & Gabbasov, R. 2017, Strongly Misaligned Triple System in SR 24 Revealed by ALMA, Astrophysical Journal, 845, 10. doi:10.3847/1538-4357/aa7d51

Flaherty, K. M., Hughes, A. M., Rose, S. C., et al. 2017, A Three-dimensional View of Turbulence: Constraints on Turbulent Motions in the HD 163296 Protoplanetary Disk Using DCO^+, Astrophysical Journal, 843, 150. doi:10.3847/1538-4357/aa79f9

Fleck, Jr., J. A. & Canfield, E. H. 1984, A Random Walk Procedure for Improving the Computational Efficiency of the Implicit Monte Carlo Method for Nonlinear Radiation Transport, Journal of Computational Physics, 54, 508–523. doi:10.1016/0021-9991(84)90130-X

Forgan, D. & Rice, K. 2010, Stellar encounters in the context of outburst phenomena, Monthly Notices of the Royal Astronomical Society, 402, 1349–1356. doi:10.1111/j.1365-2966.2009.15974.x

Foucart, F. & Lai, D. 2011, Evolution of spin direction of accreting magnetic protostars and spin-orbit misalignment in exoplanetary systems - II. Warped discs, Monthly Notices of the Royal Astronomical Society, 412, 2799–2815. doi:10.1111/j.1365-2966.2010.18176.x

Foucart, F. & Lai, D. 2013, Assembly of Protoplanetary Disks and Inclinations of Circumbinary Planets, Astrophysical Journal, 764, 106. doi:10.1088/0004-637X/764/1/106

Foucart, F. & Lai, D. 2014, Evolution of linear warps in accretion discs and applications to protoplanetary discs in binaries, Monthly Notices of the Royal Astronomical Society, 445, 1731–1744. doi:10.1093/mnras/stu1869

Fragner, M. M. & Nelson, R. P. 2009, Giant planet formation in stellar clusters: the effects of stellar fly-bys, Astronomy and Astrophysics, 505, 873–889. doi:10.1051/0004-6361/200912292

Fragner, M. M. & Nelson, R. P. 2010, Evolution of warped and twisted accretion discs in close binary systems, Astronomy and Astrophysics, 511, A77. doi:10.1051/0004-6361/200913088

Francis, L. & van der Marel, N. 2020, Dust-depleted Inner Disks in a Large Sample of Transition Disks through Long-baseline ALMA Observations, Astrophysical Journal, 892, 111. doi:10.3847/1538-4357/ab7b63

Fung, J. & Ono, T. 2021, Cooling-induced Vortex Decay in Keplerian Disks, Astrophysical Journal, 922, 13. doi:10.3847/1538-4357/ac1d4e

Gaia Collaboration, Brown, A. G. A., Vallenari, A., et al. 2021, Gaia Early Data Release 3. Summary of the contents and survey properties, Astronomy and Astrophysics, 649, A1. doi:10.1051/0004-6361/202039657

Gaia Collaboration, Brown, A. G. A., Vallenari, A., et al. 2016, Gaia Data Release 1. Summary of the astrometric, photometric, and survey properties, Astronomy and Astrophysics, 595, A2. doi:10.1051/0004-6361/201629512

Gaia Collaboration, Vallenari, A., Brown, A. G. A., et al. 2023, Gaia Data Release 3. Summary of the content and survey properties, Astronomy and Astrophysics, 674, A1. doi:10.1051/0004-6361/202243940

Gammie, C. F. 1996, Layered Accretion in T Tauri Disks, Astrophysical Journal, 457, 355. doi:10.1086/176735

Gammie, C. F., Goodman, J., & Ogilvie, G. I. 2000, Linear and non-linear theory of a parametric instability of hydrodynamic warps in Keplerian discs, Monthly Notices of the Royal Astronomical Society, 318, 1005–1016. doi:10.1046/j.1365-8711.2000.03669.x

Garg, H., Pinte, C., Christiaens, V., et al. 2021, Non-Keplerian spirals, a gas-pressure dust trap, and an eccentric gas cavity in the circumbinary disc around HD 142527, Monthly Notices of the Royal Astronomical Society, 504, 782–791. doi:10.1093/mnras/stab800

Garufi, A., Benisty, M., Pinilla, P., et al. 2018, Evolution of protoplanetary disks from their taxonomy in scattered light: spirals, rings, cavities, and shadows, Astronomy and Astrophysics, 620, A94. doi:10.1051/0004-6361/201833872

Garufi, A., Dominik, C., Ginski, C., et al. 2022, A SPHERE survey of self-shadowed planet-forming disks, Astronomy and Astrophysics, 658, A137. doi:10.1051/0004-6361/202141692

Garufi, A., Ginski, C., van Holstein, R. G., et al. 2024, The SPHERE view of the Taurus star-forming region. The full census of planet-forming disks with GTO and DESTINYS programs, Astronomy and Astrophysics, 685, A53. doi:10.1051/0004-6361/202347586

Garufi, A., Quanz, S. P., Schmid, H. M., et al. 2016, The SPHERE view of the planet-forming disk around HD 100546, Astronomy and Astrophysics, 588, A8. doi:10.1051/0004-6361/201527940

Ghez, A. M., Neugebauer, G., & Matthews, K. 1993, The Multiplicity of T Tauri Stars in the Star Forming Regions Taurus-Auriga and Ophiuchus-Scorpius: A 2.2 Micron Speckle Imaging Survey, Astronomical Journal, 106, 2005. doi:10.1086/116782

Ghez, A. M., White, R. J., & Simon, M. 1997, High Spatial Resolution Imaging of Pre-Main-Sequence Binary Stars: Resolving the Relationship between Disks and Close Companions, Astrophysical Journal, 490, 353–367. doi:10.1086/304856

Gingold, R. A. & Monaghan, J. J. 1977, Smoothed particle hydrodynamics: theory and application to non-spherical stars., Monthly Notices of the Royal Astronomical Society, 181, 375–389. doi:10.1093/mnras/181.3.375

Ginski, C., Facchini, S., Huang, J., et al. 2021, Disk Evolution Study Through Imaging of Nearby Young Stars (DESTINYS): Late Infall Causing Disk Misalignment and Dynamic Structures in SU Aur, Astrophysical Journal, Letters, 908, L25. doi:10.3847/2041-8213/abdf57

Goldreich, P. & Tremaine, S. 1979, The excitation of density waves at the Lindblad and corotation resonances by an external potential., Astrophysical Journal, 233, 857–871. doi:10.1086/157448

Gonzalez, J.-F., van der Plas, G., Pinte, C., et al. 2020, Spirals, shadows, and precession in HD 100453 - I. The orbit of the binary, Monthly Notices of the Royal Astronomical Society, 499, 3837–3856. doi:10.1093/mnras/staa2938

Greene, T. 2001, Protostars, American Scientist, 89, 316. doi:10.1511/2001.4.316

Grosso, N., Alves, J., Wood, K., et al. 2003, Spatial Study with the Very Large Telescope of a New Resolved Edge-on Circumstellar Dust Disk Discovered at the Periphery of the ρ Ophiuchi Dark Cloud, Astrophysical Journal, 586, 296–305. doi:10.1086/367557

Guarcello, M. G., Drake, J. J., Wright, N. J., et al. 2023, Photoevaporation and Close Encounters: How the Environment around Cygnus OB2 Affects the Evolution of Protoplanetary Disks, Astrophysical Journal, Supplement, 269, 13. doi:10.3847/1538-4365/acdd67

Hammer, M., Lin, M.-K., Kratter, K. M., & Pinilla, P. 2021, Which planets trigger longer lived vortices: low-mass or high-mass?, Monthly Notices of the Royal Astronomical Society, 504, 3963–3985. doi:10.1093/mnras/stab1079

Harris, C. R., Millman, K. J., van der Walt, S. J., et al. 2020, Array programming with NumPy, Nature, 585, 357–362. doi:10.1038/s41586-020-2649-2

Hartigan, P., Edwards, S., & Ghandour, L. 1995, Disk Accretion and Mass Loss from Young Stars, Astrophysical Journal, 452, 736. doi:10.1086/176344

Hartmann, L., Herczeg, G., & Calvet, N. 2016, Accretion onto Pre-Main-Sequence Stars, Annual Review of Astronomy and Astrophysics, 54, 135–180. doi:10.1146/annurev-astro-081915-023347

Hashimoto, J., Dong, R., Muto, T., Liu, H. B., & Terada, Y. 2024, Shadowing in the Protoplanetary Disk of ZZ Tau IRS with HST, Astronomical Journal, 167, 75. doi:10.3847/1538-3881/ad1b5e

Held, L. E. & Ogilvie, G. I. 2024, Instability and warping in vertically oscillating accretion discs, Monthly Notices of the Royal Astronomical Society, 535, 3108–3128. doi:10.1093/mnras/stae2487

Heller, C. H. 1995, Encounters with Protostellar Disks. II. Disruption and Binary Formation, Astrophysical Journal, 455, 252. doi:10.1086/176573

Hirth, G. A., Mundt, R., Solf, J., & Ray, T. P. 1994, Asymmetries in Bipolar Jets from Young Stars, Astrophysical Journal, Letters, 427, L99. doi:10.1086/187374

Hopkins, P. F. 2015, A new class of accurate, mesh-free hydrodynamic simulation methods, Monthly Notices of the Royal Astronomical Society, 450, 53–110. doi:10.1093/mnras/stv195

Hunter, J. D. 2007, Matplotlib: A 2D Graphics Environment, Computing in Science Engineering, 9, 90–95. doi:10.1109/MCSE.2007.55

Icke, V. 1991, The hydrodynamics of aspherical planetary nebulae. I - Analytic evaluation of hydrodynamic difference schemes, Astronomy and Astrophysics, 251, 369–381

Jeans, J. H. 1902, The Stability of a Spherical Nebula, Philosophical Transactions of the Royal Society of London Series A, 199, 1–53. doi:10.1098/rsta.1902.0012

Jílková, L., Hamers, A. S., Hammer, M., & Portegies Zwart, S. 2016, Mass transfer between debris discs during close stellar encounters, Monthly Notices of the Royal Astronomical Society, 457, 4218–4235. doi:10.1093/mnras/stw264

Jordan, L. M. & Rometsch, T. 2025, Hydrodynamical simulations with strong indirect terms in FARGO-like codes: Numerical aspects of the non-inertial

frame and artificial viscosity, Astronomy and Astrophysics, 693, A177. doi:10.1051/0004-6361/202450383

Juhász, A. & Facchini, S. 2017, Observational signatures of linear warps in circumbinary discs, Monthly Notices of the Royal Astronomical Society, 466, 4053–4073. doi:10.1093/mnras/stw3389

Kanagawa, K. D., Tanaka, H., & Szuszkiewicz, E. 2018, Radial Migration of Gap-opening Planets in Protoplanetary Disks. I. The Case of a Single Planet, Astrophysical Journal, 861, 140. doi:10.3847/1538-4357/aac8d9

Karnath, N., Prchlik, J. J., Gutermuth, R. A., et al. 2019, The Dynamics, Structure, and Fate of a Young Cluster during Gas Dispersal: Hectoschelle, Chandra, Spitzer, and Gaia Observations of Cep OB3b, Astrophysical Journal, 871, 46. doi:10.3847/1538-4357/aaf4c1

Kenyon, S. J. & Hartmann, L. 1987, Spectral Energy Distributions of T Tauri Stars: Disk Flaring and Limits on Accretion, Astrophysical Journal, 323, 714. doi:10.1086/165866

Keppler, M., Penzlin, A., Benisty, M., et al. 2020, Gap, shadows, spirals, and streamers: SPHERE observations of binary-disk interactions in GG Tauri A, Astronomy and Astrophysics, 639, A62. doi:10.1051/0004-6361/202038032

Keyte, L. & Haworth, T. J. 2025, Impact of photoevaporative winds in chemical models of externally irradiated protoplanetary discs, Monthly Notices of the Royal Astronomical Society, 537, 598–616. doi:10.1093/mnras/staf047

Kimmig, C. N. & Dullemond, C. P. 2024, Warped disk evolution in grid-based simulations, Astronomy and Astrophysics, 689, A45. doi:10.1051/0004-6361/202348660

Kimmig, C. N., Dullemond, C. P., & Kley, W. 2020, Effect of wind-driven accretion on planetary migration, Astronomy and Astrophysics, 633, A4. doi:10.1051/0004-6361/201936412

Kimmig, C. N. & Villenave, M. 2025, Asymmetric Signatures of Warps in Edge-on Disks, arXiv e-prints, arXiv:2504.05399. doi:10.48550/arXiv.2504.05399

Kirchhoff, G. 1860, Ueber das Verhältniss zwischen dem Emissionsvermögen und dem Absorptionsvermögen der Körper für Wärme und Licht, Annalen der Physik, 185, 275–301. doi:10.1002/andp.18601850205

Kley, W. & Nelson, R. P. 2012, Planet-Disk Interaction and Orbital Evolution, Annual Review of Astronomy and Astrophysics, 50, 211–249. doi:10.1146/annurev-astro-081811-125523

Kluska, J., Berger, J. P., Malbet, F., et al. 2020, A family portrait of disk inner rims around Herbig Ae/Be stars. Hunting for warps, rings, self shadowing, and misalignments in the inner astronomical units, Astronomy and Astrophysics, 636, A116. doi:10.1051/0004-6361/201833774

Kobayashi, H. & Ida, S. 2001, The Effects of a Stellar Encounter on a Planetesimal Disk, Icarus, 153, 416–429. doi:10.1006/icar.2001.6700

Kratter, K. & Lodato, G. 2016, Gravitational Instabilities in Circumstellar Disks, Annual Review of Astronomy and Astrophysics, 54, 271–311. doi:10.1146/annurev-astro-081915-023307

Kraus, S., Kreplin, A., Young, A. K., et al. 2020, A triple-star system with a misaligned and warped circumstellar disk shaped by disk tearing, Science, 369, 1233–1238. doi:10.1126/science.aba4633

Krause, M. G. H., Offner, S. S. R., Charbonnel, C., et al. 2020, The Physics of Star Cluster Formation and Evolution, Space Science Reviews, 216, 64. doi:10.1007/s11214-020-00689-4

Krieger, A., Kuffmeier, M., Reissl, S., et al. 2024, Feasibility of detecting shadows in disks induced by infall, Astronomy and Astrophysics, 686, A111. doi:10.1051/0004-6361/202348354

Krist, J. E., Stapelfeldt, K. R., Burrows, C. J., et al. 1998, Hubble Space Telescope WFPC2 Imaging of FS Tauri and Haro 6-5B, Astrophysical Journal, 501, 841–852. doi:10.1086/305861

Kuffmeier, M., Dullemond, C. P., Reissl, S., & Goicovic, F. G. 2021, Misaligned disks induced by infall, Astronomy and Astrophysics, 656, A161. doi:10.1051/0004-6361/202039614

Kuffmeier, M., Pineda, J. E., Segura-Cox, D., & Haugbølle, T. 2024, Constraints on the primordial misalignment of star-disk systems, Astronomy and Astrophysics, 690, A297. doi:10.1051/0004-6361/202450410

Kuhn, M. A., Hillenbrand, L. A., Sills, A., Feigelson, E. D., & Getman, K. V. 2019, Kinematics in Young Star Clusters and Associations with Gaia DR2, Astrophysical Journal, 870, 32. doi:10.3847/1538-4357/aaef8c

Kurtovic, N. T., Facchini, S., Benisty, M., et al. 2024, Binary orbit and disks properties of the RW Aur system using ALMA observations, Astronomy and Astrophysics, 692, A155. doi:10.1051/0004-6361/202347583

Kurtovic, N. T., Pérez, L. M., Benisty, M., et al. 2018, The Disk Substructures at High Angular Resolution Project (DSHARP). IV. Characterizing Substructures and Interactions in Disks around Multiple Star Systems, Astrophysical Journal, Letters, 869, L44. doi:10.3847/2041-8213/aaf746

Lada, C. J. 1987, Star formation: from OB associations to protostars., in Star Forming Regions, ed. M. Peimbert & J. Jugaku, 1

Lada, C. J. 2005, Star Formation in the Galaxy: An Observational Overview, Progress of Theoretical Physics Supplement, 158, 1–23. doi:10.1143/PTPS.158.1

Larwood, J. D. 1997, The tidal disruption of protoplanetary accretion discs, Monthly Notices of the Royal Astronomical Society, 290, 490–504. doi:10.1093/mnras/290.3.490

Lebreuilly, U., Hennebelle, P., Colman, T., et al. 2021, Protoplanetary Disk Birth in Massive Star-forming Clumps: The Essential Role of the Magnetic Field, Astrophysical Journal, Letters, 917, L10. doi:10.3847/2041-8213/ac158c

Lebreuilly, U., Hennebelle, P., Colman, T., et al. 2024, Synthetic populations of protoplanetary disks: Impact of magnetic fields and radiative transfer, Astronomy and Astrophysics, 682, A30. doi:10.1051/0004-6361/202346558

Lega, E., Morbidelli, A., Nelson, R. P., et al. 2022, Migration of Jupiter mass planets in discs with laminar accretion flows, Astronomy and Astrophysics, 658, A32. doi:10.1051/0004-6361/202141675

Léna, P., Rouan, D., Lebrun, F., Mignard, F., & Pelat, D. 2012, Observational Astrophysics, Springer Nature, 256 et seq. doi:10.1007/978-3-642-21815-6

Lesur, G. 2021, Magnetohydrodynamics of protoplanetary discs, Journal of Plasma Physics, 87, 205870101. doi:10.1017/S0022377820001002

Lesur, G., Flock, M., Ercolano, B., et al. 2023, Hydro-, Magnetohydro-, and Dust-Gas Dynamics of Protoplanetary Disks, in Protostars and Planets VII, ed. S. Inutsuka, Y. Aikawa, T. Muto, K. Tomida, & M. Tamura, 465. doi:10.48550/arXiv.2203.09821

Lesur, G. & Papaloizou, J. C. B. 2009, On the stability of elliptical vortices in accretion discs, Astronomy and Astrophysics, 498, 1–12. doi:10.1051/0004-6361/200811577

Lesur, G. & Papaloizou, J. C. B. 2010, The subcritical baroclinic instability in local accretion disc models, Astronomy and Astrophysics, 513, A60. doi:10.1051/0004-6361/200913594

Li, H., Li, S., Koller, J., et al. 2005, Potential Vorticity Evolution of a Protoplanetary Disk with an Embedded Protoplanet, Astrophysical Journal, 624, 1003–1009. doi:10.1086/429367

Lin, M.-K. & Youdin, A. N. 2015, Cooling Requirements for the Vertical Shear Instability in Protoplanetary Disks, Astrophysical Journal, 811, 17. doi:10.1088/0004-637X/811/1/17

Lodato, G. & Facchini, S. 2013, Wave-like warp propagation in circumbinary discs - II. Application to KH 15D, Monthly Notices of the Royal Astronomical Society, 433, 2157–2164. doi:10.1093/mnras/stt878

Lodato, G. & Price, D. J. 2010, On the diffusive propagation of warps in thin accretion discs, Monthly Notices of the Royal Astronomical Society, 405, 1212–1226. doi:10.1111/j.1365-2966.2010.16526.x

Lodato, G. & Pringle, J. E. 2007, Warp diffusion in accretion discs: a numerical investigation, Monthly Notices of the Royal Astronomical Society, 381, 1287–1300. doi:10.1111/j.1365-2966.2007.12332.x

Long, F., Herczeg, G. J., Harsono, D., et al. 2019, Compact Disks in a High-resolution ALMA Survey of Dust Structures in the Taurus Molecular Cloud, Astrophysical Journal, 882, 49. doi:10.3847/1538-4357/ab2d2d

Longarini, C., Lodato, G., Toci, C., & Aly, H. 2021, Dynamical dust traps in misaligned circumbinary discs: analytical theory and numerical simulations, Monthly Notices of the Royal Astronomical Society, 503, 4930–4941. doi:10.1093/mnras/stab843

Loomis, R. A., Öberg, K. I., Andrews, S. M., & MacGregor, M. A. 2017, A Multi-ringed, Modestly Inclined Protoplanetary Disk around AA Tau, Astrophysical Journal, 840, 23. doi:10.3847/1538-4357/aa6c63

Louvet, F., Dougados, C., Cabrit, S., et al. 2018, The HH30 edge-on T Tauri star. A rotating and precessing monopolar outflow scrutinized by ALMA, Astronomy and Astrophysics, 618, A120. doi:10.1051/0004-6361/201731733

Lovascio, F., Paardekooper, S.-J., & McNally, C. 2022, Dynamics of dusty vortices - II. Stability of 2D dust-laden vortices, Monthly Notices of the Royal Astronomical Society, 516, 1635–1643. doi:10.1093/mnras/stac2269

Lovelace, R. V. E., Li, H., Colgate, S. A., & Nelson, A. F. 1999, Rossby Wave Instability of Keplerian Accretion Disks, Astrophysical Journal, 513, 805–810. doi:10.1086/306900

Lubow, S. H. & Ogilvie, G. I. 2000, On the Tilting of Protostellar Disks by Resonant Tidal Effects, Astrophysical Journal, 538, 326–340. doi:10.1086/309101

Lucy, L. B. 1999, Computing radiative equilibria with Monte Carlo techniques, Astronomy and Astrophysics, 344, 282–288

Lunine, J. I., Macintosh, B., & Peale, S. 2009, The detection and characterization of exoplanets, Physics Today, 62, 46. doi:10.1063/1.3141941

Maloney, P. R., Begelman, M. C., & Pringle, J. E. 1996, Radiation-driven Warping: The Origin of WARPS and Precession in Accretion Disks, Astrophysical Journal, 472, 582. doi:10.1086/178089

Malygin, M. G., Klahr, H., Semenov, D., Henning, T., & Dullemond, C. P. 2017, Efficiency of thermal relaxation by radiative processes in protoplanetary discs: constraints on hydrodynamic turbulence, Astronomy and Astrophysics, 605, A30. doi:10.1051/0004-6361/201629933

Manara, C. F., Ansdell, M., Rosotti, G. P., et al. 2023, Demographics of Young Stars and their Protoplanetary Disks: Lessons Learned on Disk Evolution and its Connection to Planet Formation, in Protostars and Planets VII, ed. S. Inutsuka, Y. Aikawa, T. Muto, K. Tomida, & M. Tamura, 539. doi:10.48550/arXiv.2203.09930

Marino, S., Perez, S., & Casassus, S. 2015, Shadows Cast by a Warp in the HD 142527 Protoplanetary Disk, Astrophysical Journal, Letters, 798, L44. doi:10.1088/2041-8205/798/2/L44

Martin, R. G., Lubow, S. H., Pringle, J. E., et al. 2019, Generalized Warped Disk Equations, Astrophysical Journal, 875, 5. doi:10.3847/1538-4357/ab0bb7

Masset, F. 2000, FARGO: A fast eulerian transport algorithm for differentially rotating disks, Astronomy and Astrophysics Supplement Series, 141, 165–173. doi:10.1051/aas:2000116

Mayama, S., Akiyama, E., Panić, O., et al. 2018, ALMA Reveals a Misaligned Inner Gas Disk inside the Large Cavity of a Transitional Disk, Astrophysical Journal, Letters, 868, L3. doi:10.3847/2041-8213/aae88b

Mayama, S., Pérez, S., Kusakabe, N., et al. 2020, Subaru Near-infrared Imaging Polarimetry of Misaligned Disks around the SR 24 Hierarchical Triple System, Astronomical Journal, 159, 12. doi:10.3847/1538-3881/ab5850

Mayama, S., Tamura, M., Hanawa, T., et al. 2010, Direct Imaging of Bridged Twin Protoplanetary Disks in a Young Multiple Star, Science, 327, 306. doi:10.1126/science.1179679

Mayor, M. & Queloz, D. 1995, A Jupiter-mass companion to a solar-type star, Nature, 378, 355–359. doi:10.1038/378355a0

McJunkin, M., France, K., Burgh, E. B., et al. 2013, Probing the Inner Regions of Protoplanetary Disks with CO Absorption Line Spectroscopy, Astrophysical Journal, 766, 12. doi:10.1088/0004-637X/766/1/12

Melnikov, S. Y., Eislöffel, J., Bacciotti, F., Woitas, J., & Ray, T. P. 2009, HST/STIS observations of the RW Aurigae bipolar jet: mapping the physical parameters close to the source, Astronomy and Astrophysics, 506, 763–777. doi:10.1051/0004-6361/200811567

Ménard, F., Cuello, N., Ginski, C., et al. 2020, Ongoing flyby in the young multiple system UX Tauri, Astronomy and Astrophysics, 639, L1. doi:10.1051/0004-6361/202038356

Min, M., Dullemond, C. P., Dominik, C., de Koter, A., & Hovenier, J. W. 2009, Radiative transfer in very optically thick circumstellar disks, Astronomy and Astrophysics, 497, 155–166. doi:10.1051/0004-6361/200811470

Min, M., Stolker, T., Dominik, C., & Benisty, M. 2017, Connecting the shadows: probing inner disk geometries using shadows in transitional disks, Astronomy and Astrophysics, 604, L10. doi:10.1051/0004-6361/201730949

Monaghan, J. J. 2005, Smoothed particle hydrodynamics, Reports on Progress in Physics, 68, 1703–1759. doi:10.1088/0034-4885/68/8/R01

Moscadelli, L., Sanna, A., Beuther, H., Oliva, A., & Kuiper, R. 2022, Snapshot of a magnetohydrodynamic disk wind traced by water maser observations, Nature Astronomy, 6, 1068–1076. doi:10.1038/s41550-022-01754-4

Muñoz, D. J., Kratter, K., Vogelsberger, M., Hernquist, L., & Springel, V. 2015, Stellar orbit evolution in close circumstellar disc encounters, Monthly Notices of the Royal Astronomical Society, 446, 2010–2029. doi:10.1093/mnras/stu2220

Muro-Arena, G. A., Benisty, M., Ginski, C., et al. 2020, Shadowing and multiple rings in the protoplanetary disk of HD 139614, Astronomy and Astrophysics, 635, A121. doi:10.1051/0004-6361/201936509

Muro-Arena, G. A., Dominik, C., Waters, L. B. F. M., et al. 2018, Dust modeling of the combined ALMA and SPHERE datasets of HD 163296. Is HD 163296 really a Meeus group II disk?, Astronomy and Astrophysics, 614, A24. doi:10.1051/0004-6361/201732299

Nagasawa, M., Ida, S., & Bessho, T. 2008, Formation of Hot Planets by a Combination of Planet Scattering, Tidal Circularization, and the Kozai Mechanism, Astrophysical Journal, 678, 498–508. doi:10.1086/529369

Nealon, R., Cuello, N., & Alexander, R. 2020a, Flyby-induced misalignments in planet-hosting discs, Monthly Notices of the Royal Astronomical Society, 491, 4108–4115. doi:10.1093/mnras/stz3186

Nealon, R., Dipierro, G., Alexander, R., Martin, R. G., & Nixon, C. 2018, Warping a protoplanetary disc with a planet on an inclined orbit, Monthly Notices of the Royal Astronomical Society, 481, 20–35. doi:10.1093/mnras/sty2267

Nealon, R., Pinte, C., Alexander, R., Mentiplay, D., & Dipierro, G. 2019, Scattered light shadows in warped protoplanetary discs, Monthly Notices of the Royal Astronomical Society, 484, 4951–4962. doi:10.1093/mnras/stz346

Nealon, R., Price, D. J., & Nixon, C. J. 2015, On the Bardeen-Petterson effect in black hole accretion discs, Monthly Notices of the Royal Astronomical Society, 448, 1526–1540. doi:10.1093/mnras/stv014

Nealon, R., Price, D. J., & Pinte, C. 2020b, Rocking shadows in broken circumbinary discs, Monthly Notices of the Royal Astronomical Society, 493, L143–L147. doi:10.1093/mnrasl/slaa026

Nelson, R. P., Gressel, O., & Umurhan, O. M. 2013, Linear and non-linear evolution of the vertical shear instability in accretion discs, Monthly Notices of the Royal Astronomical Society, 435, 2610–2632. doi:10.1093/mnras/stt1475

Nelson, R. P. & Papaloizou, J. C. B. 1999, Hydrodynamic simulations of propagating WARPS and bending waves in accretion discs, Monthly Notices of the Royal Astronomical Society, 309, 929–940. doi:10.1046/j.1365-8711.1999.02894.x

Niccolini, G., Woitke, P., & Lopez, B. 2003, High precision Monte Carlo radiative transfer in dusty media, Astronomy and Astrophysics, 399, 703–716. doi:10.1051/0004-6361:20021761

Nixon, C. & King, A. 2016, Warp Propagation in Astrophysical Discs, in Lecture Notes in Physics, ed. F. Haardt, V. Gorini, U. Moschella, A. Treves, & M. Colpi, Vol. 905, Berlin Springer Verlag, 45–63. doi:10.1007/978-3-319-19416-5_2

Nixon, C., King, A., & Price, D. 2013, Tearing up the disc: misaligned accretion on to a binary, Monthly Notices of the Royal Astronomical Society, 434, 1946–1954. doi:10.1093/mnras/stt1136

Öberg, K. I., Guzmán, V. V., Walsh, C., et al. 2021, Molecules with ALMA at Planet-forming Scales (MAPS). I. Program Overview and Highlights, Astrophysical Journal, Supplement, 257, 1. doi:10.3847/1538-4365/ac1432

Offner, S. S. R., Moe, M., Kratter, K. M., et al. 2023, The Origin and Evolution of Multiple Star Systems, in Protostars and Planets VII, ed. S. Inutsuka, Y. Aikawa, T. Muto, K. Tomida, & M. Tamura, 275. doi:10.48550/arXiv.2203.10066

Ogilvie, G. I. 1999, The non-linear fluid dynamics of a warped accretion disc, Monthly Notices of the Royal Astronomical Society, 304, 557–578. doi:10.1046/j.1365-8711.1999.02340.x

Ogilvie, G. I. 2006, Non-linear bending waves in Keplerian accretion discs, Monthly Notices of the Royal Astronomical Society, 365, 977–990. doi:10.1111/j.1365-2966.2005.09776.x

Ogilvie, G. I. & Latter, H. N. 2013a, Hydrodynamic instability in warped astrophysical discs, Monthly Notices of the Royal Astronomical Society, 433, 2420–2435. doi:10.1093/mnras/stt917

Ogilvie, G. I. & Latter, H. N. 2013b, Local and global dynamics of warped astrophysical discs, Monthly Notices of the Royal Astronomical Society, 433, 2403–2419. doi:10.1093/mnras/stt916

Ostriker, E. C. 1994, Capture and Induced Disk Accretion in Young Star Encounters, Astrophysical Journal, 424, 292. doi:10.1086/173890

Paardekooper, S., Dong, R., Duffell, P., et al. 2023, Planet-Disk Interactions and Orbital Evolution, in Protostars and Planets VII, ed. S. Inutsuka, Y. Aikawa, T. Muto, K. Tomida, & M. Tamura, 685. doi:10.48550/arXiv.2203.09595

Paardekooper, S.-J. & Ogilvie, G. I. 2019, Local numerical simulations of warped discs, Monthly Notices of the Royal Astronomical Society, 483, 3738–3753. doi:10.1093/mnras/sty3349

Papaloizou, J. C. B., Korycansky, D. G., & Terquem, C. 1995, Density waves and warps generated by tidal perturbation of a gaseous disk., Annals of the New York Academy of Sciences, 773, 261–276. doi:10.1111/j.1749-6632.1995.tb12175.x

Papaloizou, J. C. B., Larwood, J. D., Nelson, R. P., & Terquem, C. 1997, Precessing warped discs in close binary systems, in Accretion Disks - New Aspects, ed. E. Meyer-Hofmeister & H. Spruit, Vol. 487, Proceedings of the EARA Workshop on Accretion Disks (Garching, Oct. 1996), 182. doi:10.1007/BFb0105832

Papaloizou, J. C. B. & Lin, D. N. C. 1995, On the Dynamics of Warped Accretion Disks, Astrophysical Journal, 438, 841. doi:10.1086/175127

Papaloizou, J. C. B. & Pringle, J. E. 1983, The time-dependence of non-planar accretion discs, Monthly Notices of the Royal Astronomical Society, 202, 1181–1194. doi:10.1093/mnras/202.4.1181

Papaloizou, J. C. B. & Terquem, C. 1995, On the dynamics of tilted discs around young stars, Monthly Notices of the Royal Astronomical Society, 274, 987–1001. doi:10.1093/mnras/274.4.987

Pascucci, I., Cabrit, S., Edwards, S., et al. 2023, The Role of Disk Winds in the Evolution and Dispersal of Protoplanetary Disks, in Protostars and Planets VII, ed. S. Inutsuka, Y. Aikawa, T. Muto, K. Tomida, & M. Tamura, 567. doi:10.48550/arXiv.2203.10068

Pattle, K., Fissel, L., Tahani, M., Liu, T., & Ntormousi, E. 2023, Magnetic Fields in Star Formation: from Clouds to Cores, in Protostars and Planets VII, ed. S. Inutsuka, Y. Aikawa, T. Muto, K. Tomida, & M. Tamura, 193. doi:10.48550/arXiv.2203.11179

Peng, Y.-C., Wang, J.-M., Du, P., Zhai, S., & Li, Y.-R. 2025, Warped Accretion Disks and Quasars with Episodic Periodicity of Long-term Variations, Astrophysical Journal, 978, 103. doi:10.3847/1538-4357/ad9560

Pérez, L. M., Benisty, M., Andrews, S. M., et al. 2018, The Disk Substructures at High Angular Resolution Project (DSHARP). X. Multiple Rings, a Misaligned Inner Disk, and a Bright Arc in the Disk around the T Tauri star HD 143006, Astrophysical Journal, Letters, 869, L50. doi:10.3847/2041-8213/aaf745

Pérez, S., Hales, A., Liu, H. B., et al. 2020, Resolving the FU Orionis System with ALMA: Interacting Twin Disks?, Astrophysical Journal, 889, 59. doi:10.3847/1538-4357/ab5c1b

Petersen, M. R., Julien, K., & Stewart, G. R. 2007, Baroclinic Vorticity Production in Protoplanetary Disks. I. Vortex Formation, Astrophysical Journal, 658, 1236–1251. doi:10.1086/511513

Petrov, P. P., Gahm, G. F., Djupvik, A. A., et al. 2015, Another deep dimming of the classical T Tauri star RW Aurigae A, Astronomy and Astrophysics, 577, A73. doi:10.1051/0004-6361/201525845

Petterson, J. A. 1977, Twisted accretion disks. I. Derivation of the basic equations., Astrophysical Journal, 214, 550–559. doi:10.1086/155280

Pfalzner, S. 2003, Spiral Arms in Accretion Disk Encounters, Astrophysical Journal, 592, 986–1001. doi:10.1086/375808

Pfalzner, S. 2008, Encounter-driven accretion in young stellar clusters - A connection to FUors?, Astronomy and Astrophysics, 492, 735–741. doi:10.1051/0004-6361:200810879

Pfalzner, S. 2013, Early evolution of the birth cluster of the solar system, Astronomy and Astrophysics, 549, A82. doi:10.1051/0004-6361/201218792

Pfalzner, S. & Govind, A. 2021, Close Stellar Flybys Common in Low-mass Clusters, Astrophysical Journal, 921, 90. doi:10.3847/1538-4357/ac19aa

Pfalzner, S. & Vincke, K. 2020, Cradle(s) of the Sun, Astrophysical Journal, 897, 60. doi:10.3847/1538-4357/ab9533

Phuong, N. T., Dutrey, A., Di Folco, E., et al. 2020, Planet-induced spirals in the circumbinary disk of GG Tauri A, Astronomy and Astrophysics, 635, L9. doi:10.1051/0004-6361/202037682

Picogna, G. & Marzari, F. 2014, Effects of stellar flybys on planetary systems: 3D modeling of the circumstellar disk's damping effects, Astronomy and Astrophysics, 564, A28. doi:10.1051/0004-6361/201322816

Pineda, J. E., Segura-Cox, D., Caselli, P., et al. 2020, A protostellar system fed by a streamer of 10,500 au length, Nature Astronomy, 4, 1158–1163. doi:10.1038/s41550-020-1150-z

Pinilla, P., Benisty, M., de Boer, J., et al. 2018, Variable Outer Disk Shadowing around the Dipper Star RXJ1604.3-2130, Astrophysical Journal, 868, 85. doi:10.3847/1538-4357/aae824

Pinte, C., Dent, W. R. F., Ménard, F., et al. 2016, Dust and Gas in the Disk of HL Tauri: Surface Density, Dust Settling, and Dust-to-gas Ratio, Astrophysical Journal, 816, 25. doi:10.3847/0004-637X/816/1/25

Pinte, C., Ménard, F., Duchêne, G., & Bastien, P. 2006, Monte Carlo radiative transfer in protoplanetary disks, Astronomy and Astrophysics, 459, 797–804. doi:10.1051/0004-6361:20053275

Pinte, C., Teague, R., Flaherty, K., et al. 2023, Kinematic Structures in Planet-Forming Disks, in Protostars and Planets VII, ed. S. Inutsuka, Y. Aikawa, T. Muto, K. Tomida, & M. Tamura, 645. doi:10.48550/arXiv.2203.09528

Planet formation environments collaboration, Allen, M., Anania, R., et al. 2025, The past, present and future of observations of externally irradiated disks, arXiv e-prints, arXiv:2502.12255. doi:10.48550/arXiv.2502.12255

Pontoppidan, K. M., Stapelfeldt, K. R., Blake, G. A., van Dishoeck, E. F., & Dullemond, C. P. 2007, Deep Spitzer Spectroscopy of the "Flying Saucer" Edge-on Disk: Large Grains beyond 50 AU, Astrophysical Journal, Letters, 658, L111–L114. doi:10.1086/514817

Poon, M., Zanazzi, J. J., & Zhu, W. 2021, Constraining the circumbinary disc tilt in the KH 15D system, Monthly Notices of the Royal Astronomical Society, 503, 1599–1614. doi:10.1093/mnras/stab575

Pringle, J. E. 1992, A simple approach to the evolution of twisted accretion discs, Monthly Notices of the Royal Astronomical Society, 258, 811–818. doi:10.1093/mnras/258.4.811

Pringle, J. E. 1996, Self-induced warping of accretion discs, Monthly Notices of the Royal Astronomical Society, 281, 357–361. doi:10.1093/mnras/281.1.357

Qian, Y. & Wu, Y. 2024, Shadows Wreak Havoc in Transition Disks, Astrophysical Journal, 976, 5. doi:10.3847/1538-4357/ad8233

Rabago, I., Zhu, Z., Lubow, S., & Martin, R. G. 2024, Warps and breaks in circumbinary discs, Monthly Notices of the Royal Astronomical Society, 533, 360–373. doi:10.1093/mnras/stae1787

Rabago, I., Zhu, Z., Martin, R. G., & Lubow, S. H. 2023, Grid-based simulations of polar circumbinary discs: polar alignment and vortex formation, Monthly Notices of the Royal Astronomical Society, 520, 2138–2147. doi:10.1093/mnras/stad242

Rafikov, R. R. & Cimerman, N. P. 2023, Vortex weighing and dating of planets in protoplanetary discs, Monthly Notices of the Royal Astronomical Society, 519, 5800–5806. doi:10.1093/mnras/stac3692

Rawiraswattana, K. & Goodwin, S. P. 2023, On Encounter Rates in Star Clusters, Astrophysical Journal, 947, 12. doi:10.3847/1538-4357/acc104

Ren, B., Dong, R., van Holstein, R. G., et al. 2020, Dynamical Evidence of a Spiral Arm-driving Planet in the MWC 758 Protoplanetary Disk, Astrophysical Journal, Letters, 898, L38. doi:10.3847/2041-8213/aba43e

Robitaille, T. P. 2010, On the modified random walk algorithm for Monte-Carlo radiation transfer, Astronomy and Astrophysics, 520, A70. doi:10.1051/0004-6361/201015025

Rodenkirch, P. J., Klahr, H., Fendt, C., & Dullemond, C. P. 2020, Global axisymmetric simulations of photoevaporation and magnetically driven protoplanetary disk winds, Astronomy and Astrophysics, 633, A21. doi:10.1051/0004-6361/201834945

Rodriguez, J. E., Loomis, R., Cabrit, S., et al. 2018, Multiple Stellar Flybys Sculpting the Circumstellar Architecture in RW Aurigae, Astrophysical Journal, 859, 150. doi:10.3847/1538-4357/aac08f

Rodriguez, J. E., Pepper, J., Stassun, K. G., et al. 2013, Occultation of the T Tauri Star RW Aurigae A by its Tidally Disrupted Disk, Astronomical Journal, 146, 112. doi:10.1088/0004-6256/146/5/112

Rodriguez, J. E., Reed, P. A., Siverd, R. J., et al. 2016, Recurring Occultations of RW Aurigae by Coagulated Dust in the Tidally Disrupted Circumstellar Disk, Astronomical Journal, 151, 29. doi:10.3847/0004-6256/151/2/29

Romanova, M. M., Koldoba, A. V., Ustyugova, G. V., et al. 2021, 3D MHD simulations of accretion on to stars with tilted magnetic and rotational axes, Monthly Notices of the Royal Astronomical Society, 506, 372–384. doi:10.1093/mnras/stab1724

Rometsch, T., Ziampras, A., Kley, W., & Béthune, W. 2021, Survival of planet-induced vortices in 2D disks, Astronomy and Astrophysics, 656, A130. doi:10.1051/0004-6361/202142105

Rosotti, G. P. 2023, Empirical constraints on turbulence in proto-planetary discs, New Astronomy Review, 96, 101674. doi:10.1016/j.newar.2023.101674

Rosotti, G. P., Dale, J. E., de Juan Ovelar, M., et al. 2014, Protoplanetary disc evolution affected by star-disc interactions in young stellar clusters, Monthly Notices of the Royal Astronomical Society, 441, 2094–2110. doi:10.1093/mnras/stu679

Rowther, S., Nealon, R., & Meru, F. 2022, Warping Away Gravitational Instabilities in Protoplanetary Discs, Astrophysical Journal, 925, 163. doi:10.3847/1538-4357/ac3975

Rybicki, G. B. & Hummer, D. G. 1991, An accelerated lambda iteration method for multilevel radiative transfer. I. Non-overlapping lines with background continuum, Astronomy and Astrophysics, 245, 171–181

Rybicki, G. B. & Lightman, A. P. 1985, Radiative Processes in Astrophysics, Wiley-Interscience

Sai, J., Ohashi, N., Saigo, K., et al. 2020, Disk Structure around the Class I Protostar L1489 IRS Revealed by ALMA: A Warped-disk System, Astrophysical Journal, 893, 51. doi:10.3847/1538-4357/ab8065

Sakai, N., Hanawa, T., Zhang, Y., et al. 2019, A warped disk around an infant protostar, Nature, 565, 206–208. doi:10.1038/s41586-018-0819-2

Shakura, N. I. & Sunyaev, R. A. 1973, Black holes in binary systems. Observational appearance., Astronomy and Astrophysics, 24, 337–355

Shu, F. H., Lizano, S., & Adams, F. C. 1987, Star formation in molecular cloud cores, in Star Forming Regions, ed. M. Peimbert & J. Jugaku, 417–433

Smallwood, J. L., Nealon, R., Chen, C., et al. 2021, GW Ori: circumtriple rings and planets, Monthly Notices of the Royal Astronomical Society, 508, 392–407. doi:10.1093/mnras/stab2624

Smallwood, J. L., Nealon, R., Cuello, N., Dong, R., & Booth, R. A. 2024, Formation of misaligned second-generation discs through fly-by encounters, Monthly Notices of the Royal Astronomical Society, 527, 2094–2109. doi:10.1093/mnras/stad3057

Smallwood, J. L., Yang, C.-C., Zhu, Z., et al. 2023, Exciting spiral arms in protoplanetary discs from flybys, Monthly Notices of the Royal Astronomical Society, 521, 3500–3516. doi:10.1093/mnras/stad742

Sorathia, K. A., Krolik, J. H., & Hawley, J. F. 2013, Relaxation of Warped Disks: The Case of Pure Hydrodynamics, Astrophysical Journal, 768, 133. doi:10.1088/0004-637X/768/2/133

Springel, V. 2010, Smoothed Particle Hydrodynamics in Astrophysics, Annual Review of Astronomy and Astrophysics, 48, 391–430. doi:10.1146/annurev-astro-081309-130914

Spruit, H. C. 1996, Magnetohydrodynamic jets and winds from accretion disks, in Evolutionary Processes in Binary Stars, ed. R. A. M. J. Wijers, M. B. Davies, & C. A. Tout, 249–286

Stapelfeldt, K. R., Duchêne, G., Perrin, M., et al. 2014, HST Imaging of New Edge-on Circumstellar Disks in Nearby Star-forming Regions, in Exploring the Formation and Evolution of Planetary Systems, ed. M. Booth, B. C. Matthews, & J. R. Graham, 99–103. doi:10.1017/S1743921313008004

Stapelfeldt, K. R., Krist, J. E., Ménard, F., et al. 1998, An Edge-On Circumstellar Disk in the Young Binary System HK Tauri, Astrophysical Journal, Letters, 502, L65–L69. doi:10.1086/311479

Stapelfeldt, K. R., Ménard, F., Watson, A. M., et al. 2003, Hubble Space Telescope WFPC2 Imaging of the Disk and Jet of HV Tauri C, Astrophysical Journal, 589, 410–418. doi:10.1086/374374

Stapelfeldt, K. R., Watson, A. M., Krist, J. E., et al. 1999, A Variable Asymmetry in the Circumstellar Disk of HH 30, Astrophysical Journal, Letters, 516, L95–L98. doi:10.1086/312001

Stolker, T., Dominik, C., Avenhaus, H., et al. 2016, Shadows cast on the transition disk of HD 135344B. Multiwavelength VLT/SPHERE polarimetric differential imaging, Astronomy and Astrophysics, 595, A113. doi:10.1051/0004-6361/201528039

Stolker, T., Sitko, M., Lazareff, B., et al. 2017, Variable Dynamics in the Inner Disk of HD 135344B Revealed with Multi-epoch Scattered Light Imaging, Astrophysical Journal, 849, 143. doi:10.3847/1538-4357/aa886a

Stoll, M. H. R. & Kley, W. 2014, Vertical shear instability in accretion disc models with radiation transport, Astronomy and Astrophysics, 572, A77. doi:10.1051/0004-6361/201424114

Sturm, J. A., McClure, M. K., Law, C. J., et al. 2023, The edge-on protoplanetary disk HH 48 NE. I. Modeling the geometry and stellar parameters, Astronomy and Astrophysics, 677, A17. doi:10.1051/0004-6361/202346052

Su, Z. & Bai, X.-N. 2024, Dynamical Consequence of Shadows Cast to the Outer Protoplanetary Disks. I. Two-dimensional Simulations, Astrophysical Journal, 975, 126. doi:10.3847/1538-4357/ad7581

Tabone, B., Rosotti, G. P., Cridland, A. J., Armitage, P. J., & Lodato, G. 2022, Secular evolution of MHD wind-driven discs: analytical solutions in the expanded α-framework, Monthly Notices of the Royal Astronomical Society, 512, 2290–2309. doi:10.1093/mnras/stab3442

Takami, M., Fu, G., Liu, H. B., et al. 2018, Near-infrared High-resolution Imaging Polarimetry of FU Ori-type Objects: Toward a Unified Scheme for Low-mass Protostellar Evolution, Astrophysical Journal, 864, 20. doi:10.3847/1538-4357/aad2e1

Tanaka, H., Takeuchi, T., & Ward, W. R. 2002, Three-Dimensional Interaction between a Planet and an Isothermal Gaseous Disk. I. Corotation and Lindblad Torques and Planet Migration, Astrophysical Journal, 565, 1257–1274. doi:10.1086/324713

Tazaki, R., Ménard, F., Duchêne, G., et al. 2025, JWST Imaging of Edge-on Protoplanetary Disks. IV. Mid-infrared Dust Scattering in the HH 30 Disk, Astrophysical Journal, 980, 49. doi:10.3847/1538-4357/ad9c6f

Terquem, C. & Bertout, C. 1993, Tidally-induced warps in T Tauri disks. I. First-order perturbation theory., Astronomy and Astrophysics, 274, 291–303

Terquem, C., Eislöffel, J., Papaloizou, J. C. B., & Nelson, R. P. 1999, Precession of Collimated Outflows from Young Stellar Objects, Astrophysical Journal, Letters, 512, L131–L134. doi:10.1086/311880

Teyssandier, J., Terquem, C., & Papaloizou, J. C. B. 2013, Orbital evolution of a planet on an inclined orbit interacting with a disc, Monthly Notices of the Royal Astronomical Society, 428, 658–669. doi:10.1093/mnras/sts064

Thies, I., Kroupa, P., Goodwin, S. P., Stamatellos, D., & Whitworth, A. P. 2010, Tidally Induced Brown Dwarf and Planet Formation in Circumstellar Disks, Astrophysical Journal, 717, 577–585. doi:10.1088/0004-637X/717/1/577

Thies, I., Kroupa, P., Goodwin, S. P., Stamatellos, D., & Whitworth, A. P. 2011, A natural formation scenario for misaligned and short-period eccentric extrasolar planets, Monthly Notices of the Royal Astronomical Society, 417, 1817–1822. doi:10.1111/j.1365-2966.2011.19390.x

Toomre, A. 1964, On the gravitational stability of a disk of stars., Astrophysical Journal, 139, 1217–1238. doi:10.1086/147861

Urpin, V. & Brandenburg, A. 1998, Magnetic and vertical shear instabilities in accretion discs, Monthly Notices of the Royal Astronomical Society, 294, 399–406. doi:10.1046/j.1365-8711.1998.01118.x10.1111/j.1365-8711.1998.01118.x

van der Plas, G., Ménard, F., Gonzalez, J. F., et al. 2019, ALMA study of the HD 100453 AB system and the tidal interaction of the companion with the disk, Astronomy and Astrophysics, 624, A33. doi:10.1051/0004-6361/201834134

van der Plas, G., Wright, C. M., Ménard, F., et al. 2017, Cavity and other radial substructures in the disk around HD 97048, Astronomy and Astrophysics, 597, A32. doi:10.1051/0004-6361/201629523

Van Rossum, G. & Drake, F. L. 2009, Python 3 Reference Manual, Scotts Valley, CA: CreateSpace

Villenave, M., Ménard, F., Dent, W. R. F., et al. 2020, Observations of edge-on protoplanetary disks with ALMA. I. Results from continuum data, Astronomy and Astrophysics, 642, A164. doi:10.1051/0004-6361/202038087

Villenave, M., Stapelfeldt, K. R., Duchêne, G., et al. 2024, JWST Imaging of Edge-on Protoplanetary Disks. II. Appearance of Edge-on Disks with a Tilted Inner Region: Case Study of IRAS04302+2247, Astrophysical Journal, 961, 95. doi:10.3847/1538-4357/ad0c4b

Vincke, K., Breslau, A., & Pfalzner, S. 2015, Strong effect of the cluster environment on the size of protoplanetary discs?, Astronomy and Astrophysics, 577, A115. doi:10.1051/0004-6361/201425552

Virtanen, P., Gommers, R., Oliphant, T. E., et al. 2020, SciPy 1.0: Fundamental Algorithms for Scientific Computing in Python, Nature Methods, 17, 261–272. doi:10.1038/s41592-019-0686-2

Walsh, C., Daley, C., Facchini, S., & Juhász, A. 2017, CO emission tracing a warp or radial flow within $\lesssim$100 au in the HD 100546 protoplanetary disk, Astronomy and Astrophysics, 607, A114. doi:10.1051/0004-6361/201731334

Ward, W. R. 1991, Horsehoe Orbit Drag, in Lunar and Planetary Science Conference, 1463

Watson, A. M., Stapelfeldt, K. R., Wood, K., & Ménard, F. 2007, Multiwavelength Imaging of Young Stellar Object Disks: Toward an Understanding of

Disk Structure and Dust Evolution, in Protostars and Planets V, ed. B. Reipurth, D. Jewitt, & K. Keil, 523. doi:10.48550/arXiv.0707.2608

Weber, P., Pérez, S., Guidi, G., et al. 2023, The SPHERE view of three interacting twin disc systems in polarized light, Monthly Notices of the Royal Astronomical Society, 518, 5620–5642. doi:10.1093/mnras/stac3478

Williams, J. P. & Cieza, L. A. 2011, Protoplanetary Disks and Their Evolution, Annual Review of Astronomy and Astrophysics, 49, 67–117. doi:10.1146/annurev-astro-081710-102548

Williams, M. & Mohanty, S. 2025, Ionization chemistry in the inner disc: a combined treatment of ionic and thermionic emission and arbitrary grain size distributions, Monthly Notices of the Royal Astronomical Society, 536, 1518–1537. doi:10.1093/mnras/stae2510

Winter, A. J., Clarke, C. J., Rosotti, G., et al. 2018, Protoplanetary disc truncation mechanisms in stellar clusters: comparing external photoevaporation and tidal encounters, Monthly Notices of the Royal Astronomical Society, 478, 2700–2722. doi:10.1093/mnras/sty984

Winter, A. J. & Haworth, T. J. 2022, The external photoevaporation of planet-forming discs, European Physical Journal Plus, 137, 1132. doi:10.1140/epjp/s13360-022-03314-1

Woitas, J., Eislöffel, J., Mundt, R., & Ray, T. P. 2002, The Environment of FS Tauri Observed with Hubble Space Telescope Wide Field Planetary Camera 2 in Narrowband Emission Line Filters, Astrophysical Journal, 564, 834–838. doi:10.1086/324274

Woitas, J., Leinert, C., & Köhler, R. 2001, Mass ratios of the components in T Tauri binary systems and implications for multiple star formation, Astronomy and Astrophysics, 376, 982–996. doi:10.1051/0004-6361:20011034

Woitke, P., Min, M., Pinte, C., et al. 2016, Consistent dust and gas models for protoplanetary disks. I. Disk shape, dust settling, opacities, and PAHs, Astronomy and Astrophysics, 586, A103. doi:10.1051/0004-6361/201526538

Wolff, S. G., Perrin, M. D., Stapelfeldt, K., et al. 2017, Hubble Space Telescope Scattered-light Imaging and Modeling of the Edge-on Protoplanetary Disk ESO-Hα 569, Astrophysical Journal, 851, 56. doi:10.3847/1538-4357/aa9981

Xiang-Gruess, M. 2016, Generation of highly inclined protoplanetary discs through single stellar flybys, Monthly Notices of the Royal Astronomical Society, 455, 3086–3100. doi:10.1093/mnras/stv2514

Yamato, Y., Aikawa, Y., Ohashi, N., et al. 2023, Early Planet Formation in Embedded Disks (eDisk). IV. The Ringed and Warped Structure of the Disk around the Class I Protostar L1489 IRS, Astrophysical Journal, 951, 11. doi:10.3847/1538-4357/accd71

Yang, L., Liu, D., Hao, C., et al. 2025, Kinematics of Young Stellar Objects under Various Stellar Feedback, Astrophysical Journal, Supplement, 276, 22. doi:10.3847/1538-4365/ad8d53

Youdin, A. N. 2010, From Grains to Planetesimals, in EAS Publications Series, ed. T. Montmerle, D. Ehrenreich, & A. M. Lagrange, 187–207. doi:10.1051/eas/1041016

Young, A. K., Alexander, R., Rosotti, G., & Pinte, C. 2022, Characteristics of small protoplanetary disc warps in kinematic observations, Monthly Notices of the Royal Astronomical Society, 513, 487–502. doi:10.1093/mnras/stac840

Young, A. K., Alexander, R., Walsh, C., et al. 2021, Chemical signatures of a warped protoplanetary disc, Monthly Notices of the Royal Astronomical Society, 505, 4821–4837. doi:10.1093/mnras/stab1675

Young, A. K., Stevenson, S., Nixon, C. J., & Rice, K. 2023, On the conditions for warping and breaking protoplanetary discs, Monthly Notices of the Royal Astronomical Society, 525, 2616–2631. doi:10.1093/mnras/stad2451

Zanazzi, J. J. & Lai, D. 2018a, Effects of disc warping on the inclination evolution of star-disc-binary systems, Monthly Notices of the Royal Astronomical Society, 477, 5207–5219. doi:10.1093/mnras/sty951

Zanazzi, J. J. & Lai, D. 2018b, Inclination evolution of protoplanetary discs around eccentric binaries, Monthly Notices of the Royal Astronomical Society, 473, 603–615. doi:10.1093/mnras/stx2375

Zanazzi, J. J. & Lai, D. 2018c, Planet formation in discs with inclined binary companions: can primordial spin-orbit misalignment be produced?, Monthly Notices of the Royal Astronomical Society, 478, 835–851. doi:10.1093/mnras/sty1075

Zapata, L. A., Rodríguez, L. F., Fernández-López, M., et al. 2020, Tidal Interaction between the UX Tauri A/C Disk System Revealed by ALMA, Astrophysical Journal, 896, 132. doi:10.3847/1538-4357/ab8fac

Zhang, S. & Zhu, Z. 2024, 3D Radiation-hydrodynamical Simulations of Shadows on Transition Disks, Astrophysical Journal, Letters, 974, L38. doi:10.3847/2041-8213/ad815f

Zhu, Z. 2019, Inclined massive planets in a protoplanetary disc: gap opening, disc breaking, and observational signatures, Monthly Notices of the Royal Astronomical Society, 483, 4221–4241. doi:10.1093/mnras/sty3358

Ziampras, A., Dullemond, C. P., Birnstiel, T., Benisty, M., & Nelson, R. P. 2024, Spirals, rings, and vortices shaped by shadows in protoplanetary disks: from radiative hydrodynamical simulations to observable signatures, arXiv e-prints, arXiv:2410.13932. doi:10.48550/arXiv.2410.13932

Ziampras, A., Sudarshan, P., Dullemond, C. P., et al. 2025, Dusty substructures induced by planets in ALMA discs: how dust growth and dynamics changes the picture, Monthly Notices of the Royal Astronomical Society, 536, 3322–3337. doi:10.1093/mnras/stae2751

Zsom, A., Ormel, C. W., Güttler, C., Blum, J., & Dullemond, C. P. 2010, The outcome of protoplanetary dust growth: pebbles, boulders, or planetesimals? II. Introducing the bouncing barrier, Astronomy and Astrophysics, 513, A57. doi:10.1051/0004-6361/200912976

Zuleta, A., Birnstiel, T., & Teague, R. 2024, Kinematical signatures: Distinguishing between warps and radial flows, Astronomy and Astrophysics, 692, A56. doi:10.1051/0004-6361/202451145

Zurlo, A., Weber, P., Pérez, S., et al. 2024, The environment around young eruptive stars. SPHERE/IRDIS polarimetric imaging of seven protostars, Astronomy and Astrophysics, 686, A309. doi:10.1051/0004-6361/202348526